Programme: **E-ELT**

Project: **ELT MCAO Construction – MAORY**

MAORY System Optical Design and Analysis Report

Document Number: E-MAO-SF0-INA-DER-001

Document Version: 02

Document Type: Design Report (DER)

Released On: 2021-01-29

	Name	Signature	Date
Owner :	Demetrio Magrin		31/12/2021
Approved by :	Paolo Ciliegi		
Released by :	Ugo Di Giammatteo		

Authors

Name	Affiliation
Demetrio Magrin	INAF - OAPD
Giorgio Pariani	INAF - OAB
Matteo Munari	INAF - OACT
Andrea Bianco	INAF - OAB
Maria Bergomi	INAF - OAPD
Gabriele Rodeghiero	INAF – OAS, OAAb
Davide Greggio	INAF - OAPD

Change Record from previous version

Date	Affected Section(s)	Changes / Reason / Remarks
2021-01-29	All	First draft issue
2021-31-21	4.1.5.7	PDR Action MAO-925: corrected DM2 conjugation altitude typo (from 6470km to 6501km) in section 4.1.5.7
2021-31-21	3.2.14	PDR Action MAO-925: substituted reflectance to transmittance in section 3.2.14
2021-31-21	All	PDR Action MAO-842: new acronyms for opto-mechanical components: Plate to CPM M6 to M6M M7 to M7M M8 to M8M M9 to M9M M10 to M10M M11 to M11M M12 to M12M Dichroic to Dichroic LGS FM1 to LGSO-FM1 LGS L1 to LGSO-L1 LGS L2 to LGSO-L2 LGS FM2 to LGSO-FM2 LGS L3 to LGSO-L3 LGS L4 to LGSO-L4 LGS FM3 to LGSO-FM3

2021-31-12	3.2.13	AOI dichroic typo. Corrected from 13.3 to 11.3 deg

Contents

Introduction

1.1 Purpose

This specific Design and Analysis Report describes the MAORY optical design and analysis at system level.

1.2 Scope

The present document describes the optical design the Main Path Optics and the LGS Objective of the proposed configuration, hereafter called MAORY MIRRORS SYSTEM (MMS). Furthermore, it includes the performance analysis and the tolerance analysis.

1.3 Acronyms and Abbreviations

µas	Micro Arc Second
µm	Micro Meter
µsec	Micro Second
AD	Applicable Document
AIV	Assembly Integration Verification
AO	Adaptive Optics
arcsec	Arc Second
BFD	Back Focal Distance
CCS	Central Control System
CoG	Centre of Gravity
CU	Calibration Unit
CUA	Calibration Unit Assembly
CM	Compliance Matrix
CPM	Co-rotating platform of MICADO
CTE	Coefficient of Thermal Expansion
DER	Design and Analysis Report
DM	Deformable Mirror
DOF	Degree Of Freedom
E2E	End to End
ELT (E-ELT)	European Extremely Large Telescope
EMC	Electro-Magnetic Compatibility
EQ	Earth Quake
ESD	Electro Static Discharge
ESO	European Southern Observatory

F#	F Number
FL	Focal Length
FoV (FOV)	Field of View
fps	Frame per second
FWHM	Full Width at Half Maximum
GD	Green Doughnut
HE	Heat Exchanger
HO	High Order
ICD	Interface Control Document
ICH	Instrument Control Hardware
ICS	Instrument Control System
INS	Instrument
IPAG	Institut de Planétologie et d'Astrophysique de Grenoble
I/F (IF)	Interface
I/O	Input / Output
IWS	Instrument Workstation
LA	Lenslet Array
LGS	Laser Guide Star
LGSO	LGS Objective
LGSWFS	Laser Guide Star Wavefront Sensor
LLT	Laser Launch Telescope
LO	Low Order
LOR	Low Order and Reference
LORWFS	Low Order and Reference Wave Front Sensor
LOWFS	Low Order Wavefront Sensor
M4	ELT Quaternary Adaptive Mirror
MAD	Multi-conjugate Adaptive Optics Demonstrator
MAORY	Multi-conjugate Adaptive Optics RelaY
mas	Milli Arc Second
MCAO	Multi-conjugate adaptive optics
MICADO	Multi-adaptive optics Imaging Camera for Deep Observations
MMS	MAORY Mirrors System
MOI	Moment Of Inertia
MPO	Main Path Optics

mrad	Milli Radian
msec	Milli Second
NA	Sodium
NHA	Next Higher Assembly
NLA	Next Lower Assembly
NGS	Natural Guide Star
NGSWFS	Natural Guide Star Wavefront Sensor
NP	Nasmyth Platform
N/A	Not Applicable
PCCB	Project Office Configuration Control Board
PD	Power Distribution
PDR	Preliminary Design Review
PFRO	Post Focal Relay Optics
PFS	Pre Focal Station
PLC	Programmable Logic Control
PS	Power Supply
PSF	Point Spread Function
PT	Product Tree
PtV (PV)	Peak To Valley
QE	Quantum Efficiency
RD	Reference Document
RMS (r.m.s.)	Root Mean Square
RSS	Root Square Sum
RTC	Real Time Computer
RWFS	Reference Wave Front Sensor
SA	Safety
SCAO	Single Conjugate Adaptive Optics
SCP	Service Connection Point
SFE	Surface Error
SH	Shack-Hartmann
SPE	Specification
SR	Strehl Ratio
SW	Software
S/N	Signal to Noise Ratio

TBC	To Be Confirmed
TBD	To Be Defined
TBV	To Be Verified
THCS	Thermal Control System
TIR	Total Internal Reflection
TNO	Technical Note
TT	Tip Tilt
VLT	Very Large Telescope
w.r.t.	With respect to
WCoG	Weighted Centre of Gravity
WFE	Wave Front Error
WFS	WaveFront Sensor

2. Related Documents

2.1 Applicable Documents

The following applicable documents form a part of the present document to the extent specified herein. In the event of conflict between applicable documents and the content of the present document, the content of the applicable document shall be taken as superseding (i.e. the present document does not supersede the MAORY requirements documentations when in disagreement).

AD1 MAORY Agreement ESO-281109 Version 1

AD2 MAORY (E-ELT MCAO) Statement of Work ESO-257875 Version 1

AD3 MAORY (E-ELT MCAO) Technical Specification ESO-254311 Version 1

AD4 Common Requirements for E-ELT Instruments ESO-254547 Version 2

AD5 Optical Design Technical Specifications E-MAO-SF0-INA-SPE-001_1D1

AD6 Common ICD between the E-ELT Nasmyth Instruments and the Rest of the E-ELT System ESO-253082, Version 3

AD7 Standard Coordinate Systems and Basic Conventions ESO-193058, Version 5

2.2 Reference Documents

The following documents, of the exact version shown herein, are listed as background references only. They are not to be construed as a binding complement to the present document.

RD1 Common ICD between the ELT Nasmyth Instruments and the Rest of the ELT System ESO-253082_4Draft

RD2 E-MAO-SF0-INA-SPE-001_1D1 Optical Design Technical Specifications

RD3 MAORY & MICADO Design Volume (DWG) CAD-118347_2

RD4 MAORY & MICADO Design Volume Location & Access (DWG) CAD-130610_1

RD5 E-MAO-SE0-INA-DER-001_01D1 MAORY System DESIGN REPORT

RD6 MICADO-MAORY I/F document (in progress)

RD7 CRE (ET-951) - MAORY second port technical requirements specifications_Part1

RD8 Relevant Atmospheric Parameters for E-ELT AO Analysis and Simulations ESO-258292

RD9 E-MAO-SF0-INA-MOD-001 MMS reference optical design (Zemax Model)

RD10 Rakich, A. “Optical systems capable of forming highly corrected images of 3-dimensional objects”, International Patent Application No. PCT/NZ2020/050105 (publication pending)

RD11 E-MAO-PD0-INA-ANR-001 Deformable Mirrors Analysis Report

RD12 E-MAO-PT0-INA-ANR-001 Thermal Control System Analysis Report

RD13 E-MAO-PF0-INA-ANR-001 Opto-Mechanical analysis

RD14 ESO-191766, E-ELT Environmental Conditions, v7

RD15 ELT-TNO-MCD-56304-0069_0.3_SpecsOpticalRelayFromScaoReqs

RD16 ESO-193058, Standard Coordinate Systems and Basic Conventions, v6

RD17 Performance and limitations of using ELT and MCAO for 50 μas astrometry, Rodeghiero, G. et al., Proc. of SPIE 2020.

RD18 E-MAO-SE0-INA-ANR-001 MAORY System Analysis Report

3. Nominal optical baseline configuration

A general description of MAORY instrument can be found in [RD5].

The MAORY optical system, basically, has to provide:

- The optical system has to provide an almost one-to-one image of the ELT focal plane to MICADO entrance focal plane (science FoV) and to the NGSWFS entrance focal plane (technical FoV).
- The optical system has to allow the separation between the beam incoming from infinite conjugated sources and the beam generated by the LGS conjugated at the sodium layer, then focused on the LGSWFS entrance focal plane.
- The optical system has to provide the possibility to accommodate up to two deformable mirrors (DMs) along the optical path conjugated at certain specific heights.
- The optical system has to provide the possibility to feed a second instrument and dedicated NGSWFS module having similar optical requirements and performance as MICADO.

In the previous phases of the project, several optical solutions have been studied and developed, spanning from parabolic mirrors designs to fully aspherical mirrors designs, from modified Offner designs to mixed aspherical/spherical mirrors designs. As far as the requirements maturity increased and the specification of the constraints (environmental and I/F) evolved, the baseline has been changed.

In this report, we describe the selected optical configuration, namely MMS (MAORY Mirrors System) and the related analysis.

3.1 MMS Nominal Optical Model description

The MMS configuration has been initially proposed by Bernard Delabre. It is based on 4 powered mirrors (2 aspherical and 2 spherical) able to deliver high quality in terms of WFE and field distortion. It is highly tolerant to defocus and astigmatism aberrations that can be compensated by acting on the last mirror with power. This configuration implements also the concept first introduced by Andrew Rakich of using an aspherical plate near the telescope focal surface to allow for the correction of multiple object conjugate distances [RD10]. By adding this correcting plate (CPM) close to the entrance focal surface, it is possible to greatly improve the quality of the exit pupil image, of the DMs meta-pupil image and of the LGS images at different conjugation altitudes, without degrading the quality for the infinite conjugated surface. We have re-optimized and adapted the general optical solution to the MAORY specific requirements and constraints.

The optical layout of the Main Path Optics (MPO) of MMS is shown in Figure 1. In the figure, blue rays represent the science and NGS path to MICADO, green rays represent the science beam path and NGS path to the second instrument, cyan rays represent the LGS path. Figure 2 shows the optical layout of the LGS Objective (LGSO. Light green and cyan rays represent the light incoming from two different LGS conjugation altitudes. In Figure 3 it is shown a 3D view of the MAORY optical configuration.

Most of the optical elements extend along a plane perpendicular to the ELT focal plane and to the Nasmyth platform. Such solution has been adopted in order to lower the center

of gravity of the whole system (ELT focal plane is located at 6 m above the Nasmyth platform) and to minimize the overall space-envelope. The mass budget is indeed quite limited forcing the opto-mechanical bench to develop along the vertical direction, increasing the stability at the same time.

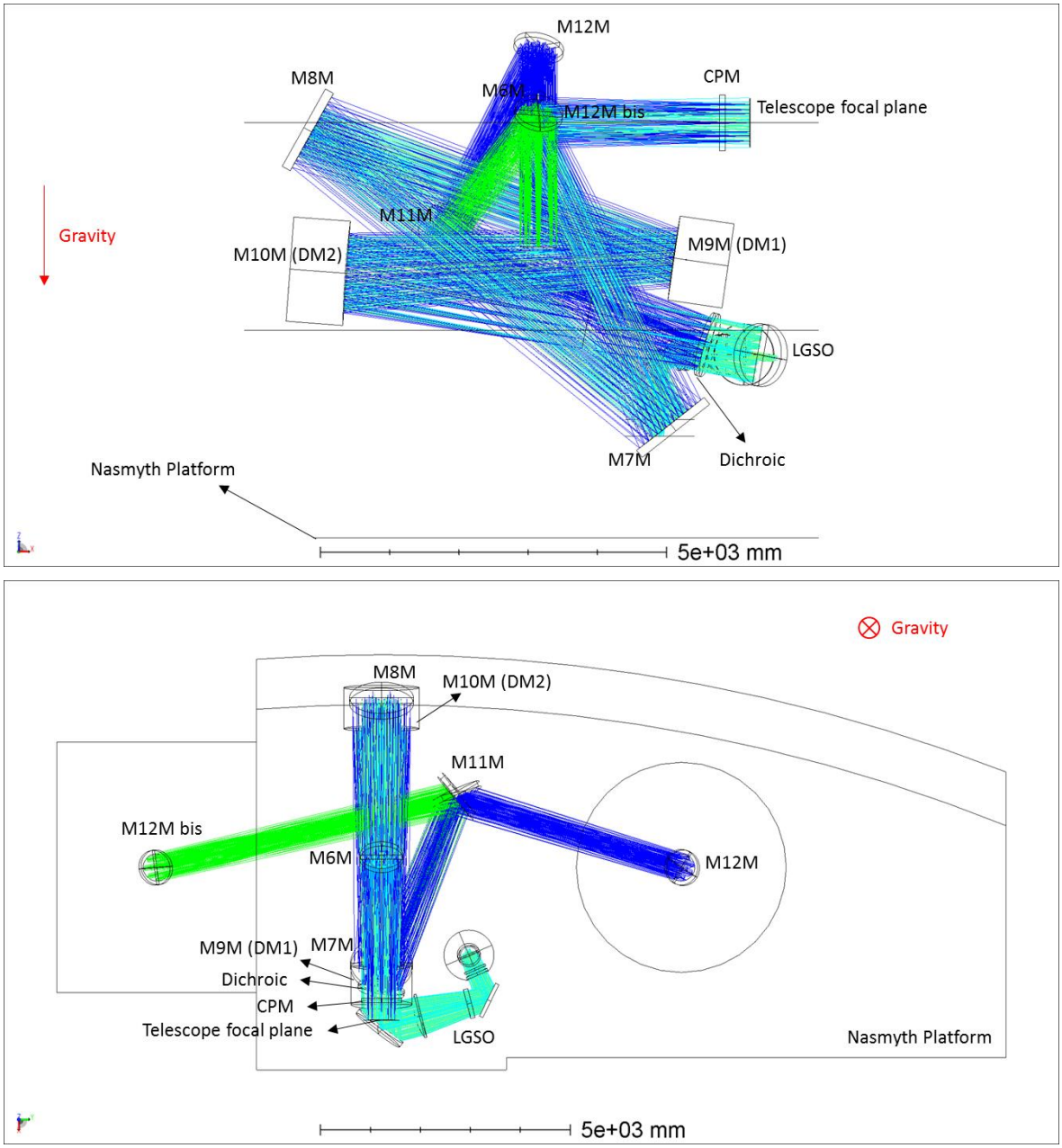

Figure 1. MPO MMS side view layout (top) and top view layout (bottom). Blue rays represent the science and NGS path to MICADO, green rays represent the science and NGS path to second instrument, cyan rays represent the LGS path.

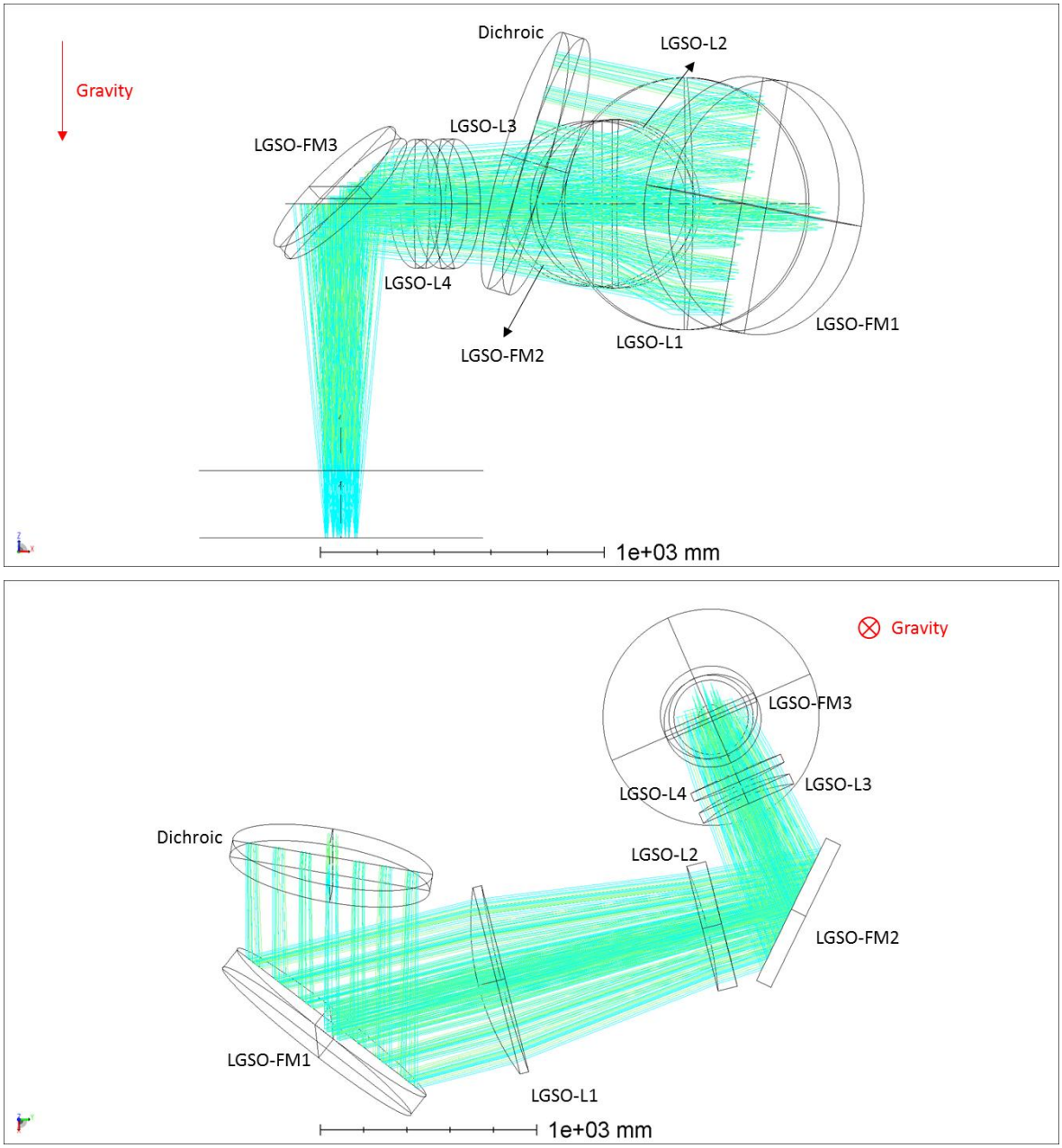

Figure 2. LGSO side view layout (top) and top view layout (bottom). The two colors represent rays incoming from two different LGS apparent conjugation altitudes.

The F/17.75 beam incoming from the ELT focal surface initially passes through the CPM. It is a window that thermally separates the external and internal environment. The second surface of the CPM is aspherical and allows increasing the quality of multiple object conjugated distances. Following the path, there is a first flat mirror, M6M, folding the beam down to the first aspherical concave mirror M7M. The beam is reflected up to the second aspherical concave mirror M8M, and then down again towards the first DM, M9M, having spherical surface (conjugated to the meta-pupil at 17.5 km). This mirror is the only convex surface of the main path. After that, the beam is reflected by the second DM, M10M,

which is concave and spherical (conjugated at meta-pupil at 6.5 km). For the time being, the decision to install or not the second DM has not been already taken. However, the optical configuration has been designed to accommodate it. If this element will be not a deformable mirror, it will be substituted with a monolithic mirror with the same optical characteristics. All the other optical surfaces downstream M10M are flat.

After M10M, the image of the pupil is formed, and just after this image, the light is separated between science and NGS light and LGS light by means of a dichroic filter (DICHROIC). The LGS light (589 nm) is transmitted, while science and NGS light (>600nm-2400nm) is reflected. The reflected light then reaches M11M, a flat flip mirror that allows the selection of the MICADO path or of the second instrument path through a rotational axis. Finally, the light is reflected by a flat mirror, M12M (or M12M bis), installed over MICADO (or, as previously mentioned, some future second instrument) and comes to a focus at the gravity invariant entrance focal surface of the instruments. MICADO and the second instrument share the DMs and the LGS WFS module, while the NGS WFS module is duplicated. Focal surfaces delivered to MICADO and to the second instrument have the same nominal performance characteristic.

The LGS Objective (LGSO) reduces the LGS beam F/# at wavelength 589 nm from about 19 at the dichroic to 5 at the LGS WFS module entrance focal surface. It is composed of four silica spherical lenses (LGSO-L1, LGSO-L2, LGSO-L3 and LGSO-L4) and three fold mirrors (LGSO-FM1, LGSO-FM2 and LGSO-FM3). The first two mirrors have been introduced in order to maintain the objective within the available envelope, while the third mirror allows to feed the LGS module with a gravity invariant and telecentric focus. The LGS asterism required by MAORY is fixed to field angle 45 arcsec with a FoV of ± 16.8 arcsec (LGS elongation). As the ELT declination angle varies (Zenith angle 0-60 degrees), the LGS launchers will maintain the LGS sources on the sodium layer at the fixed angle of 45 arcsec. Thanks to the telecentric beam and the constant F/# delivered by the LGSO, the radial coordinate of the LGS images on the LGSO focal surface will not change as the apparent altitude (84-180 km above entrance pupil) of the sodium layer varies. In this way, the LGS module just needs to rotate around its central axis and to move up and down in order to follow the declination variation effect.

The main optical parameters of the Main path and LGS path are reported in Table 1.

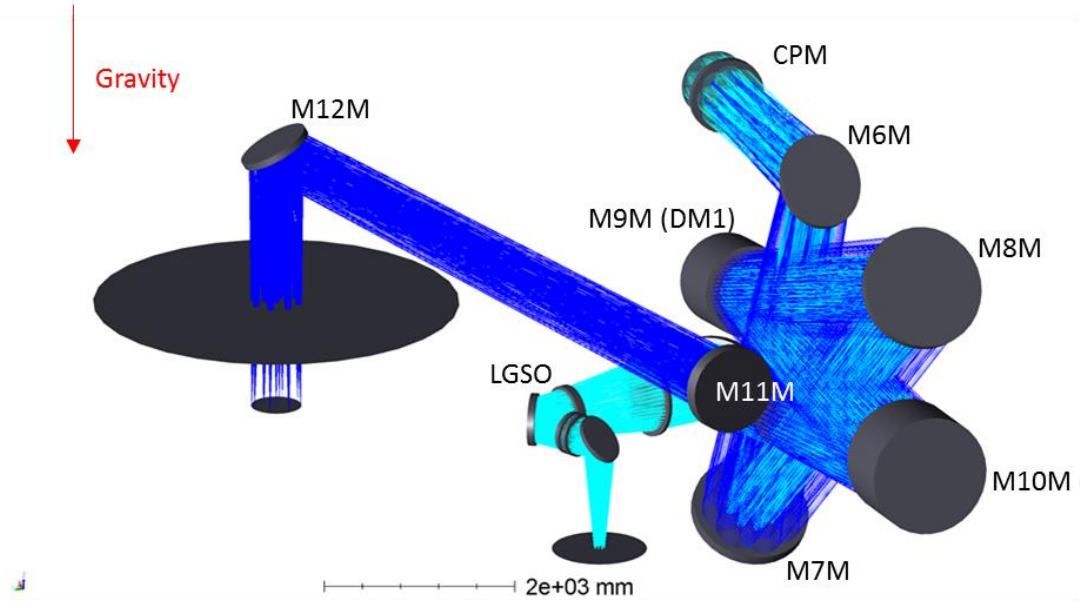

Figure 3. 3D view of the MAORY optical configuration. Blue rays represent the science and NGS path to MICADO, cyan rays represent the LGS path.

MAIN PATH		
Image space F/#	17,755	
Effective focal length	684302	mm
Plate scale	0,3014	arcsec/mm
Entrance pupil diameter	38542	mm
Entrance pupil obstruction diameter	10952	mm
Scientific FoV diameter	76	arcsec
Technical FoV diameter	160	arcsec
Field curvature	infinity	mm
Exit pupil distance	14361	mm

LGS PATH		
Image space F/#	5,025	
Sodium layer conjugation range	84-180	km
Effective focal length	193645	mm
Plate scale	1,065	arcsec/mm
LGS asterism radius	45	arcsec
LGS FoV	±15	arcsec
Field curvature	infinity for 45 arcsec asterism	mm
Exit pupil distance	infinity	mm

Table 1. Main optical parameters of the main path (left) and the LGS path (right).

Table 2 and Table 3 report the optical elements data for the MPO and LGSO of MMS respectively.

In the tables, for each element, it has been specified:

- Type: it is an etiquette determining the optical shape or the functionality of the element.
- Surface: in case of refractive elements, S1 represents the front surface while S2 represents the rear surface.
- Radius of curvature: values are given with respect to the Local Reference System (see Appendix 7), i.e. the native Zemax raytracing software local coordinate system.
- Thickness: for refractive elements it represents the central thickness; in case of reflective elements it represents the thickness of the glass substrate; in case of deformable mirrors it represents the maximum linear envelope of the whole element structure. For mirrors, the substrate thickness has been set to 1/10 of the

glass aperture. This value has to be intended as maximum thickness (i.e. safe envelope) given that smaller thicknesses have been analysed down to 1/20 of the glass aperture in order to diminish the impact on the overall mass budget.

- Material: material of the optical element/substrate.
- Concavity: concavity of the surface. CV = concave, CX = convex.
- Aspheric terms: CPM second surface, M7M and M8M aspheric components have been expressed through Zernike standard sag definition (native in Zemax raytracing software). For each surface it has been specified the normalization radius of the Zernike surface. Z6 = astigmatism, Z7 = coma, Z9 = trefoil, Z11 = spherical aberration, Z12 = 2^{nd} astigmatism. Values are given with respect to the Local Reference System.
- Aperture type: shape of the aperture. In case of elliptical aperture, X axis and Y axis are given.
- Clear aperture: it has to be intended as the clear aperture of the nominal design.
- Mechanical aperture: it has to be intended as aperture of the physical glass/substrate of the optical element. For most of the optics (the larger ones), we have assumed an enlargement of 100 mm over the diameter with respect to the clear aperture. We are assuming the first +50 mm are polished surface accounting margins for footprints shifts, while the second +50 mm represent the margins for edge polishing m and, eventually, for mounting clips that may introduce vignetting.
- Aperture decenter: decenter of the aperture center in X and Y direction with respect to the surface local reference system.
- Coating: coating name or coating functionality.

Due to internal consortium strategy during the AIV phase and in order to minimize the impact on the schedule due to DMs delivery time, monolithic versions (simulacra) of the DMs are required.

MMS main path

	type	Surface	Radius of curvature [mm]	Thickness optic/substrate [mm]	Material	Concavity
CPM	entrance window	S1	infinity	85	suprasil 3002	Flat
		S2	infinity			Flat
M6M	Fold 1		infinity	100	zerodur	Flat
M7M	Free Form 1		-35094.937	124	zerodur	CV
M8M	Free Form 2		38403.193	128	zerodur	CV
M9M DM1 Simulacrum	Deformable Mirror		15456.015	98	zerodur	CX
M10M DM2 Simulacrum	Deformable Mirror		14946.890	126	zerodur	CV
Dichroic	Dichroic	S1	infinity	80	suprasil 3002	Flat
		S2	infinity			Flat
M11M	Fold2-Flip mirror		infinity	122	zerodur	Flat
M12M	Fold 3		infinity	78	zerodur	Flat

	Aspheric terms						
	type [mm]	Normalization radius [mm]	Z6 [mm]	Z7 [mm]	Z9 [mm]	Z11 [mm]	Z12 [mm]
CPM							
	Zernike Standard Sag	350	8.02336E-02	9.06846E-03	-2.52709E-04	-1.14298E-03	
M6M							
M7M	Zernike Standard Sag	570.240	1.33808E-02	9.15126E-03	3.88534E-04	8.19550E-04	3.21440E-05
M8M	Zernike Standard Sag	585.621	6.04576E-02	6.01545E-03	1.76372E-04	3.59100E-04	3.84119E-06
M9M DM1 Simulacrum							
M10M DM2 Simulacrum							
Dichroic							
M11M							
M12M							

	type	Aperture type	Clear Aperture [mm]	Mechanical Aperture [mm]	Aperture decenter X[mm]; Y[mm]	Coating
CPM	entrance window	circular	710	810	0; 0	AR (0.589-2.4 µm)
		circular				
M6M	Fold 1	elliptical	760x900	860x1000	0; 10	Protected Silver
M7M	Free Form 1	circular	1140	1240	0; 0	Protected Silver
M8M	Free Form 2	circular	1180	1280	0; 0	Protected Silver
M9M DM1 Simulacrum	Deformable Mirror	circular	880	980	0; 0	Protected Silver
M10M DM2 Simulacrum	Deformable Mirror	circular	1164	1264	0; 0	Protected Silver
Dichroic	Dichroic	circular	840	940	0; 0	Special
		circular			0; 0	AR (0.589 µm)
M11M	Fold2-Flip mirror	elliptical	1120x820	1220x920	7; 3	Protected Silver
M12M	Fold 3	elliptical	600x674	700x774	0; -2	Protected Silver

Table 2. MMS MPO elements data.

MMS LGS Objective

	type	Surface	Radius of curvature [mm]	Thickness [mm]	Material
LGSO-FM1	Fold 1		infinity	111	zerodur
LGSO-L1	meniscus	S1	-1210.000	108	silica
		S2	-5621.000		
LGSO-L2	meniscus	S1	2077.000	70	silica
		S2	infinity		
LGSO-FM2	Fold 2		Infinity	74	zerodur
LGSO-L3	meniscus	S1	-746.700	40	silica
		S2	-1031.500		
LGSO-L4	biconvex	S1	1831.500	60	silica
		S2	-4943.000		
LGSO-FM3	Fold 3		Infinity	60	zerodur

	Concavity	Aperture type	Clear Aperture [mm]	Mechanical [mm]	Aperture decenter X[mm]; Y[mm]	Coating
LGSO-FM1	Flat	elliptical	1010x800	1110x900	1; 0	Laser Line (0.589 µm)
LGSO-L1	CX	circular	788	888	0; 0	AR (0.589 µm)
	CV					AR (0.589 µm)
LGSO-L2	CV	circular	534	594	0; 0	AR (0.589 µm)
	CX					AR (0.589 µm)
LGSO-FM2	Flat	elliptical	632x484	732x584	-18; 0	Laser Line (0.589 µm)
LGSO-L3	CV	circular	416	456	0; 0	AR (0.589 µm)
	CX					AR (0.589 µm)
LGSO-L4	CX	circular	414	454	0; 0	AR (0.589 µm)
	CX					AR (0.589 µm)
LGSO-FM3	Flat	elliptical	354x500	454x600	0; -25	Laser Line (0.589 µm)

Table 3. MMS LGSO elements data.

3.1.1 Mathematical model description

The mathematical model, describing the nominal optical design, has been implemented in the Zemax ray-tracing software file: E-MAO-SF0-INA-MOD-001 MMS reference optical design [RD9]. Such model has been used for the nominal design and performance analysis. The ELT optical recipe [RD1] has been implemented in the Zemax model.

The Zemax model implements eight configurations:

- **Configuration 1**: it describes the main path optical train from the ELT entrance focal plane to the MICADO and technical focal plane. The sources are at infinite distance; the circular FoV diameter is 160 arcsec (MICADO FoV diameter is 76 arcsec); the ELT entrance pupil determines the optical system aperture; the reference wavelengths are 1 µm, 1.65 µm and 2.2 µm.
- **Configuration 2**: it describes the main path optical train from the ELT entrance focal plane to the second instrument focal plane. The sources are at infinite distance; the circular FoV diameter is 160 arcsec; the ELT entrance pupil determines the optical system aperture; the reference wavelengths are 1 µm, 1.65 µm and 2.2 µm. The selection between MICADO and second instrument port is obtained by flipping the fold mirror M11M.
- **Configuration 3**: it describes the optical path from the high metapupil layer to DM (M9M). The sources are on the meta-pupil and at the meta-pupil distance; the FoV is determined by the meta-pupil diameter; the optical system aperture is determined by the cone angle of aperture 160 arcsec and by imposing the telecentricity in the object space. The reference wavelengths are 1 µm, 1.65 µm and 2.2 µm.
- **Configuration 4**: it describes the optical path from the low metapupil layer to DM (M10M). The sources are on the meta-pupil and at the meta-pupil distance; the FoV is determined by the meta-pupil diameter; the optical system aperture is determined by the cone angle of aperture 160 arcsec and by imposing the telecentricity in the object space. The reference wavelengths are 1 µm, 1.65 µm and 2.2 µm.
- **Configuration 5**: it describes the optical path from ELT entrance pupil and the main path exit pupil. The sources are on the entrance pupil; the FoV is determined by the entrance pupil diameter; the optical system aperture is determined by the cone angle of aperture 76 arcsec and by imposing the telecentricity in the object space. The reference wavelengths are 1 µm, 1.65 µm and 2.2 µm.
- **Configuration 6**: it describes the optical path from sodium layer at lower altitude (zenith angle 0 degrees) and the LGSWFS module entrance focal plane. The sources are at the sodium layer; the FoV is determined by an annulus having diameter 45 +/- 15 arcsec; the ELT entrance pupil determines the optical system aperture. The reference wavelength is 0.589 µm.
- **Configuration 7**: it describes the optical path from sodium layer at medium altitude (zenith angle 30 degrees) and the LGSWFS module entrance focal plane. The sources are at the sodium layer; the FoV is determined by an annulus having diameter 45 +/- 15 arcsec; the ELT entrance pupil determines the optical system aperture. The reference wavelength is 0.589 µm.

- **Configuration 8**: it describes the optical path from sodium layer at higher altitude (zenith angle 60 degrees) and the LGSWFS module entrance focal plane. The sources are at the sodium layer; the FoV is determined by an annulus having diameter 45 +/- 15 arcsec; the ELT entrance pupil determines the optical system aperture. The reference wavelength is 0.589 µm.

3.2 MMS design drivers, design constraints and design performance requirements

The optimization of the optical design has followed the evolution of the constraints and the maturity process of the requirements. Moreover, the design optimization has dealt with some not formalized desiderata. In particular, at the time being, the optical I/F with MICADO has not been completely frozen. In this section, we reported the constraints and the requirements, which drove the optimization process, and we show how the MMS baseline meets them.

3.2.1 General requirements, envelope constraints, I/F positioning requirements, gravity invariance

MAO-SF0-1.2.3.5: *PFRO shall define position and shape of the optics for the primary path [RD2].*

The MMS main path optics position and shape are defined by mean of the Zemax model [RD9].

MAO-SF0-1.3.1: *When applicable SF0 shall comply with the interfaces specified in ESO-253082 i.e. MAO-SF0-3 [RD2].*

The model of the telescope has been implemented in the ZEMAX model [RD9] following the recipe in the appendix of RD1. This document has been used as input for the optical I/F with the telescope. In the following, we explicitly report the relevant contents and the reference to RD1, when needed.

MAO-SF0-1.2.2.1: *Unless otherwise explicitly indicated, all the dimensions in drawings CAD-118347 [RD3] and CAD-130610 [RD4] shall be assumed to be valid at 20°C (ISO 1) [RD2].*

In the Zemax model [RD9], the temperature has been set to 20°C.

These two drawings RD3 and RD4 define the coordinates system and the envelope available for the installation MAORY and MICADO over the Nasmyth A at Focus A. The same envelope has been accounted during the design optimization and it has been superimposed to the optical layout in Figure 1. The optical layout is enclosed in the envelope but for the second instrument port, not accounted in the MICADO – MAORY envelope drawings.

Desideratum: the MMS has been designed and folded in order to minimize the overall space envelope and to minimize the center of gravity height over the Nasmyth platform with the aim to minimize the overall mass.

Desideratum: the MMS opto-mechanics have been oriented in order to minimize the number of attachment points to 3 on the Nasmyth platform, reducing the impact on the overall mass and on the potential distortion induced by the Nasmyth deformations, with the aim to increase the stability of the system.

I-INS/ELT-118: *The foci shall be at the nominal positions given in the following table expressed in the azimuth coordinate system [RD1]:*

			X		Y		Z
Surface			mm		mm		mm
Straight Through Focus (A1)							
Object at Infinity			-27200		0		0

We have defined the MAORY standard coordinate system [RD5], having origin on the nominal ELT focal plane (Focus A1) for object at infinity, X axis pointing to the ELT M5 and normal to gravity and Z parallel and opposite to gravity (see also appendix 7).

MAO-SF0-1.3.4.2: *The output port on MICADO shall be located in X=-3050mm, Y=+6000mm, Z=-1800mm in the* MAORY standard reference system [RD2].

MMS has been designed to have the output focal plane at these coordinates. In particular, X and Y specifications are the chief ray coordinates of the central field.

MAO-SF0-1.2.3.7: *PFRO shall define the volume of the primary port optical beam [RD2].*

The Zemax model [RD9] defines the optical beam path from ELT focal plane to MICADO entrance focal plane (Science and technical FoV). The optics size and position have been set to avoid aperture or mechanical vignetting. The verification has been done on the Zemax model [RD9].

MAO-SF0-1.3.4.20: *The PFRO design shall allow to the MICADO instrument to be gravity invariant [RD2]*.

The focal plane of MICADO is normal to the gravity. MMS achieves it through the flat mirror M12M, installed above MICADO structure.

Desideratum: MMS has no optics over MICADO envelope area, apart for M12M that is mounted directly over the MICADO structure and it is mechanically decoupled from MAORY structure. This allows install/uninstall/maintenance activities on MAORY and MICADO separately, minimizing the mutual procedure impacts.

The MICADO envelope area considered (see Figure 1) is a cylinder centred at X=-3050mm, Y=+6000mm, Z=-6000mm, having diameter 3850mm and height 5350mm. This envelope is mimicking the top part of MICADO envelope, where possible mechanical interferences and beam vignetting can most likely occur.

MAO-SF0-1.2.3.4: *PFRO shall be designed to provide SCAO mode with telescope M4 [RD2].*

MICADO will already mount a single conjugated adaptive optics unit in stand-alone mode. MMS main path allows the SCAO mode by design (Zemax model [RD9]), assuming the capability of the post focal DMs to maintain the nominal static shape.

MAO-SF0-1.2.3.8: *PFRO shall provide an upgrade path to direct the science beam to a second instrument port [*RD2*].*

MMS can feed the two output ports by flipping the flat mirror M11M (port selector device). Given that there are no more optical elements with power in the optical path downstream M11M, the nominal optical parameters and performances for the two ports are nominally the same.

MAO-SF0-1.2.3.11: *For the second port client, MAORY shall provide:*

a) Deformable mirror(s)

b) Optical relay (up to the exit port selector device, excluded if not shared with MICADO)

c) Laser Guide star wavefront sensors module

d) Dichroic beam splitter for the LGS beams

e) Access to the calibration units (MAORY and MICADO).

*The above components shall be shared with MICADO, without duplication of hardware [*RD2*].*

This requirement affects the optical design by constraining the position along the optical path where the port selecting device is placed. For the MMS, the selection is achieved by flipping the flat mirror M11M. M11M is located along the optical path after the DMs and the dichroic, allowing the common use also of the LGS module.

MAO-SF0-1.2.3.9: *MAORY shall deliver a second port output focus located inside the second instrument design volume, with the following coordinates:*

- X focus = -30250 +/- 250 mm

- Y focus = -4500 +/- 250 mm

- -2000 mm < Z focus < 0 mm

given in the Telescope Azimuth Structure coordinate frame.

The focus output position may be reached by using one last folding mirror located inside the second instrument design volume and part of the second instrument [RD2].

In the MAORY standard coordinate system, these correspond to X = -3050+/-250mm, Y = -4500+/-250mm, -2000mm < Z < 0 mm. MMS has been designed to deliver the second port focal plane at coordinates X=-3050mm, Y=-4500mm, Z=-1800mm, mimicking MICADO focal plane position in a specular way. We have assumed the installation of a flat mirror (M12Mbis) over the second instrument structure, similarly as in MICADO.

MAO-SF0-1.2.3.13: *the PFRO shall define the volume of the secondary port optical beam [RD2].*

The Zemax model [RD9] defines the optical beam path from ELT focal plane to second instrument entrance focal plane (Science and technical FoV). The optics size and position have been set to avoid aperture or mechanical vignetting. The verification has been done on the Zemax model [RD9].

MAO-SF0-1.2.3.20: *MAORY's second port shall provide a gravity invariant focus with an output optical axis oriented along gravity [RD2].*

MMS provides a beam over the second instruments that can be bended along the gravity and focused at the second instrument focal plane by mean of flat mirror M12Mbis. M12Mbis is not part of the consortium deliverable.

MAO-SF0-1.2.3.10 Secondary port focal extraction: *The back focal distance defined as the distance between the second port's focal plane and the closest physical surface (optical or mechanical) of MAORY shall be at least 1 m [RD2].*

None of the opto-mechanical elements of the MMS is closer than 1 m to the second instrument focal plane, as shown in Figure 1. However, M12Mbis will be mounted over the second instrument structure.

MAO-SF0-1.3.3.5.11: *The PFRO design shall allow the LGSWFS subsystem to be gravity invariant [RD2].*

The last flat mirror LGSO-FM3 of LGSO allows to deliver a gravity invariant focal plane to the LGS WFS subsystem.

3.2.2 Wavelength range

We have assumed MICADO and the second instrument working in J, H and K bands. The reference wavelengths for the simulations are 1 µm, 1.65 µm and 2.2 µm.

MAO-SF0-1.3.3.5.12: *LGS WFS shall operate in 589 nm narrowband [RD2].*

The reference wavelength for the simulations is 0.589 µm.

The NGSWFS implements the LOR, working in J band, and the RWFS, working the wavelength range 0.6-1.0 µm. The reference wavelengths for the simulations are 1.65 µm and 0.8 µm respectively.

The SCAO WFS works in the wavelength range 0.6-1.0 µm. The reference wavelength for the simulations is 0.8 µm.

3.2.3 Entrance pupil

The entrance pupil of the ELT model is circular and diameter has been set to 38542 mm (I-INS/ELT-151 [RD1]) with a central circular obscuration has a diameter equal to 10952 mm (I-INS/ELT-153 [RD1]).

3.2.4 Effective focal length and plate scale

MAO-SF0-1.2.3.16: *The MAORY optics shall, as a design goal, provide a plate scale of 0.3016+/-0.0013 arcsec/mm (this is equal to 3.316+/-0.014 mm/arcsec) [RD2].*

This requirement refers to the main path; it is stating that the MAORY has to deliver an almost one to one focal plane image from ELT to MICADO.

The effective focal length of the MMS main path has been computed as follow: we have considered the centroid coordinates on the exit focal plane of 4 fields having sky coordinates A = (1; 0), B = (-1; 0), C = (0; 1) and D = (0; -1) arcsec. We have computed the half-linear distance along the two directions, i.e. (A-B)/2 and (C-D)/2, and then we took the average of the obtained values. By dividing the result by 1 arcsec (in radians), we obtain that the MMS main path EFL is 684302 mm. The computation was done at wavelength equal to 1 µm. By repeating the same computation at wavelengths 1.65 µm and 2.2 µm, we obtained the same value for the plate scale. Results are summarized in Table 4.

Wavelength	EFL	Plate scale
[µm]	[mm]	[arcsec/mm]
1	684302	0,3014
1,65	684307	0,3014
2,2	684312	0,3014

Table 4. MMS main path effective focal length and plate scale for the three reference wavelengths.

The MMS main path plate scale is 0.3014 arcsec/mm (3.318 mm/arcsec). The same computation and results are valid for the second port instrument.

The LGSO has a paraxial effective focal length equal to 192710 mm (entrance pupil diameter × F number). We have done a similar computation as for the main path. The results are reported in Table 5.

sodium layer height	EFL	plate scale
[Km]	[mm]	arcsec/mm
84	193645	1,065
100	193654	1,065
180	193677	1,065

Table 5. MMS LGSO effective focal length and plate scale for the three reference sodium layer heights.

3.2.5 Field of views

MAO-SF0-1.2.3.19: *the PFRO shall be designed to deliver a field of view of at least 160 arcsec diameter at the LOR focal plane [RD2].*

MAO-SF0-1.3.4.1: *the PFRO shall be designed to deliver a field of view of at least 75 arcsec diameter at the MICADO instrument port [RD2].*

The MMS has been designed assuming a circular technical FoV having diameter of 160 arcsec.

For MICADO, it has been assumed a square focal plane assembly having size 53 arcsec, i.e. having a diagonal of about 75 arcsec. The MMS has been designed assuming a circular MICADO FoV having diameter of 76 arcsec.

MAO-SF0-1.2.3.12: *the PFRO shall be designed to deliver an unvignetted field of view of at least 2.5 arcmin diameter at the secondary port [RD2].*

The MMS has been designed to deliver to the second port instrument a circular FoV having maximum diameter equal to the 160 arcsec (2.67 arcmin). However, in the following, for the computation of the optical parameters and performances, we have assumed a second instrument scientific FoV equal to the MICADO one.

MAO-SF0-1.3.4.15: *MICADO SCAO mode has a NGS WFS patrolling a field of 38 arcsec diameter. [RD2].*

The MMS allows the SCAO NGSWFS patrolling FoV.

MAO-SF0-1.2.4.1: *MAORY shall be capable of observing at zenith angles greater than 1.5 degrees and smaller than 60 degrees. Operation with lasers is restricted to zenith angle < 60 degrees [RD2].*

MAO-SF0-1.2.3.3: *LGS WFS subsystem shall implement 6 WFS units in on-sky hexagonal geometry (eventually compatible with 8), arranged on an asterism of 45 arcsec radius. [RD2].*

MAO-SF0-1.2.3.18: *The sodium layer median altitude is 87-93 km at zenith above sea level, and 186 km at zenith angle = 60 degrees [RD2].*

In [RD8], section 3.2.1 Sodium layer profile, it is stated that the centroid altitude of the sodium layer profile is 90 Km above the sea level, while the centroid altitude range is 87-93 Km above the sea level. ELT will be located in the Cerro Armazones (Chile) at an altitude of 3 Km above the sea level. This translates in a relative distance between the centroid altitude range of the sodium layer profile and ELT of 84-90 Km.

At zenith angle = 0 degrees, the lower altitude of the sodium profile centroid is 84 km. At zenith angle = 60 degrees, the higher altitude of the sodium layer profile centroid is 180 Km.

For the MMS design, we have assumed 84-180Km as the altitude range for the sodium profile centroid, i.e. the minimum and the maximum distance between the ELT entrance pupil and the LGS sources.

The LGS asterism is fixed on the sky (the laser launchers compensate for sodium layer different apparent altitudes as the zenith angle varies) and have an asterism of 45 arcsec, i.e. the chief ray angle subtended at the entrance pupil center is 45 arcsec, despite the sodium layer profile centroid altitude.

MAO-SF0-1.3.3.5.1: *The FoV delivered to LGS WFS is 16.8 x 16.8 arcsec (square) [RD2].*

At the entrance focal plane of the LGS module, for each LGS WFS, it is placed a squared mask having angular size 16.8 arcsec (diagonal about 23.8 arcsec), which defines the local FoV for each WFS unit.

We have assumed a circular LGS WFS FoV equal to 30 arcsec, accounting for possible redefinition of the mask size and including margins.

Summarizing, the MMS has been optimized assuming an annular LGS FoV of 45±15 arcsec. The lower object plane height is 84 km (zenith angle = 0 degrees) over the entrance pupil while the higher object plane height is 180 km (zenith angle = 60 degrees) over the entrance pupil. In the following analysis, the reference altitudes for the sodium profile centroid are 84 km (zenith angle 0 degrees), 100 km (zenith angle 30 degrees) and 180 km (zenith angle 60 degrees)

A scheme of the assumed Field of Views during the design for MICADO, technical FoV and LGS asterism and LGS WFS FoV is shown in Figure 4.

Such FoV definitions have been used to define the nominal clear aperture of the optical elements of the MMS. In the MPO, the clear aperture is determined by the technical FoV but for the entrance CPM and the dichroic, where the footprint of the 84 km LGS asterism is the largest. In the LGSO, footprint of 84 km LGS asterism determines the nominal clear aperture of the optical elements.

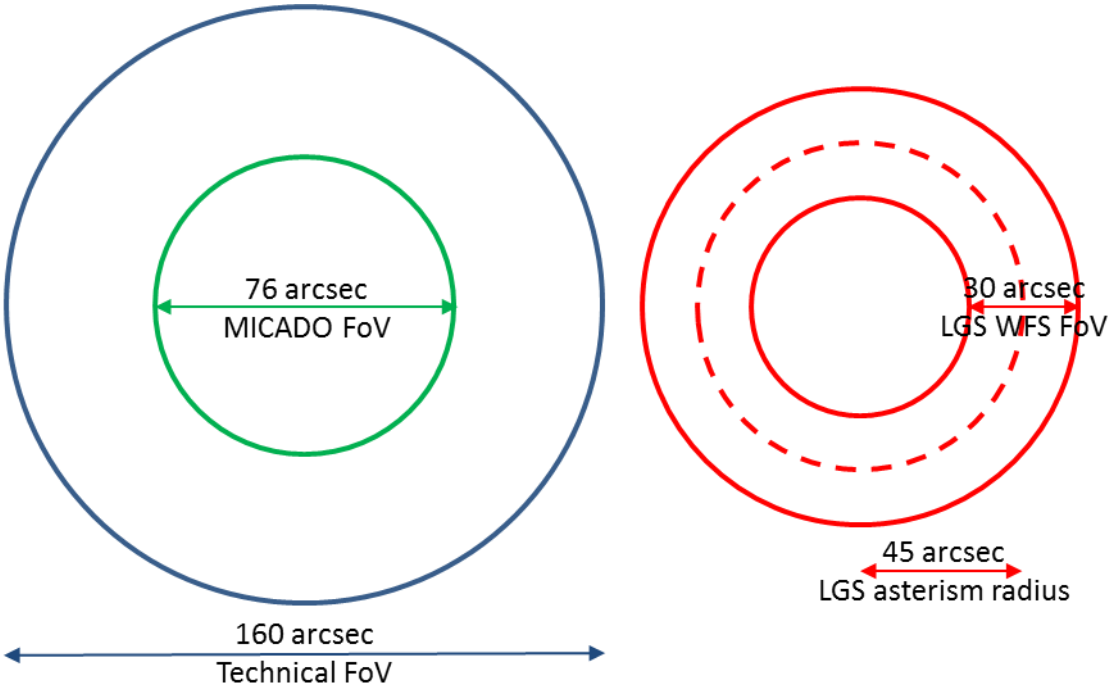

Figure 4. MICADO FoV in green line. Technical FoV in blue line. LGS asterism radius in red line dashed line.

MAO-SF0-1.3.3.5.20: *The LGS asterism centroids shall be imaged by the PFRO within the annulus 45 +/- 0.5 arcsec at the LGS WFS entrance focal plane, assuming a paraxial F number equal to 5, for each sodium layer altitude in the working range [RD2].*

This requirement assures that LGS images delivered at LGSO focal plane are within the acceptance range of the LGS WFS module, avoiding the need to apply a radial correction as sodium layer apparent altitude varies.

The centroid radial positions of the LGS 45 arcsec asterism in the LGSO focal plane along the full azimuthal angle for the LGS reference heights are shown in Figure 5.

Assuming paraxial F/# equal to 5, the paraxial effective focal length is equal to 192710 mm, giving a requirement linear range of 42.043 +/- 0.467 mm. Nominally, the LGSO delivers the LGS 45 arcsec asterism image in a circle having average radius 42.25 mm with negligible dispersion. The discrepancy (0.21 mm) with respect to 42.04 mm is due to the fact that the LGSO departs from a paraxial system. The plate scale of the system is given in Table 5. However, this small difference can be compensated during the integration of the LGS WFS channels.

We have done a similar computation also for circular fields having asterism radius at 30 arcsec and 60 arcsec (see Figure 6). Assuming the paraxial focal length, the two corresponding annulus are 28.029 +/- 0.467 mm and 56.057 +/- 0.467 mm respectively. The nominal radius of the two asterisms is about 28.17 mm and 56.34 mm respectively.

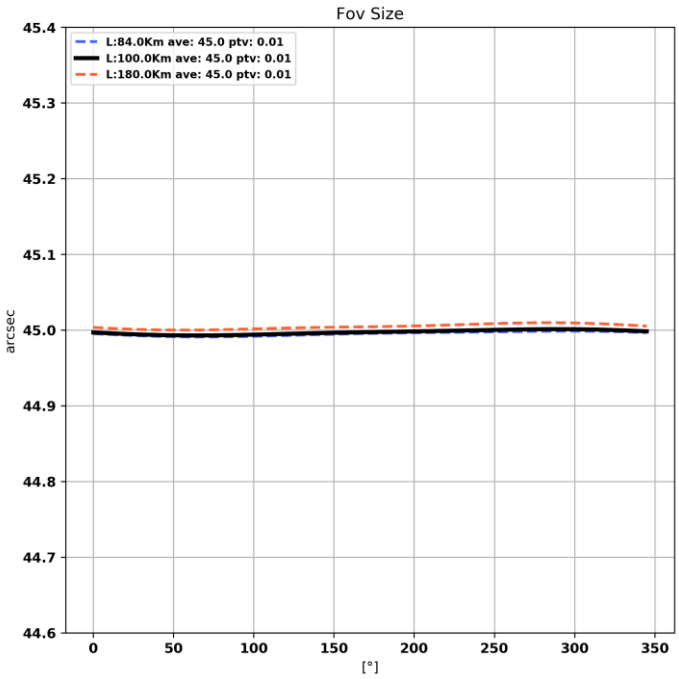

Figure 5. Centroid radial positions of the LGS 45 arcsec asterism in the LGSO focal plane along the full azimuthal angle for the LGS reference heights.

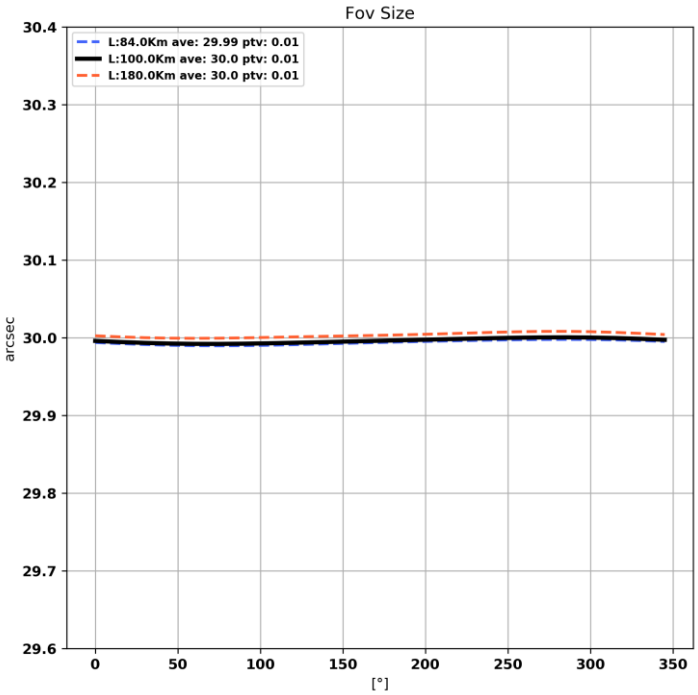

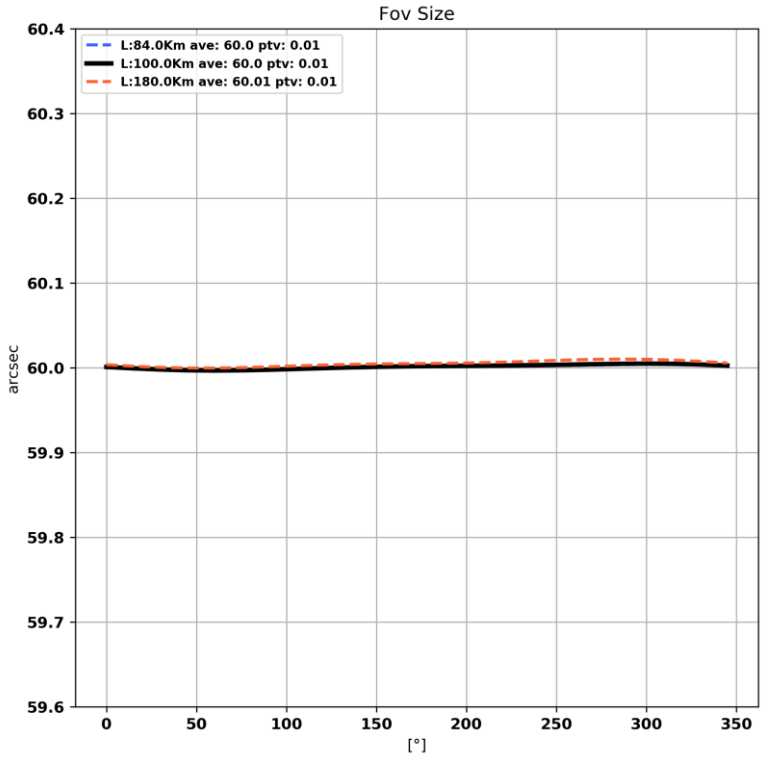

Figure 6. Centroid radial positions of the LGS 30 arcsec asterism (top) and LGS 30 arcsec asterism (bottom) in the LGSO focal plane along the full azimuthal angle for the LGS reference heights.

3.2.6 F number and Exit Pupil

MAO-SF0-1.2.3.14: *The MAORY optics shall, as a design goal, deliver an F number equal to F/17.75 +/-0.08 [RD2].*

MAO-SF0-1.3.4.3*: The MAORY optics should, as a design goal, provide a 1:1 relay of the beam at both ports. The agreed image space F number with MICADO is F/17.75 +/-0.01 [RD2].*

This requirement is related to the F/# delivered by the MMS main path to MICADO and its technical FoV, and to the second port. They stated, basically, that MMS main path should deliver an almost one to one focal plane image from ELT to MICADO. This choice facilitated the design of MICADO and its stand-alone relay.

The ELT Image Space F/# is 17.75+/-0.08 (I-INS/ELT-137 [RD1]). Looking to the Zemax model of the ELT, the nominal Image Space F/# is 17.747.

We computed the MMS main path Image Space F/# as the ratio between the effective focal length (see Table 4) and the entrance pupil diameter. Results are given in Table 6.

Wavelength	F/#
[µm]	[mm]
1	17,755
1,65	17,755
2,2	17,755

Table 6. MMS main path Image Space F/# for the reference wavelengths.

However, MICADO is an infrared instrument, and along its optical path, it has a real pupil image where a cold stop is placed for thermal background rejection. The under-sizing of the cold stop is driven by the blurring at the edge of the exit pupil and its ellipticity. This gives a certain degree of freedom on the definition of the exit pupil position, ranging within the depth of focus of the exit pupil edge blur. It has been agreed between the two consortia also on a definition of polychromatic exit pupil F/#, given by the ratio of the exit pupil distance and exit pupil diameter.

MAO-SF0-1.3.4.11: *The MAORY optics shall, as a design goal, deliver a polychromatic exit pupil F number equal to F/17.74 +-0.01 to MICADO [RD2].*

The nominal polychromatic exit pupil F-number is 17.744 (see below for the value computation).

During the optimization process, the position of the exit pupil has been determined by the minimization of the RMS spot size at the exit pupil corresponding to fields located at the entrance pupil of ELT. The optical system aperture is determined by the cone angle (telecentric beams in the object space) defined by the MICADO FoV (76 arcsec diameter). We have defined 8 fields at the edge of the ELT entrance pupil and 8 fields at one-half of its semi-aperture, as shown in Figure 7. In the merit function, the weight associated to the external fields is five times larger than the weight associated to the inner ones. The circular size of the exit pupil is computed by interpolating a circle through the spot centroids of the external fields. The optimization and the computation were done at wavelength equal to 1 µm. The polychromatic (1 µm, 1.65 µm and 2.2 µm) spot diagram at the MMS exit pupil is shown in Figure 8.

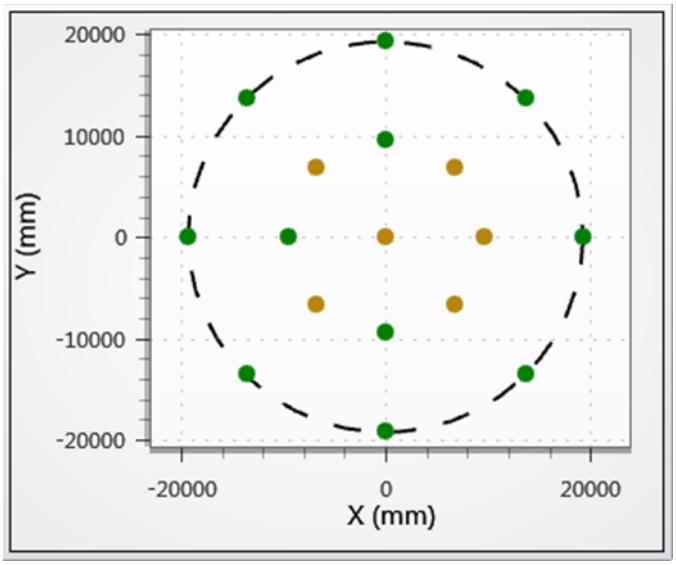

Figure 7. Fields location on ELT entrance pupil used during MMS Exit Pupil optimization.

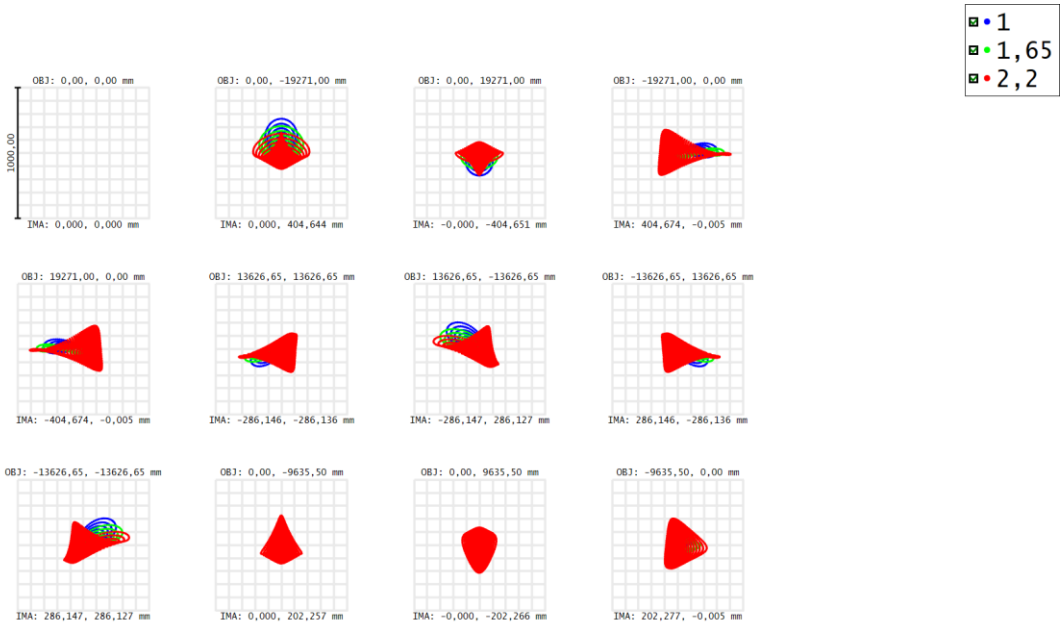

Surface: IMA

Spot Diagram

, 28/10/2020
Units are µm. Legend items refer to Wavelengths

Field	1	2	3	4	5	6	7	8	9	10	11	12
RMS radius :	0,000	91,335	74,290	132,491	132,491	106,585	114,645	106,585	114,645	88,911	88,630	102,989
GEO radius :	0,000	262,866	179,897	407,831	407,831	328,838	354,723	328,838	354,723	226,020	212,273	226,218

Scale bar : 1000 Reference : Centroid

Figure 8. Polychromatic spot diagram at the MMS exit pupil. Used wavelengths are 1 µm, 1.65 µm and 2.2 µm.

MAO-SF0-1.2.3.17: *The MAORY optics should provide, as a design goal, an Exit Pupil position at 14362+/-600 mm towards the telescope [RD2].*

The MMS has a nominal exit pupil position equal to 14361 mm.

The MMS has a nominal exit pupil diameter equal to 809.322 mm.

These two values determine the nominal polychromatic exit pupil F/#.

The wavelengths dependency is negligible. The difference between the polychromatic exit pupil diameter and the exit pupil diameter computed at 1 µm is about 0.006 mm.

MAO-SF0-1.3.4.9: *The MAORY optics shall provide an Exit Pupil quality such that the MICADO cold stop shall not be linearly under-sized by more than 2% (goal 1%) with respect to the nominal pupil size over the MICADO Field of View [RD2].*

In order to verify this requirement, we have estimated the polychromatic geometrical spot size (worst case) and the effect of the ellipticity. The wavelengths used are 1 µm, 1.65 µm and 2.2 µm.

The polychromatic geometrical spot diameter (i.e. the diameter of the circle centred on the spot centroid and inscribing all the rays) has been evaluated all over the pupil as shown in Figure 9. The maximum polychromatic geometrical spot diameter is 0.816 mm. By comparing the spot size with the exit pupil diameter, it turns that its impact on the cold stop undersize budget is about 0.1%

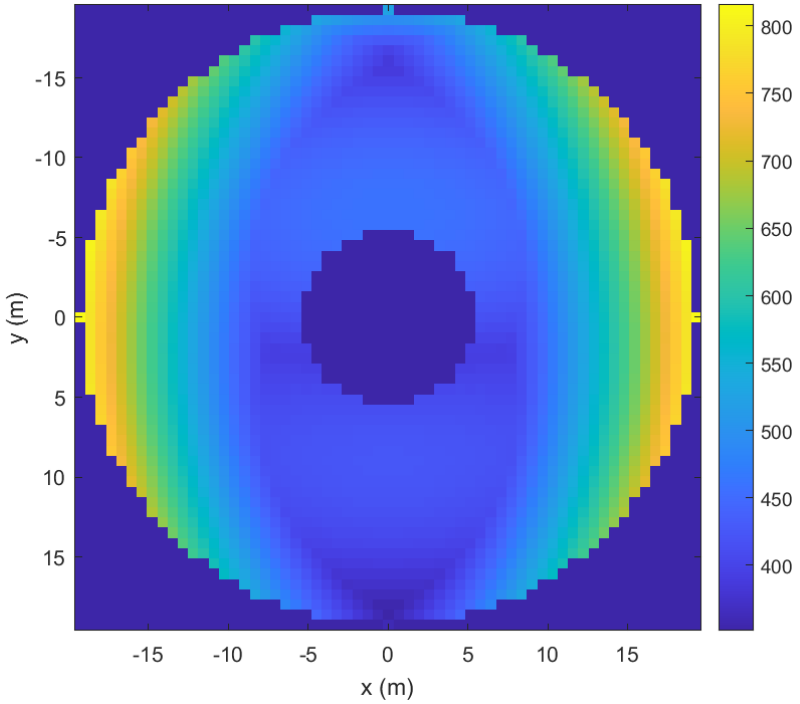

Figure 9. Polychromatic geometrical spot diameter at the exit pupil. Color scale is in micron unit.

In order to estimate the effect of the ellipticity, we have considered 32 fields at the edge of the pupil (see Figure 10). The circle fitting the polychromatic spot centroids have a diameter of 809.322 mm.

The ellipticity effect has been evaluated by computing the difference between the spot centroids at the edge of the pupil and the fitting circle. The maximum deviation of the spot

centroids is < 15 µm. For this effect, the cold stop has to be undersized by about 0.002%, i.e. it is negligible.

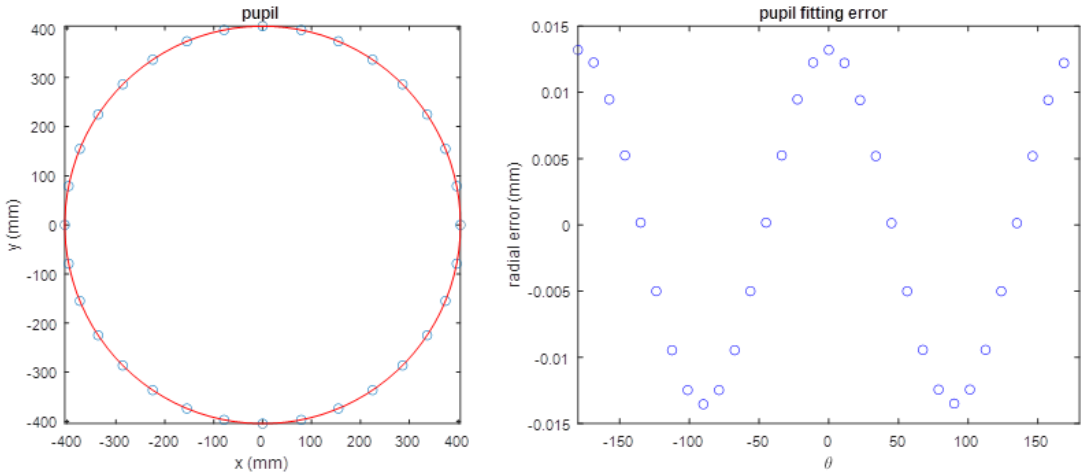

Figure 10. Fields location on exit pupil used for pupil blur and ellipticity estimate (left). Ellipticity effect (right).

Given that M11M (flip mirror) is placed after the exit pupil image and that there are no optical elements with power after it, the same nominal values in this section are valid for the second port instrument (assuming a scientific FoV equal to MICADO).

MAO-SF0-1.3.3.6.7: *The PFRO shall deliver an exit pupil ellipticity at any position in the LOR and REF WFS technical FoV below 1/20 of the sub-aperture [RD2].*

MAO-SF0-1.3.3.6.8: *The PFRO shall deliver an exit pupil blur at any position in the LOR and REF WFS technical FoV below 1/20 of sub-aperture [RD2].*

The LOR and REF WFS sample the pupil image with 2×2 and 10×10 sub-apertures respectively. The requirements can be rephrased then as function of the pupil diameter; assuming the more stringent value (REF WFS), it means that the requirements have to be satisfied over 1/200 (0.5%) of the exit pupil diameter.

We have considered eight point sources located at the entrance pupil edge as shown in Figure 11. The optical system aperture has been set to be a circle, having diameter 1 arcsec, located at about 40 arcsec and 78 arcsec radial coordinate on the technical focal plane. The aperture size determines the FoV of the sensor and we have supposed to correspond to seeing size. The performance in terms of blur is worst when the aperture is close to the edge of the technical FoV. We have varied the position of the aperture over the azimuthal angle with step of 30 degrees, for the two radial coordinates, and, for each case, we have computed the centroid coordinates and spot size on the exit pupil plane. The computation has been done for wavelength 1650 nm (H-band) and 800 nm (R band).

In Figure 12 shows the centroids position on the exit pupil plane for NGS WFS located on the circle having radius 76 arcsec. Given the weak dependency of the centroid by the wavelength with respect to the azimuthal angle variation, for each radial circle, we have applied a circular fit and determined the exit pupil diameter without separating the colors effect.

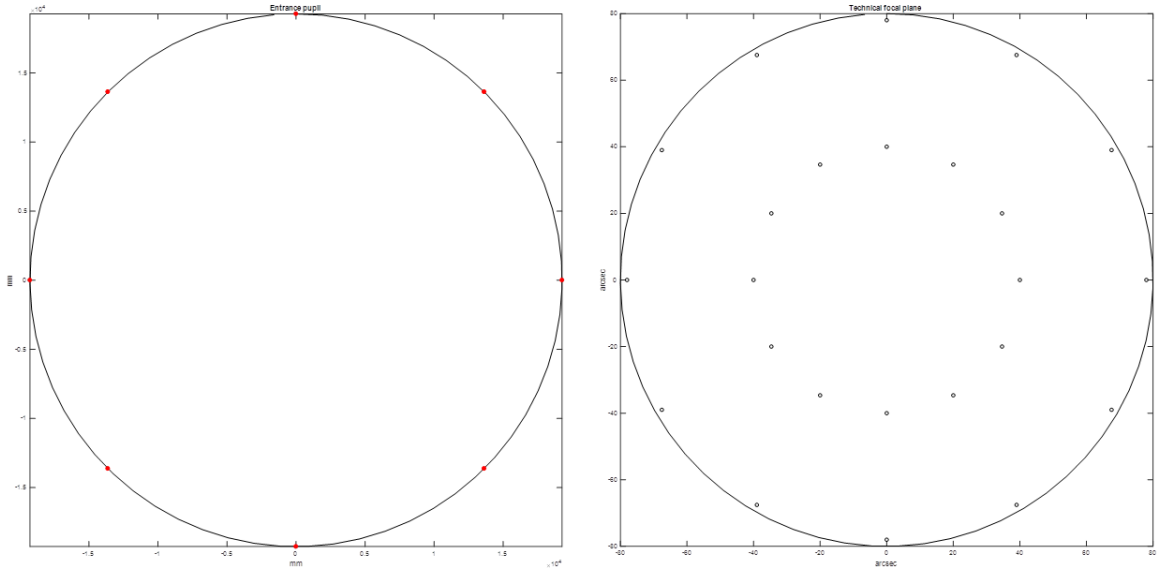

Figure 11. Fields location on entrance pupil (left) and aperture stop locations of the NGS WFS on the technical FoV used for pupil blur and ellipticity estimate.

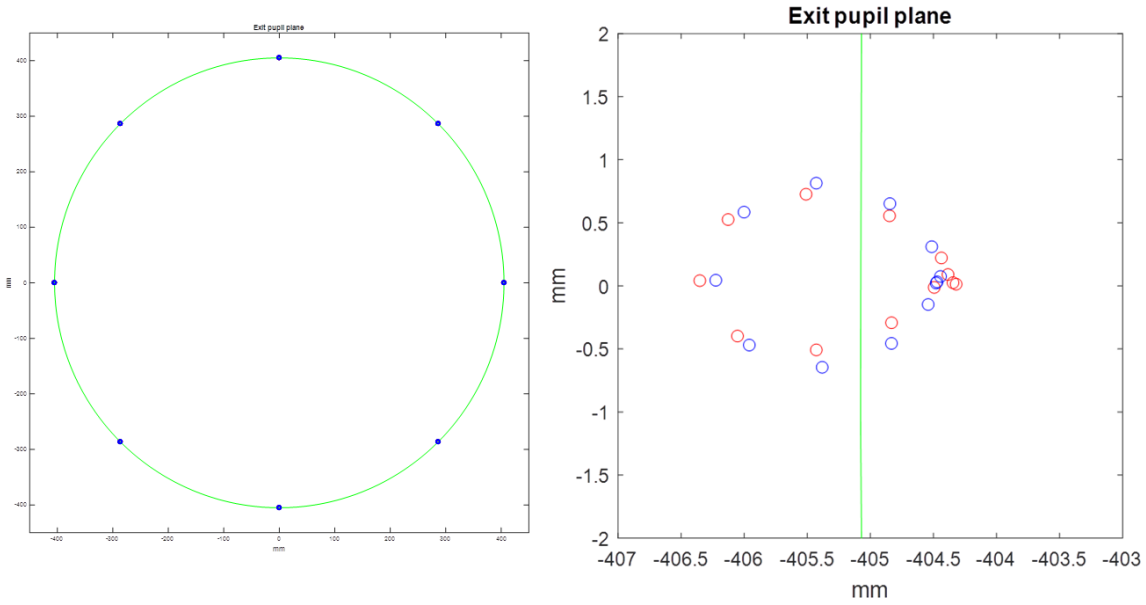

Figure 12 Centroids position on the exit pupil plane for NGS WFS located on the circle having radius 76 arcsec (left). Detail of a centroids distribution (red circles correspond to wavelength 1650 nm, blue circle correspond to wavelength 800 nm) due to the azimuthal angle variation of NGSWFS.

The fitting circle at field radial coordinates 40 arcsec has a radius equal to 404.68 mm.

The fitting circle at field radial coordinates 78 arcsec has a radius equal to 405.08 mm.

By moving from the inner part to the outer part of the technical field along radial direction, the exit pupil diameter seen by the NGS WFS change by about 0.4 mm, corresponding to 0.1% of the exit pupil diameter.

The maximum dispersion among the centroids position and the fitting circle occurs on the outer part of the technical field. The maximum dispersion is 1.27 mm, corresponding to 0.3% of the exit pupil diameter.

The maximum geometrical spot diameter occurs on the outer part of the technical field as well. The maximum geometrical spot diameter is 0.06 mm, corresponding to 0.007% of the exit pupil diameter.

In conclusion, the largest effect on the pupil size and ellipticity is due to the azimuthal angle variation of the NGS WFS. However, even applying a linear sum of the contributors, the expected maximum variation is about 0.4% of the exit pupil diameter. The blur effect due to the spot size is negligible.

MAO-SF0-1.3.3.6.10: *The PFRO shall deliver an exit pupil distortion in the LOR and REF WFS technical FoV below 1/20 of the sub-aperture [RD2].*

With reference to Figure 11, we have computed the field distortion map on the exit pupil for each of the twelve positions of the NGS WFS having radius 78 arcsec on the technical field of view, given that the field distortion is higher at the edge of the FoV. An example of field distortion map is shown in Figure 13.

The maximum distortion at the edge of the technical FoV is 0.12%, well below the 0.5% corresponding to 1/20 sub-apertures of the REF WFS.

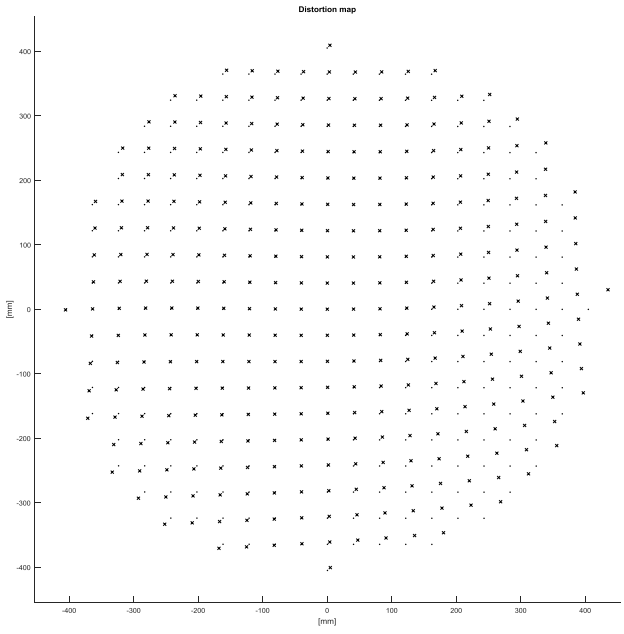

Figure 13 Example of distortion map of the exit pupil as seen by the NGS WFS positioned at the edge of the technical FoV. Dots represent the undistorted map, while crosses represent the distorted map. The distortion has been amplified by 100 times to highlight the effect.

MAO-SF0-1.3.4.16: *MAORY shall deliver a SCAO Output Pupil distortion below 0.5% variation for any field point with respect to the on-axis case [RD2].*

The interface requirements with MICADO SCAO module are still ongoing. A description of desiderata towards MAORY is reported in [RD15]. In particular:

SMS-0170: The optical quality of the ELT exit pupil plane re-imaged on the WFS detector shall be such that the spot diagram is less than 0.12% of the pupil diameter, when considering the rays passing through a field of 1 arcsec diameter. Potential chromatism must be accounted for by considering the spot diagram resulting from the combination of the multi-wavelength spot diagrams in the WFS bandpass. Warning: this specification involves the optical design of either MAORY or relay optics (MICADO stand-alone case). This spec may be relaxed (up to …? TBD 0.5%? 1%?) if the spot diagram is "uniform and symmetric" over the pupil, and can be relaxed if the modulation mirror is out of a pupil plane (additional pupil blurring by the modulation pattern).

SMS-0171: The distortion of the pupil image on the detector shall be less than 0.12% of its own diameter. (This spec is different from SMS-0170 in the sense that it addresses the distortion of pupil image. Potential chromatism must be accounted for by considering the pupil image resulting from the combination of the pupil images at the wavelengths in the WFS bandpass.SMS-0170 ensures the pupil image is sharp, the present ones ensures it's not elliptical or else).Warning: this specification involves either MAORY optical design, on that of the relay optics (MICADO stand-alone case).

As for the LOR case simulation, we have considered eight point sources located at the entrance pupil edge as shown in Figure 11. The optical system aperture has been set to be a circle, having diameter 1 arcsec, located at about 17.5 arcsec. We have varied the position of the aperture over the azimuthal angle with step of 45 degrees, and, for each case, we have computed the centroid coordinates and spot size on the exit pupil plane. The computation has been done for wavelength 600 nm, 800 nm and 1000 nm.

We have compared the maximum polychromatic geometrical spot diameter obtained in among all cases with the exit pupil diameter as seen when the aperture is at the center of MICADO FoV. The ratio is 0.006%.

We have compare the maximum deviation between the polychromatic spot centroids coordinates among all the cases with the radius of the exit pupil fitting circle as seen when the aperture is at the center of MICADO FoV. The ratio is 0.018%.

MAO-SF0-1.3.3.5.2: *The beam delivered to LGS WFS entrance focal plane shall have a paraxial F number equal to 5 [RD2].*

The LGSO has been optimized to deliver a paraxial F/# equal to 5 to the LGS WFS entrance focal plane. The paraxial F number is defined as $1/(2\tan(\theta))$, where θ is the marginal ray angle with respect to the chief ray.

MAO-SF0-1.3.3.5.5: *The beam delivered to LGS WFS shall be telecentric (pupil at infinite) [RD2].*

The LGSO delivers by design a telecentric beam to the LGS WFS module, so that the exit pupil is at infinite.

MAO-SF0-1.3.3.5.21: *The image of the pupil in the LGS WFS channels shall have a diameter variation, due to PFRO, within +/-1/20 of the pupil sub-apertures size for the LGS 45 arcsec asterism and for each sodium layer altitude in the working range [RD2].*

MAO-SF0-1.3.3.5.22: *The telecentricity error induced by PFRO shall be within +/-1/20 pupil sub-apertures size, averaging opposite pupil edges positions, for the LGS 45 arcsec asterism and for each sodium layer altitude in the working range [RD2].*

MAO-SF0-1.3.3.5.3: *The number of sub-apertures to be considered in the LGSWFS is 68 x 68 [RD2].*

In the current baseline, the LGS WFS samples the pupil with 68×68 sub-apertures. The acceptable range in terms of pupil diameter is then +/- 1/1360, i.e. 0.074%.

The computation has been implemented as follow. With reference to Figure 14, given a field in the 45 arcsec asterism, we have considered the two opposite marginal rays every 30 degrees pupil azimuthal angle around the pupil. These rays form an angle α1 and α2 with the normal to the flat focal plane. In a paraxial F/5 system the *tan(α)=0.1.* The percentage of pupil diameter deviation from the nominal value has been computed as:

$$D = (\tan(|\alpha 1|) + \tan(|\alpha 2|))/0.2$$

for each couple of opposite rays and averaging the results over the pupil azimuthal angle.

We have computed the telecentricity error as:

$$\Delta = \left| \frac{\left(\frac{|\tan(\alpha 1)|}{0.1} - 1\right) - \left(\frac{|\tan(\alpha 2)|}{0.1} - 1\right)}{2} \right|$$

for each opposite rays and averaging the results over the pupil azimuthal angle.

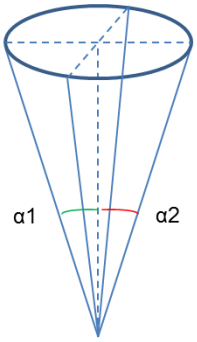

Figure 14. Scheme of the telecentric beam.

The results around the LGS 45 arcsec for the LGS reference heights are shown in Figure 15.

The nominal LGS WFS pupil diameter percentage variation and telecentricity error is well within the acceptable range +/- 0.074% for all the LGS WFS position around the 45 arcsec asterism and all the LGS reference heights.

We have repeated the same computation also for circular fields having asterism radius at 30 arcsec and 60 arcsec. Results are shown in Figure 16 and Figure 17 respectively.

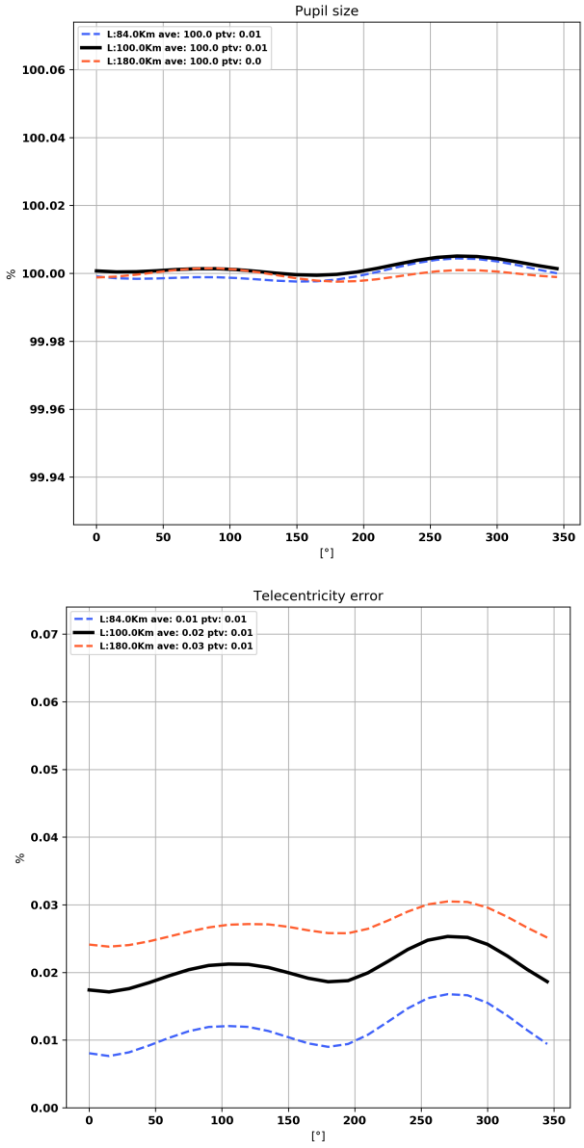

Figure 15. LGS WFS pupil diameter percentage variation (top) and telecentricity error (bottom) induced by LGSO for the LGS 45 arcsec asterism circle at the LGS reference heights.

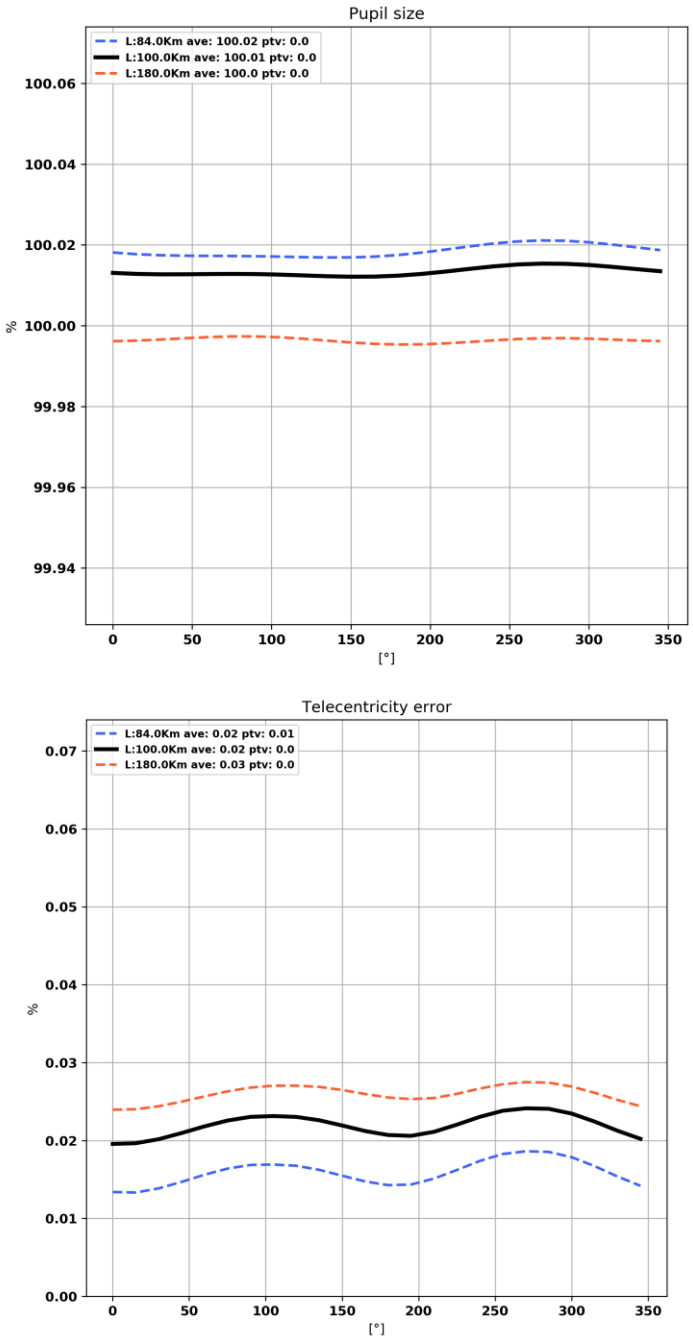

Figure 16. LGS WFS pupil diameter percentage variation (top) and telecentricity error (bottom) induced by LGSO for the LGS 30 arcsec asterism circle at the LGS reference heights.

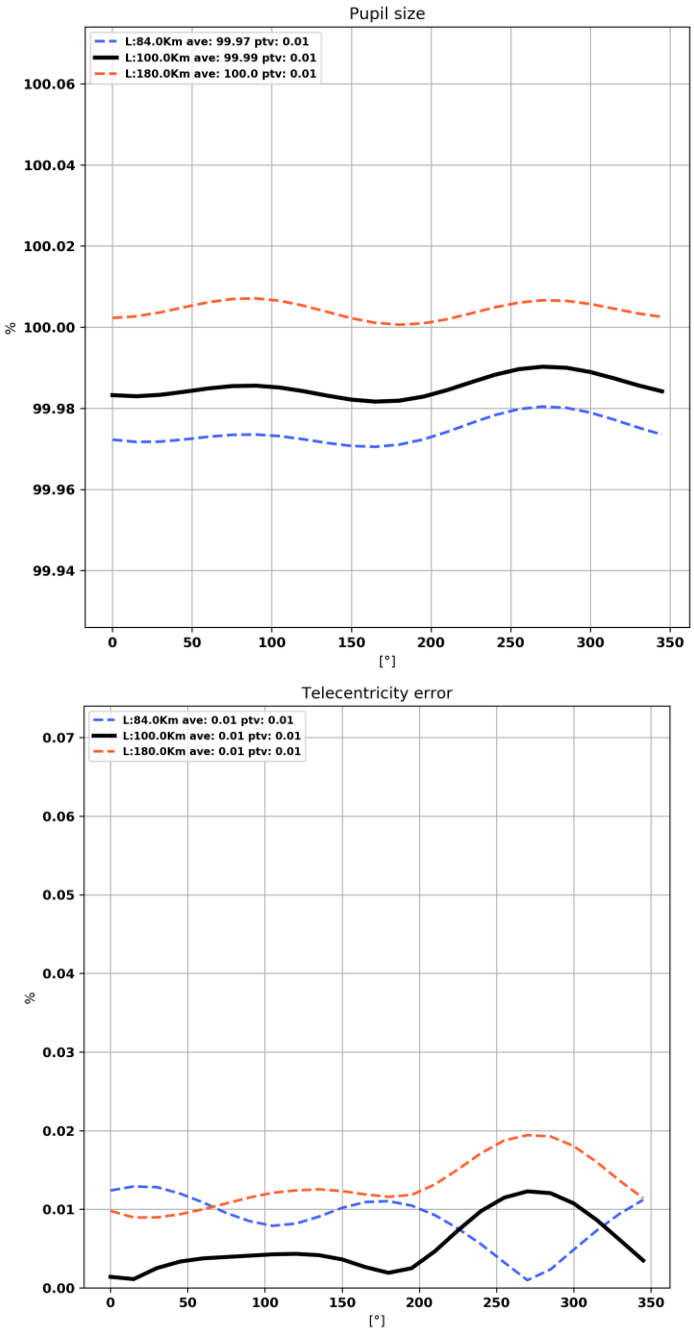

Figure 17. LGS WFS pupil diameter percentage variation (top) and telecentricity error (bottom) induced by LGSO for the LGS 60 arcsec asterism circle at the LGS reference heights.

MAO-SF0-1.3.3.5.7 Pupil distortions: *The distortion on LGS WFS pupil due to the PFRO shall be below 1/10 of the sub-aperture for the LGS 45 arcsec asterism and for each sodium layer altitude in the working range [RD2].*

We have verified this requirement through the following simulation: we have considered as object plane the ELT entrance pupil and as aperture stop a circle having diameter 1 arcsec (seeing disk), positioned on the LGSWFS entrance focal plane at 45 arcsec (42.24

mm) from the optical axis. In order to materialize the entrance pupil image, we have inserted a paraxial lens having EFL 96 mm (collimator) at the same distance from the entrance focal plane. The paraxial pupil size is 19.2 mm and, assuming 68 sub-aperture, the sub-aperture size is 0.282 mm. We have varied the position of the aperture stop by rotating it around the LGSWFS rotation axis (optical axis) from 0 to 360 degrees with step of 30 degrees and by moving it along the optical axis to the three focal planes conjugated at 84, 100 and 180 km. The collimator and the pupil plane follow the movements. A scheme is shown in Figure 18.

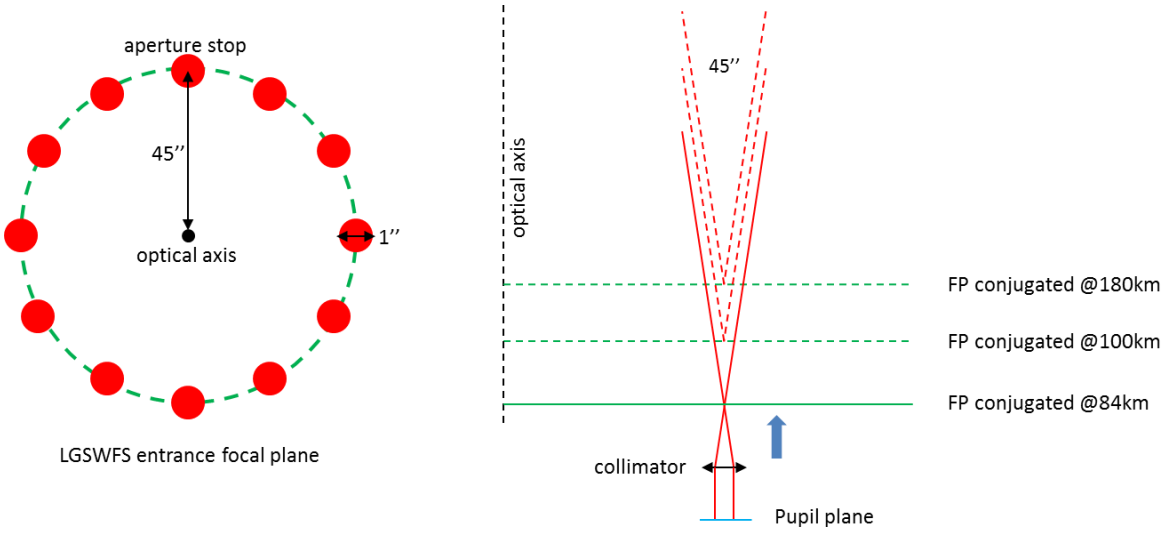

Figure 18. Twelve simulated position of the aperture stop around the optical axis on a circle having radius 45 arcsec (left). Three simulated LGSWFS entrance focal plane conjugated at altitude 84, 100 and 180 km (right).

For each configuration, we have computed the chief ray coordinates, sampling the pupil with a regular grid of 20×20 fields. For each pupil position, we have computed the centroid of the 36 chief rays (12 azimuthal positions × 3 axial planes). See Figure 19.

We have computed the pupil distortion as the deviation of the chief rays centroids with respect to a regular 68×68 sub-apertures array and estimated the deviation in terms of sub-aperture percentage. The distortion variation with the rotation around and the translation along the optical axis has been estimated as the maximum deviation between the chief ray spot and the corresponding centroid.

The results are shown in Figure 20 in terms of sub-aperture percentage. The maximum centroids deviation with respect to the undistorted position is 6.4% of the sub-aperture size. This term can be mitigated up to a certain level during the calibration campaign. The maximum chief rays deviation with respect to the centroid is 1.7% of the sub-aperture size. This terms represent the pupil distortion variation as the LGS WFS module rotate and translate, following the LGS conjugation altitudes.

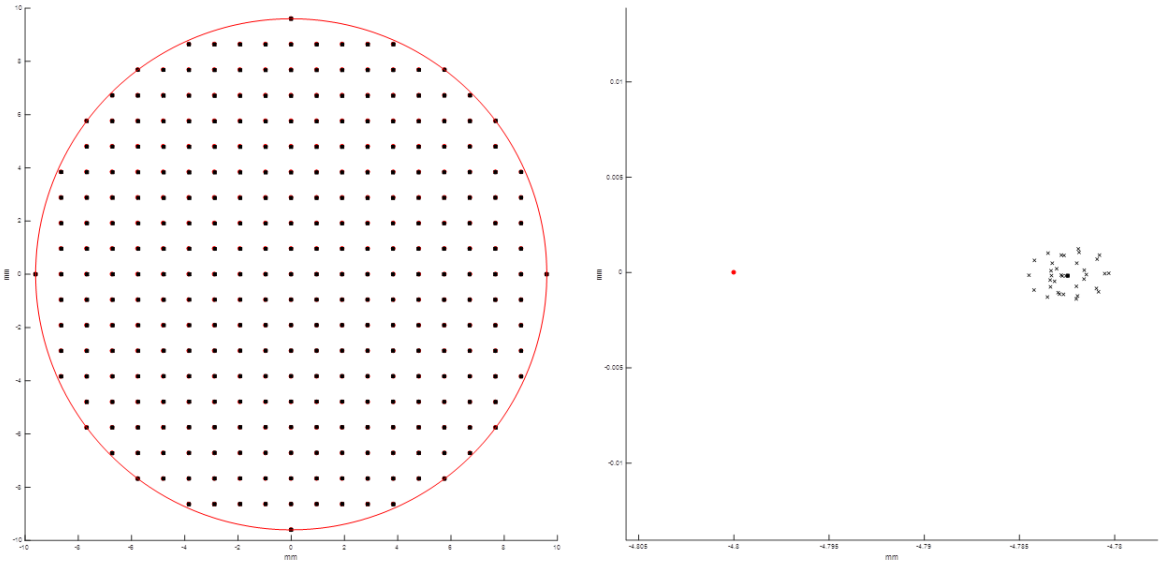

Figure 19. Undistorted positions (red circle), chief rays positions (black cross) and chief rays centroids positions (black square) on the left. Zoom of the worst case in terms of centroid deviation on the right.

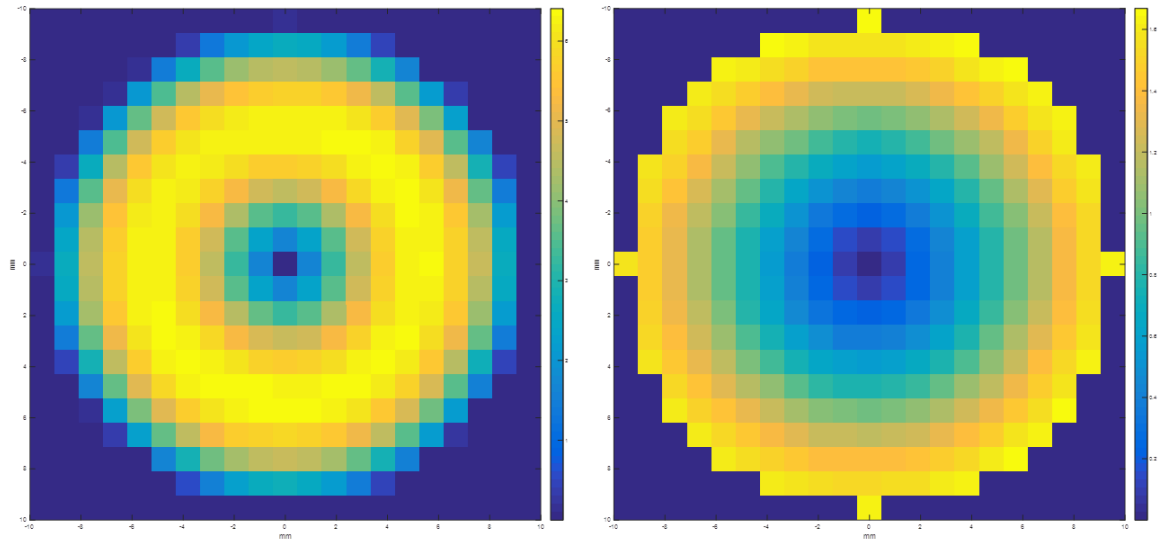

Figure 20. Chief rays centroids deviation with respect to the undistorted position in percentage of sub-aperture (left). Maximum chief rays deviation with respect to the centroid (right).

3.2.7 Field curvature and focal extraction

MAO-SF0-1.2.3.15: *The MAORY optics should deliver a field curvature lower than -9884 mm [RD2].*

This requirement states that the main path of MAORY has to deliver a science and technical focal plane having curvature equal to the one delivered by ELT at the entrance focal plane of MAORY. The sign 'minus' means that the center of curvature of the focal plane is located towards the telescope. However, the requirement has been superseded by the following one:

MAO-SF0-1.3.4.4: *MICADO and MAORY are departing from ESO ELT characteristic and consortia agreed on an infinite curvature, i.e. a flat field, at the entrance of the MICADO instrument. In this context of flat field, the tolerance on any field aberration should be included in the WFE budget at the MAORY exit pupil [RD2].*

The MMS has been designed to deliver a flat focal plane at the entrance of MICADO (and second port instrument).

MAO-SF0-1.3.4.21 Focal extraction: *The PFRO design shall provide at least 1200 mm of focal extraction from MICADO focal plane [RD2].*

The MMS main path has as last optical element the flat mirror M12M over MICADO. The distance between the center of M12M and MICADO focal plane is about 2847 mm.

In the case of the second instrument the distance between M12Mbis and the focal plane is about 1905 mm. Assuming a similar constraints as the MICADO one, the MMS is compliant.

MAO-SF0-1.3.3.5.19 Back focal Distance: *The LGS WFS back-focal distance (i.e. between last optical element and LGS focal plane) is greater than 200 mm [RD2].*

For the LGSO, the field curvature and the focal extraction are interconnected. At a given sodium layer height, the LGSO focal plane position has been determined by the quality along a concave focal plane for the fields at 30, 45 and 60 arcsec. However, in the Zemax model, the focal extraction is determined by the intersection of the curved plane position with the optical axis. A scheme representing the LGSO focal plane is shown in Figure 21.

The LGS WFS should be aligned so that the entrance focal plane is flat and has best performances for fields having radius 45 arcsec (green line in the picture). The compensation to be introduced is reported in Table 7, together with the focal extraction, the field curvature for sodium layer height of 84, 100 and 180 km.

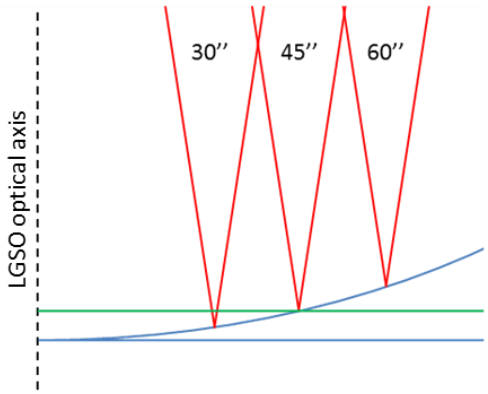

Figure 21. Scheme of the LGSO focal plane. Blue line perpendicular to the optical axis determines the nominal focal extraction. Blue curved line represents the best curved focal plane for 30, 45 and 60 arcsec (red cones) and determines the field curvature. The green line represents the position of the best flat focal plane at 45 arcsec.

sodium layer height	Focal extraction	Curvature	Focal plane compensation
[Km]	[mm]	[mm]	[mm]
84	1178	5770	0,155
100	1107	5486	0,163
180	940	4947	0,180

Table 7. MMS LGSO focal extraction, field curvature and compensation required to align the LGS WFS module entrance focal plane.

The LGSO delivers a focal extraction larger than 200 mm. The focal plane offset introduced by the field curvature will be compensated by the LGS WFS module axis along the gravity direction.

MAO-SF0-1.3.3.5.15: *All LGS-WFS channels shall have the same common focus to within +/-0.1mm for the LGS 45 arcsec asterism [RD2].*

The LGSO delivers a flat focal plane for around the LGS 45 arcsec asterism. The deviation from the planarity is considered in the analysis as RMS WFE defocus term Z4. The +/- 0.1 mm range corresponds to a Z4 range equal to +/-144 nm. In Figure 22, it is shown the Z4 values for the LGS 45 arcsec asterism and for the LGS reference heights. The values are well within the acceptable range.

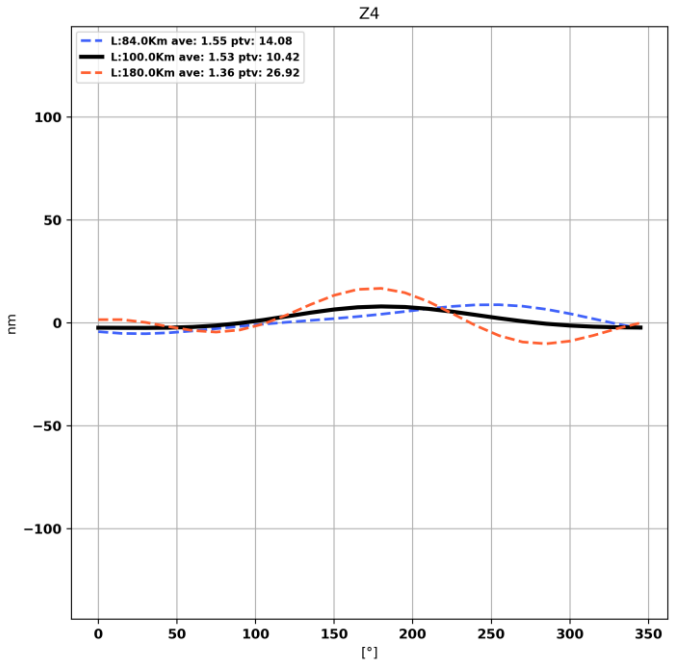

Figure 22. Z4 values around the LGS 45 arcsec asterism for the LGS reference heights.

A similar analysis has been done for the LGS 30 arcsec and 60 arcsec asterisms. Results are shown in Figure 23.

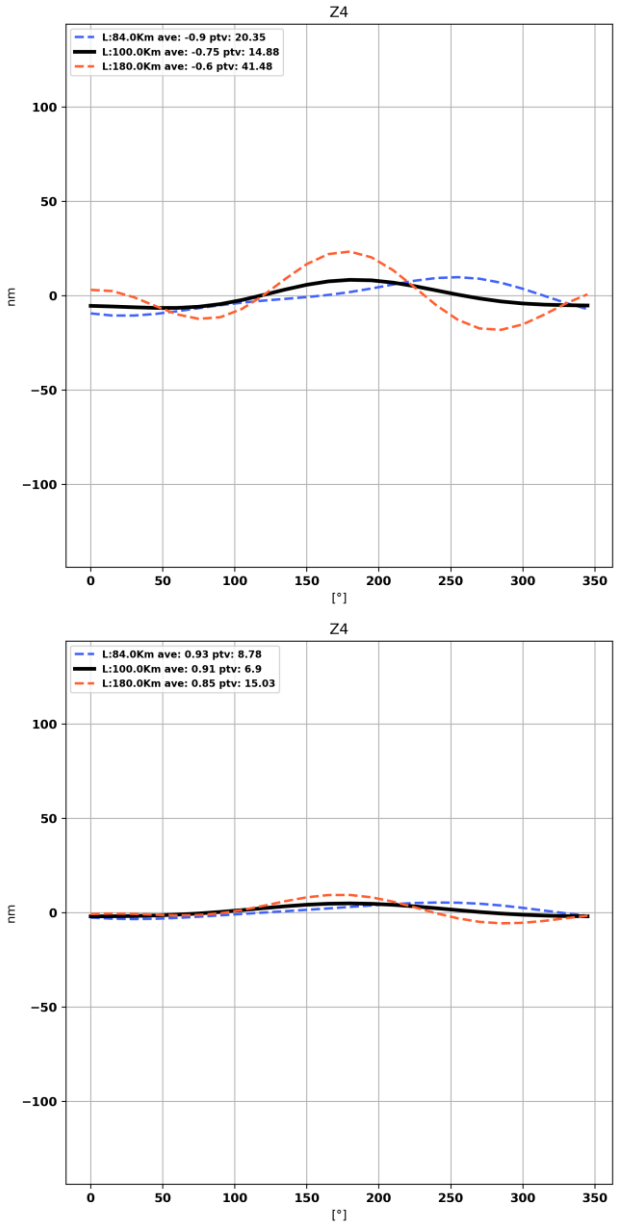

Figure 23. Z4 values around the LGS 30 arcsec (top) and 60 arcsec (bottom) asterisms for the LGS reference heights.

3.2.8 Wavefront Error

The MMS main path has been optimized in both the scientific FoV (here intended as MICADO FoV, circle having diameter 76 arcsec) and the Technical FoV (circle having diameter 160 arcsec).

During the optimization, we have considered 41 fields. Such large number was required to assure the control of the field distortion (see section 3.2.9). A scheme of the fields is shown in Figure 24. We have imposed in the merit function more weight to the MICADO

FoV, and, in particular, the central field has a weight 10 times larger and the fields in the MICADO FoV 5 times larger than the other fields. The optimization has been done at wavelength equal to 1 µm.

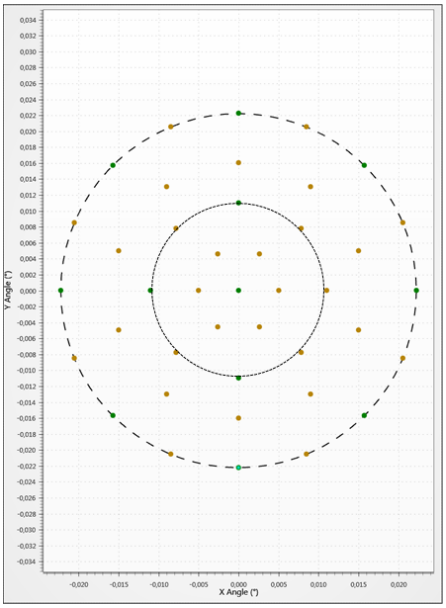

Figure 24. Fields location used for MMS main path WFE optimization. Dashed line refers to Technical FoV. Dotted line refers to MICADO FoV.

The spot diagrams at the edge of the technical FoV and at the edge of the MICADO FoV at wavelengths of 1 µm, 1.65 µm and 2.2 µm are shown in Figure 25. In the figure, the square box has 100 µm size and it is shown the airy disk at 1 µm (at 1 µm the airy radius is 21.66 µm, at 2.2 µm the airy radius 47.65 µm).

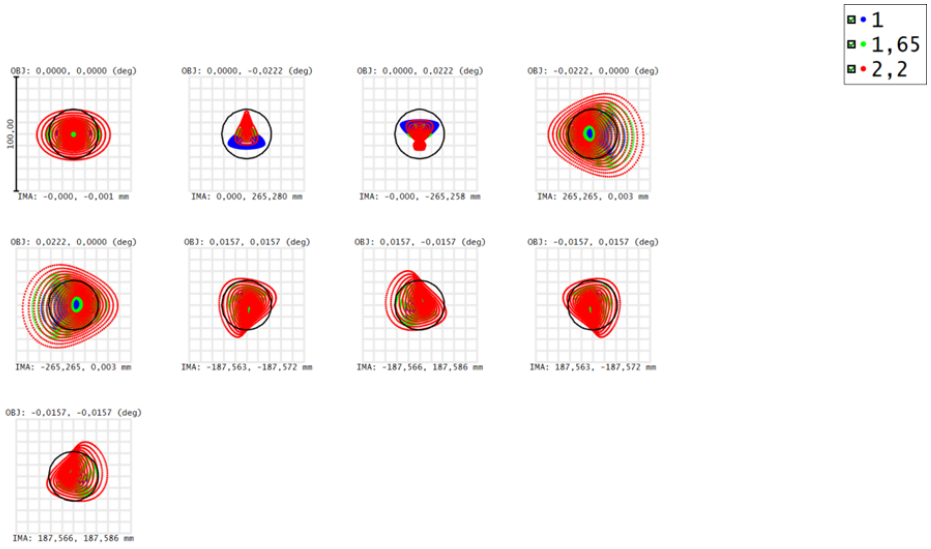

Surface: IMA

Spot Diagram

, 28/10/2020
Units are µm. Airy Radius: 21,66 µm. Legend items refer to Wavelengths

Field	1	2	3	4	5	6	7	8	9
RMS radius :	11,448	9,517	8,925	19,202	19,202	10,957	11,145	10,957	11,145
GEO radius :	32,038	19,984	18,588	45,423	45,423	29,289	32,492	29,289	32,492

Scale bar : 100 Reference : Centroid

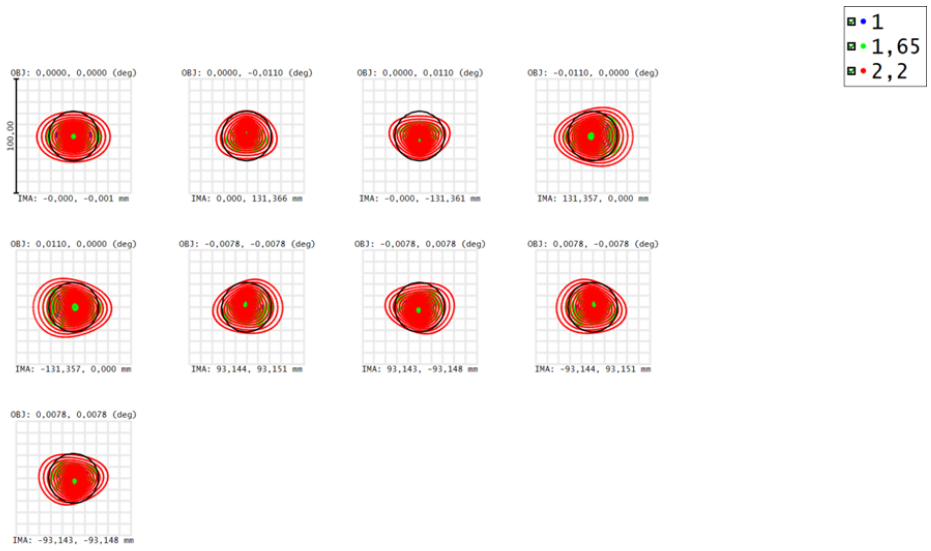

Surface: IMA

Spot Diagram

, 28/10/2020
Units are µm. Airy Radius: 21,66 µm. Legend items refer to Wavelengths

Field	1	2	3	4	5	6	7	8	9
RMS radius :	11,448	9,497	9,198	13,168	13,168	11,271	11,004	11,271	11,004
GEO radius :	32,038	26,801	26,721	35,200	35,200	31,621	30,367	31,621	30,367

Scale bar : 100 Reference : Centroid

Figure 25. Spot diagram at the edge of the technical FoV (top) and at the edge of the MICADO FoV (bottom) at wavelengths 1 µm, 1.65 µm and 2.2 µm.

The nominal quality is diffraction limited all over the technical FoV and for all the wavelengths. However, due to the presence of the CPM, the main path presents a chromatic focal shift of about 0.629 mm from 1 µm to 2.2 µm (the redder wavelengths are focused before the bluer wavelengths). The nominal focal plane at the MICADO nominal coordinates has been set in order to have the best performance at 1 µm wavelength. Eventually, the performance can be maximized at 1.65 µm and 2.2 µm, depending on the wavelength filter of the observation, by introducing a defocus during the pre-set of MAORY by offsetting the LOR WFS position (or the defocus signal sent by LOR WFS). The LOR wavelength working range is H band.

MAO-SF0-1.3.4.5*: The nominal design of PFRO shall not introduce more than 40 nm RMS Wavefront error on the scientific field of view at the reference wavelength of 1 µm [RD2].*

MAO-SF0-1.3.3.6.9: *The nominal design of PFRO shall not introduce more than 100 nm RMS Wavefront error on the technical field of view at the reference wavelength of 1 µm [RD2].*

We have evaluated the nominal WFE through the Wavefront Error RMS map. The results are shown in Figure 26. In the figure, the top line represents the WFE RMS map on the technical FoV and on the MICADO FoV at wavelength equal to 1 µm.

The maximum nominal WFE delivered by MMS main path at wavelength 1 µm in the MICADO FoV is 20.1 nm (average 13.7 nm), while in the Technical FoV is 74.7 nm (average 25.5 nm). The average values on the NGS WFS FoV is about 29 nm.

In the figure, the middle line and the bottom line refer to wavelengths 1.65 µm and 2.2 µm respectively. At 1.65 µm, the maximum nominal wavefront error delivered by MMS main path in the MICADO FoV is 48.7 nm (average 36.6 nm), i.e. 0.03 waves, while in the technical FoV is 85.0 nm (average 39.9 nm), i.e. 0.05 waves. At 2.2 µm, the maximum nominal wavefront error delivered by MMS main path in the MICADO FoV is 84.6 nm (average 72.0 nm), i.e. 0.04 waves, while in the technical FoV is 121.2 nm (average 71.4 nm), i.e. 0.06 waves.

As already stated above, the wavefront error variation as function of the wavelength is due to pure chromatic focal shift effect. By applying a focal shift of 0.309 mm and 0.629 mm, the quality is fully recovered at wavelength 1.65 µm and 2.2 µm, as shown in Figure 27.

The LOR WFS sense the wavefront in H band (1.5 µm – 1.8 µm). The chromatic focal shift could, in principle, to make them slightly sensible to reference stars colors. The chromatic focal shift between the two edges of the band is 0.143 mm, corresponding to RMS defocus Zernike coefficient Z4 equal to 16 nm. This value represents the maximum contribution due to chromatic effect (worst case) and it has been considered negligible.

The R WFS sense the wavefront in the visible (0.6 µm – 1 µm). We assume the center of the band at 0.8 µm. The chromatic focal shift between the center of the R WFS band and LO WFS band is nominally 0.426 mm. During the integration of the two channels, R WFS should be mounted with respect to the LO WFS focal plane farther by the same amount, in order to compensate a Z4 of 49 nm. However, even without compensation, the Z4 amount is well within the dynamic range of the R WFS.

If we consider the two edges of the R WFS, the chromatic shift is about 306 nm, corresponding to a maximum Z4 equal to 35 nm. This value has no impact, given the fact that the Z4 signal of the R WFS is not used in the AO loop.

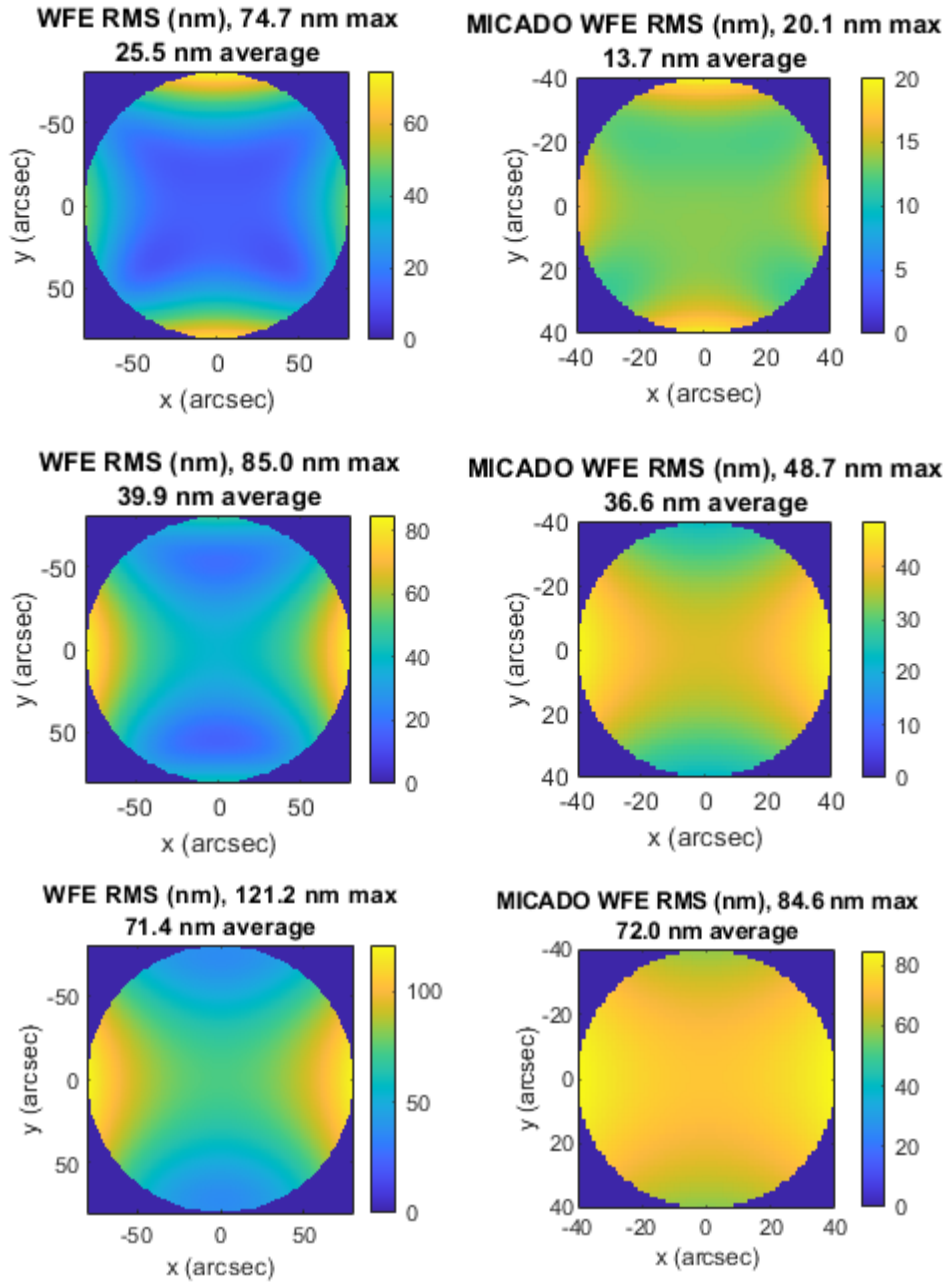

Figure 26. RMS wavefront map over the technical FoV (left) and MICADO FoV (right) at wavelength 1 µm (top), 1.65 µm (middle) and 2.2 µm (bottom). Color bar units are nanometers.

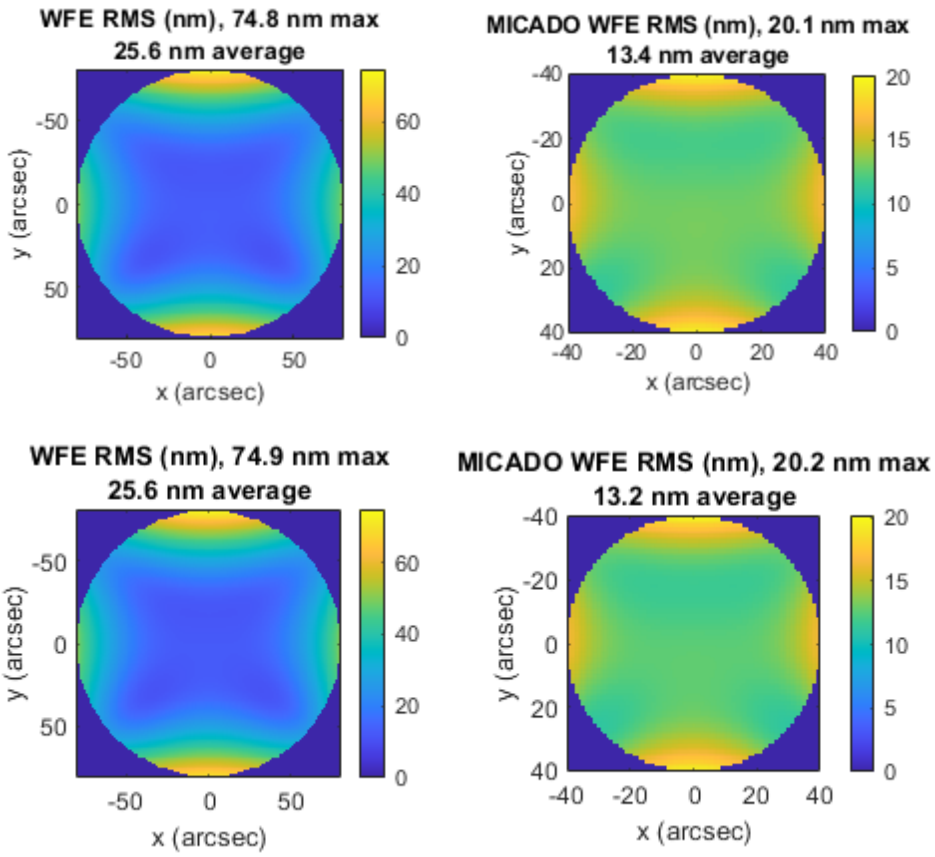

Figure 27. RMS wavefront map over the technical FoV (left) and MICADO FoV (right) at wavelength 1.65 µm (top) and 2.2 µm (bottom) after applying a focal shift of 0.309 mm and 0.629 mm respectively. Color bar units are nanometers.

MAO-SF0-1.3.3.5.6 WFE at exit port: *The nominal WFE (tilt and defocus corrected) delivered by the PFRO shall be below 200 nm RMS for the LGS 45 arcsec asterism [RD2].*

During the optimization process of the LGSO, we have tried to minimize the RMS WFE for all LGS asterisms at all the LGS reference heights (giving more weight to LGS 45 arcsec asterism and to 30 degrees zenith angle) and, at the same time, to reduce the manufacturing complexity of the objective, minimizing the number of optical elements and avoiding aspherical surfaces. Moreover, we have tried to minimize the number of low-order aberrations and the variations magnitude with the azimuthal angle and LGS reference heights, in order to, potentially, simplify the LGS path calibration procedures.

In Figure 28, it is shown the RMS WFE (in waves) for the LGS 45 arcsec asterism at all the LGS reference heights after removing in sequence tilt, defocus, astigmatism, spherical aberration, coma, trefoil, secondary coma and secondary spherical aberration.

The RMS WFE mean value, after removing tilt and defocus, is 0.21 waves (124 nm) at 84 km, 0.15 waves (88 nm) at 100 km and 0.23 waves (135 nm) at 180 km. Nominally, the aberration having the largest variation with the azimuth angle is the astigmatism, while the spherical aberration have the largest variation with the LGS heights.

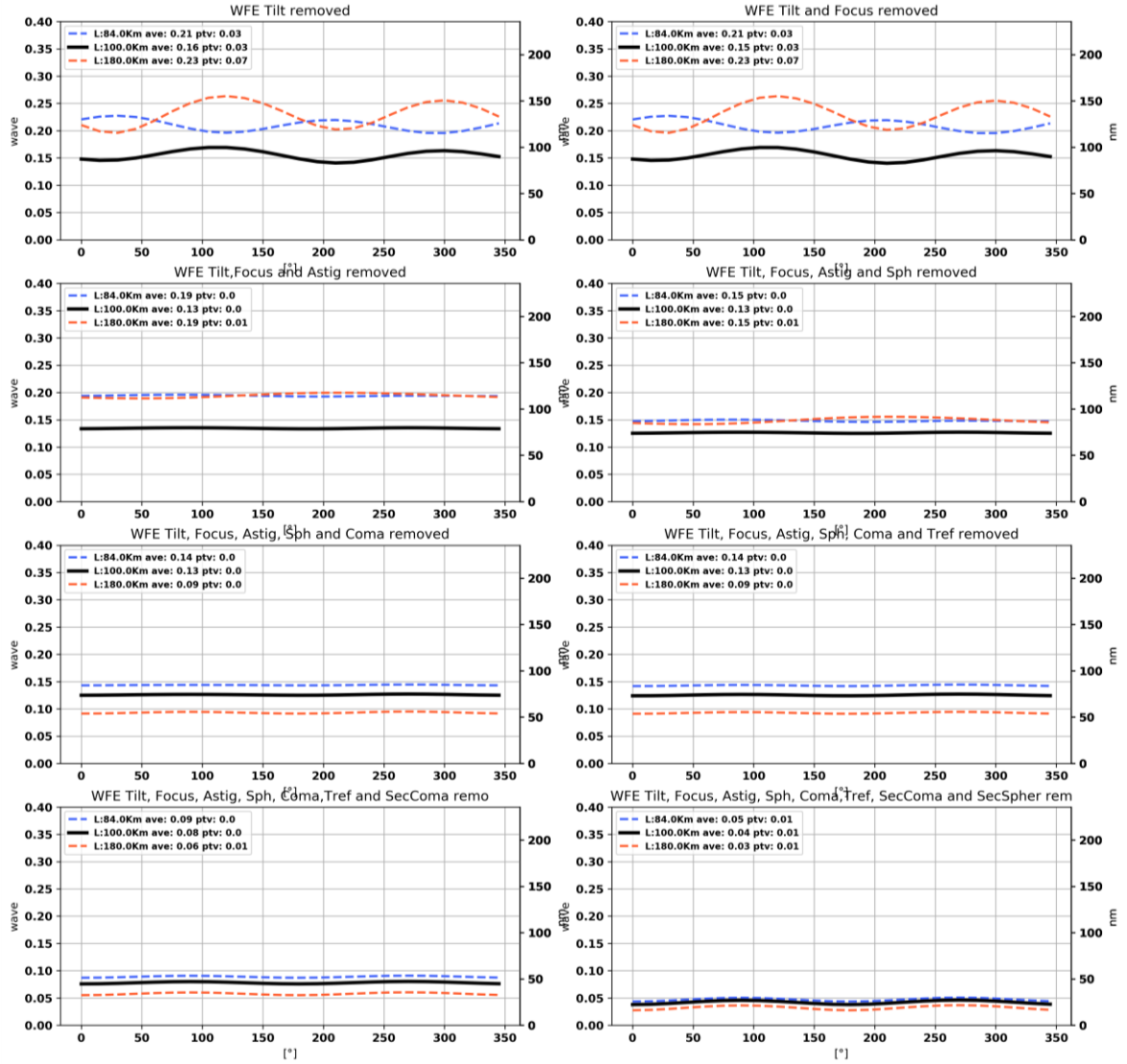

Figure 28. RMS wavefront around the LGS 45 arcsec asterism at all the LGS reference heights after removing in sequence tilt, defocus, astigmatism, spherical aberration, coma, trefoil, secondary coma and secondary spherical aberration.

We have repeated a similar computation also for circular fields having asterism radius at 30 arcsec and 60 arcsec. Results are shown in Figure 29 and Figure 30.

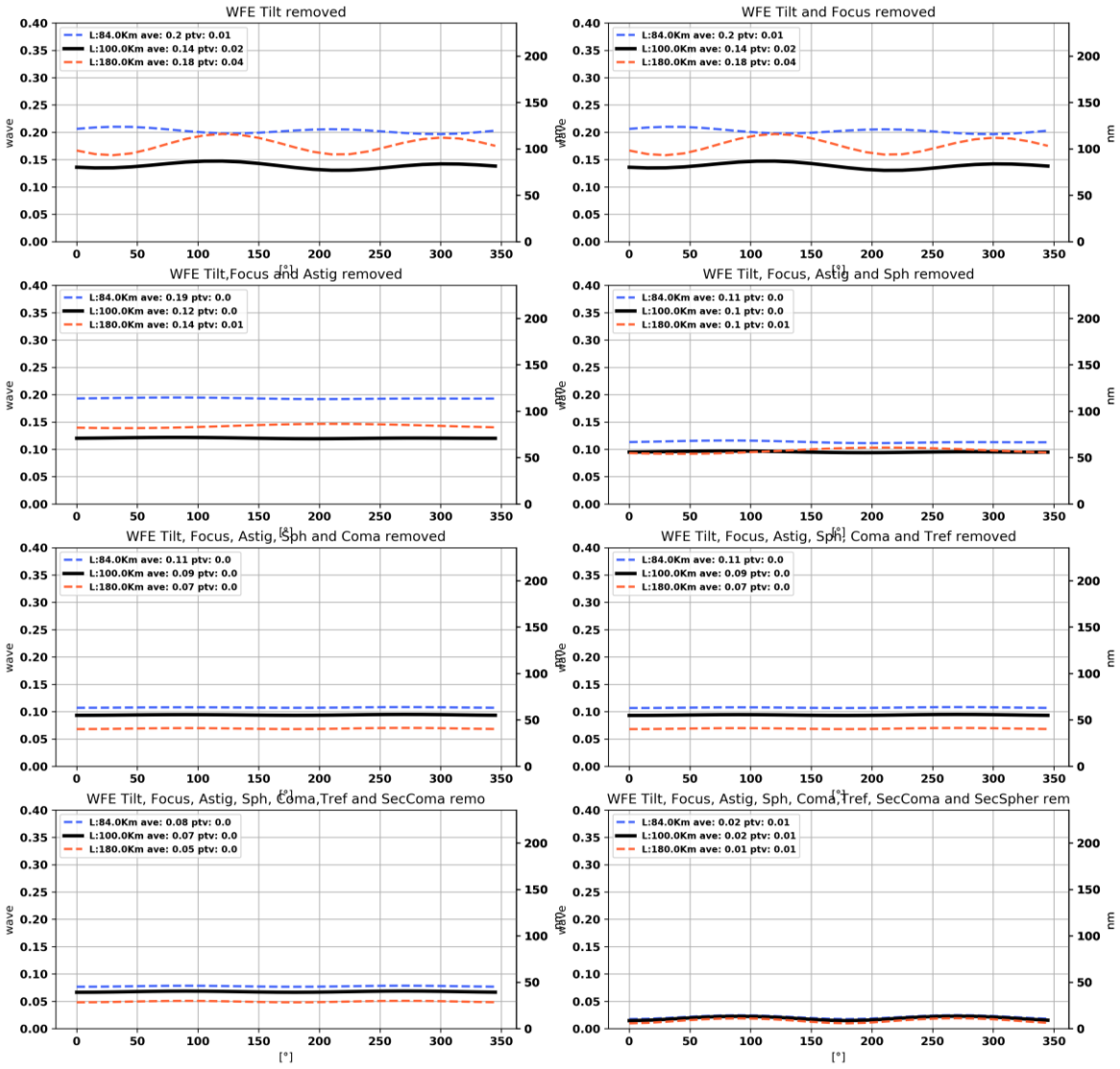

Figure 29. RMS wavefront around the LGS 30 arcsec asterism at all the LGS reference heights after removing in sequence tilt, defocus, astigmatism, spherical aberration, coma, trefoil, secondary coma and secondary spherical aberration.

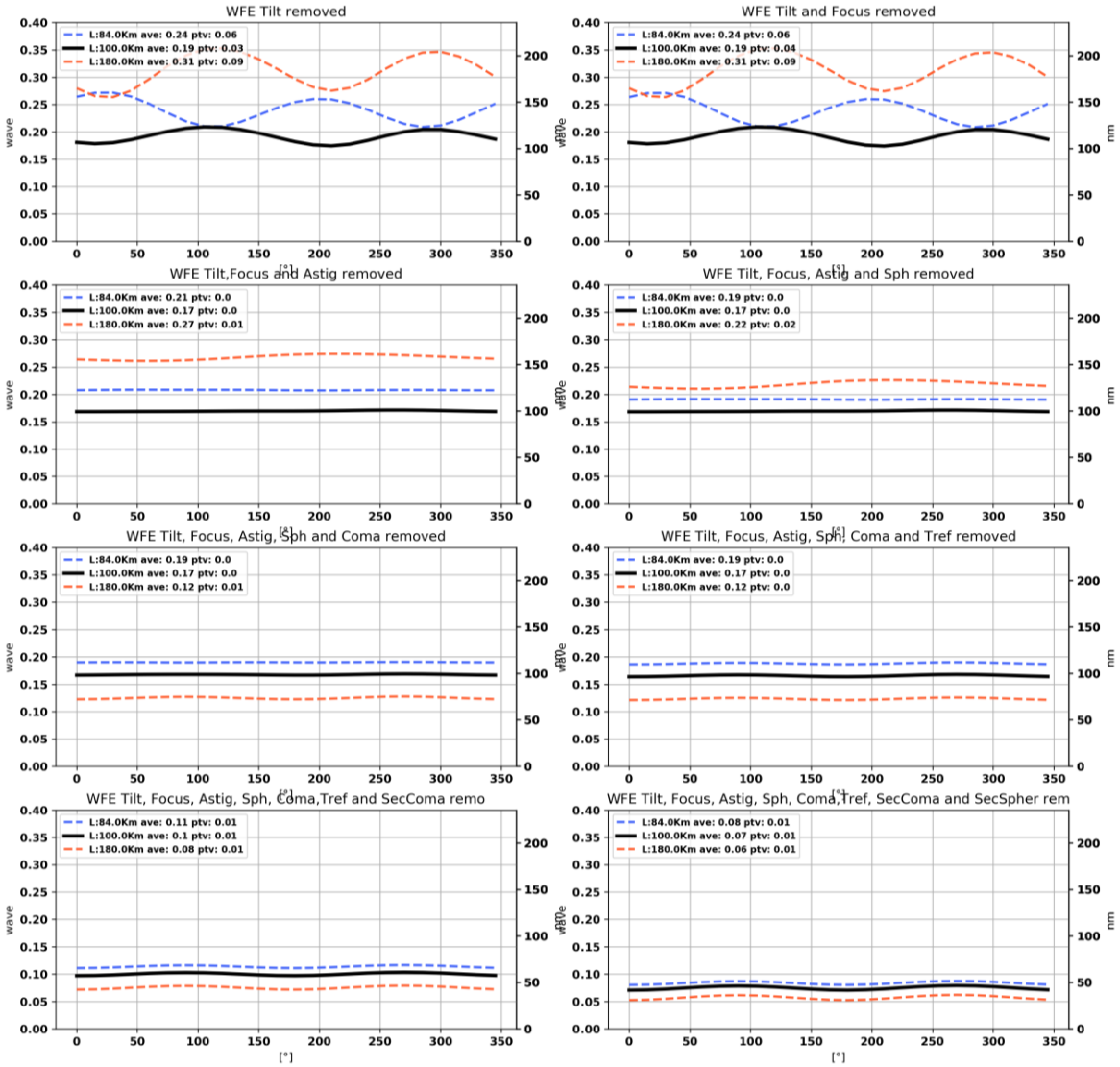

Figure 30. RMS wavefront around the LGS 60 arcsec asterism at all the LGS reference heights after removing in sequence tilt, defocus, astigmatism, spherical aberration, coma, trefoil, secondary coma and secondary spherical aberration.

3.2.9 Field distortion, intra-epoch distortion variation, inter-epoch distortion variation

The MMS main path has been optimized in order to minimize the field distortion and the intra-epoch distortion variation due to field rotation at wavelength equal to 1 µm. The minimization of the field distortion includes also the telescope nominal component.

The radial component, tangential component and the modulus of the field distortion computed at wavelength 1 µm (top), 1.65 µm (middle) and 2.2 µm (bottom) over the technical FoV are shown in Figure 31. The computation has been done by comparing the nominal position with the undistorted position of the centroids for a regular grid with a sampling of 1 arcsec.

The MMS main path has a nominal maximum field distortion (barrel) ≤ 154 micron (46 mas) all over the technical FoV (both towards MICADO and towards the second instrument), corresponding to -0.058%.

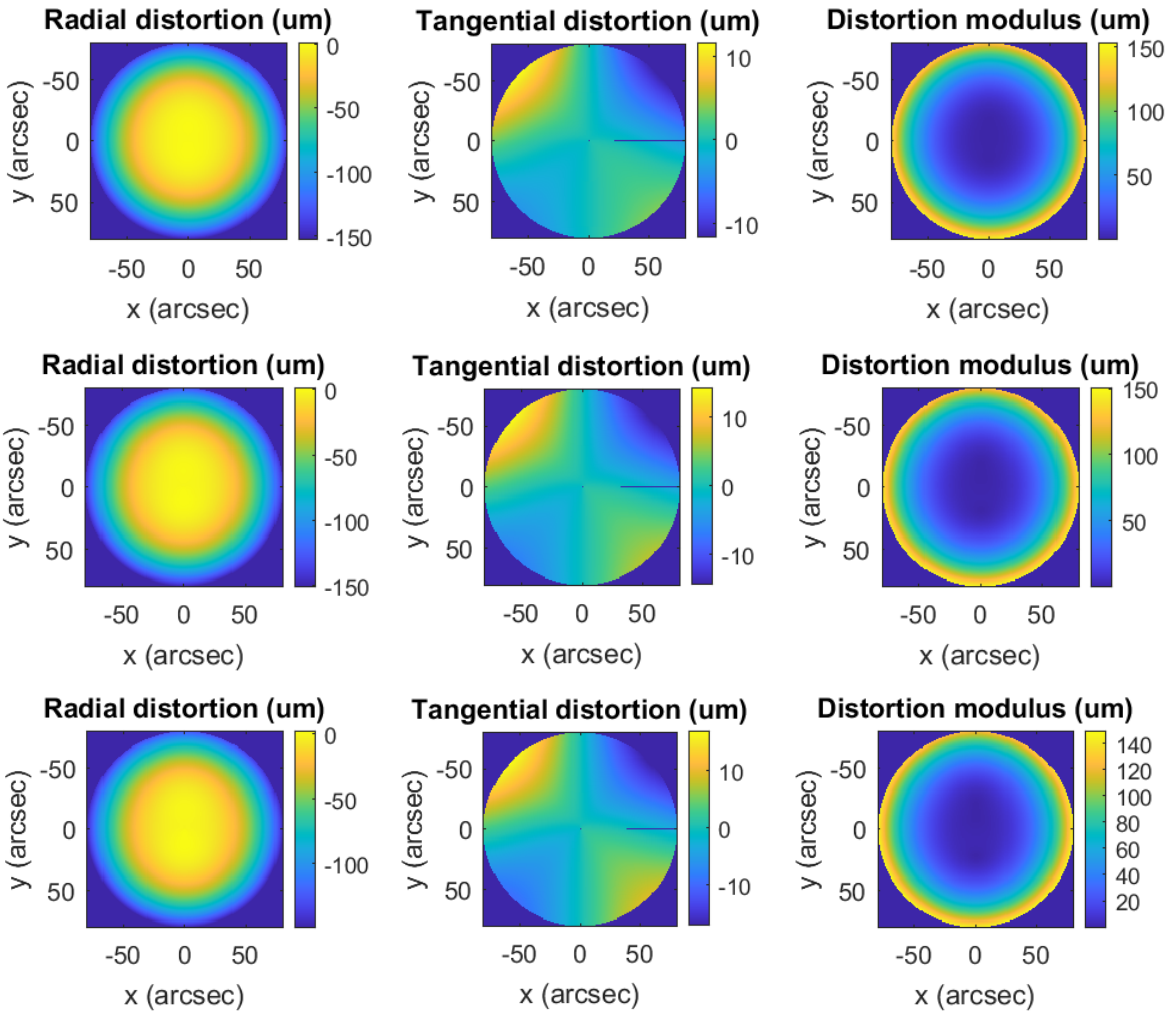

Figure 31. Radial component, tangential component and modulus of the field distortion computed at wavelength 1 µm (top), 1.65 µm (middle) and 2.2 µm (bottom) over the technical FoV.

We have also evaluated the field distortion residuals after applying the polynomial fit of the distortion pattern with respect to the undistorted map (see Figure 32) at wavelength 1 µm. We have sequentially applied the correction of first order polynomial fit (scale), third order polynomials fit (theoretical field distortion power) and fifth order polynomial fit. After correcting for the first order polynomial fit the residual of the distortion, the maximum residual diminishes from about 46 mas to 16 mas. By applying also the third order correction, the residual further diminishes to about 0.17 mas as expected for a nominal optical system. The fifth order correction lowers the residual below 2 micro-arcsec.

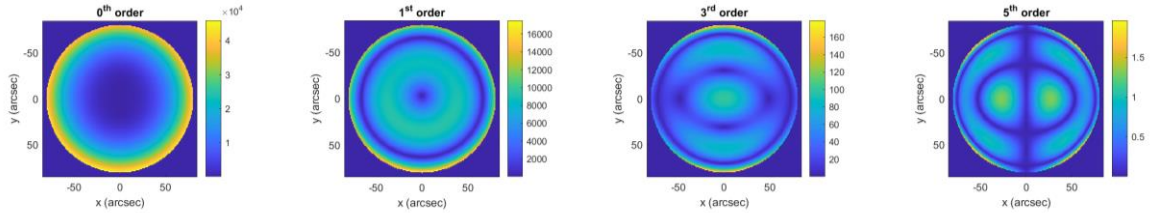

Figure 32. Modulus of the distortion with no correction (first column), after a 1st order polynomial fit correction (second column), a 3rd order polynomial fit correction (third column) and a 5th order polynomials fit correction (fourth column) of the field distortion map with respect to the undistorted map. Color bar units are micro-arcsec.

MAO-SF0-1.3.4.7 intra-epoch field distortion variation: *MAORY shall not introduce a PSF centroids drift larger than 3.8 mas (intra-epoch distortion variation) over the technical Field of View during an astrometric observation of 120 sec with target altitude equal to 80 degrees.*

The angular rate of field rotation is given by V = K × cos(Az)/cos(Alt), where K is the angular rate of field rotation, K = Earth angular rate rotation(degrees/hour) × cos(latitude) = 13.67616 degrees/hour (assuming Cerro Armazones latitude = 24° 35′ 51″ S; Earth angular rate rotation = 15.04106858 degrees/hour).

Assuming Az = 0 degrees (meridian, worst case) and Alt = 80 degrees, we obtain that V = 78.758 degrees/hour = 0.0219 degrees/sec. The maximum rotation angle of the field for 120 sec observation is then 2.6 degrees.

During the MMS main path optimization, we have minimized the intra-epoch distortion variation by implementing the field rotation of 2.6 degrees of the sky and a counter-rotation of MICADO (same results are valid for the second instrument). A scheme is shown in Figure 33. We have considered the centroids position at the edge of the technical field of view, every 15 degrees azimuthal rotation angle, in the nominal position. We have rotated the sky coordinates by 2.6 degrees and counter-rotated the MICADO entrance focal plane (rotator) by the same amount. We have then compared the centroids coordinates before and after the rotation/counter-rotation. The optimization has been done at wavelength of 1 µm. The budget of 3.8 mas corresponds to 12.6 micron.

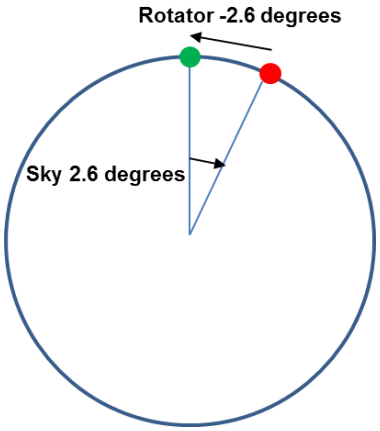

Figure 33. Scheme of the intra-epoch distortion variation implementation during the optimization process.

In Figure 34, radial component, tangential component and modulus of the intra-epoch distortion variation computed at wavelength 1 µm (top), 1.65 µm (middle) and 2.2 µm (bottom) over the technical FoV are shown.

The MMS main path has a nominal maximum intra-epoch distortion variation ≤ 1.5 micron all over the technical FoV, corresponding to 0.5 mas.

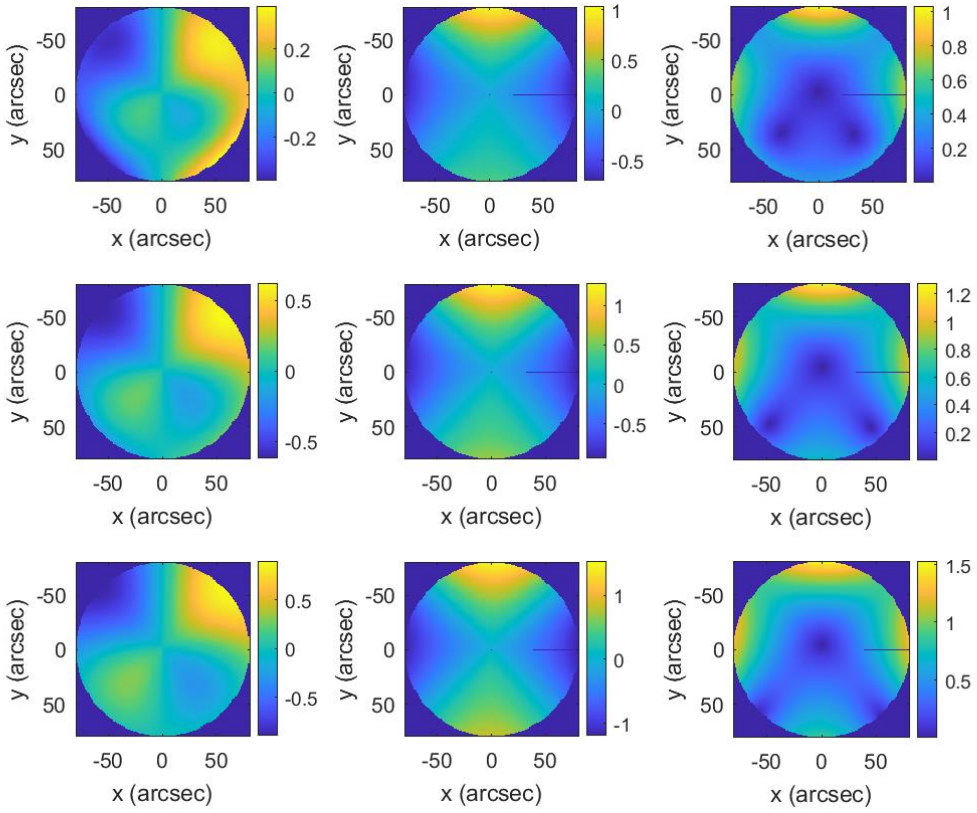

Figure 34. Radial component (first column), tangential component (second column) and modulus (third column) of the intra-epoch distortion variation computed at wavelength 1 µm (top), 1.65 µm (middle) and 2.2 µm (bottom) over the technical FoV. Color bar units are micron.

MAO-SF0-1.3.4.8 Inter-epoch field distortion variation: *MAORY shall permit inter-epoch observations such that the relative position on the sky among unresolved, unconfused sources 1 arcsec apart, having optimal brightness with respect to an optimal set of reference sources must be reproducible to within 50 μas (goal: 10 μas) over a central, circular field of 20 arcsec diameter (goal: 75 arcsec diameter), after having applied astrometric polynomial fit of the distortion pattern.*

This requirement is still at too higher level to be properly implemented in the optimization of the optical design. However, we have verified it a posteriori as follow.

We have considered the centroids position corresponding to a set of test stars placed over a regular square grid, having step of 1 arcsec over the MICADO FoV. We have computed the image centroids position of the grid all over the azimuthal rotation angle (up to 180 degrees given the optical system symmetry) with step of 5 degrees. We have assumed as reference the image centroids position of the grid having azimuthal angle 0 degrees.

For each azimuthal rotation angle, we have computed the residual between the corresponding centroids grid and the reference centroids grid. On the residuals, we have applied, in sequential steps, the astrometric correction by mean of the first, third and fifth order polynomials fit. An example of the analysis results, corresponding to the distortion map at azimuthal angle 30 degrees with respect to the reference distortion map at azimuthal angle 0 degrees, is shown in Figure 35.

Finally, we have estimated the astrometric error among sources having relative on sky distance 1 arcsec (both in X and Y directions) by subtracting their residuals. An example, corresponding to the distortion map at azimuthal angle 30 degrees with respect to the reference distortion map at azimuthal angle 0 degrees, is shown in Figure 36.

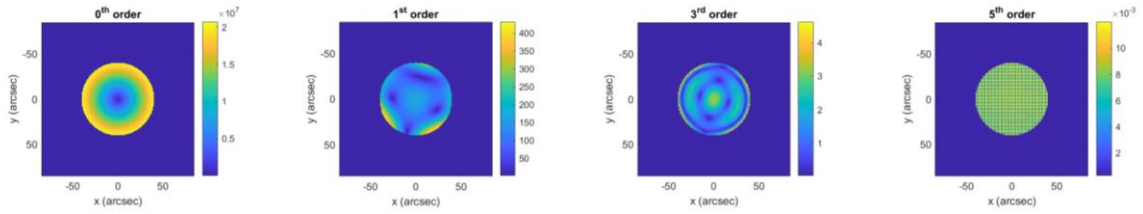

Figure 35. Modulus of the distortion residuals with no correction (first column), after a 1st order polynomial fit correction (second column), a 3rd order polynomial fit correction (third column) and a 5th order polynomials fit correction (fourth column) of the distortion map corresponding to 30 degrees azimuthal angle, assuming the reference distortion map at 0 degrees azimuthal angle. Color bar units are micro-arcsec.

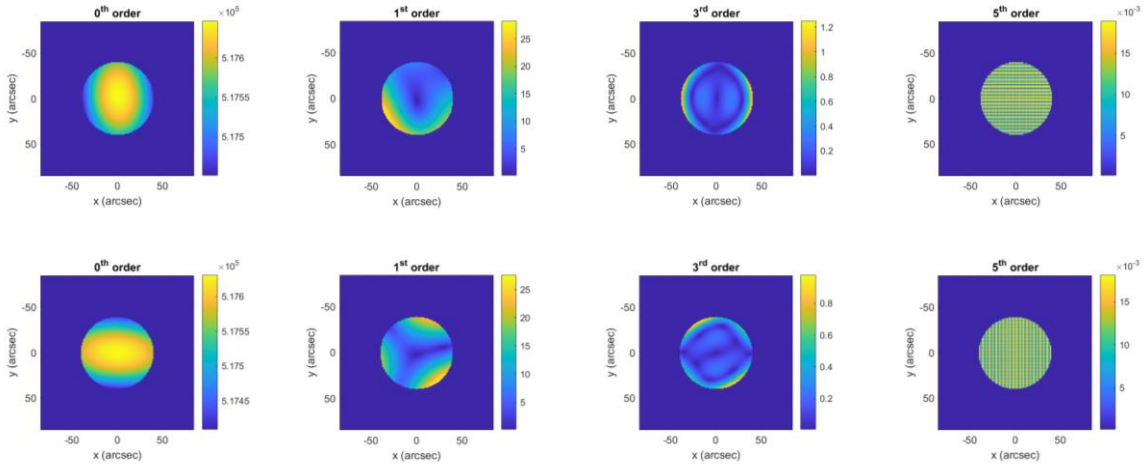

Figure 36. Modulus of the distortion residuals between two stars having on sky distance 1 arcsec in X direction (top) and Y direction (bottom) with no correction (first column), after a 1st order polynomial fit correction (second column), a 3rd order polynomial fit correction (third column) and a 5th order polynomials fit correction (fourth column) of the distortion map corresponding to 30 degrees azimuthal angle, assuming the reference distortion map at 0 degrees azimuthal angle. Color bar units are micro-arcsec.

Figure 37 shows the nominal residuals between two stars having on sky distance 1 arcsec, cumulated over X and Y directions, as function of the azimuthal angle of the distortion map, assuming the reference distortion map at 0 degrees azimuthal angle, with no correction, after a 1st order polynomial fit correction, a 3rd order polynomial fit correction and a 5th order polynomials fit correction. In the figure, the central mark indicates the median, and the bottom and top edges of the box indicate the 25th and 75th percentiles, respectively. The whiskers extend to the most extreme data points.

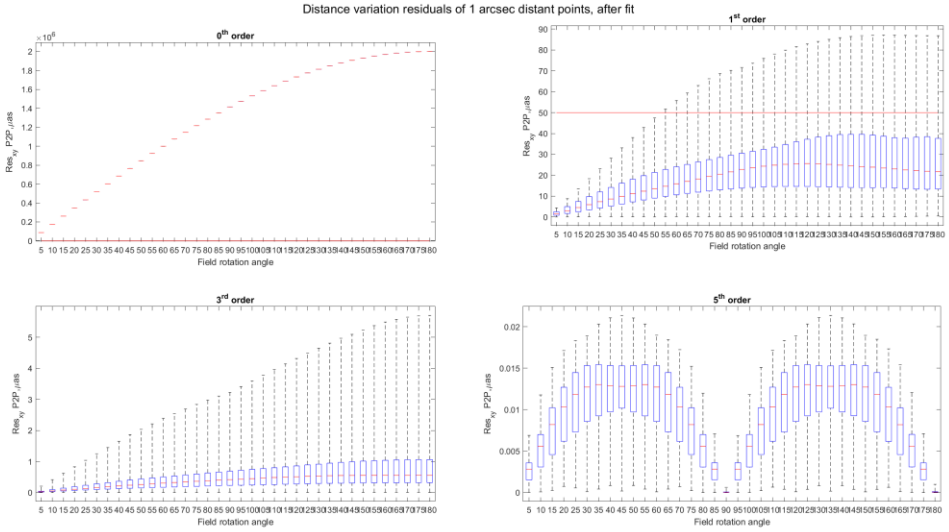

Figure 37. Nominal residuals between two stars having on sky distance 1 arcsec, cumulated over X direction and Y direction, as function of the azimuthal angle of the distortion map, assuming the reference distortion map at 0 degrees azimuthal angle, after

applying no correction, a 1st order polynomial fit correction, a 3rd order polynomial fit correction and a 5th order polynomials fit correction.

Just after the first order correction, the astrometric error associated to two stars 1 arcsec apart is below 50 micro-arcsec up to a azimuthal rotation angle of 50 degrees over the full MICADO FoV. The third order correction lowers the residual below 6 micro-arcsec for all azimuthal rotation angles. After the fifth order correction, the residual is dominated by the numerical errors of the computation.

All the simulations shown in this section refer to the nominal MMS design and the distortion patterns do not take into account any possible distortion generated by manufacturing residual errors of the optics. The estimate of the additional distortions coming from the optics manufacturing is discussed in sections 4.1.5.3, 4.1.5.4 and 5.

3.2.10 Deformable Mirrors

MAO-SF0-1.3.3.1: *The PFRO shall consider two post focal DMs [RD2].*

MMS has been designed to accommodate two post-focal DMs (M9M and M10M), one conjugated at high altitude and one at low altitude. The trade-off on the cost/benefit of the low DM is not yet concluded. If the low DM will be not installed, it will be substituted by a monolithic mirror with identical optical characteristics and interfaces.

MAO-SF0-1.3.3.2.1*: The static shape and position of the Deformable mirrors is defined in Zemax E-MAO-SF0-INA-MOD-001 MMS reference optical design [RD2].*

The DMs optical parameters, defining the shape, and positioning coordinates are included in the Zemax model [RD9].

During the optimization, we have considered a set of point sources located on the meta-pupil (see Figure 38). The optical system aperture is determined by the cone angle (telecentric beams in the object space) defined by the technical FoV (160 arcsec). The image of the meta-pupil has been optimized in terms of RMS spot diameters over the curved and tilted surface corresponding to the DM surface. The conjugation altitudes and the size of the meta-pupils footprints on the DMs have been optimized within the required range.

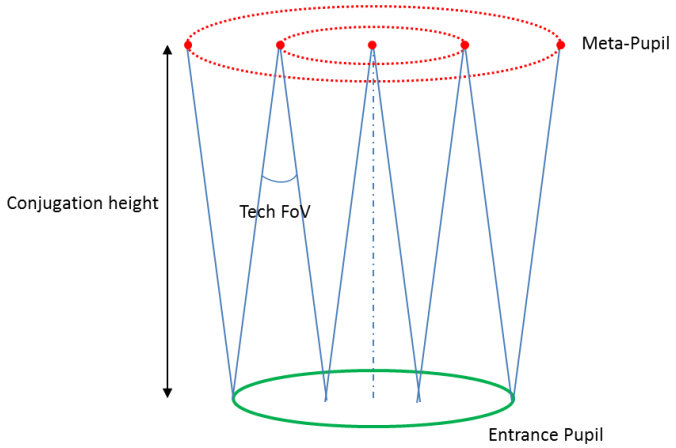

Figure 38. Scheme of the meta-pupil sources on the metapupil in the optimization process of DMs.

MAO-SF0-1.2.3.1: *The two DMs shall be conjugated within 6-12 km and 17-20 km over the telescope entrance pupil [RD2].*

The nominal conjugation altitude of high DM (M9M) is 17.461 Km, corresponding to a meta-pupil diameter of about 52.087 m. The nominal conjugation altitude of low DM (M10M) is 6.501 km, corresponding to a meta-pupil diameter of about 43.561 m.

MAO-SF0-1.3.3.2.2: *The two DMs shall have at least 30 actuators over the meta-pupil image diameter* assuming an actuator pitch of 25 mm *[RD2].*

The high DM (M9M) has a meta-pupil footprint diameter of about 867 mm in X direction and 872 mm in Y direction. The low DM (M10M) has a meta-pupil footprint diameter of about 1153 mm in X direction and 1146 mm in Y direction.

Assuming voice-coil actuators technology with typical actuator pitch of 25 mm, the number of actuators of high DM and low DM over the meta-pupil image diameter is about 35 and 46 respectively.

MAO-SF0-1.2.3.2: *The images on DMs of the conjugated layers shall have an RMS spot diameter < 1/10 of the DM pitch [RD2].*

We have computed the polychromatic RMS spot diameter corresponding to a grid of point sources covering the meta-pupils. Results are shown in Figure 39.

The maximum polychromatic RMS spot diameter is below 1.85 mm (<2.5 mm corresponding to 1/10 DMs pitch).

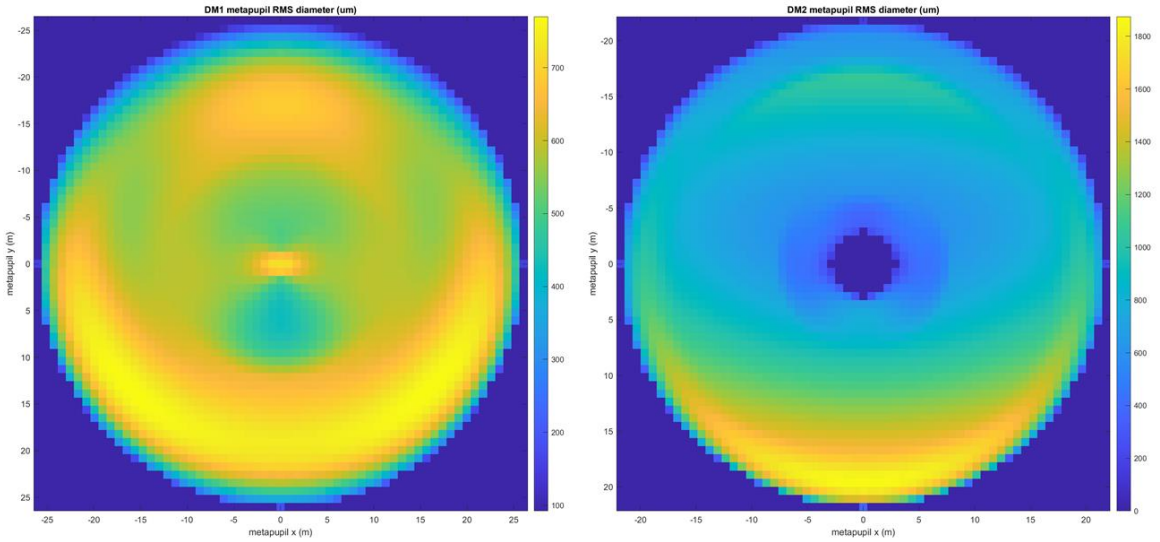

Figure 39. RMS spot diameter maps in meta-pupil coordinates for the high DM (left) and low DM (right). Color bar units are microns.

3.2.11 Aspherical surfaces

The MMS implements three aspherical surfaces:

- Second surface of the CPM
- Concave mirror M7M
- Concave mirror M8M

The aspheric surface on the CPM has been inserted in order to correct the optical system for conjugated planes not located at infinite. This correction allows to improve the quality of the exit pupil, DMs conjugated planes and of the LGS conjugated planes, so that at the MPO deliver to the LGSO an image quality basically equal to the one delivered by ELT, impacting on the design simplification of the LGSO itself.

By placing the CPM aspheric surface close to the entrance focal plane the impact on the quality of the main path is almost negligible. However, the closer to the focal plane, the worst for the main path field distortion. The CPM has been positioned at 350 mm from the focal plane where the main path field distortion can be controlled below acceptable value and the WFE impact is negligible. At this distance, indeed, the footprint diameter of a point source at infinity is about 19.73 mm, and the footprints of two stars 1 arcsec apart are overlapping, with distance between centroids equal to 3.35 mm. The overlapping allows to relax the constraint on the manufacturing high frequency amplitude, that might impact on the inter-epoch distortion variation (see 4.1.5.4).

Moreover, placing the CPM far from the focal plane mitigates the contamination effect on the photometric signal. A 20 micron particle generates a signal loss of the order of 10^{-6}.

Finally, we decided to place the aspheric surface on the second surface of the CPM to mitigate the thermal deformation due to thermal gradient between internal and external environment.

The surface sag, tangential slope and sagittal slope of the CPM second surface over the aperture diameter 810 mm are shown in Figure 40. The PtV sag is about 0.588 mm. The maximum slope is about 2.21 mrad. The PtV sag over the polished diameter (760 mm) is 0.507 mm.

The aspheric surfaces on M7M and M8M allows to control the WFE introduced on the system by the tilt of the optical elements with power (M7M, M8M, M9M, M10M), mostly astigmatism and coma, and allows at the same time to minimize the field distortion of the main path. During the optimization process, we have minimized the optical elements tilt, compatibly with the clearance of the optical beam, in order to reduce the aspheric sag. At the same time, we have aimed to reduce the size of the aspheric surface to polished diameter below 1250 mm, given that it represents an upper limit for most of the potential provider companies. The aspheric surfaces are on-axis.

The surface sag, tangential slope and sagittal slope of M7M surface after removing the nominal radius of curvature over the aperture diameter 1240 mm (the required polished diameter is 50 mm less) are shown in Figure 41. The PtV sag is about 0.127 mm (0.110 mm over the polished diameter of 1190 mm). The maximum slope is about 0.46 mrad. The surface sag, tangential slope and sagittal slope of M8M surface after removing the nominal radius of curvature over the aperture diameter 1280 mm (the required polished diameter is 50 mm less) are shown in Figure 42. The PtV sag is about 0.383 mm (0.350 mm over the polished diameter of 1230 mm). The maximum slope is about 0.78 mrad.

Even if the sag departures are relatively large, the slopes are well below the 15-20 mrad representing a manufacturing limit provided by potential providers.

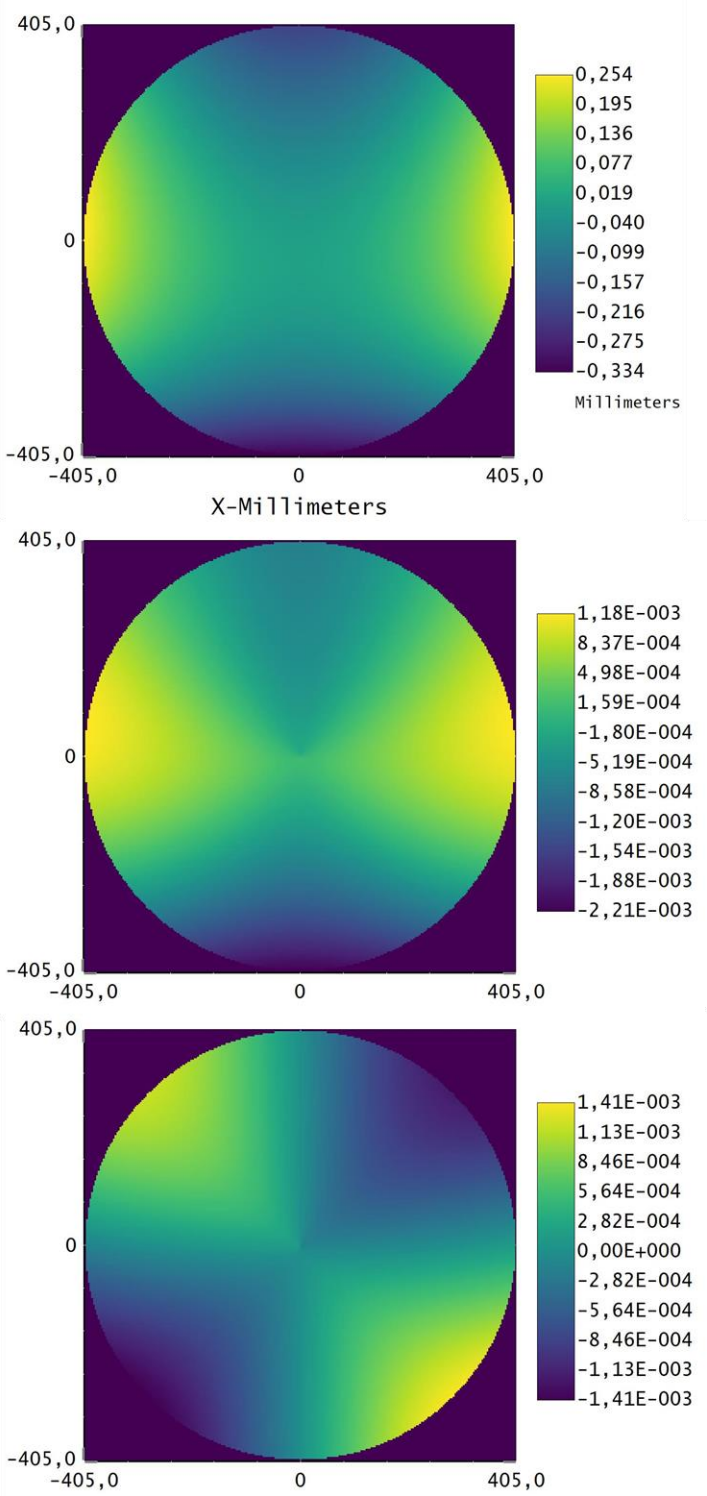

Figure 40. Surface sag in mm (top), tangential slope in radians (middle) and sagittal slope in radians (bottom) of the second surface of the CPM.

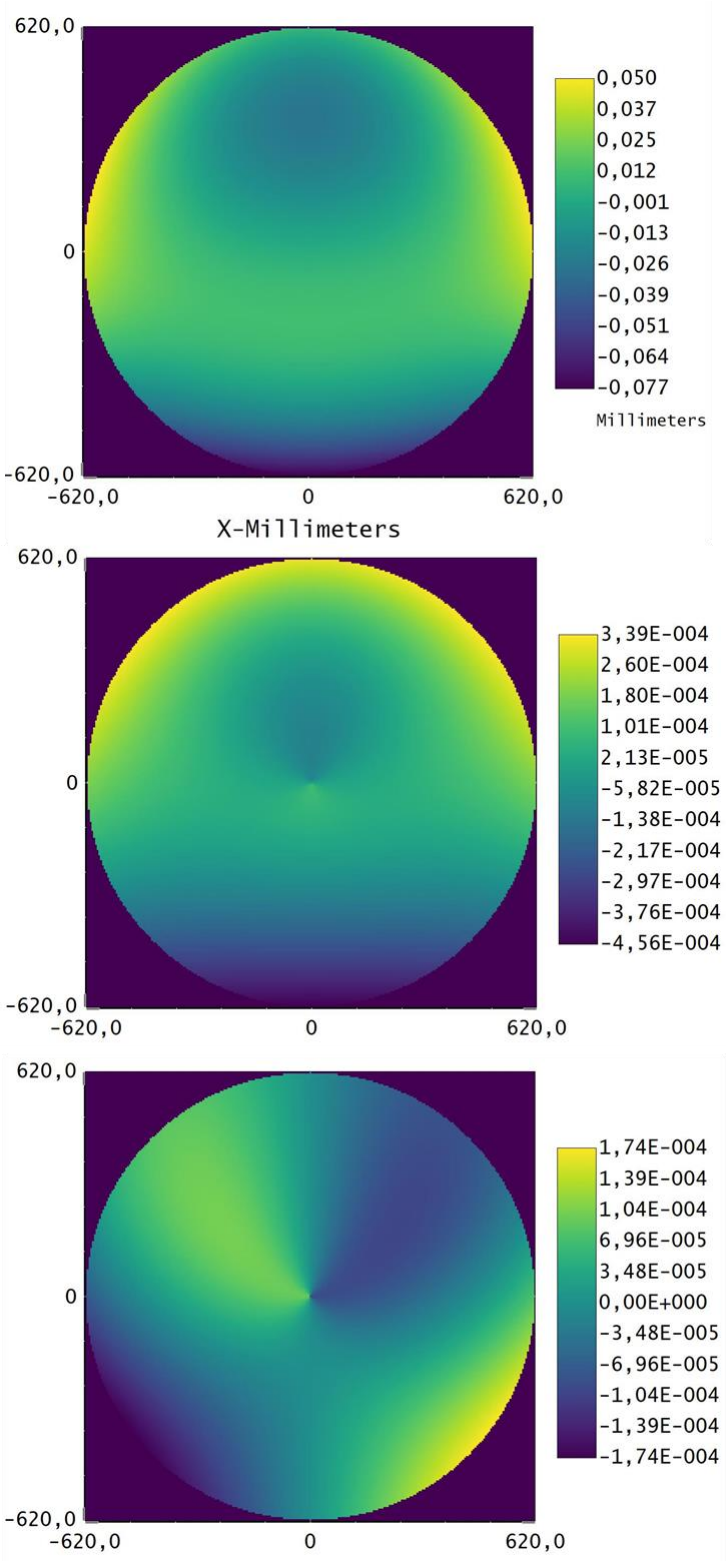

Figure 41. Surface sag in mm (top), tangential slope in radians (middle) and sagittal slope in radians (bottom) of M7M surface after removing the nominal radius of curvature.

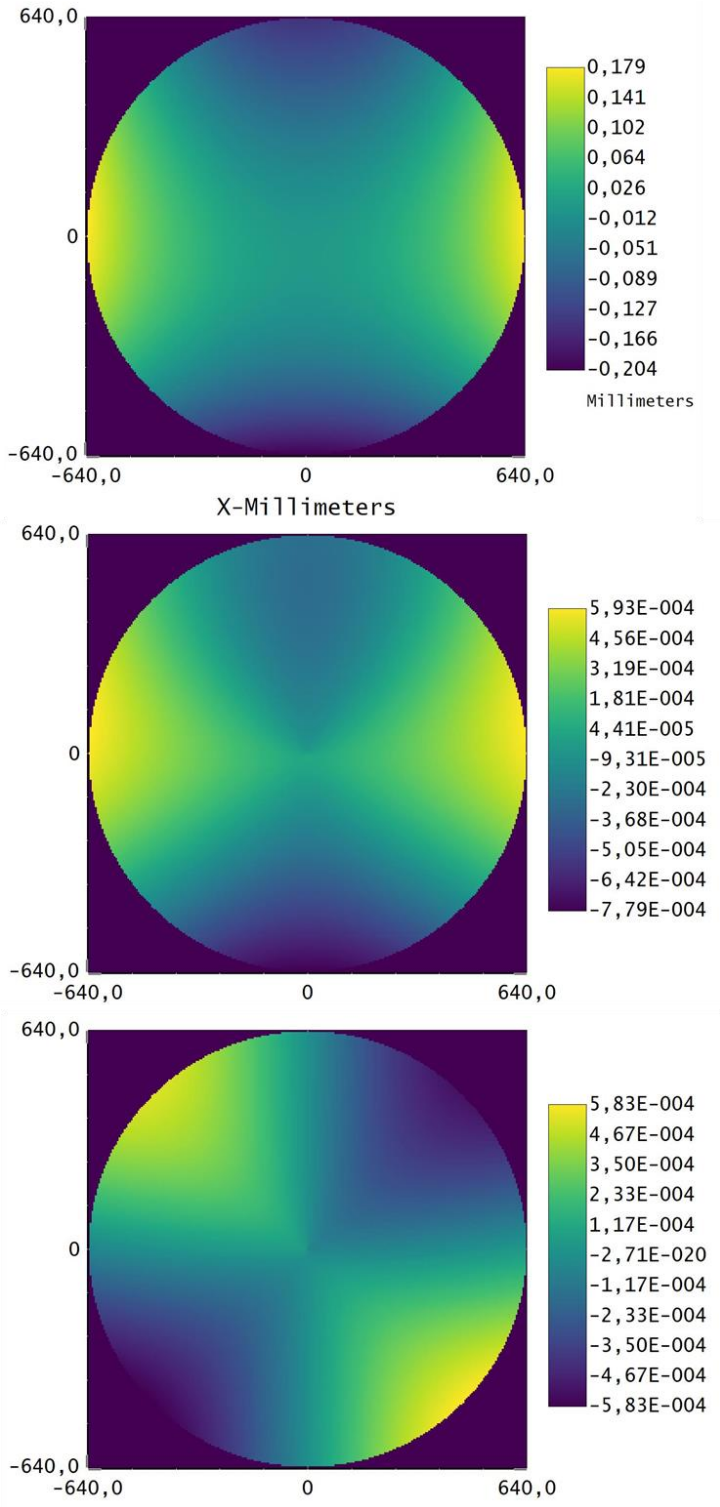

Figure 42. Surface sag in mm (top), tangential slope in radians (middle) and sagittal slope in radians (bottom) of M8M surface after removing the nominal radius of curvature.

3.2.12 Flip Mirror

The selection between MICADO and second port instrument is done by flipping the flat mirror M11M. At this working level, we are assuming that the only difference between the two channels is given by the differential gravity load effect on the surface of M11M between the two positions.

The detailed description of the analysis of the gravity load effect is given in [RD13].

In Figure 43 it is shown the differential effect on M11M surface due to gravity load between MICADO feed position and second port instrument feed position.

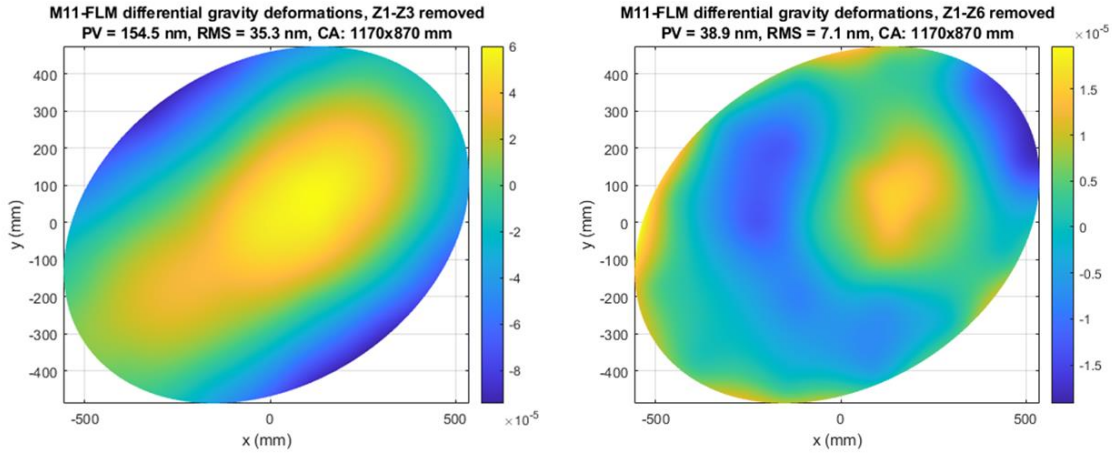

Figure 43. M11M differential surface gravity deformation between MICADO feed position and second port instrument feed position after removing pistons and tip/tilt (left) and defocus and astigmatism (right).

After removing piston and tip/tilt, the differential RMS surface error has been estimated 35.3 nm. However, the MMS alignment and collimation procedure (see paragraph 4.1.5.1.2) allow to minimize defocus and astigmatisms of the system. Removing such aberrations by the differential RMS surface error has been estimated 7.1 nm.

3.2.13 Dichroic

In the MMS optical configuration, one of the key elements is a large size dichroic mirror that can be considered as a high performances hot mirror. Being a hot mirror, it reflects NIR light, but, at the same time, it is required to reflect the visible portion of the spectrum down to 600 nm for SCAO and LGS WFS and to transmit the LGS light at 589 nm.

The detailed spectral specifications of the filter, we are aiming and currently discussing with provider companies, are reported in Table 8.

Description	**Requirement**
Wavelength range	0.589-2.4 µm (goal 2.5 µm)
Wavelength separation	· transmitting LGS, reflecting SCI+TECH FoV: IR-reflecting dichroic · wavelength < 0.6 µm, transmitted (T) · wavelength >0.6 µm, reflected (R)
Shape of transition at cut-off	Not specified – not critical

Spectral behavior < 0.6 µm	Short-pass type filter Notch type filter (i.e. band-pass around 0.589 µm)
Efficiency	o Wavelength 0.6 – 0.7 µm R > 80 % average o Wavelength 0.7 – 1.0 µm: R > 92% average o Wavelength >1.0 µm: R > 95% o Wavelength > 1.9 µm: R > 95% (goal R > 98%) o Wavelength 0.589 µm: T > 95% **NOTE:** in case the requirements above could not be met, suppliers are invited to maximize the efficiency in the wavelength range 1.9-2.4 (2.5 goal) µm.

Table 8. Dichroic filter spectral specifications.

We highlight here the wide reflection range, i.e. from 0.7 to 2.4 µm. The shortest wavelength is about a factor 3 less than the longest wavelength. This has an impact on the modulations and on the ripples in the reflected spectrum, especially at the shortest wavelengths. Accounting for that behaviour, and given that the most important science spectral range is in the J, H, K band, we have set the specification on the reflectivity below 1 µm as average value. However, the complexity of the coating is high: it requires many layers to match the specifications and this turns into a large coating thickness. The transmitted spectrum is limited to the LGS signal (Na line at 0.589 µm) with no particular requirement on the bandwidth (a few nm).

On the second surface of the dichroic, we foresee the deposition of an AR coating for the wavelength 0.589 µm. This coating can easily have reflectivity below 0.05% and it leaves quite large degrees of freedom to counterbalance the mechanical bending of the substrate, which can be introduced by the hot mirror coating.

The nominal clear aperture of the dichroic is 840 mm diameter while the mechanical aperture is 940 mm diameter. As for the other optical surfaces, we require 50 mm margin over the diameter with respect to the nominal aperture diameter, for alignment and handling. The thickness of the substrate is 80 mm. The thickness-diameter ratio is close to 1/10. The aperture diameter of the dichroic is determined by the footprints of the external fields of the LGS path on its second surface as shown in Figure 44.

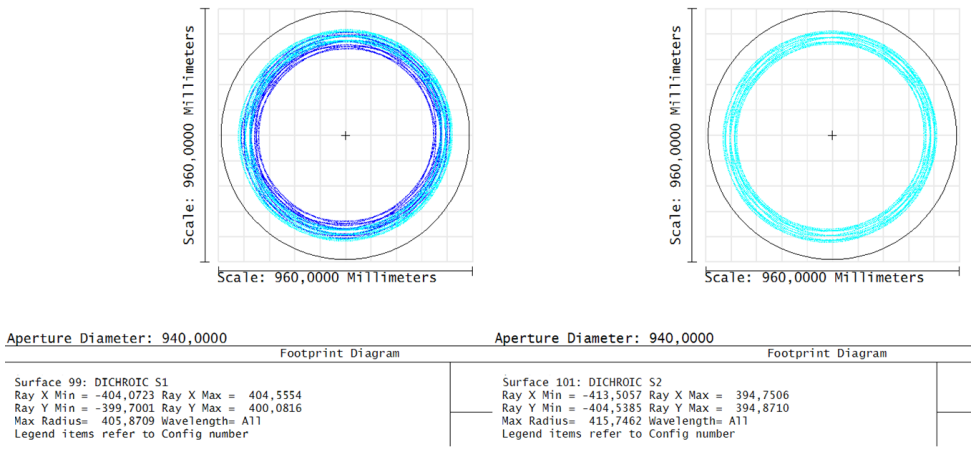

Figure 44. Footprints on the dichroic first surface (left) and second surface (right) of the external fields of the main path (blue) and of the LGS path at 84 km (cyan).

Nominally, the AOI of central field chief ray is 11.3 degrees, while the maximum and the minimum AOI at the edge of the FoV are 14.0 degrees and 8.6 degrees respectively.

The assumed substrate material is Suprasil 3002. It has the highest internal transmissivity in the VIS-NIR band among the silica glasses (see Figure 45). It is the same material of the CPM, and allows to minimize the thermal background. Suprasil 3002 can reach high refractive index homogeneity also on one-meter-class blank, ≤ 5-10 ppm PtV. Moreover, most of the non-homogeneity has, basically, defocus-like shape with the wings concentrated on the outer part of the circular blank, outside the polished aperture. The region of interest can reach homogeneity close to 1-1.5 ppm PtV, again mainly defocus. This high homogeneity allows to minimize the NCPA that has to be calibrated between the main path and the LGS path.

Another important aspect is the impact of the dichroic mirror surface on the WFE. At the time being, we are assuming that the surface error is largely dominated by defocus with small residuals for higher terms (see Table 10, Table 12 and Table 13 in section 4). The defocus and the astigmatism on the dichroic surface can be compensated during the alignment of the MMS. The higher order aberrations should have low amplitude since the surface is close to the pupil image and directly affect the WFE. However, depending on the spatial frequency of the surface error, it can be corrected by ELT M4.

In the following, we elaborate on the two key aspects of this optical element: the spectral performances and the surface error control.

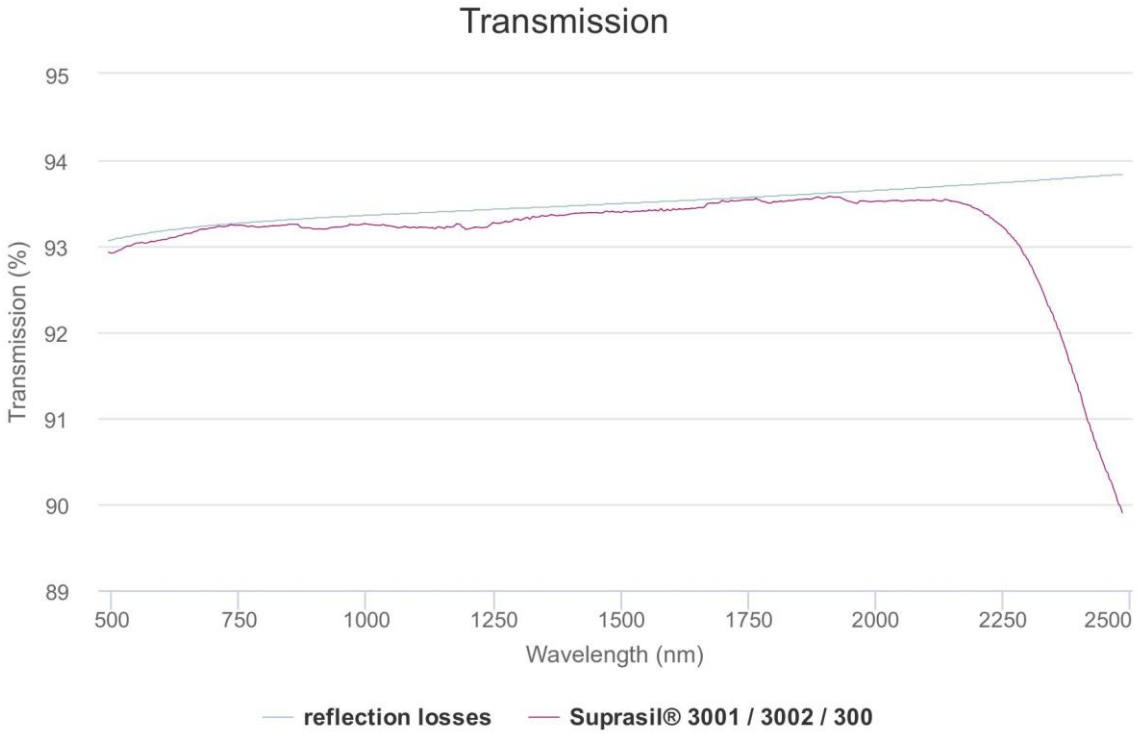

Figure 45. Transmissivity curve of a Suprasil 3002 slab having thickness 80 mm. The internal transmissivity is given by the difference between reflection loss and transmission curves.

3.2.13.1 Spectral response of the filter

The spectral response is a function of the stack layers, the materials used and the incidence angle. As for the materials, they depend on the manufacturer. Usually, such hot mirrors are based on SiO_2 and TiO_2. In some cases, MgF_2 can be used as L material and Ta_2O_5, Nb_2O_5, HfO_2 as H materials. For example, MATERION (one of the potential manufacturer we are in touch with) uses SiO_2 and Nb_2O_5. Since this material has a smaller refractive index than TiO_2, the coating will be thicker assuming similar performances. According to these two materials, we performed some simulations of the filter. The results are shown in Figure 46.

The coating has a thickness of about 13.7 μm and consists of 68 layers. The coating is not simple at all and it is quite thick, but certainly feasible. Assuming a thickness tolerance of 1% (typical value for standard deposition) the performance are within the spec above 1.15 μm and marginally out of spec below (see Figure 47). The transmittance at 589 nm gets worse to about 85% in the worst case.

However, it is important to underline that this coating does not represent a possible recipe, since it will strictly depend on the effective refractive index of the deposited layers, and this varies according to the manufacturer deposition technique, conditions, etc.

Materion has provided their own simulation of the coating (similar recipe). The reflectance curve is shown in Figure 48. This coating is slightly thicker (15 μm) and provides optimal performances, especially in NIR region. This coating design is feasible by MATERION and, at the moment, it represents the reference design.

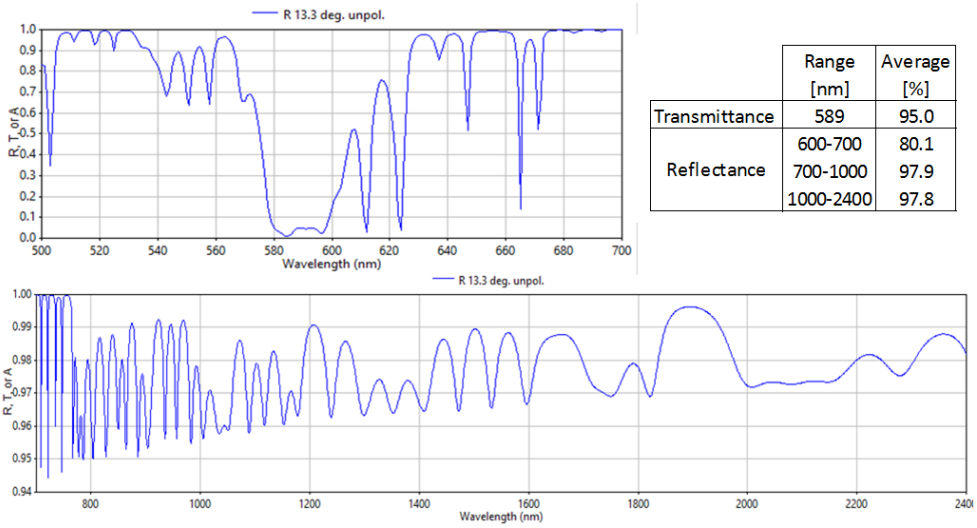

	Range [nm]	Average [%]
Transmittance	589	95.0
Reflectance	600-700	80.1
	700-1000	97.9
	1000-2400	97.8

Figure 46. Reflectance curve of the dichroic filter (recipe SiO_2 and Nb_2O_5, 68 layers) simulated by the consortium (nominal performance).

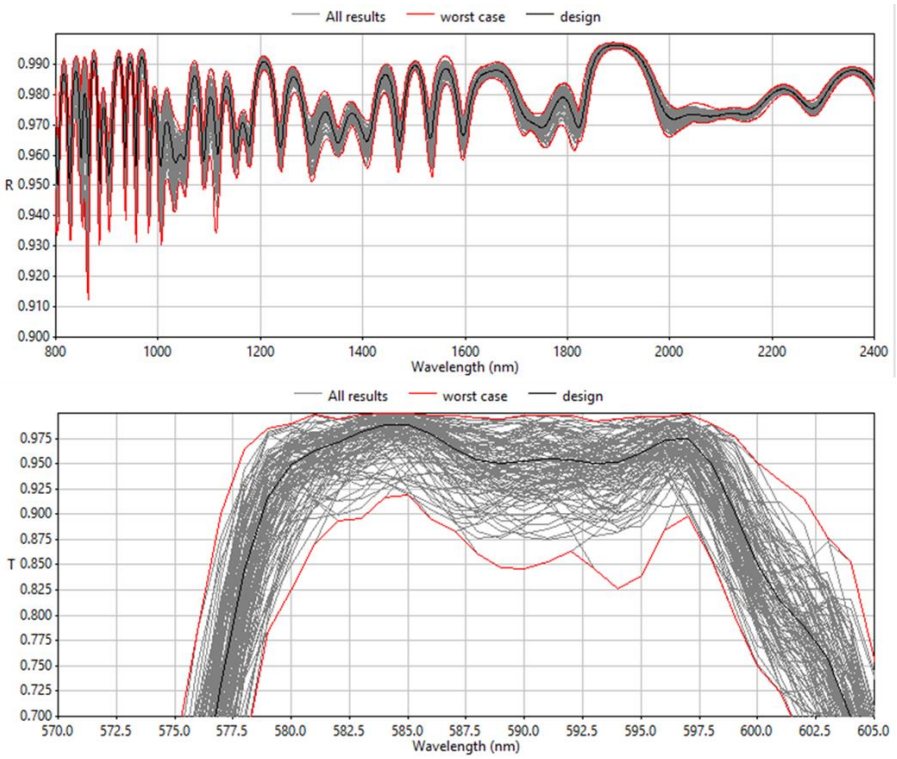

Figure 47. Reflectance curve in the 800 – 2400 nm range for a tolerated design considering 1% random thickness variation (top). Transmittance curve at 589 nm (bottom).

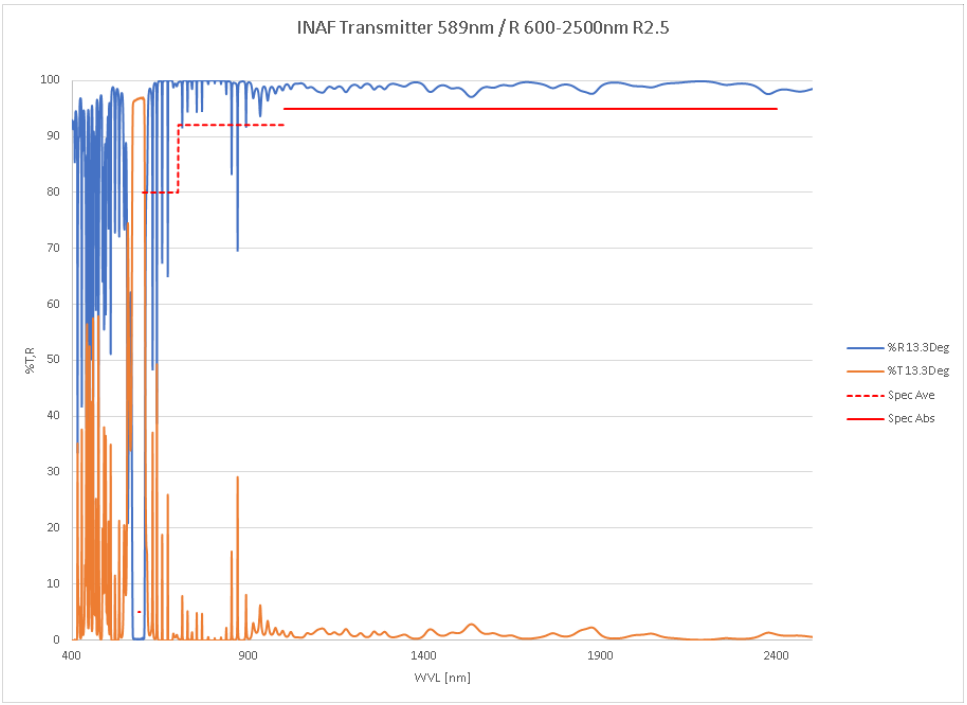

Figure 48. Reflectance (blue) and Transmittance (orange) curve of the dichroic filter proposed by MATERION (nominal design).

Both the dichroic filters shown above have an intrinsic large thickness. This might represent an issue for the final surface quality of the hot mirror. For this reason, we have explored also the possibility of thin coating filters. SAFRAN REOSC (one of the potential manufacturer) has proposed a coating filter having thickness of about 0.5 μm. The reflectance and transmittance curves are shown in Figure 49.

This design does not fully match the specification especially below 700 nm (R = 38%) and for the transmissivity of the LGS light (T = 77%).

However, despite the thin coating, it does not present ripples. Moreover, removing the coating does not require the re-polishing of the substrate surface mitigating the impacts of potential errors during the deposition process. This coating is conceptually different and it is based on different materials, probably metals (the recipe materials were not provided). The coating design is feasible by SAFRAN REOSC and it represents the back-up design.

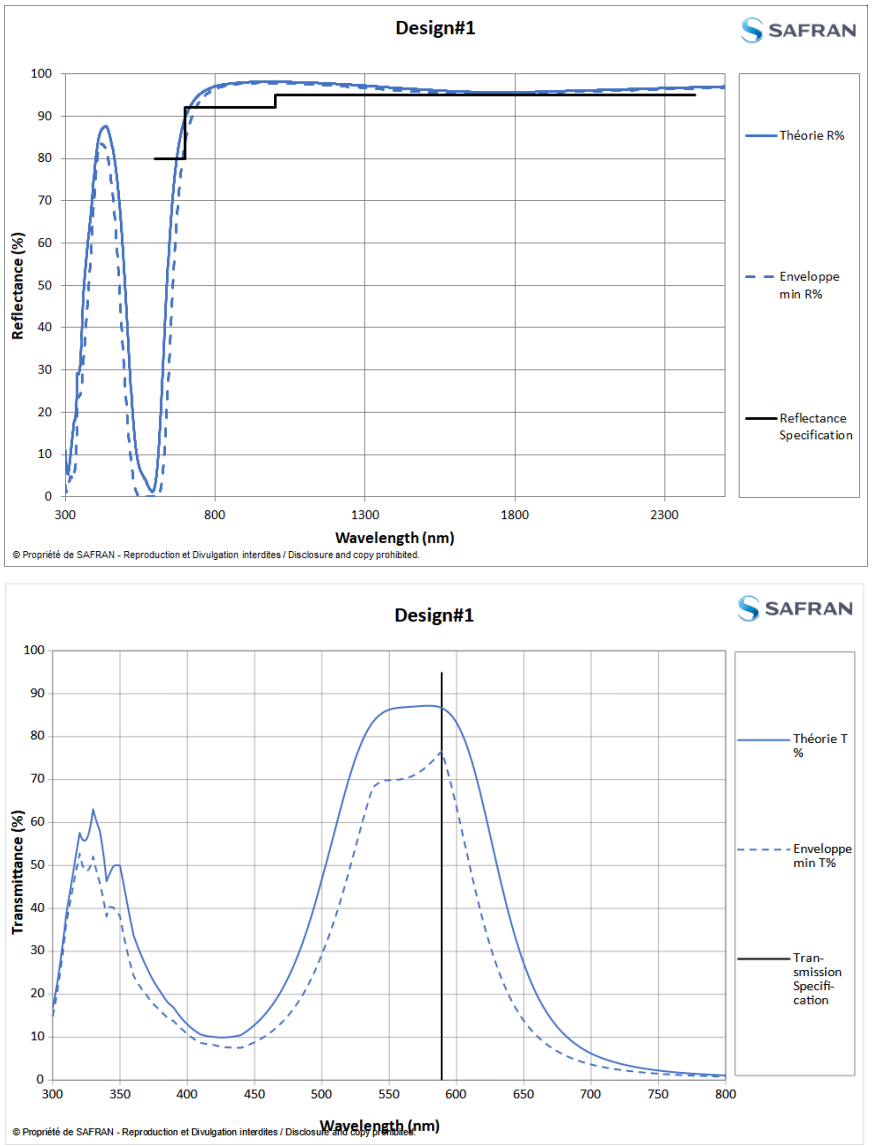

Figure 49. Theoretical reflectance (blue line) and tolerated reflectance (blue dashed line) curve (top) and theoretical transmittance (blue line) and transmittance reflectance (blue dashed line) at 589 nm of the dichroic filter proposed by SAFRAN REOSC.

3.2.13.2 Surface error control

The second aspect to consider is the control of the surface error. Since the filter is close to the pupil of the system, the surface error turns directly into a degradation of the image quality. Considering the coating, the surface error can be originated by two sources:

- The macroscopic mechanical deformation induced by the stresses added during the deposition. The coating on the other surface of the substrate can compensate such deformation. The mechanical deformation is directly proportional to the coating thickness. The effect on the surface is typically defocus, while the residuals after the compensation are typically astigmatisms.

- The inhomogeneity in the deposition process of each single layer introduces a variation of the overall film thickness. This thickness variation increases with the number of deposited layers. Interestingly, this variation is not random, has a smooth variation with the diameter (almost all defocus), and presents circular symmetry.

The back-up solution is much better for the surface error control point of view, given the small thickness and the, probably, small number of layers. Conversely, the reference solution is more challenging.

Actually, we are tuning together with MATERION the coating recipe with the aim of reducing the overall coating thickness. The preliminary information we received by the company is that reducing the coating thickness to 10 μm will allow to achieve the surface quality specification. However, the spectral performance will be not matched entirely.

We are currently working with MATERION on the definition of bread boarding activities with the aim to improve the overall knowledge of the expected performance, both spectral and surface quality.

In conclusion, the trade-off between the spectral and surface quality performance is still ongoing on the reference solution. The feasibility robustness will be improved through bread boarding activities. If during this process a show stopper appears, we will de-scope the spectral performance, aiming to the back-up solution.

3.2.14 Coatings

In the main path the coating deposited on the optical surfaces are:

- Broadband (0.6-2.4 μm) AR coating on CPM surfaces
- Protected silver on M6M, M7M, M8M, (M10M if it will be not a DM), M11M, M12M.
- Aluminium on M9M and M10M (if DMs).
- Dichroic filter in the first surface of the dichroic
- Narrowband (589 nm) AR coating on the second surface of dichroic, LGSO-L1, LGSO-L2, LGSO-L3 and LGSO-L4.
- Laser-line coating (589 nm) for LGSO-FM1, LGSO-FM2 and LGSO-FM3.

The reflectance of an already existing broadband AR coating provided by the company OFFICINA STELLARE is shown in Figure 50. The performances in the figure are nominal. The reflectance is below 1.8% overall spectral range.

We have assumed as reflectance of the protected silver coating and of the aluminum coating, the one assumed for the ELT surfaces. Figure 51 and Figure 52 respectively show the nominal reflectance.

The dichroic filter reflectance/transmittance is reported in section 3.2.13.

The narrowband AR coating at 589 nm has typically a transmittance > 99.5%.

The laser-line coating at 589 nm has typically a reflectance > 99.5%. It is a well-established technology in the field of high-power laser facilities.

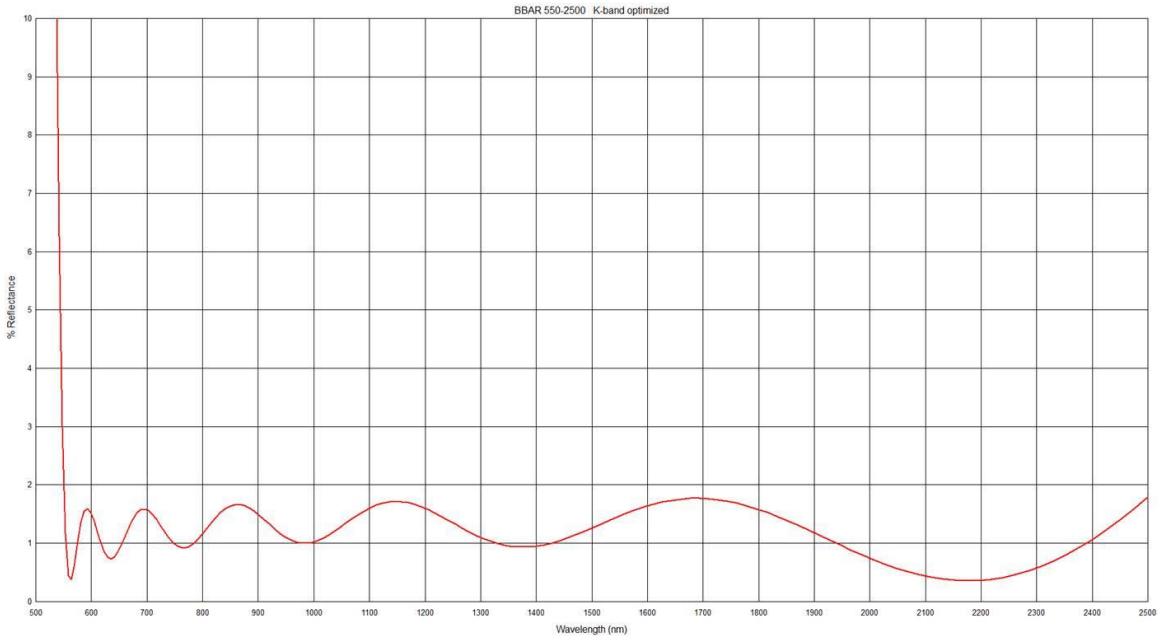

Figure 50. Nominal reflectance of a broadband AR coating by OFFICINA STELLARE.

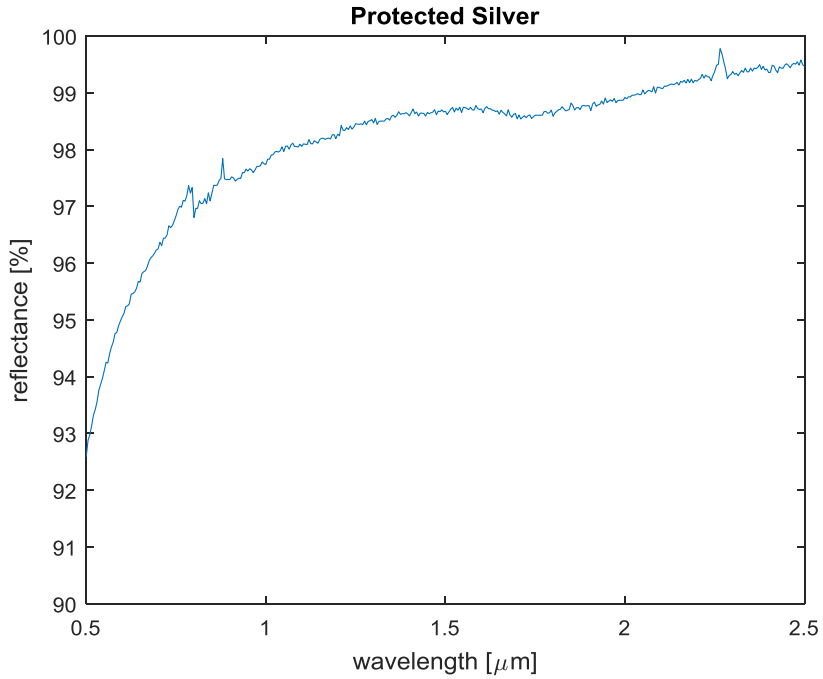

Figure 51. Nominal reflectance of protected silver coating.

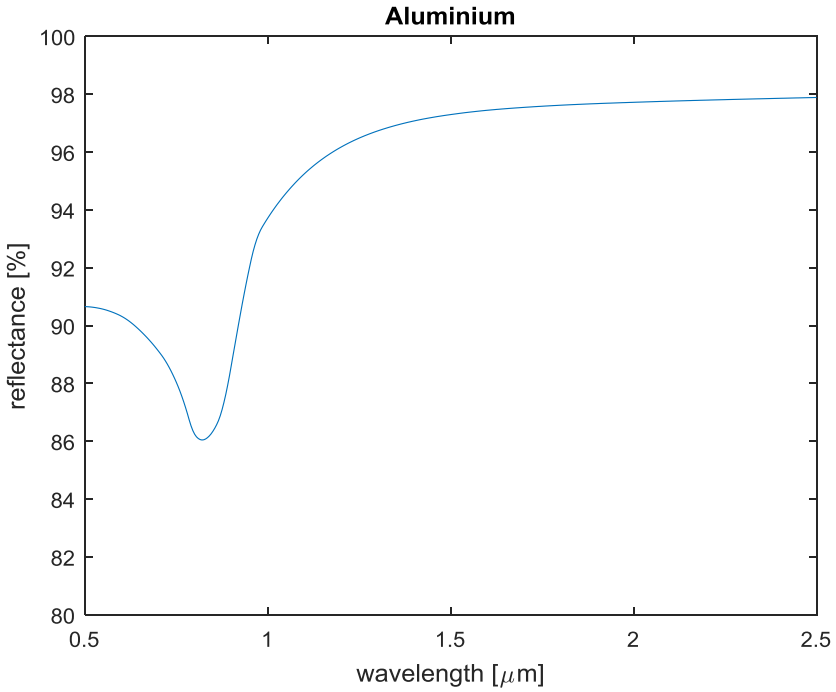

Figure 52. Nominal reflectance of aluminium coating.

3.2.15 Throughput

MAO-SF0-1.2.4.7: *MAORY optics from the entrance focal plane to the output primary port (2 DMs to be considered as worst case) shall have BOL transmission over the science fields of view greater than 80% on average in the wavelengths range 1.5-2.5 µm. [RD2].*

MAO-SF0-1.2.4.8: *MAORY optics from the entrance focal plane to the output primary port (2 DMs to be considered as worst case) shall have BOL transmission over the science fields of view greater than 65% on average in the wavelengths range 1.0-1.5 µm. [RD2].*

MAO-SF0-1.2.4.9: *MAORY optics from the entrance focal plane to the output primary port (2 DMs to be considered as worst case) shall have BOL transmission over the science fields of view greater than 55% on average in the wavelengths range 0.6-1.0 µm. [RD2].*

MAO-SF0-1.2.4.10: *MAORY optics from the entrance focal plane to the focal plane delivered to the LGSWFS module (2 DMs to be considered as worst case) shall have BOL transmission over the science fields of view greater than 53% at 589 nm.*

In the case of the main path throughput computation, we have assumed a CPM overall transmissivity equal to 95% (average) over the full spectral range (0.6-2.5 µm), five protected silver reflections (M6M, M7M, M8M, M11M, M12M) having reflectance as in Figure 51 and 2 aluminium reflections (M9M, M10M) having reflectance as in Figure 52. For the dichroic, we have assumed a MATERION-like filter throughput based on consortium tolerance estimate (average and worst case) and a SAFRAN-like filter throughput (worst case).

In the case of the LGS path (0.589 µm), we have assumed a CPM overall transmissivity equal to 95%, three protected silver reflections (M6M, M7M, M8M) having reflectance as

in Figure 51, three 589 nm laser-line coating (LGSO-FM1, LGSO-FM2, LGSO-FM3) having reflectance 99%, 2 aluminium reflections (M9M, M10M) having reflectance as in Figure 52 and four fused silica lenses (LGSO-L1, LGSO-L2, LGSO-L3, LGSO-L4) having overall transmissivity equal to 2% each. For the dichroic, we have considered similar scenarios as for the main path.

The assumed dichroic throughput scenarios are shown in Figure 53. The dichroic throughput of the LGS path has being specified equal to 95%. In the MATERION-like scenario, the throughput varies from 94.8% (average) to 85.2% (worst). In the SAFRAN-like scenario, the throughput is about 77% (worst).

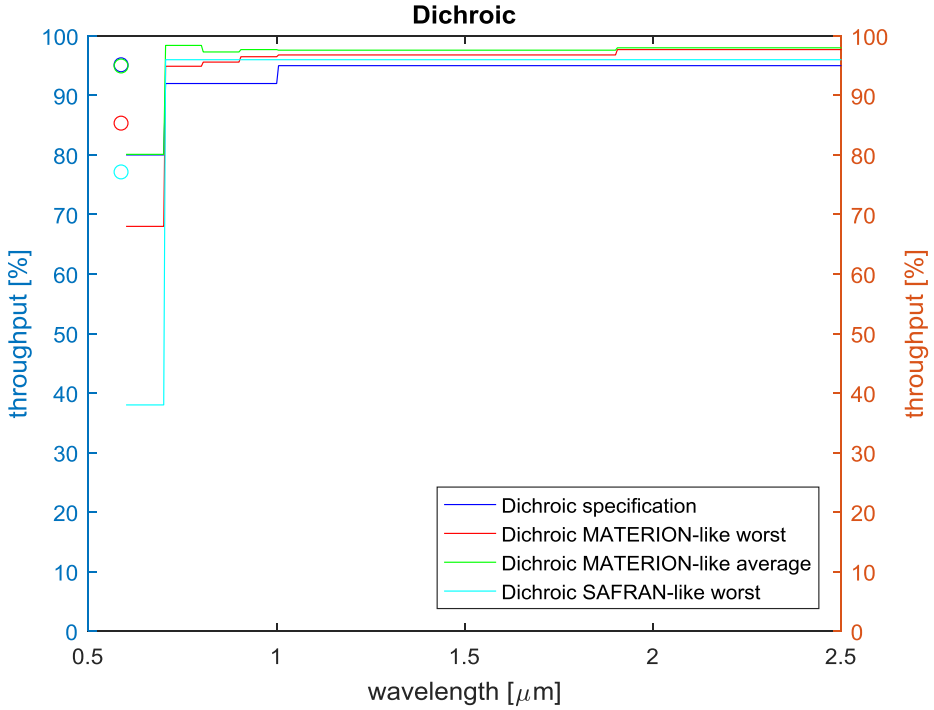

Figure 53. Dichroic throughput scenarios.

The overall throughput for the assumed scenarios is shown in Figure 54.

In the range 1500-2500 nm and 1000-1500 nm all the scenarios are compliant. In the range 600-1000 nm, MATERION-like scenario (both average and worst case, 60.0 and 57.1 average respectively) are compliant while SAFRAN-like scenario is marginally non-compliant (52.5% average). At 589 nm, MATERION-like average scenario is compliant (56.3%) while MATERION-like worst scenario is marginally non-compliant (50.6%). The SAFRAN-like average scenario is non-compliant (45.7%).

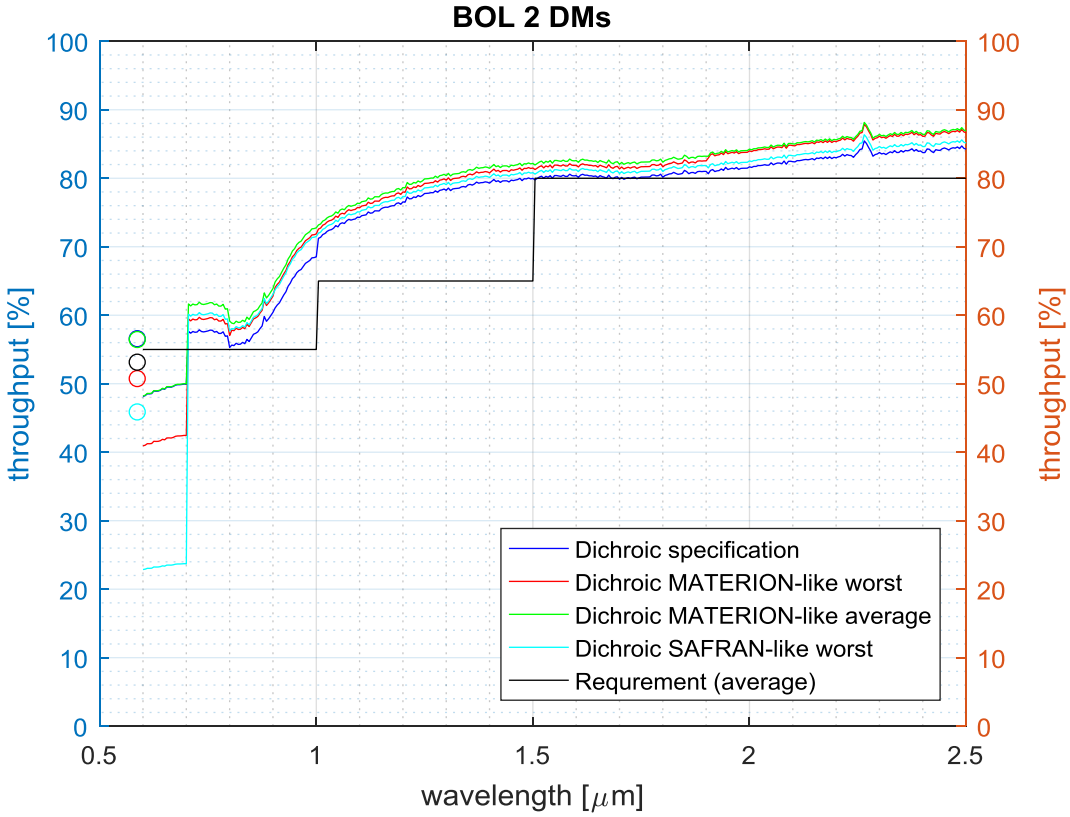

Figure 54. Throughput of the main path (curves) and LGS path (circles). Blue is the throughput assuming the dichroic as in the specification. Green and red are the throughput assuming the dichroic MATERION-like average and worst case respectively. Cyan is the throughput assuming the dichroic SAFRAN-like worst case. Black curve represents the requirements.

3.2.16 Thermal Background

MAO-SF0-1.2.4.5: *The PFRO thermal emissivity should, as a design goal, be less than 55% (TBC) of the thermal background from the sky and telescope measured in a Ks filter. [RD2].*

The detailed description of the computation of the thermal background can be found in [RD18]. In the computation, we have distinguished between a best case, corresponding to fresh coated surfaces and no dust deposition, and a worst case corresponding to 4 years coating ageing and 4 years dust deposition.

The results are given in Table 9.

For all the combination, we are compliant but for Worst MAORY and Best ELT. However, this is considered to be almost an unlikely condition, considering the fact that when MAORY will start its operations, the telescope would be already operative by many years.

Cleanliness cases	1 DM	2 DMs
Best ELT Best MAORY	32,6	28,9
Worst ELT Best MAORY	23,2	26,3
Best ELT Worst MAORY	53,5	57,3
Worst ELT Worst MAORY	48,6	52,1

Table 9. MAORY IR background contribution with respect to Sky and ELT.

3.2.17 Ghost analysis

MAO-SF0-1.3.4.13: *In imaging mode, the maximum irradiance from ghost-images from any source in the field shall not exceed 0.1% of the source image irradiance [RD2].*

This requirement refers to the optical path towards MICADO (and second instrument). This is taken to mean that the ratio between the irradiance of a ghost and the irradiance of the point source generating the ghost shall be less than 0.1% on the scientific focal plane.

There are two optics that can generate ghost images: the entrance CPM and the dichroic.

The CPM generates ghost because of two bounce internal reflection, as shown in Figure 55.

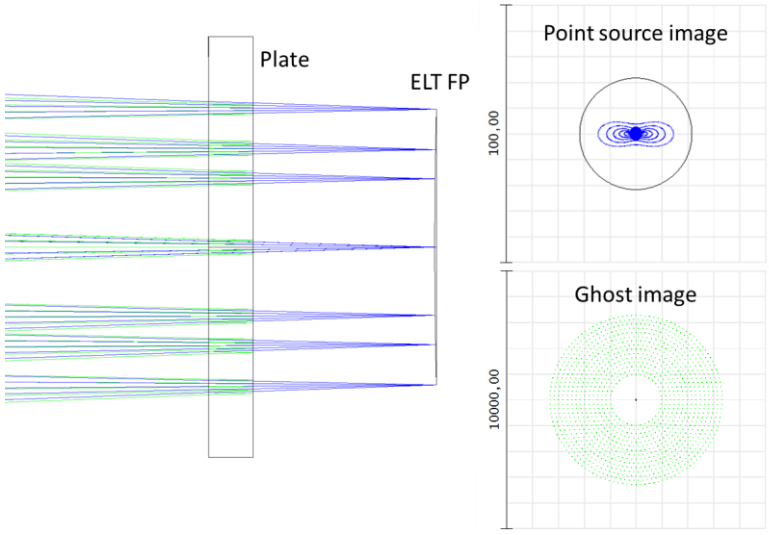

Figure 55. Two bounce internal reflection on the CPM (left). Image of point source and generated ghost at the main path focal plane (right). Units are micron.

The ghost image radius is 3.33 mm with an obstruction radius of 0.99 mm. The ghost-illuminated area is then about 31.77 mm^2.

Assuming the source flux concentrated within the Airy disk (closed loop regime), at a wavelength of 2.2 µm (larger image), the illuminated area is about 0.007 mm^2.

The ratio between the ghost and the source areas is 2.3 10^{-4}, i.e. 0.023%.

Assuming an AR coating of 2% in both the CPM surfaces, in the double internal reflection the ghost signal diminishes by 0.04%.

The ratio between the irradiance of a ghost and the irradiance of the point source generating the ghost is then 0.00001%. The background signal generated by the ghost is likely outside of the detector dynamics for most of the observing scenario.

We have done a similar analysis for the dichroic.

The ghost image radius is 3.07 mm with an obstruction radius of 0.91 mm. The ghost-illuminated area is then about 27.10 mm^2.

The ratio between the ghost and the source areas at 2.2 µm is 0.026%.

Assuming a dichroic with reflectivity of 95% on the first surface and an AR coating of 3% on the second surface, the ghost signal diminishes by 0.01%

The ratio between the irradiance of a ghost and the irradiance of the point source generating the ghost is then 0.000003%, again, outside of the detector dynamics for most of the observing scenario.

The impact of the ghosts on NGS WFS and LGS WFS will be analysed in the next phase. However, in both cases, we do not expect particular issues, given that for the NGS path the ratio ghost/source irradiance is similar to the main path one, while for LGS path the AR coating is expected to be quite efficient (0.5-1%).

3.2.18 Straylight analysis and internal baffling

During this working phase, the evolution of the opto-mechanical model and the lack of information did not allow to estimate the impact of the straylight and eventually the need of an internal baffling system. Such analysis has been postponed to the next phase.

4. Tolerance analysis

In this section, we describe the tolerance analysis and results, accounting for both the manufacturing errors and alignment procedure.

The MMS is a quite complex optical system. In order to simplify the tolerance simulations, we have separated the analysis in two main subsystems: the main path (from the ELT focal plane to MICADO focal plane) and LGS path (from the dichroic to the LGSWFS entrance focal plane). The two results have then been merged together, assuming to align the LGSO to the main path.

The assumptions on the manufacturing tolerance ranges are the results of budgets trade-off, internal simulations and iterations with potential provider companies (THALES SESO, SAFRAN REOSC, KIWISTAR OPTICS, AMOS, OFFICINA STELLARE).

We have identified alignment procedures with the aim to maintain them as simple as possible, limiting the degrees of freedom and the number of required observables.

The main path alignment procedure coincides with the MAORY collimation procedure before operations.

4.1 Main Path

The manufacturing errors of the main path have been separated in low-orders (radius of curvature/defocus and astigmatism) and high-orders errors. The low-orders errors accounts for the uncertainties of the surface deviation introduced by the gravity, for which we expected the larger contribution, and of the surface characterization. For these components, we require both accuracy and precision measurements by the manufacturers. For the high-order errors, we required higher accuracy of the measurements.

The integration procedure of the main path is based on the positioning of the opto-mechanics through laser tracker. The knowledge of the surface position is given by the characterization of the surface itself with respect to mechanical fiducial (SMR). After this initial positioning, the main path is aligned using as degrees of freedom the piston and tip/tilt movements of M10M to re-optimize the WFE in terms of defocus and astigmatisms and the tip/tilt of M11M and M12M to re-align the focal plane and the exit pupil to MICADO.

The tolerance procedure for the main path has been implemented in three steps:

1. **As-manufactured and positioning**: we assume to reposition opto-mechanics after the as-built measurements provided by the manufacturers. Only low-orders manufacturing errors are considered and with infinite precision.
2. **High order manufacturing errors**: we introduce the high-orders manufacturing errors which information is not used in step 1.
3. **Characterization errors and alignment**: we introduce the uncertainties on the low-orders manufacturing errors used in step 1, the characterization errors of the surface knowledge and we apply the alignment procedure.

After each step, we have evaluated some quality parameters and alignment parameters:

- WFE
- Intra-epoch distortion variation
- Polychromatic exit pupil F/#
- Effective focal length (plate scale)
- Exit pupil property (position, diameter, quality)
- DMs conjugation altitudes and quality
- Angle of incidence on dichroic
- Optical elements displacements (dx, dy, dz, tx, ty, tz)
- Footprints displacement and size variation
- Inter-epoch distortion variation

4.1.1 Implementation of the tolerance process

The tolerance process has been implemented by mean of Monte Carlo simulations (MC). The parameter driving the process is the WFE.

In step 1, we have simulated 3000 MC occurrences assuming a parabolic statistic for the errors distribution. The parabolic statistic is pessimistic; however, it is mimicking somehow the fact that, for some manufacturing parameters, the providers will limit the manufacturing time to the minimum, i.e. just after the match of the specification. We have selected a 98-percentile occurrence in terms of WFE as input for the next step. This choice allows to exclude outliers, due to limited optimization cycles, and counterbalance the pessimistic statistic.

As in step 1, in the step 2 we have simulated 3000 MC occurrences assuming a parabolic statistic for the errors distribution, starting from the selected 98-percentile occurrence. We have then selected a 98-percentile occurrence in terms of WFE from the step 2 distribution as input for the next step.

Using as starting point the 98-percentile occurrence of step 2, in the step 3 we have simulated 3000 MC occurrences assuming a uniform statistic for the errors distribution. This choice is pessimistic given that the measurement uncertainties have typically a normal distribution. We have then selected a 98-percentile occurrence in terms of WFE.

This last occurrence represents the WFE we expect to have after the manufacturing and characterization of the opto-mechanics and the alignment process.

All the other parameters have been computed separately after each step. As conservative approach, we have considered as overall variation range the linear sum of the maximum variation of the three steps.

The entire simulation has been implemented in Amazon HTC cloud platform.

4.1.2 Step 1

This step is mimicking the fact that we will re-define the nominal positions of M7M, M8M, M9M, M10M, M11M and M12M through a re-optimization of the optical system, using as input the as-built opto-mechanics characterization data provided by the manufacturers.

Only low-orders errors are accounting. We assume that the precision measurement data is infinite. This operation will be done in the Zemax model.

The manufacturing errors of the opto-mechanics we considered are:

- Radius of curvature of M7M, M8M, M9M, M10M
- Zernike RMS defocus Z4 of CPM surfaces, M6M, dichroic first surface, M11M, M12M
- Zernike RMS astigmatism Z5, Z6 of CPM surfaces, M6M, M7M, M8M, M9M, M10M, dichroic first surface, M11M, M12M
- CPM thickness, wedge, refractive index, Abbe number

The required accuracies are shown in Table 10. These values have been used as offenders in the MC simulation and has to be intended as +/-.

		RoC [mm]	Z4 RMS [nm]	Z5 RMS [nm]	Z6 RMS [nm]
CPM	nominal		0	0	0
	accuracy		100	8	8
	precision				
CPM	nominal		0	0	80234
	accuracy		100	30	250
	precision				
M6M	nominal		0	0	0
	accuracy		100	8	8
	precision				
M7M	nominal	-35094.937		0	13381
	accuracy	0.10%		40	40
	precision				
M8M	nominal	38403.193		0	60458
	accuracy	0.10%		40	180
	precision				
M9M	nominal	15456.015		0	0
	accuracy	0.10%		10	10
	precision				
M10M	nominal	14946.890		0	0
	accuracy	0.10%		10	10
	precision				
Dichroic S1	nominal		0	0	0
	accuracy		100	8	8
	precision				
M11M	nominal		0	0	0
	accuracy		100	8	8
	precision				
M12M	nominal		0	0	0
	accuracy		100	8	8
	precision				

CPM		
	accuracy	precision
Refractive index	5.00E-04	
Abbe number	1%	
thickness [mm]	1	
wedge [arcsec]	25	

Table 10. Assumed accuracies on the manufacturing of the opto-mechanics in the step 1.Values has to be intended as +/-. Zernike polynomials refer to surface error.

Each MC occurrence has been re-optimized in two steps:

1. Merit function based on technical field WFE, intra-epoch distortion variation, working F/# and limited footprint displacements with respect to the optics aperture. The degrees of freedom in the local coordinate system are:

   M7M dz, tx, ty

   M8M dz, tx, ty

   M9M dx, dy, dz, tx, ty (forced to maintain chief ray x, y coordinates as nominal)

   M10M dx, dy, dz, tx, ty (forced to maintain chief ray x, y coordinates as nominal)

2. Merit function based on MICADO focal plane and exit pupil alignment. The degrees of freedom in the local coordinate system are:

   M11M tx, ty

   M12M dz, tx, ty

   Exit pupil distance (just to find the new position along z-axis)

   Metapupil altitudes (just to find the new DMs conjugation altitudes)

A scheme of the degrees of freedom is shown in Figure 56.

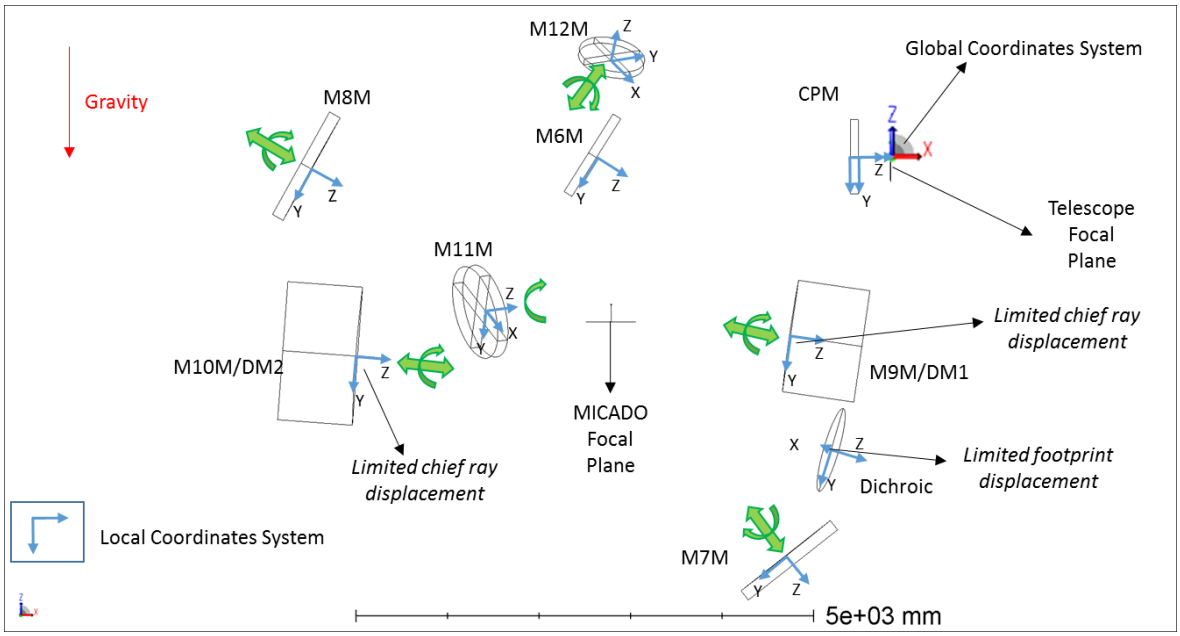

Figure 56. Scheme of the degrees of freedom implemented in the step 2.

We have selected the 98-percentile MC occurrence based on WFE merit function value. We were able to find an occurrence representing also the 98-percentile for the intra-epoch distortion variation, even if it does not correlate with the WFE, as shown in Figure 57. This occurrence has been set as starting point for the step 2.

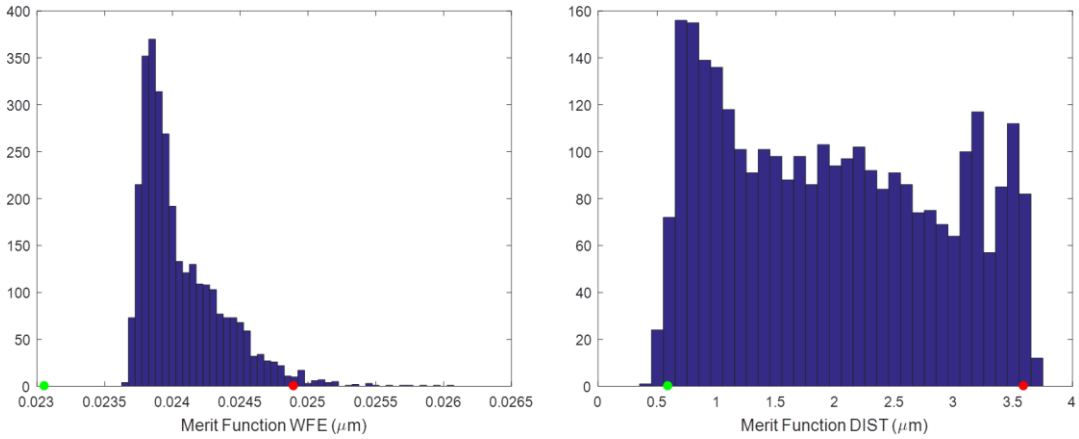

Figure 57. Merit function distribution of the MC population based on WFE (left) and intra-epoch distortion variation (right). Green dot represents the starting value (nominal design). Red point represents the selected 98-percentile occurrence.

The maximum expected range of the degrees of freedom, in the local coordinate system, is given in Table 11. Values have to be intended as +/-. These are the adjustable ranges that have to be foreseen on the mounting of the opto-mechanics over the mechanical bench.

At the time being, the simulation results do not present evidence of mechanical interferences neither beam vignetting, both internally and with MICADO structure.

	dx [mm]	dy [mm]	dz [mm]	tx [deg]	ty [deg]	tz [deg]
CPM	0.000	0.000	0.000	0.0000	0.0000	0.0000
M6M	0.000	0.000	0.000	0.0000	0.0000	0.0000
M7M	0.000	0.000	28.523	0.0206	0.0050	0.0000
M8M	0.000	0.000	65.797	0.0400	0.0164	0.0000
M9M	2.062	11.757	1.680	0.1624	0.0420	0.0000
M10M	3.628	11.086	3.988	0.1873	0.0461	0.0000
Dichroic	0.000	0.000	0.000	0.0000	0.0000	0.0000
M11M	0.000	0.000	0.000	0.1314	0.0756	0.0000
M12M	0.000	0.000	0.196	0.0415	0.0214	0.0000

Table 11. Maximum range of the degrees of freedom for the as-built re-alignment. Movements are given in the local coordinates system. Value have to be intended as +/-.

We have verified for each optic and each occurrence that the footprints envelope of the edge FoV fields is within the polished area. An example for M8M is shown in Figure 58. We have fit with an ellipse the footprints envelope of fields located at the edge of the field of view for infinite conjugated sources and LGS conjugated at 84 km (larger envelope for LGS path). We have traced the semi-axis and center variation of the ellipse for each optic.

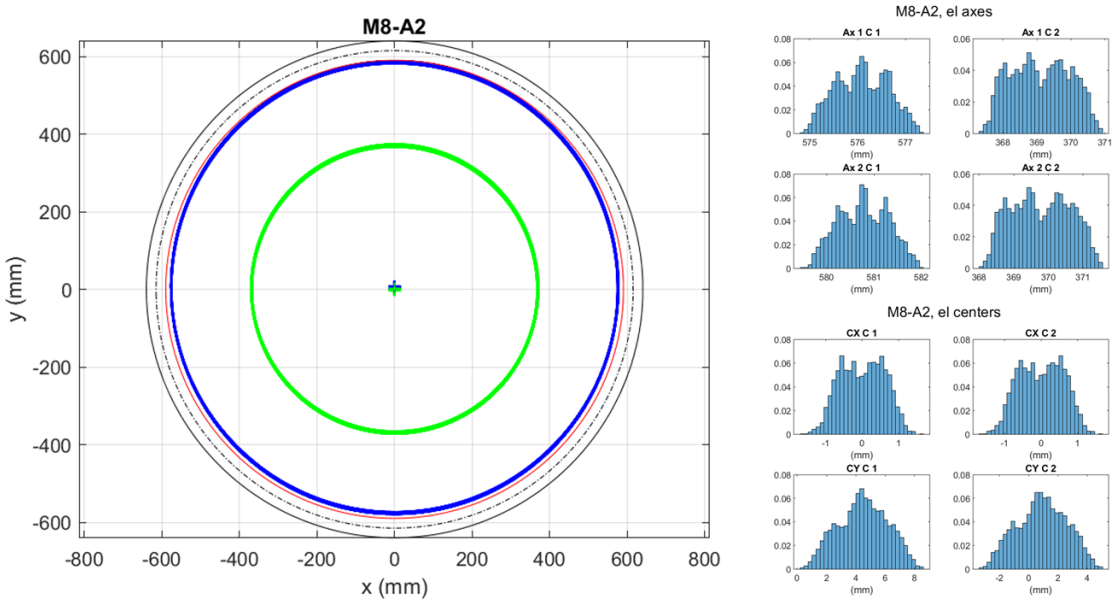

Figure 58. Footprints envelope of fields located at the edge of the field of view for infinite conjugated sources (blue circle) and LGS conjugated at 84 km (green circle). Red circle represents the nominal aperture. The black circle represents the mechanical aperture. The black dash circle represents the polished surface edge. The histograms on the left represent the semi-axis and center variation of the ellipse fitting the envelopes for infinite conjugated sources and LGS conjugated at 84 km.

Particular attention has been paid to the centring on the two DMs (M9M and M10M) in order to maintain as much as possible the alignment between the footprints and the actuators. Actually, the envelope ellipse center variation is within ±0.6 mm while the semi-axis variation is within ±2.5 mm.

We have also constrained the footprints envelope on the dichroic to have center variation within ±1.0 mm and semi-axis variation to ±4.0 mm. This helps to maintain the intermediate pupil close to the nominal position, facilitating the alignment and the integration of the LGSO.

4.1.3 Step 2

We introduce the surface errors on high-order Zernike polynomials (>Z6). The manufacturing errors we considered are:

- Z4-Z11 Zernike RMS polynomials are specified singularly
- Z12-Z36 Zernike RMS polynomials have the same RMS value
- Z27-Z120 Zernike RMS polynomials have the same RMS value
- Z121-Z231 Zernike RMS polynomials have the same RMS value

The required accuracies are shown in Table 12. These values have been used as offenders in the MC simulation and has to be intended as +/-.

No re-optimization was done on MC occurrences.

		Z7 RMS [nm]	Z8 RMS [nm]	Z9 RMS [nm]	Z10 RMS [nm]	Z11 RMS [nm]	Z12-Z36 RMS [nm]	Z37-Z120 RMS [nm]	Z121-Z231 RMS [nm]
CPM	nominal	0	0	0	0	0	0	0	0
	accuracy	5	5	3	3	5	2.4	0.87	0.38
CPM	nominal	9068	0	-253	0	-1143	0	0	0
	accuracy	30	30	15	15	20	4	1.42	0.76
M6M	nominal	0	0	0	0	0	0	0	0
	accuracy	5	5	3	3	5	2.4	0.87	0.38
M7M	nominal	9151	0	389	0	820	0	0	0
	accuracy	15	15	5	5	5	4	1.42	0.76
M8M	nominal	6015	0	176	0	359	0	0	0
	accuracy	15	15	5	5	5	4	1.42	0.76
M9M	nominal	0	0	0	0	0	0	0	0
	accuracy	5	5	4	4	5	2.8	1.09	0.57
M10M	nominal	0	0	0	0	0	0	0	0
	accuracy	5	5	3	3	5	2.4	0.87	0.38
Dichroic S1	nominal	0	0	0	0	0	0	0	0
	accuracy	5	5	3	3	5	2.4	0.87	0.38
M11M	nominal	0	0	0	0	0	0	0	0
	accuracy	5	5	3	3	5	2.4	0.87	0.38
M12M	nominal	0	0	0	0	0	0	0	0
	accuracy	5	5	3	3	5	2.4	0.87	0.38

Z12-Z36 Overall RMS [nm]	Z37-Z120 overall RMS [nm]	Z121-Z231 overall RMS [nm]
12	8	4
20	13	8
12	8	4
20	13	8
20	13	8
14	10	6
12	8	4
12	8	4
12	8	4
12	8	4

Table 12. Assumed accuracy on the manufacturing of the optics in the step 2.Values has to be intended as +/-. Zernike polynomials refer to surface error. The Zernike polynomials values of Z12-Z26, Z37-Z120 and Z121-Z231 are given as single range value on the table in the left and as RSS in the table in the right.

We have selected the 98-percentile MC occurrence based on WFE merit function value. In this case, we were not able to find an occurrence representing also the 98-percentile for the intra-epoch distortion variation at the same time (it is a 95-percentile), but the distribution has a relative small spread. This occurrence has been set as starting point for the step 3. The merit function distributions are shown in Figure 59.

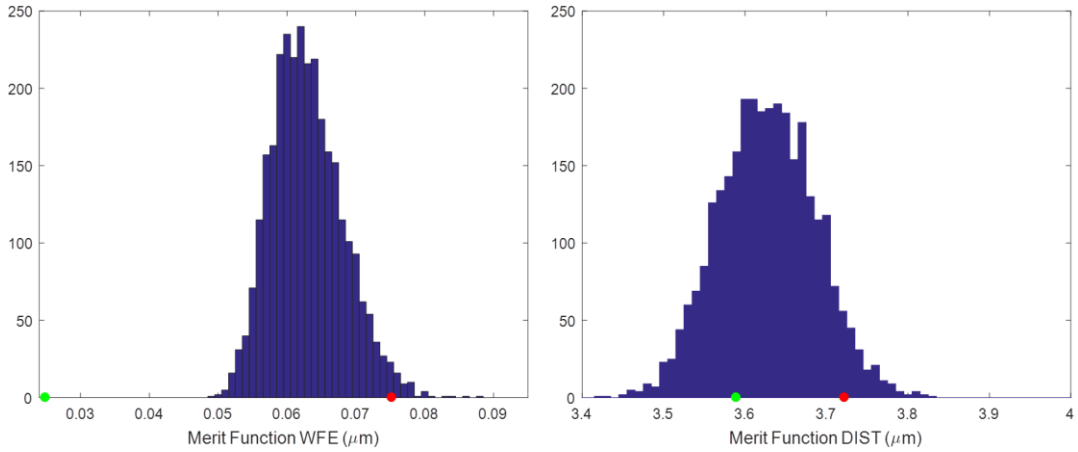

Figure 59. Merit function distribution of the MC population based on WFE (left) and intra-epoch distortion variation (right). Green dot represents the starting value (98-percentile occurrence of step 1). Red point represents the selected 98-percentile occurrence.

4.1.4 Step 3

We introduce the measurement precision on the optical parameters considered in step 1, the errors on the positions of the optics due to the characterization accuracy of the optical surfaces with respect to SMRs in working conditions and to laser tracker accuracy.

The precisions on the measurements of the opto-mechanics in working conditions are:

- Radius of curvature of M7M, M8M, M9M, M10M
- Zernike RMS defocus Z4 of CPM surfaces, M6M, dichroic first surface, M11M, M12M
- Zernike RMS astigmatism Z5, Z6 of CPM surfaces, M6M, M7M, M8M, M9M, M10M, dichroic first surface, M11M, M12M
- CPM thickness, wedge, refractive index, Abbe number

The required accuracy is shown in Table 13. These values have been used as offenders in the MC simulation and has to be intended as +/-.

The positioning errors of the opto-mechanics in working conditions given in the local coordinate system are:

- dx, dy for all the opto-mechanics; for flat surfaces, they impacts only on footprints position with respect to the polished aperture
- dz for all the opto-mechanics with flat surface; for mirror with power it is included in the accuracy of the radius of curvature; for M10M it is a degree of freedom
- tx, ty for all the opto-mechanics; for M10M, M11M and M12M they are degrees of freedom
- tz for opto-mechanics with non-centrosymmetric optical surface (CPM, M7M, M8M)

The assumed positioning errors are shown in Table 14. These values have been used as offenders in the MC simulation and has to be intended as +/-.

		RoC [mm]	Z4 RMS [nm]	Z5 RMS [nm]	Z6 RMS [nm]
CPM	nominal		0	0	0
	accuracy				
	precision		10	5	5
CPM	nominal		0	0	80234
	accuracy				
	precision		20	30	30
M6M	nominal		0	0	0
	accuracy				
	precision		10	5	5
M7M	nominal	-35094.937		0	13381
	accuracy				
	precision	0.03%		40	40
M8M	nominal	38403.193		0	60458
	accuracy				
	precision	0.03%		40	40
M9M	nominal	15456.015		0	0
	accuracy				
	precision	0.03%		15	15
M10M	nominal	14946.890		0	0
	accuracy				
	precision	0.03%		15	15
Dichroic S1	nominal		0	0	0
	accuracy				
	precision		10	5	5
M11M	nominal		0	0	0
	accuracy				
	precision		10	5	5
M12M	nominal		0	0	0
	accuracy				
	precision		10	5	5

CPM		
	accuracy	precision
Refractive index		5.00E-05
Abbe number		0%
thickness [mm]		0.1
wedge [arcsec]		2.5

Table 13. Assumed precisions on the measurements of the opto-mechanics in the step 3. Values has to be intended as +/-. Zernike polynomials refer to surface error.

	dx [mm]	dy [mm]	dz [mm]	tx [deg]	ty [deg]	tz [deg]
CPM	1.000	1.000	1.000	0.0083	0.0083	0.1666
M6M	1.000	1.000	0.300	0.0083	0.0083	0.0000
M7M	2.000	2.000	0.000	0.0083	0.0083	0.0833
M8M	2.000	2.000	0.000	0.0083	0.0083	0.0833
M9M	2.000	2.000	0.000	0.0083	0.0083	0.0000
M10M	2.000	2.000	DoF	DoF	DoF	0.0000
Dichroic	1.000	1.000	0.300	0.0083	0.0083	0.0000
M11M	1.000	1.000	0.300	DoF	DoF	0.0000
M12M	1.000	1.000	0.300	DoF	DoF	0.0000

Table 14. Assumed positioning errors of the opto-mechanics in the step 3. Values has to be intended as +/-.

The optimization of MC occurrences has been done mimicking the alignment procedure. The degrees of freedom we assumed are:

M10M dz, tx, ty

M11M tx, ty

M12M tx, ty

A scheme of the degrees of freedom and the positioning errors is shown in Figure 60.

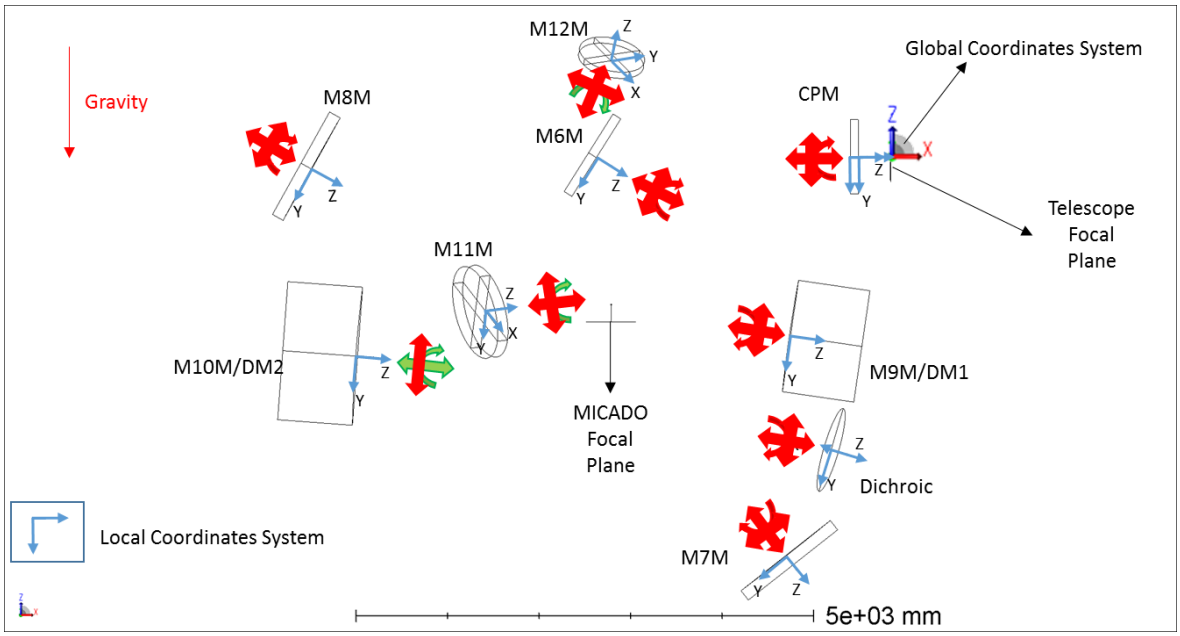

Figure 60. Scheme of the degrees of freedom and the positioning errors of the step 3.

The optimization has been initially done assuming:

- Merit function based on technical field WFE, MICADO focal plane and exit pupil alignment

A posteriori, we have re-optimized the exit pupil distance in order to find to find its new distance from the exit focal plane and the metapupil altitudes in order to find the new DMs conjugation altitudes.

This assumption is optimistic, given that we will have no access to several field position all over the technical FoV for which we minimize the WFE during the alignment phase. It is somehow representing the best performance we can obtain.

Then we have verified the impact on the WFE of a more realistic approach in terms of the alignment observables. We re-optimize the MC occurrences starting from the non-aligned condition, assuming:

- Merit function based on the defocus and astigmatisms minimization of five fields in the MICADO FoV, MICADO focal plane and exit pupil alignment

We have randomly selected 300 occurrences over the 3000 and we have optimized them assuming as observables the defocus and astigmatism signals of five fields, one at the center of the MICADO FoV and four at the edge of the MICADO FoV in cross configuration. We have then compared the impact on the WFE with respect to the previous optimization.

After the first optimization approach, we have selected the 98-percentile MC occurrence based on WFE merit function value. In this case, we were not able to find an occurrence representing also the 98-percentile for the intra-epoch distortion variation at the same time. The merit function distributions are shown in Figure 61.

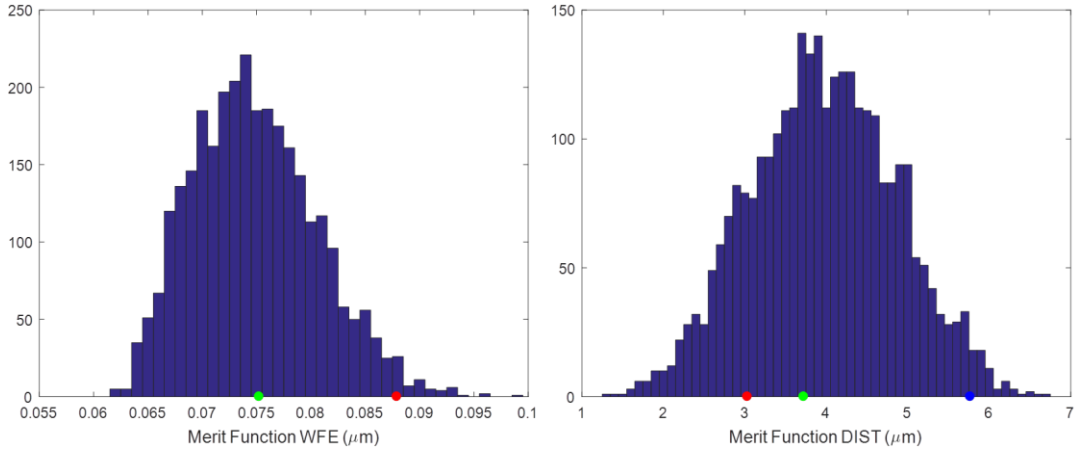

Figure 61. Merit function distribution of the MC population based on WFE (left) and intra-epoch distortion variation (right). Green dot represents the starting value (98-percentile occurrence of step 2). Red point represents the selected 98-percentile occurrence for WFE. Blue point represents the selected 98-percentile occurrence for intra-epoch distortion variation.

The maximum expected range of the degrees of freedom, in the local coordinate system, is given in Table 15. Values have to be intended as +/-. These adjustable ranges have to be foreseen during alignment.

	dx [mm]	dy [mm]	dz [mm]	tx [deg]	ty [deg]	tz [deg]
M10M			6.943	0.0277	0.0321	
M11M				0.1006	0.1020	
M12M				0.0758	0.0868	

Table 15. Maximum range of the degrees of freedom during alignment. Movements are given in the local coordinates system. Value have to be intended as +/-.

4.1.5 Tolerance analysis results and requirements verification

In this section, we present the output results of the tolerance analysis together with the verification of the requirements. Most of I/F requirements with MICADO are still under discussion and not already frozen.

4.1.5.1 Wavefront Error

For each tolerance analysis step, we have monitored the WFE in the technical and MICADO FoV by mean of the average value, the RMS value and the maximum value of the RMS WFE maps. Results are shown in Figure 62. The statistic for the step refers to the optimization over the full technical FoV. The main impact on the WFE is introduced by the step 2, i.e. the manufacturing error for which we have no compensators.

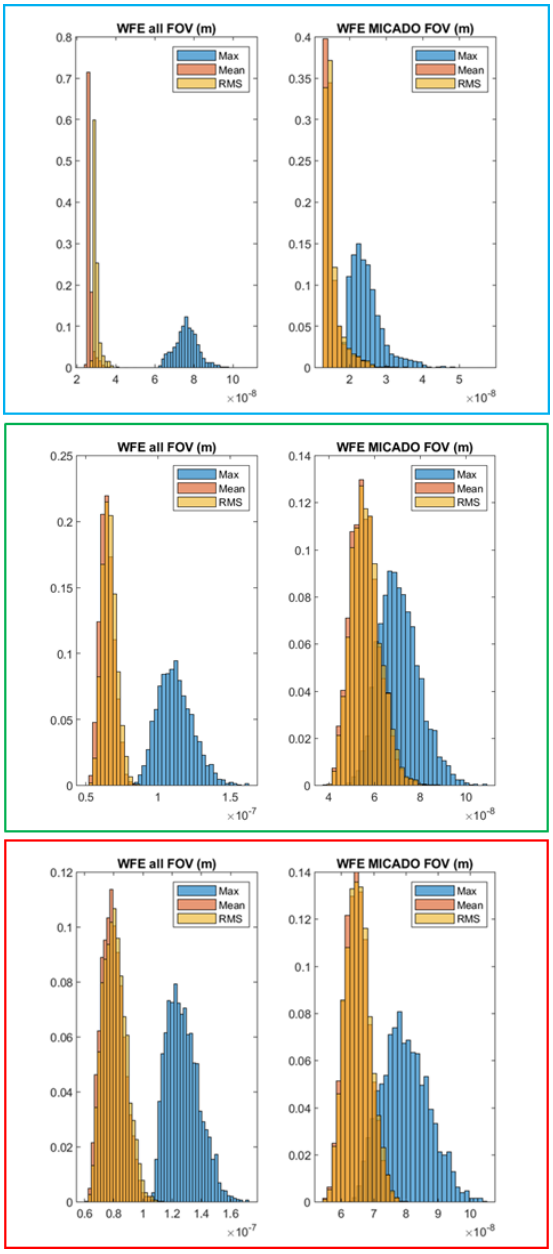

Figure 62. Average value, RMS value and maximum value of the RMS WFE maps in the technical and MICADO FoV for the tolerance analysis step 1 (top), step 2 (middle) and step 3 (bottom).

In the optimistic assumption of an alignment process based on the full technical FoV and minimizing the full WFE, the 98 percentile of the RMS WFE in the MICADO FoV has an average value of about 74 nm and a maximum value of about 96 nm. The 98 percentile of the RMS WFE in the Technical FoV has an average value of about 97 nm and a maximum value of about 153 nm. Excluding the MICADO FoV form the full technical FoV, i.e. considering the FoV annulus patrolled by the NGS WFS, the average RMS FoV is 104 nm.

We have randomly selected 300 MC occurrences from the step 2 MC population, in pre-optimization conditions, in order to cover statistically the entire population. The 300 MC

occurrences have been then optimized by limiting the merit function to the five fields in the MICADO FoV and the feedback signals to defocus and astigmatisms Zernike polynomials. We have compared the RMS WFE map average and maximum value of the two optimizations methods. Results are shown in Figure 63.

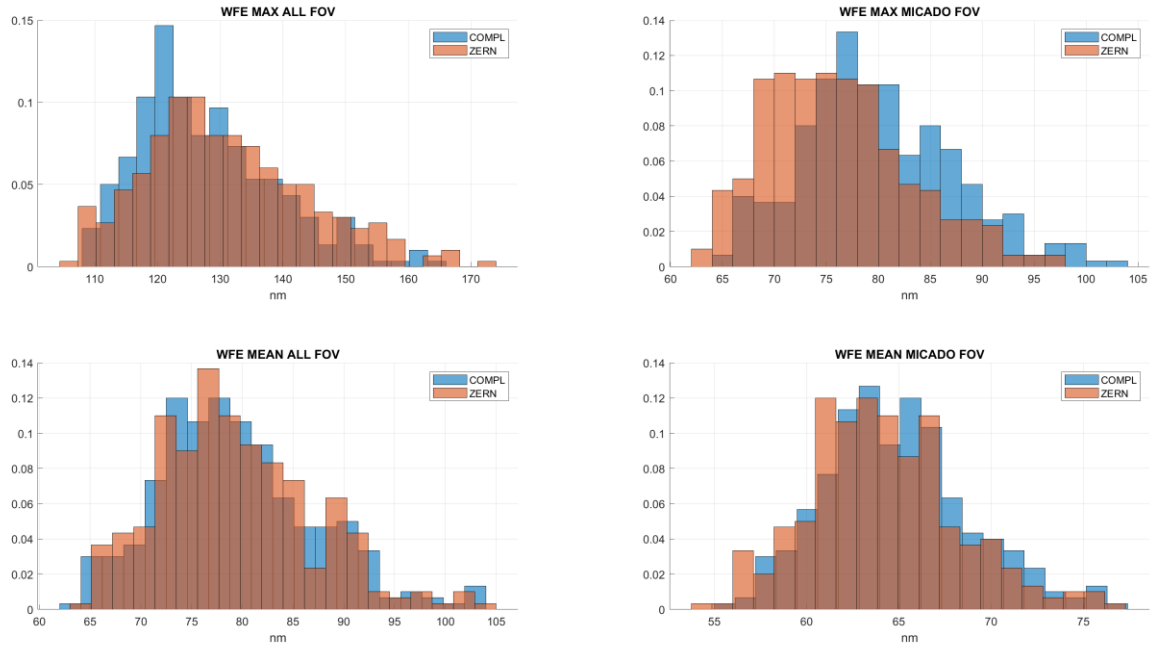

Figure 63. Average value (bottom) and maximum value (top) of the RMS WFE maps in the technical (left) and MICADO (right) FoV after the alignment optimization over the full technical FoV (blue histogram) and over 5 fields on the MICADO FoV limiting the feedback to Zernike polynomials Z4, Z5, Z6 (orange histogram).

By limiting the alignment procedure feedback to 5 fields over the MICADO FoV (one at the center and four at the edge in cross configuration), the impact on the overall RMS WFE is negligible.

We have verified the chromatic effect on the RMS WFE maps on a 98-percentile of the RMS WFE distribution. Results are shown in Figure 64. As for the nominal case, after refocusing for the proper wavelength, the RMS WFE maps variation at wavelengths 1 µm, 1.65 µm and 2.2 µm is negligible.

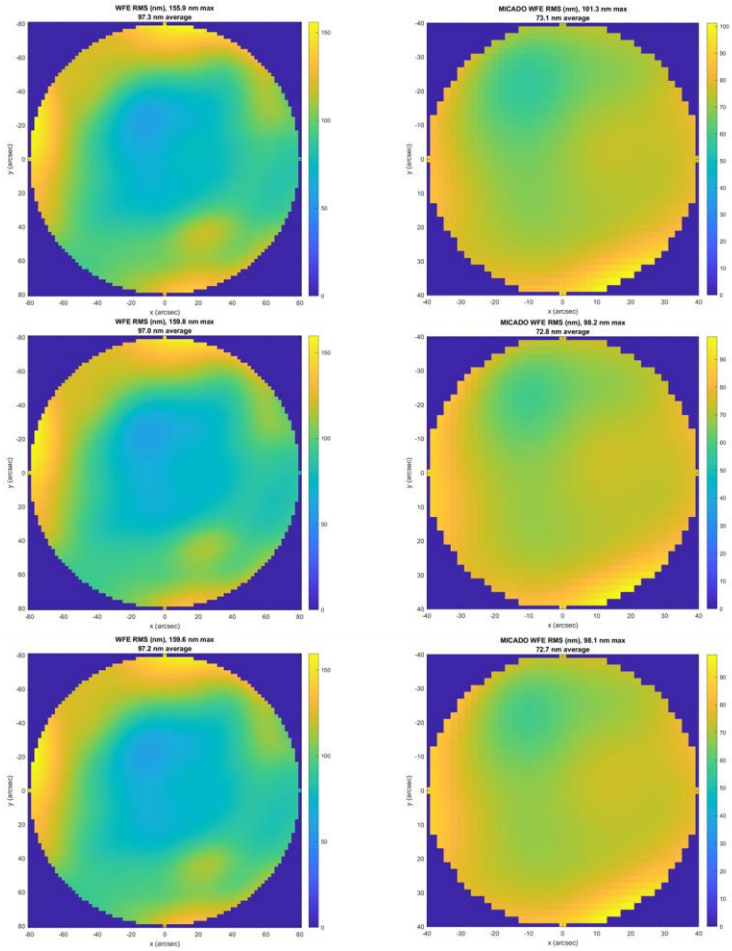

Figure 64. RMS WFE maps for the technical FoV (left) and MICADO FoV (right) at wavelengths 1 µm (top), 1.65 µm (middle) and 2.2 µm (bottom).

4.1.5.1.1 DMs contribution to WFE

In the tolerance simulation, the DMs (M9M and M10M) have been considered monolithic mirrors. The detailed analysis of the expected DMs surface errors due to thin shell manufacturing residuals, gravity deformations, thermal deformations and calibration errors is reported in [RD11].

The thin shell manufacturing error budget has been set to surface error 15 nm RMS. Such surface deviation is expected to be at high order spatial frequencies (higher than the actuators control spacing). The tolerance simulation does not account for such errors. At this working level, we have assumed 30 nm RMS WFE for each DMs to be RSS with the average value of the simulation:

$$WFE_{MICADO} = \sqrt{74^2 + 2 \times 30^2} = 85\ nm\ RMS$$

$$WFE_{NGSWFS} = \sqrt{104^2 + 2 \times 30^2} = 112\ nm\ RMS$$

The DMS calibration surface error residuals budget has been set to 15 nm RMS. They are typically low order spatial frequencies. At this working level, we have assumed that such deviation is included in the tolerance simulation budget between Z4 and Z21 Zernike polynomials.

The effect induced by gravity loads (< 2 nm RMS WFE) is negligible and it has been assumed to be included in the tolerance simulation budget.

4.1.5.1.2 Mountings gravitational load contribution to WFE

We have evaluated the impact of the gravity effect over the opto-mechanics on the delivered WFE in operational conditions.

We are assuming that the gravity effect can be mitigated through the polishing on the optical surfaces. Depending on the potential provider company approach, it can be done by directly measuring the optical surface of the opto-mechanical assembly in operational condition or through a detailed FEM analysis. In the first approach, in principle, the gravity load effect can be null (a part for the measurement accuracy capability of the test set-up). In the second approach, a safe estimate of the FEM analysis accuracy has been set to 10%.

At this working level, we have assumed that the gravity load deformations induced on the optical surfaces can be reduced to 10% during the manufacturing and the characterization of the opto-mechanical assemblies.

The gravity load analysis on the opto-mechanical assemblies is described in details in [RD13]. For each opto-mechanical element, the gravity deformation on the optical surface has been computed.

In Table 16, we reported the 10% of the expected RMS surfaces deformation expressed in Zernike standard polynomials.

Z RMS [nm]	PLATE S1	PLATE S2	M6-FM1	M7-A1	M8-A2	DICHROIC S1	M11-FLM 1st port	M12-FM2
1	0,0	0,0	587,9	-1491,3	4356,5	-322,9	-81,1	602,0
2	-0,8	-0,7	-0,6	-2,0	3,5	1,9	-23,4	-0,4
3	3,7	-3,5	187,7	383,3	356,2	10,3	144,2	146,2
4	0,0	0,0	-11,0	-5,6	21,8	13,9	4,0	-7,8
5	-0,1	-0,1	-0,1	-0,1	-0,2	0,4	-2,5	-0,1
6	-0,5	0,5	8,4	9,7	-3,0	-4,0	18,0	5,1
7	0,0	0,0	-4,2	-4,7	-8,4	0,0	-8,6	-2,8
8	0,0	0,0	0,0	0,0	0,0	0,0	-0,6	0,0
9	0,0	0,0	1,1	-1,2	1,1	0,5	-0,7	0,6
10	0,0	0,0	0,0	0,0	0,0	0,0	1,6	0,0
11	0,0	0,0	1,1	-0,7	-1,9	-0,7	-0,3	0,6
12	0,0	0,0	0,0	-0,9	-0,5	0,1	-0,7	-0,1
13	0,0	0,0	0,0	0,0	0,0	0,0	0,2	0,0
14	0,0	0,0	0,4	0,0	-1,0	-0,3	0,3	0,2
15	0,0	0,0	0,0	0,0	0,0	0,1	-0,2	0,0
16	0,0	0,0	0,0	0,0	0,0	0,0	0,4	0,0
17	0,0	0,0	1,2	1,4	3,1	0,0	2,0	0,3
18	0,0	0,0	0,0	0,0	0,0	0,0	-0,1	0,0
19	0,0	0,0	0,1	0,3	-0,4	0,0	0,4	0,1
20	0,0	0,0	0,0	0,0	0,0	0,0	-0,2	0,0
21	0,0	0,0	0,6	0,1	0,2	0,0	0,0	0,3
22	0,0	0,0	-0,2	0,2	0,1	0,0	0,0	-0,2
23	0,0	0,0	0,0	0,0	0,0	0,0	-0,1	0,0
24	0,0	0,0	-0,1	0,2	0,3	0,0	0,2	0,0
25	0,0	0,0	0,0	0,0	0,0	0,0	0,0	0,0
26	0,0	0,0	-0,1	0,0	0,2	0,0	-0,2	-0,1
27	0,0	0,0	0,0	0,0	0,0	-0,4	0,0	0,0
28	0,0	0,0	-0,1	0,2	0,0	0,9	0,0	-0,1
29	0,0	0,0	0,1	0,0	-0,8	0,0	-1,6	0,4
30	0,0	0,0	0,0	0,0	0,0	0,0	0,2	0,0
31	0,0	0,0	0,1	-0,1	0,1	0,0	0,2	0,1
32	0,0	0,0	0,0	0,0	0,0	0,0	-0,1	0,0
33	0,0	0,0	-0,2	0,0	-0,1	0,0	-0,3	-0,1
34	0,0	0,0	0,0	0,0	0,0	0,0	0,0	0,0
35	0,0	0,0	0,1	0,0	0,0	0,0	0,3	0,0
36	0,0	0,0	0,0	0,0	0,0	0,0	-0,1	0,0

Table 16. 10% surface RMS Zernike polynomials of the gravity load deformation induced on the opto-mechanical assemblies in operational conditions.

The values in the table are well within the budget assumed for the tolerance simulations, a part for few small deviations: Z6 of M6M and M11M, Z7 of M11M. For this reason, at this working level, we have assumed that the gravity load impact on the WFE is already included in the tolerance simulation.

However, we have verified that the impact on the WFE before and after the collimation of MAORY. The RMS WFE maps are shown in Figure 65. After the collimation of MAORY the impact is negligible.

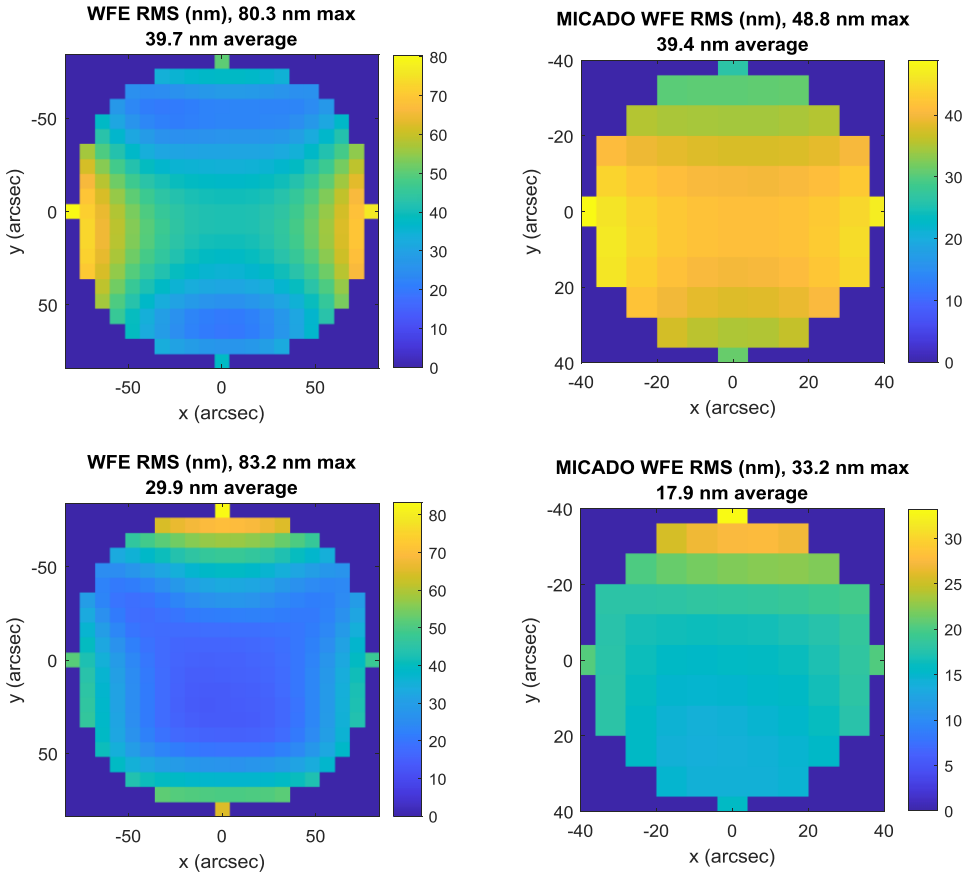

Figure 65. RMS WFE maps for the technical FoV (left) and MICADO FoV (right) induced by gravitational loads on the opto-mechanical assemblies before (top) and after (bottom) MAORY collimation.

We have also verified the impact of the gravity load on M11M when set to second port feeding configuration. We assumed that the figuring of M11M has been optimized for MICADO (i.e. the 10% gravity load residuals on surface refers to MICADO feeding configuration). In order to compare the impacts, we have assumed a second instrument FoV equal to MICADO FoV and the same MAORY collimation procedure. The RMS WFE maps before and after MAORY collimation are shown in Figure 66.

After the MAORY collimation, the two instruments present basically the same RMS WFE map.

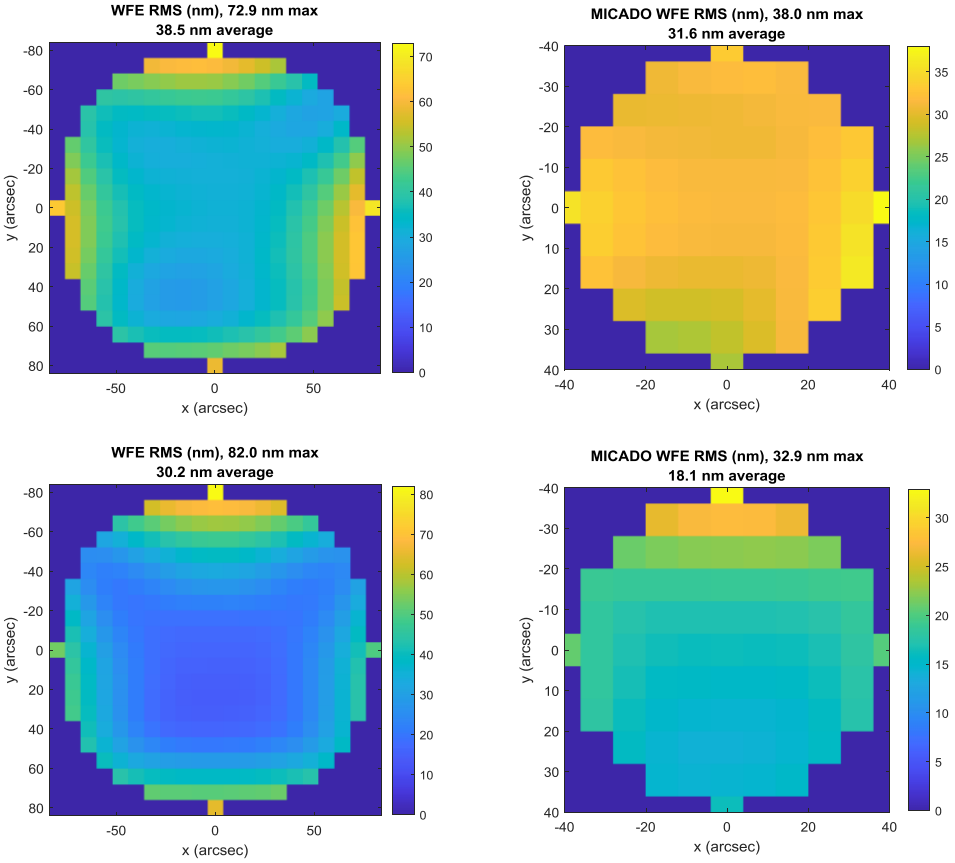

Figure 66. RMS WFE maps for the technical FoV (left) and second instrument FoV (right) induced by gravitational loads on the opto-mechanical assemblies before (top) and after (bottom) MAORY collimation.

4.1.5.1.3 Summary on WFE budget

The tolerance simulation account for manufacturing error, positioning errors, alignment procedure and characterization uncertainties in operational conditions, i.e. for the as-built 'static' opto-mechanical model.

MAO-SF0-1.2.4.4*: The as-built PFRO shall not introduce more than 150 nm RMS (goal 100 nm RMS) Wavefront error in average on the scientific field of view at the reference wavelength of 1 µm [RD2].*

MAO-SF0-1.2.4.3*: The as-built PFRO shall not introduce more than 200 nm RMS Wavefront error in average on the technical field of view at the reference wavelength of 1 µm [RD2].*

After the tolerance analysis, the estimated WFE in average on the MICADO FoV is 85 nm and in average on the NGS patrol FoV 112 nm.

4.1.5.2 Field distortion

Even if there is not a requirement on the absolute distortion, we report here the analysis after the manufacturing and alignment simulation on a 98 percentile of the population of the intra-epoch distortion variation distribution.

We have computed the field distortion map at wavelength 1 µm, 1.65 µm and 2.2 µm over the Technical FoV, as shown in Figure 67. The maximum values are 205 µm, 207 µm and 209 µm respectively. The color dependency of the distortion has a small effect (< 5 µm at FoV edge, i.e. < 1.5 mas).

We have evaluated the field distortion residuals after applying the astrometric polynomial fit of the distortion pattern with respect to the undistorted map at wavelength 1 µm, 1.65 µm and 2.2 µm. We have sequentially applied the correction of first order polynomial fit (scale), third order polynomials fit (theoretical field distortion power) and fifth order polynomial fit. Results are shown in Figure 68.

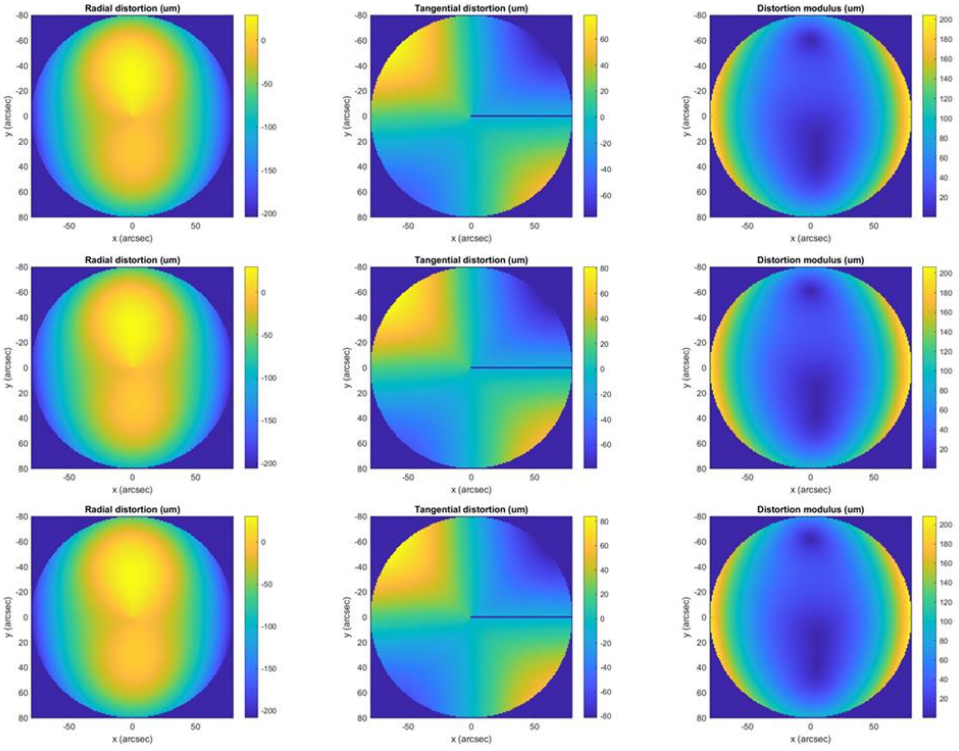

Figure 67. Radial component, tangential component and modulus of the field distortion computed at wavelength 1 µm (top), 1.65 µm (middle) and 2.2 µm (bottom) over the technical FoV.

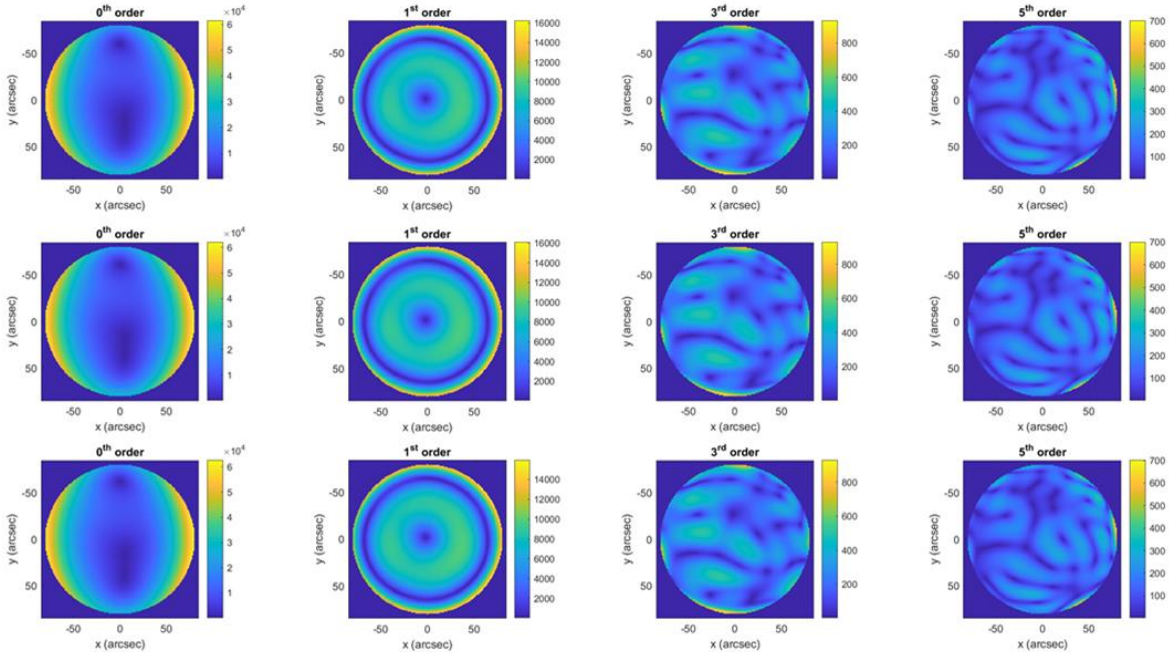

Figure 68. Modulus of the distortion residuals on the technical FoV after applying sequentially no correction, a 1storder , a 3rd order and a 5th order polynomials fit correction between the field distortion map and the undistorted map for wavelength 1 µm (top), 1.65 µm (middle) and 2.2 µm (bottom). Color bar units are micro-arcsec. These distortions maps refer to static field distortion (no sky rotation).

After applying the 3rd order polynomials fit correction, the chromatic effect becomes negligible. The 5rd order polynomials fit correction left a residual of about 700 µas in the technical FoV.

By limiting the analysis to the MICADO FoV, where the MICADO astrometric requirements apply and observations will be carried out, the 5rd order polynomials fit correction residual is below 70 µas, as shown in Figure 69.

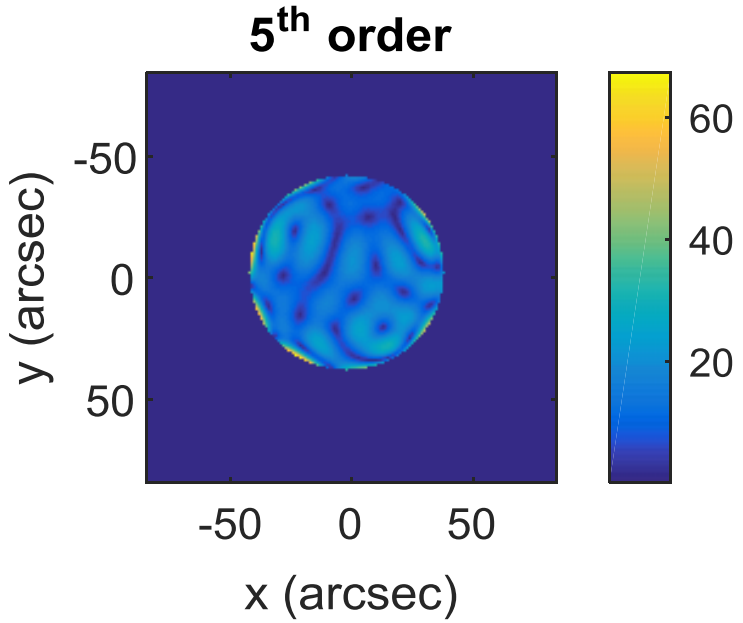

Figure 69. Modulus of the distortion residuals on the MICADO FoV after applying sequentially no correction, a 1st order , a 3rd order and a 5th order polynomials fit correction between the field distortion map and the undistorted map at wavelength 1 µm. Color bar units are micro-arcsec. This distortion map refers to static field distortion (no sky rotation).

4.1.5.3 Intra-epoch field distortion variation

Even if the intra-epoch distortion variation is not correlated with the WFE, in the first two steps we have selected occurrences that are close to the 98 percentile of the population also for this merit function. For this reason, we have limited the analysis to the step 3 statistic. The results are shown in Figure 70.

The 98 percentile of the intra-epoch distortion variation in the MICADO FoV has an average value of about 1.9 µm and a maximum value of about 3.4 µm. The 98 percentile of the intra-epoch distortion variation in the Technical FoV has an average value of about 3.7 µm and a maximum value of about 6.9 µm.

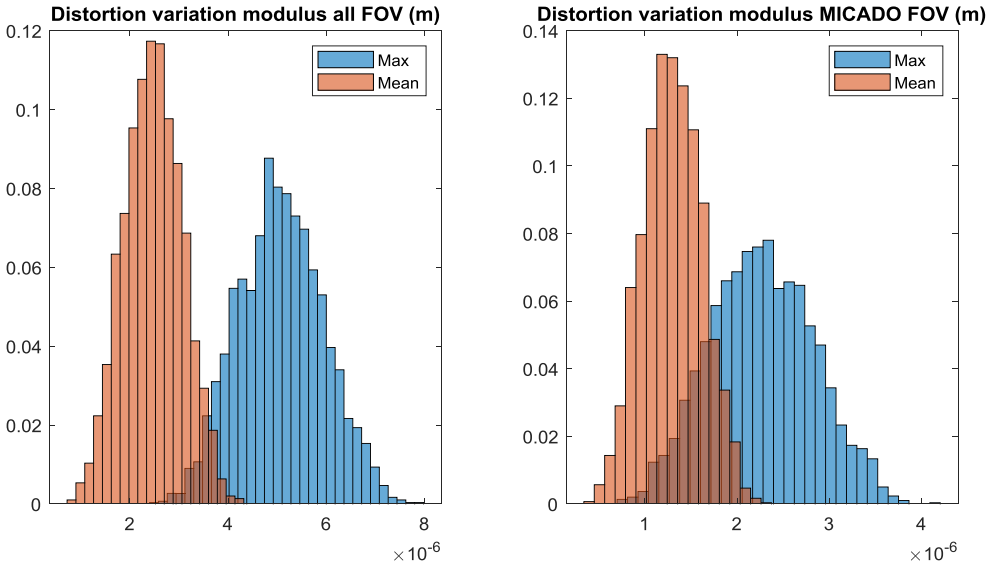

Figure 70. Average value and maximum value of the intra-epoch distortion variation in the technical (left) and MICADO (right) FoV after the tolerance step 3.

The wavelengths dependency has been verified on a 98-percentile occurrence of the intra-epoch distortion variation distribution, assuming that the distribution behavior does not change with the colors in this range.

In Figure 71, it is shown the radial component, tangential component and modulus of the intra-epoch field distortion variation computed at wavelength 1 µm, 1.65 µm and 2.2 µm over the technical FoV. The maximum values are 6.9 µm, 7.2 µm and 7.5 µm respectively.

MAO-SF0-1.3.4.7 intra-epoch field distortion variation: *MAORY shall not introduce a PSF centroids drift larger than 3.8 mas (intra-epoch distortion variation) over the technical Field of View during an astrometric observation of 120 sec with target altitude equal to 80 degrees.*

The maximum value of the PSF centroids drift after the manufacturing and alignment simulation is below 7.5 µm, corresponding to 2.3 mas.

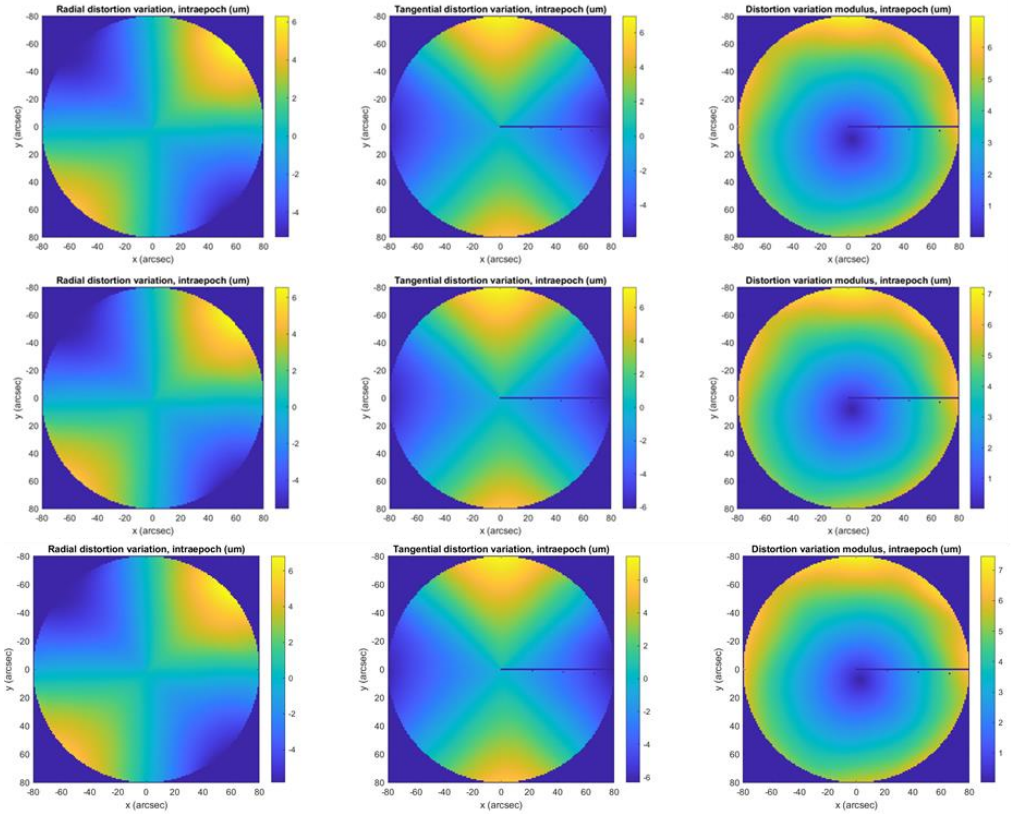

Figure 71. Radial component, tangential component and modulus of the intra-epoch field distortion variation computed at wavelength 1 µm (top), 1.65 µm (middle) and 2.2 µm (bottom) over the technical FoV.

4.1.5.4 Inter-epoch field distortion variation

The inter-epoch field distortion variation is a quite computing time consuming analysis to be applied statistically. At this phase level, we assume that there is correlation between the intra-epoch and the inter-epoch distortion variation. We have selected a 98-percentile occurrence from the intra-epoch distortion variation distribution and we have fully analyzed such occurrence.

MAO-SF0-1.3.4.8 Inter-epoch field distortion variation: *MAORY shall permit inter-epoch observations such that the relative position on the sky among unresolved, unconfused sources 1 arcsec apart, having optimal brightness with respect to an optimal set of reference sources must be reproducible to within 50 µas (goal: 10 µas) over a central, circular field of 20 arcsec diameter (goal: 75 arcsec diameter), after having applied astrometric polynomial fit of the distortion pattern.*

We have computed the residuals after the polynomials fit corrections as function of the azimuthal rotation angle over the MICADO FoV. The fields sampling is a regular grid having step 1 arcsec in X and Y directions. An example of the residuals between the astrometric reference at rotation angle 0 degrees and the image at rotation angle 25 degrees at wavelength 1 µm, 1.65 µm and 2.2 µm are shown in Figure 72. After the 3rd order correction the chromatic effect is negligible.

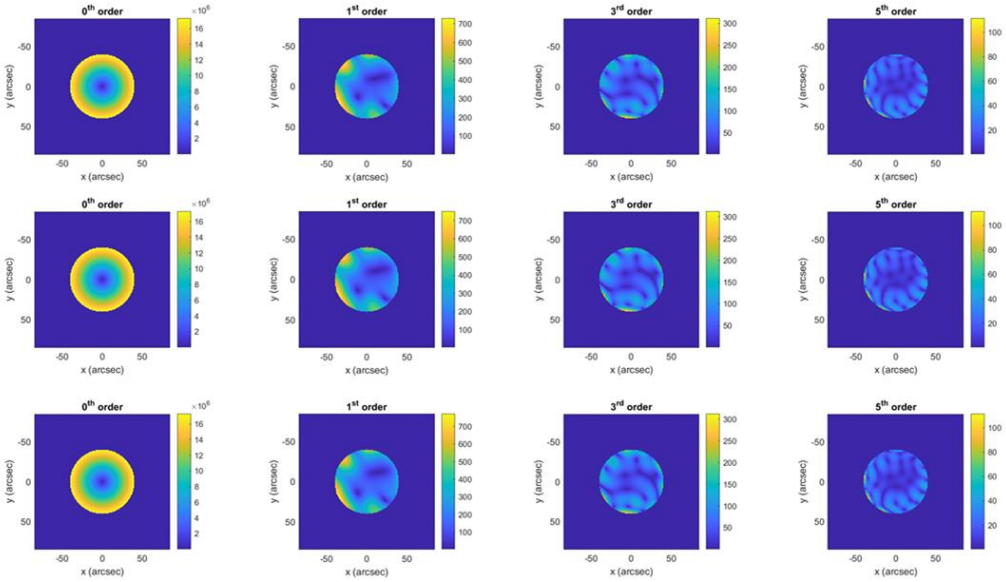

Figure 72. Modulus of the distortion residuals over the MICADO FoV after applying sequentially no correction, a 1storder , a 3rd order and a 5th order polynomials fit correction between the field distortion map corresponding to 25 degrees rotation angle, assuming the reference distortion map at 0 degrees rotation angle. Color bar units are micro-arcsec.

We have then repeated the computation, but limiting the analysis to the case of two sources 1 arcsec apart (in ±X and ±Y direction) on the MICADO FoV. An example of the residuals between the astrometric reference at rotation angle 0 degrees and the image at rotation angle 25 degrees is shown Figure 73.

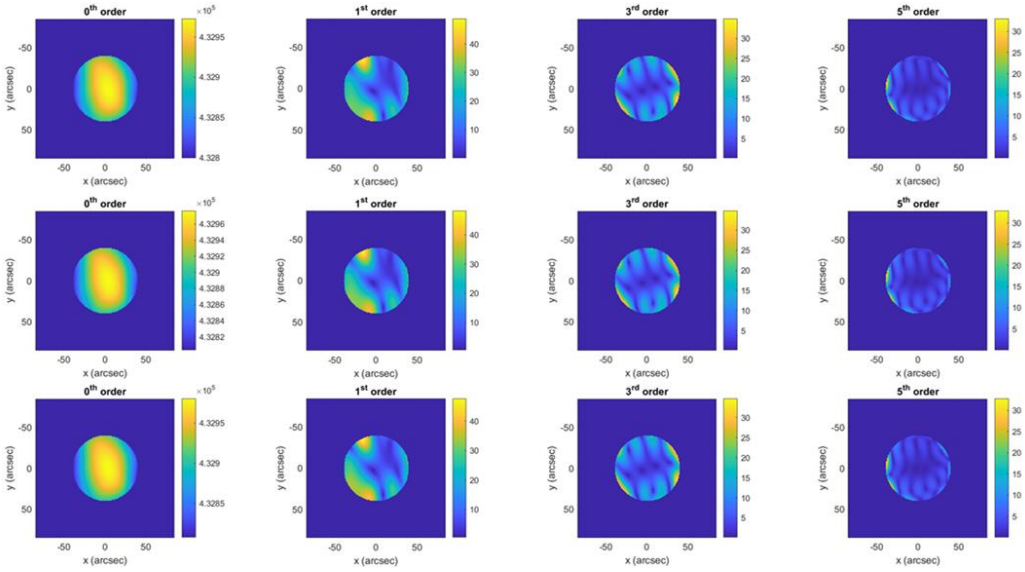

Figure 73. Modulus of the distortion residuals two sources 1 arcsec apart in +X direction over the MICADO FoV after applying sequentially no correction, a 1storder , a 3rd order and a 5th order polynomials fit correction between the field distortion map corresponding to 25 degrees rotation angle, assuming the reference distortion map at 0 degrees rotation angle. Color bar units are micro-arcsec.

The variations of the residual as function of the rotation azimuthal angle, assuming the astrometric reference image at 0 degrees, for the MICADO FoV and for two sources 1 arcsec apart are shown in Figure 74.

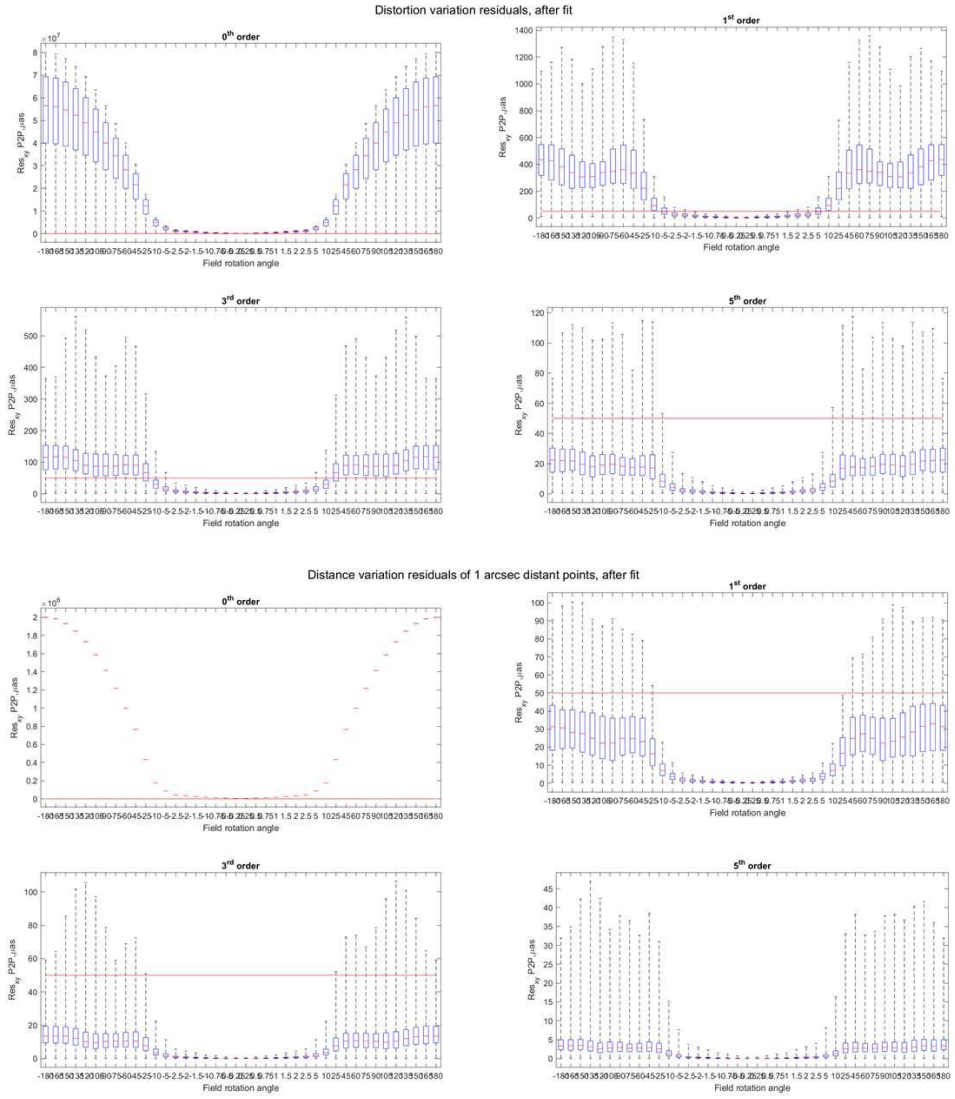

Figure 74. Variations of the residual as function of the rotation azimuthal angle over the MICADO FoV (top) and for two sources 1 arcsec apart (bottom). The central red mark indicates the median, and the bottom and top edges of the box indicate the 25th and 75th percentiles, respectively. The whiskers extend to the extreme data points.

After the 5th order correction, the residuals of the relative astrometry between two stars 1 arcsec apart are below 50 μas for any rotation angle and over the full MICADO FoV. The large majority of the couple of sources in the MICADO FoV has a residual error below 10 μas.

The tolerance simulation does not account for mid and high spatial frequency surface errors (the Zernike polynomials are limited to radial order 21). The simulations involving this spatial regime are quite complicated and computational time consuming, but it

typically represent the worst offenders for the astrometric performance. From a recent study (see [RD17]), the mid-spatial frequency distortion corrupt the astrometric requirement already within 2 degrees of relative rotation between MICADO and MAORY over the full MICADO FoV. This preliminary result seems to indicate that full complaisance with astrometric requirement is achievable within 2 arcsec square patches of the FoV over the full rotation angle. However, in the next phase we will improve the mid-spatial frequency effect by mean of ad hoc simulations and iteration with provider companies.

Such surface error can introduce a distortion variation when in particular the source footprint size on the surface is comparable with half period of the high frequency surface error. Assuming the surface error sag described by a sinusoidal function having amplitude A and spatial period P, there are three regimes:

- Source footprint size on the surface >> P/2: the surface error introduces an aberration on the source image but centroid position is basically unaffected.
- Source footprint size on the surface ~ P/2: the source footprint sees the surface error as almost pure tilt. For a given A, the tilt is maximum in this regime.
- Source footprint size on the surface << P/2: the source footprint sees the surface error as pure tilt. For a given A, the tilt decreases as P increases.

The surface error frequency and amplitude depend by the specific manufacturing process. Typically, PtV amplitude errors are few tenths of nanometers, while the frequency depends by the manufacturing tool size, and, typically, are in the range between millimeters and tenths of millimeters.

In the MMS, the affected surfaces are the ones of the CPM, being close to the entrance focal plane. The CPM first surface is located at 350 mm after the entrance focal plane and the footprint size on the first surface is about 19.7 mm.

As case study, we have implemented the simulation on the nominal MMS model. We have simulated the high-frequency surface errors by mean of a periodic function placed on the first surface of the CPM, having shape:

$$S(X,Y) = A \cdot \left(\frac{1}{4}\big(1 + cos(2\pi fX)\big)\big(1 + cos(2\pi fY)\big) - 1\right)$$

Where A is the PtV amplitude and f is the spatial frequency. An example of the surface sag is shown in Figure 75.

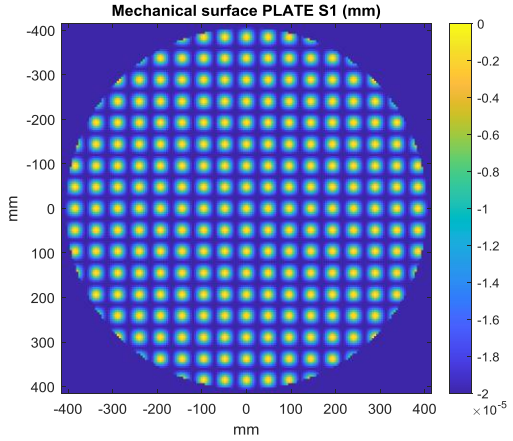

Figure 75. CPM first surface sag having amplitude PtV 20 nm.

We have simulated three PtV amplitudes of the periodic function: 10 nm, 20 nm and 50 nm. We have varied the period of the periodic function from 5 mm to 60 mm. We have computed the mean values of the residuals after the 5th order polynomials fit correction over the MICADO FoV and the for two sources 1 arcsec apart for azimuthal rotation angle in the range 0.25 - 50 degrees. Results are shown in Figure 76.

We have verified that, given the small amplitude of the surface error, the WFE and the Intra-epoch distortion variation, basically, are unaffected.

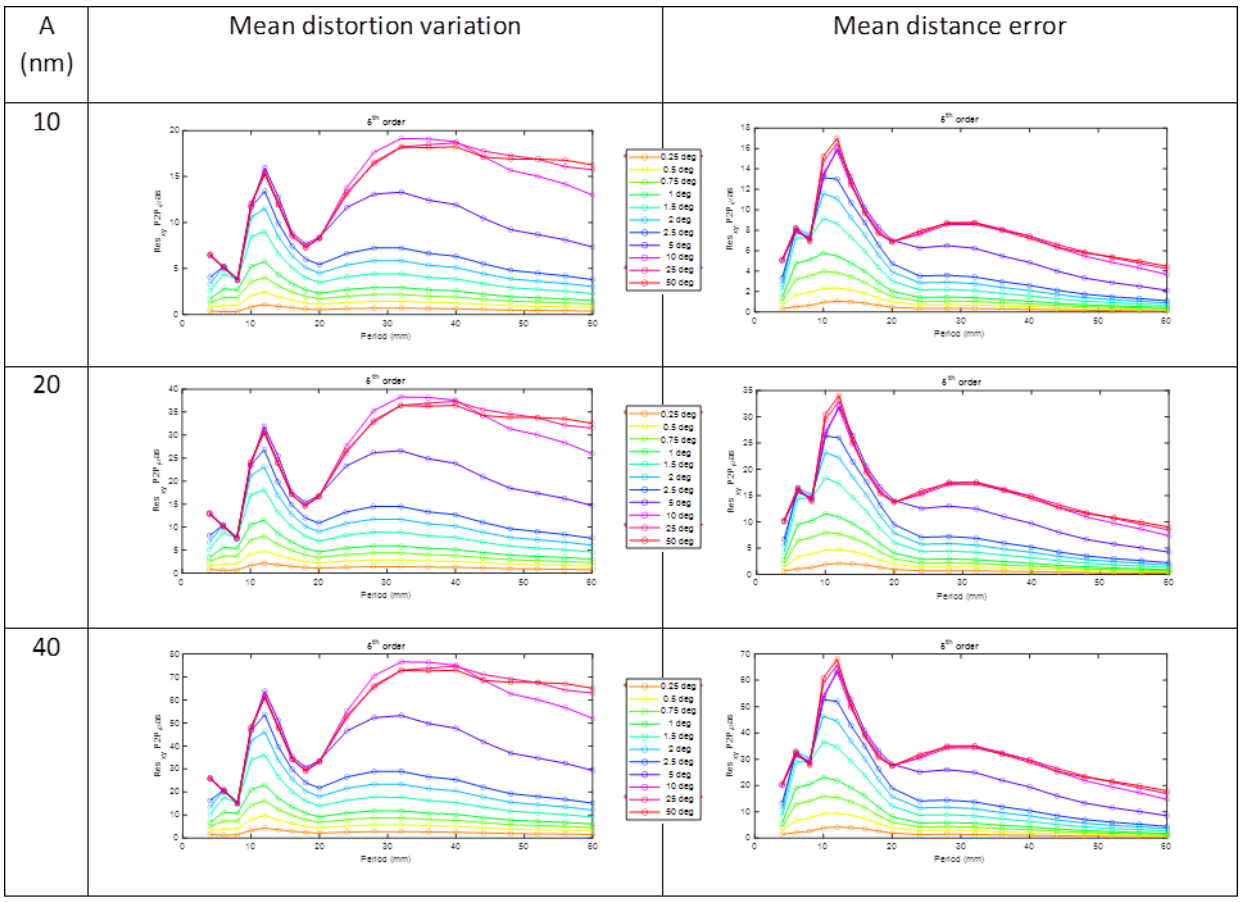

Figure 76. Mean values of the residuals after the 5th order polynomials fit correction over the MICADO FoV (left) and the for two sources 1 arcsec apart (right) for azimuthal rotation angle in the range 0.25 - 50 degrees as function of the sinusoidal function period and for amplitude equal to 10 nm (top), 20 nm (middle) and 50 nm (bottom).

As expected the residual curves over the MICADO FoV present a maximum close to period 30-40 mm (the footprint on the CPM has size about 20 mm). This effect is amplified at larger rotation angle. This is due to the regular grid sampling of one arcsec: for small rotations, there is not enough PSFs having a centroid drift large enough to impact statistically on the average value. The maximum on the curves is attenuated by a factor 2 when we limit the residuals to two sources 1 arcsec apart. This is due to the fact the two footprints overlaps on the CPM first surface; the two centroids are displaced by about 3.3 mm. The two PSF centroids are basically deviated together in the same direction.

We have verified that the amplitude dependency of the residuals is linear (see Figure 77). In particular, for the peaks of the curves the slope doubling the amplitude doubles the residual value.

However, both the residual curves over the MICADO FoV and for two sources 1 arcsec apart present a second peak at a sinusoidal function period of about 12 mm. This spatial period is characteristic for the case of two sources 1 arcsec apart. With reference to Figure 78, it exists, in fact, a certain phase for which the two footprints non-overlapping areas experience opposite slopes. The overlapping area will be transmitted in the same direction, while the two wings will be transmitted in the opposite directions. The effect is a relative displacement of the centroids of the two sources, generating a peak on the residuals curve for spatial period close to this characteristic value.

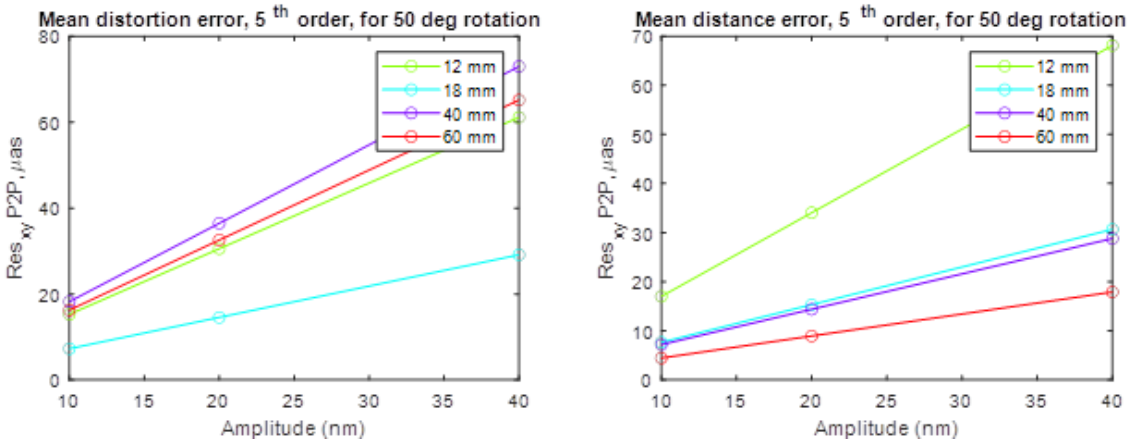

Figure 77. Mean values of the residuals after the 5th order polynomials fit correction over the MICADO FoV (left) and the for two sources 1 arcsec apart (right) for azimuthal rotation angle in the range degrees as function of the sinusoidal function amplitude and for period equal to 12 mm, 18 mm, 40 mm and 60 mm.

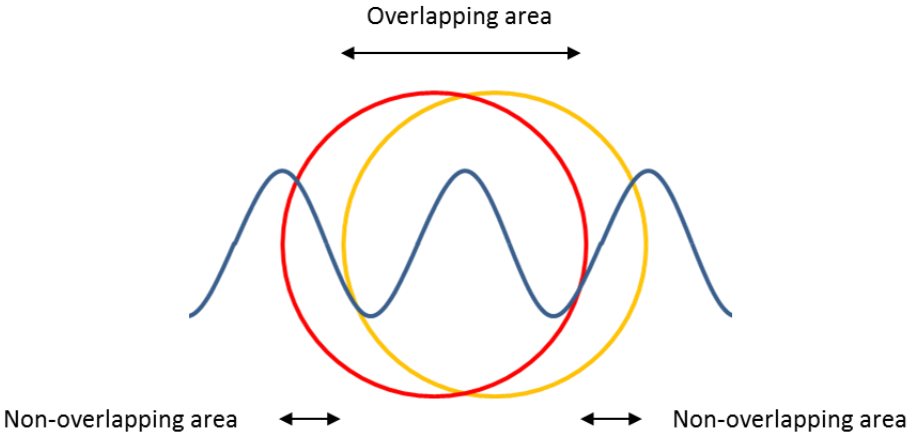

Figure 78. Scheme of the overlapping footprints (red and orange circle) of two sources 1 arcsec apart on the CPM first surface. The super imposed 1-D sinusoidal function has a spatial period that is half of the footprint plus the footprints displacement.

The high frequency surface error on the CPM surfaces may easily be the worst offender for the inter-epoch distortion variation residuals. The simulation has to be considered a

worst offender given the regularity of the pattern. The pattern can be somehow randomized in the spatial frequency domain by rasterized the manufacturing procedure (e.g. spiral patterns). Typically, the amplitudes at this frequency can be reduced with the use of pitch in post-polishing phase. In the current phase, we assume an amplitude PtV <15-20 nm (goal 10 nm) in this frequency domain. However, detailed discussion with manufacturers will be carried out in the next phase.

4.1.5.5 Effective focal length, plate scale, image space F/#

The effective focal length is not traced directly by the merit functions of the MC simulation. There is no strict correlation with the 98 percentile occurrences based on WFE or Intra-epoch distortion variation. In order to estimate the expected variation, we have computed the effective focal length MC distribution for each step, as shown in Figure 79.

For each step, we have computed the range including the 98 percentile of the population. We have then computed the maximum difference in modulus between the step initial value and the edges of the 98 percentile range. We have then linearly sum the resulting maximum differences of each step, assuming the sum as representative of the ±range error.

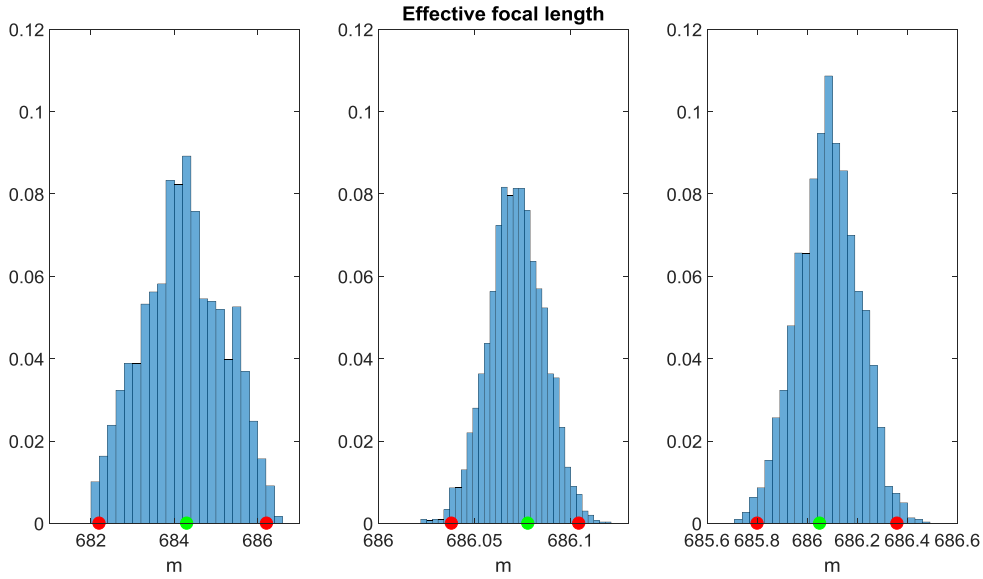

Figure 79. Effective focal length distributions for step 1 (left), step 2 (center) and step 3 (lright). Green dots are the step initial value. Red dots are the edges of the range including the 98 percentile of the population.

After the manufacturing and alignment simulation, the effective focal length has a value of 684302 ± 2452 mm.

The plate scale after the manufacturing and alignment simulation has a value of 0.3014 ± 0.0011 arcsec/mm (3.318 ± 0.012 mm/arcsec).

The image space F/# after the manufacturing and alignment simulation has a value of 17.755 ± 0.064.

4.1.5.6 Exit pupil and exit pupil F/#

We have followed a similar approach as for the effective focal length. The MC distributions of the exit pupil distance and diameter for the three steps are shown in Figure 80. Note that in the step 2, the MC occurrences have not been optimized for the exit pupil distance.

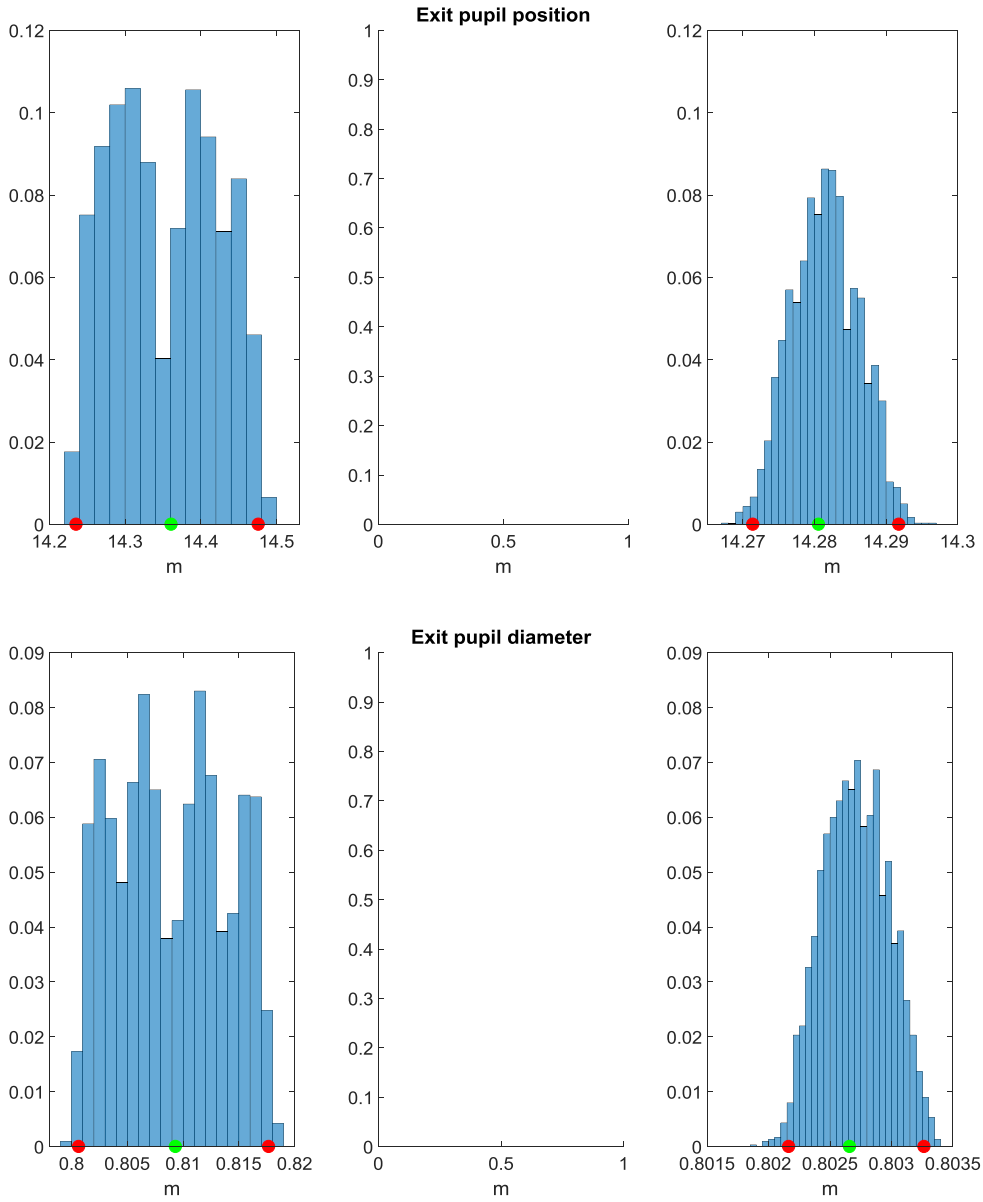

Figure 80. Exit pupil distance (top) and diameter (bottom) distributions for step 1 (left), and step 3 (right). Green dots are the step initial value. Red dots are the edges of the range including the 98 percentile of the population.

The exit pupil distance after the manufacturing and alignment simulation has a value of 14361 ± 137 mm.

The exit pupil diameter after the manufacturing and alignment simulation has a value of 809.32 ± 9.3 mm.

The MC distributions of the exit pupil F/# for the three steps are shown in Figure 81.

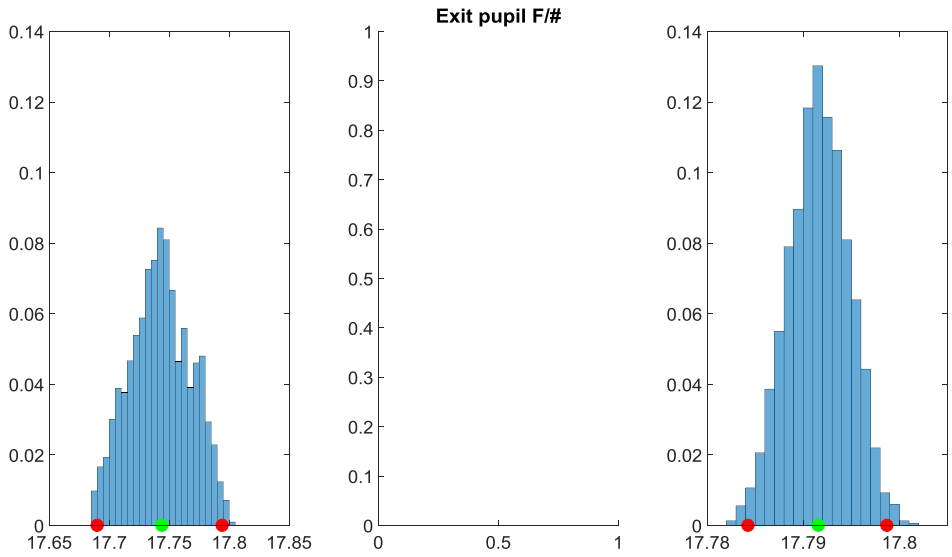

Figure 81. Exit pupil F/# distributions for step 1 (left), and step 3 (right). Green dots are the step initial value. Red dots are the edges of the range including the 98 percentile of the population.

The polychromatic exit pupil F/#, after the manufacturing and alignment simulation, has a value of 17.744 ± 0.061.

The computation has been limited to the monochromatic wavelength of 1 µm. However, we have verified on few occurrences that the wavelength dependency is negligible. By considering the wavelengths 1 µm, 1.65 µm and 2.2 µm for the minimization of the exit pupil spots instead of just 1 µm wavelength , the position of the exit pupil varies of about 0.1 mm, the diameter of the exit pupil varies by 0.006 mm, while the exit pupil F/# is not affected.

The MC distributions of the exit pupil F/# for the three steps are shown in Figure 82.

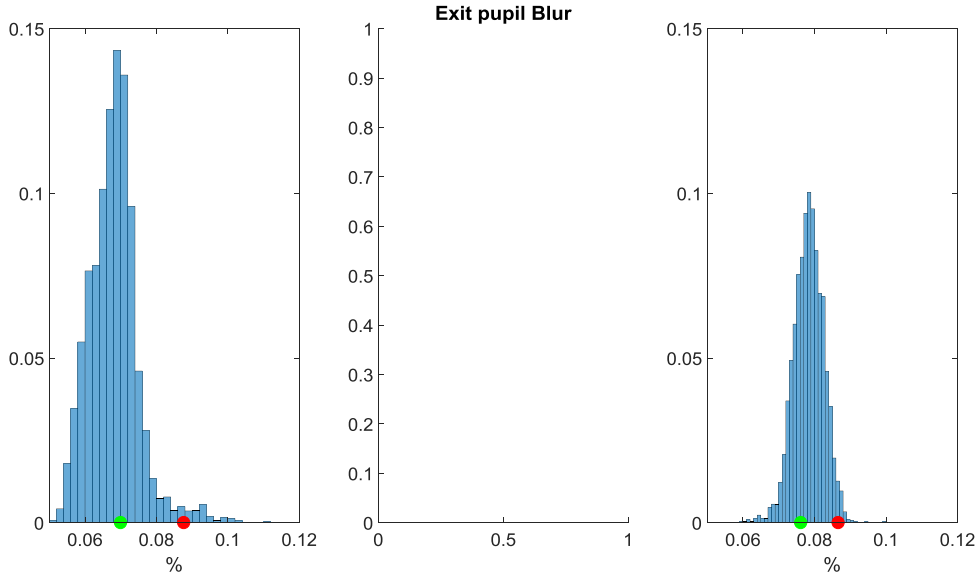

Figure 82. Pupil blur distributions for step 1 (left), and step 3 (right). Green dots are the step initial value. Red dots are the edges of the range including the 98 percentile of the population.

MAO-SF0-1.3.4.9 Pupil Blur: *The MAORY optics shall provide an Exit Pupil quality such that the MICADO cold stop shall not be linearly under-sized by more than 2% (goal 1%) with respect to the nominal pupil size over the MICADO Field of View [RD2].*

The computation has been limited to the monochromatic wavelength of 1 µm. The percent enlargement of the ratio between the maximum spot diameter and the exit pupil diameter is 0.028%. We have estimated, by analyzing a few occurrences, that between the 1 µm and the polychromatic case there is an underestimation of the blur variation of about 25%.

The pupil blur effect in terms of exit pupil diameter percent, after the manufacturing and alignment simulation, has a value below 0.135%.

We have evaluated the ellipticity of the exit pupil on a few occurrences, representative of 98-percentile of the intra-epoch distortion variation. We expect, indeed, that pupil ellipticity correlate with the field distortion because of the Lagrange invariant.

An example of the deviation between the polychromatic pupil centroids of the fields at the edge of the pupil with respect to the circular pupil circle is shown in Figure 83.

The expected maximum deviation is of the order of 0.1 mm. The exit pupil ellipticity effect in terms of exit pupil diameter percent, after the manufacturing and alignment simulation, has a value below 0.025%.

The expected impact of the exit pupil quality on the MICADO cold stop under-sizing, after the manufacturing and alignment simulation, is 0.160%.

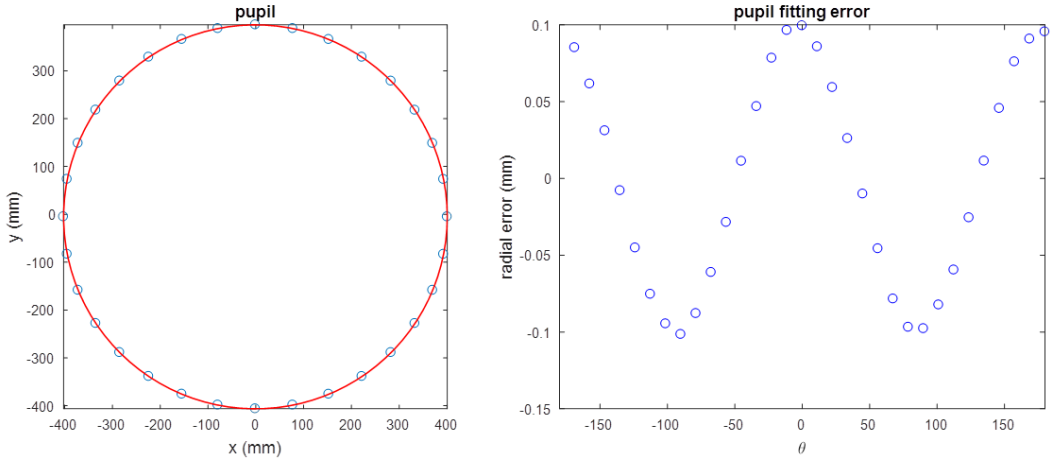

Figure 83. Example of the deviation between the polychromatic pupil centroids of the fields at the edge of the pupil with respect to the circular pupil circle.

4.1.5.7 Deformable Mirrors

We have followed a similar approach as for the exit pupil. The MC distributions of the DMs conjugation altitudes for the three steps are shown in Figure 84.

MAO-SF0-1.2.3.1 DM conjugation: *The two DMs shall be conjugated within 6-12 km and 17-20 km over the telescope entrance pupil [RD2].*

The DM1 (M9M) conjugation altitude, after the manufacturing and alignment simulation, has a value of 17461±390 m.

The DM2 (M10M) conjugation altitude, after the manufacturing and alignment simulation, has a value of 6501±378 m.

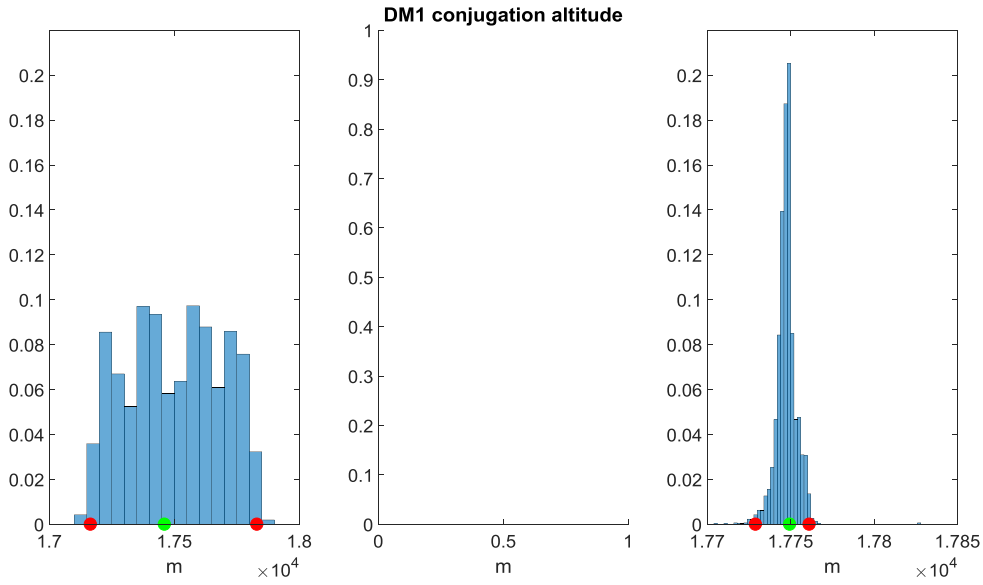

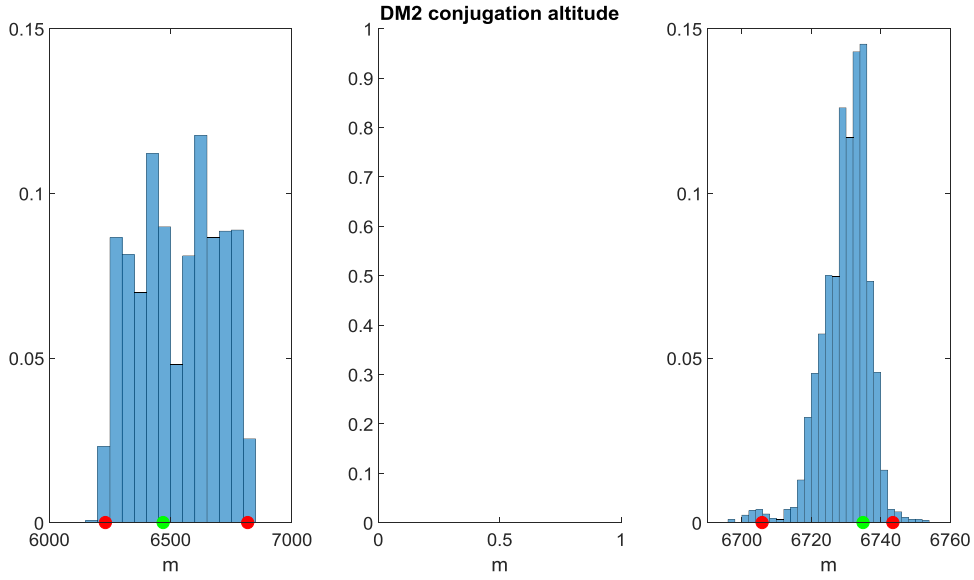

Figure 84. DM1 (top) and DM2 (bottom) conjugation altitude distributions for step 1 (left), and step 3 (right). Green dots are the step initial value. Red dots are the edges of the range including the 98 percentile of the population.

MAO-SF0-1.2.3.2 Image quality on DM: *The images on DMs of the conjugated layers shall have an RMS spot diameter < 1/10 of the DM pitch [RD2].*

We have computed the polychromatic RMS spot diameter corresponding to a grid of point sources covering the meta-pupils. The MC distributions of the DMs maximum RMS spot diameter for the three steps are shown in Figure 85.

The maximum RMS spot diameter, after the manufacturing and alignment simulation, is expected for the DM2 with value below 2.26 mm (<2.5 mm, 1/10 of DM pitch).

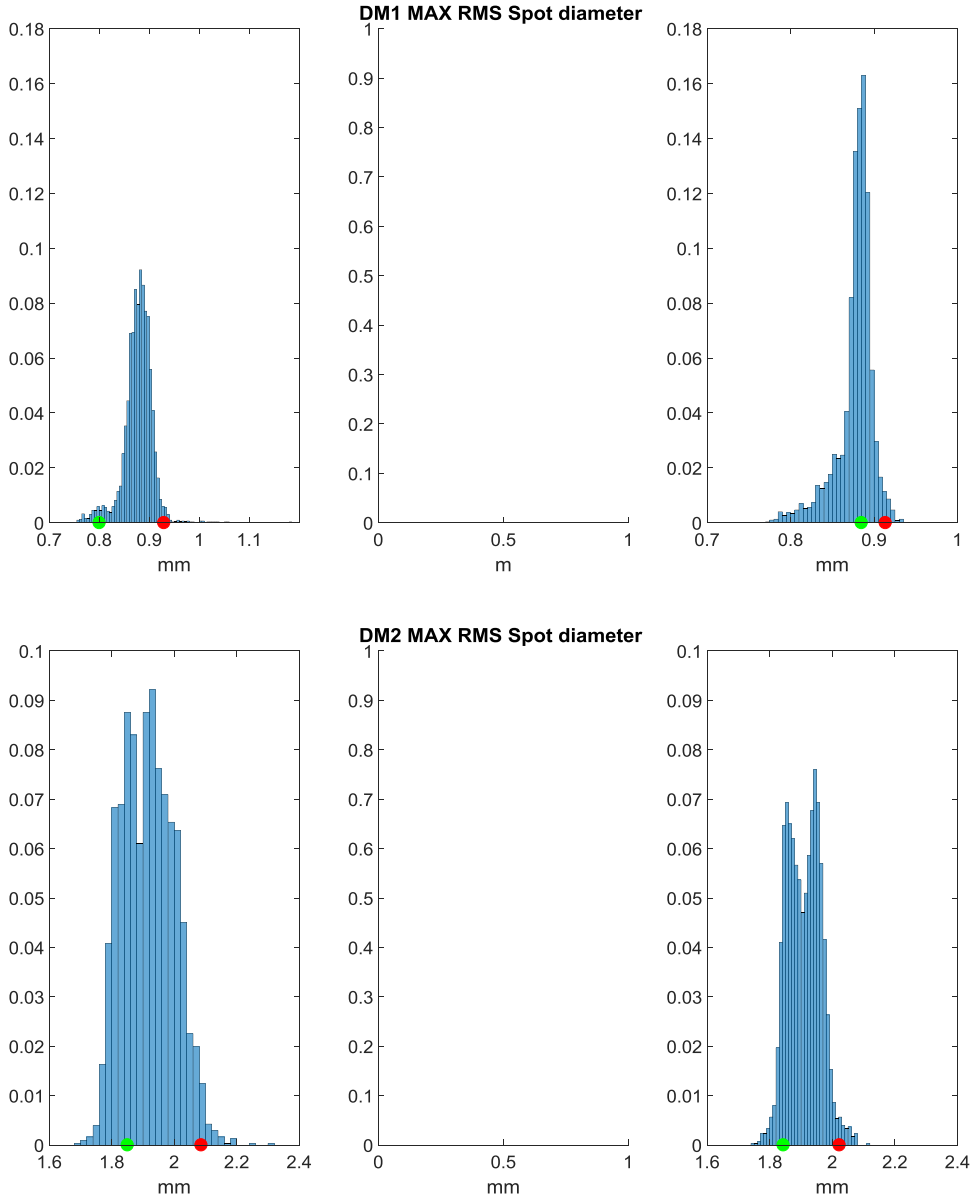

Figure 85. DM1 (top) and DM2 (bottom) maximum RMS spot diameter distributions for step 1 (left), and step 3 (right). Green dots are the step initial value. Red dots are the edges of the range including the 98 percentile of the population.

4.1.5.8 Dichroic angle of incidence

We have evaluated the dichroic angle of incidence variation after the manufacturing and alignment process. The distributions are shown in Figure 86. The computation considered both the main path and LGS path footprints on first surface of the dichroic.

The maximum angle of incidence on the dichroic is 14.09 degrees.

The minimum angle of incidence on the dichroic is 8.54 degrees.

This range has been used for the specs of the dichroic filters.

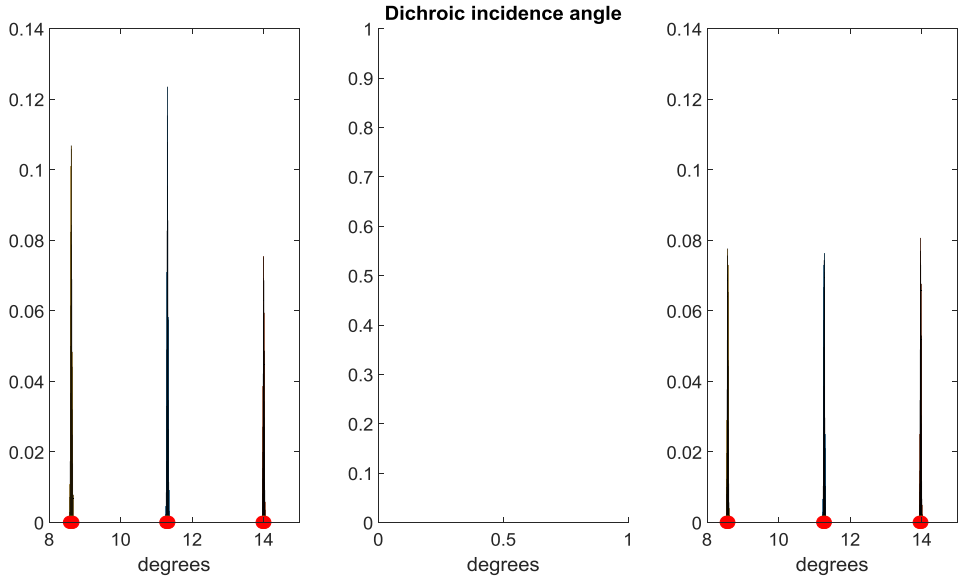

Figure 86. Minimum, chief rays and maximum dichroic AOI distributions for step 1 (left), and step 3 (right). Green dots are the step initial value. Red dots are the edges of the range including the 98 percentile of the population.

4.1.5.9 Footprints envelope

We have evaluated the movement and the envelope of the footprints for each optics surface. We have considered rays coming from infinite conjugated sources (in case of M11M for both the main path and the second port path) and LGS conjugated at 84 km, being the ones that determine the largest possible footprints. The fields have been chosen at the FoV edges. The computation has been done for each occurrence of step 1 and 3.

For each surface, we have computed the envelope of the footprints and we have fit its edge with an ellipse. The outputs of the computation are the ellipse center shift with respect to the nominal clear aperture and the ellipse semi-axis. Some examples are shown in Figure 87.

For each step and each surface, we have considered the maximum ellipse center relative shift in X and Y direction and the maximum X and Y ellipse semi-axis variation. As worst case, for each surface, we linearly sum the maximum center shift and the maximum semi-axis variation in each step. We have then computed the difference between the obtained results and the nominal clear aperture for each surface. The results are shown in Table 17.

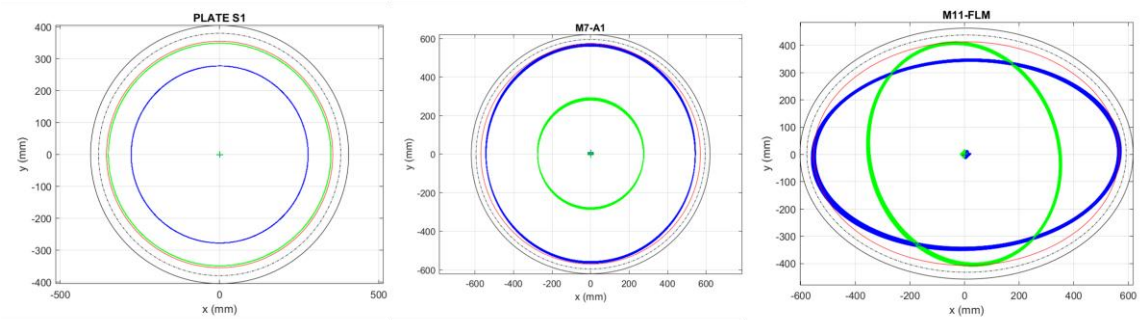

Figure 87. Footprints envelopes on the first surface of the CPM, M7M and M11M due to infinite conjugated sources (blue circle) and LGS conjugated at 84 km or second instrument path for M11M (green circle). Red circle represents the nominal aperture. The black circle represents the mechanical aperture. The black dash circle represents the polished surface edge. Footprints are the results of the step 1.

	Step 1				Step 2				Overall					
	maximum footprint decenter wrt aperture center		maximum footprint semi-axis		maximum footprint relative decenter wrt aperture center		maximum footprint semi-axis variation		maximum footprint decenter wrt aperture center		maximum footprint semi-axis		maximum footprint envelope	
	X [mm]	Y [mm]	X [mm]	Y [mm]	X [mm]	Y [mm]	X [mm]	Y [mm]	X [mm]	Y [mm]	X [mm]	Y [mm]	X [mm]	Y [mm]
CPM S1	0,0	0,0	349,2	349,2	1,0	1,0	0,0	0,0	1,0	1,0	349,2	349,2	350,2	350,2
CPM S2	0,0	0,0	348,1	348,1	1,0	1,0	0,0	0,0	1,0	1,0	348,1	348,1	349,1	349,1
M6M	0,2	0,5	376,2	448,0	1,0	1,2	0,0	0,1	1,2	1,7	376,2	448,0	377,4	449,7
M7M	0,4	9,1	544,8	564,8	3,2	3,5	0,0	0,1	3,6	12,6	544,8	564,9	548,4	577,5
M8M	1,7	8,6	577,3	582,0	6,1	6,6	0,1	0,2	7,8	15,3	577,4	582,2	585,2	597,4
M9M	0,0	0,9	435,0	437,4	8,6	9,6	0,2	0,3	8,6	10,5	435,2	437,7	443,8	448,2
M10M	0,0	3,2	575,1	579,0	16,5	16,4	0,5	0,6	16,6	19,6	575,6	579,5	592,2	599,1
Dichroic S1	1,3	1,3	408,0	403,6	14,0	15,8	0,2	0,3	15,2	17,0	408,2	403,9	423,4	420,9
Dichroic S2	10,4	5,9	407,8	403,4	14,0	15,7	0,2	0,3	24,4	21,7	408,0	403,6	432,4	425,3
M11M	8,3	7,3	560,5	408,2	24,4	16,6	1,2	0,6	32,8	23,9	561,7	408,8	594,5	432,7
MICADO Mec	1,6	3,4	317,6	317,7	6,5	6,3	0,1	0,1	8,0	9,8	317,7	317,9	325,7	327,6
M12M	0,5	0,4	296,4	335,8	1,1	1,2	0,1	0,3	1,6	1,5	296,5	336,0	298,1	337,6

Table 17. Step1 maximum footprints displacement with respect to surface aperture center and maximum footprints semi-axis, step 2 relative footprints displacement with respect to surface aperture center and maximum footprints semi-axis variation and combined effect (linear sum).

We have compared the semi-axis of the maximum footprints envelope with the semi-axis of the nominal clear aperture and the polished clear aperture. The results are summarized in Table 18. In the table, negative value means that the maximum footprint is outside the surface aperture.

Assuming +25 mm margin for the polished aperture, after the manufacturing and alignment simulation, the only mirror having a footprint outside of it is M11M. This behaviour has been marginally traced also by the step 3 directly as shown in Figure 88. The current possible strategy are:

1) Increase the mechanical and the polished aperture diameter of M11M by 20-30 mm. It has been already verified that from the mechanical interferences point of view there is no issue to increase M11M size in that bench position.
2) Re-center the mirror. This approach requires to materialize the footprints.

This issue will be addressed in the next phase. However, the vignetting occurs for field at the very edge of the technical FoV.

	Nominal clear aperture semi-axis		Margins		polished clear aperture semi-axis		Margins	
	X [mm]	Y [mm]	X [mm]	Y [mm]	X [mm]	Y [mm]	X [mm]	Y [mm]
CPM S1	355,0	355,0	4,8	4,8	380,0	380,0	29,8	29,8
CPM S2	355,0	355,0	5,9	5,9	380,0	380,0	30,9	30,9
M6M	380,0	450,0	2,6	0,3	405,0	475,0	27,6	25,3
M7M	570,0	570,0	21,6	-7,5	595,0	595,0	46,6	17,5
M8M	590,0	590,0	4,8	-7,4	615,0	615,0	29,8	17,6
M9M	440,0	440,0	-3,8	-8,2	465,0	465,0	21,2	16,8
M10M	580,0	580,0	-12,2	-19,1	605,0	605,0	12,8	5,9
Dichroic S1	420,0	420,0	-3,4	-0,9	445,0	445,0	21,6	24,1
Dichroic S2	420,0	420,0	-12,4	-5,3	445,0	445,0	12,6	19,7
M11M	560,0	410,0	-34,5	-22,7	585,0	435,0	-9,5	2,3
MICADO Mec	320,0	320,0	-5,7	-7,6	345,0	345,0	19,3	17,4
M12M	300,0	337,0	1,9	-0,6	325,0	362,0	26,9	24,4

Table 18. Difference between the maximum variation of the footprints envelope due to center displacement and semi-axis variation with respect to the surface nominal clear aperture and polished aperture.

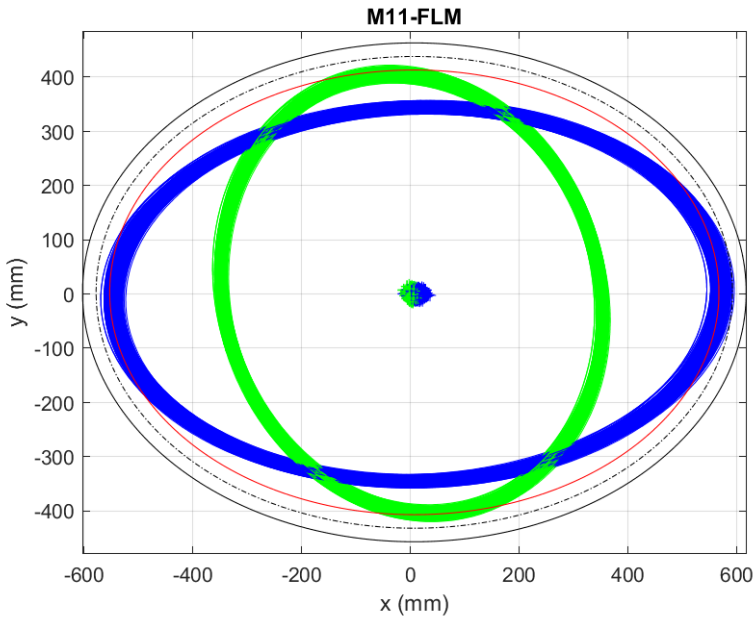

Figure 88. Footprints envelopes M11M due to main path (blue circle) and second instrument path (green circle). Red circle represents the nominal aperture. The black circle represents the mechanical aperture. The black dash circle represents the polished surface edge. Footprints are the results of the step 3.

On the DMs, the maximum footprint variation is within the additional actuator circle, assuming an actuator pitch of 25 mm. However, this variation can be, at least partially, recovered by rotating the DM itself around its center of curvature during the integration. In

particular, for M10M, this operation should be viable also through the hexapod axis. This solution will be studied and eventually implemented in the next phase.

4.1.6 Discussion on assumptions

The assumed values for the tolerance simulation have been verified through both consortium simulations and provider company consultations. In the following, we elaborate on some aspects related with the tolerance simulations assumptions.

4.1.6.1 CPM glass inhomogeneity

The inhomogeneity of the CPM glass has not been simulated at this working level. We are assuming a CPM of Suprasil 3002 having thickness 80 mm. Suprasil 3002 can reach high homogeneity also on one-meter-class blank, ≤ 10-5 ppm PtV. Moreover, most of the non-homogeneity has, basically, defocus-like shape with the wings concentrated on the outer part of the circular blank, outside the polished aperture. The region of interest can reach homogeneity close to 1.5-1.0 ppm PtV, again mainly defocus and very low order spatial frequency terms. Given that the CPM position is close to the entrance focal plane (350 nm), we do not expect an impact on the main path WFE. In addition, the distortion variation should not be dramatically affected, but for large field rotation angles, for which anyhow calibration maps are already foreseen. In the case of the LGS path, the effect on the WFE is expected to be larger (given the larger footprints), but also in this case it can be calibrated.

The CPM inhomogeneity effects will be better addressed in the next phase. One possible mitigation strategy is to measure the aspheric surface of the CPM during manufacturing process in transmission with a collimated beam, compensating in this way also inhomogeneity. The discussion with provider companies is ongoing and it will be finalized in the next phase.

4.1.6.2 Aspheric mirrors test set-up

We have explored a potentially feasible test set-up for the aspheric surfaces (M7M and M8M) and we estimated the expected errors as function of the setup alignment. This work was propaedeutic for the definition of the low order aberration requirements on such mirrors. This setup was suggested by Officina Stellare as a possible solution for the aspherical mirrors and CPM testing. Alternative test setups were proposed by SAFRAN and AMOS, with similar results in terms of achievable accuracies.

We describe hereafter the setup for M8M, but a similar configuration with comparable results were obtained for M7M.

With reference to Figure 89, the main setup (setup 1) is composed by the interferometer (INT) equipped with a CGH, an auxiliary spherical mirror (SM) having 10 m radius of curvature, and the test mirror to close the cavity. The spherical mirror is tilted to compensate for the large astigmatism of M8M, also leaving space to access the spherical mirror from its center of curvature, for alignment and verification purposes (setup 2). In fact, the shape of the spherical mirror can be measured simultaneously and subtracted from the main cavity WFE. The CGH is necessary to correct for the residual aberrations of the main setup. The overall test size is about 10 m in length.

The double pass WFE of the main cavity is well corrected by the CGH, for which we verified the feasibility for what concern the size and the fringe density (see Figure 90).

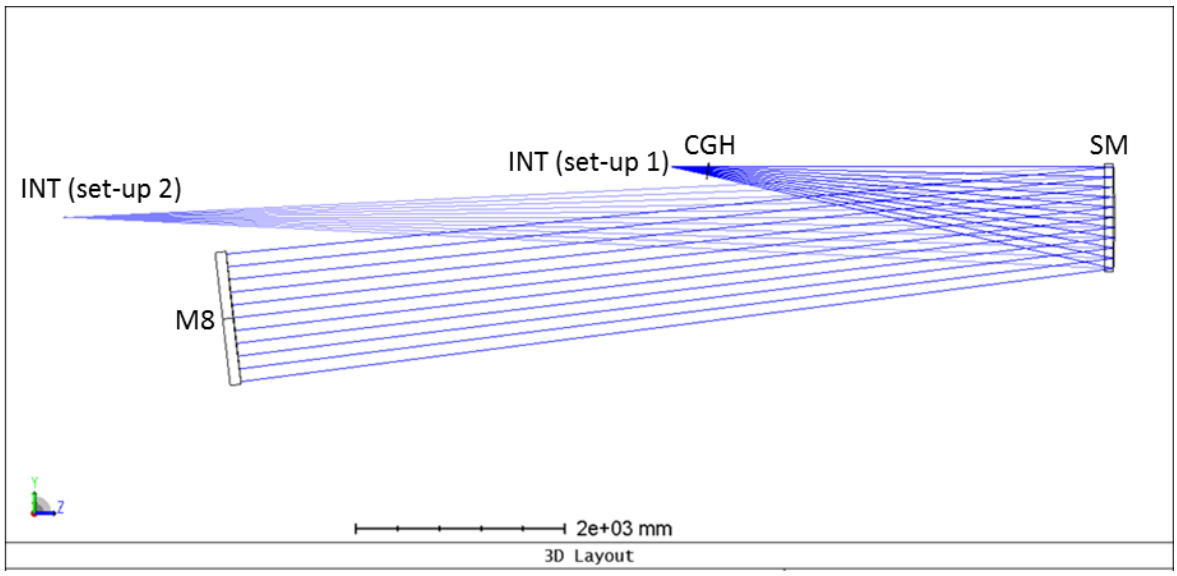

Figure 89. Test set-up for the aspheric mirror M8M.

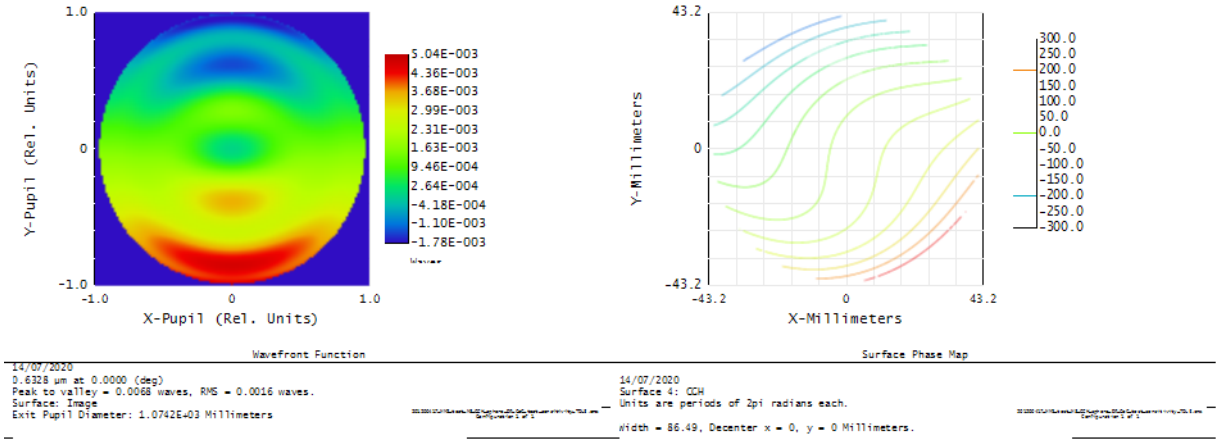

Figure 90. Double-pass WFE (left) and CGH phase function (right).

The main hypothesis is that all the large elements are placed with Laser Tracker, i.e., the group INT+CGH, the SM, and the test mirror M8M. The CGH is aligned to the interferometer with auxiliary patterns to very tight tolerances:

CGH	
dx	+/- 1 um
dy	+/- 1 um
dz	+/- 10 um
tx	+/- 10"
ty	+/- 10"
tz	+/- 20"

We consider to measure the position of the interferometer focus with the SMR to the Laser Tracker accuracy and the tilt/clock of the group with markers projected at 2-4 meter in front of the CGH. The considered tolerances for the group INT+CGH are the following:

INT+CGH	
dx	+/- 100 um
dy	+/- 100 um
dz	+/- 100 um
tx	+/- 2"
ty	+/- 2"
tz	+/- 10 "

For what concern the SM, its center of curvature is determined with the ball method in the setup 2, and it is used to define its radius of curvature and its position (see Figure 91). Initially, the cavity is closed between the interferometer and the SM. Then the cavity is closed between the interferometer and the SMR. Finally, the distance between the SMR and the SM is measured with Laser Tracker.

The radius of curvature of the spherical mirror must be measured before the CGH design. In the tolerance analysis, only its knowledge error is considered.

The interferometer error contribution on the definition of the SM position, assuming 1/10 wave single pass WFE for focus and 0.5 waves single pass WFE for tilt (1 fringe), is calculated as:

Diameter	1.00000	m		
Wavelength	0.63200	um		
Tolerance (z)	0.10000	waves WFE single pass =	0.2	fringes
Tolerance (x,y)	0.50000	waves WFE single pass =	1.0	fringes

RoC (m)	Sag (m)	h (um)	dh/dr	dr/dh	dz = dRoC (um)	dx (um)
10.000	1.25E-02	1.25E+04	-0.00125	-798.5	-50.4	3.2

The Laser Tracker error has been assumed to be 50 µm in each direction. Taking margins on both the interferometer and laser tracker errors, we defined the following tolerances:

Spherical mirror	
dx	+/- 100 um
dy	+/- 100 um
dz	+/- 100 um
tx	+/- 2"
ty	+/- 2"
dRoC	+/- 100 um

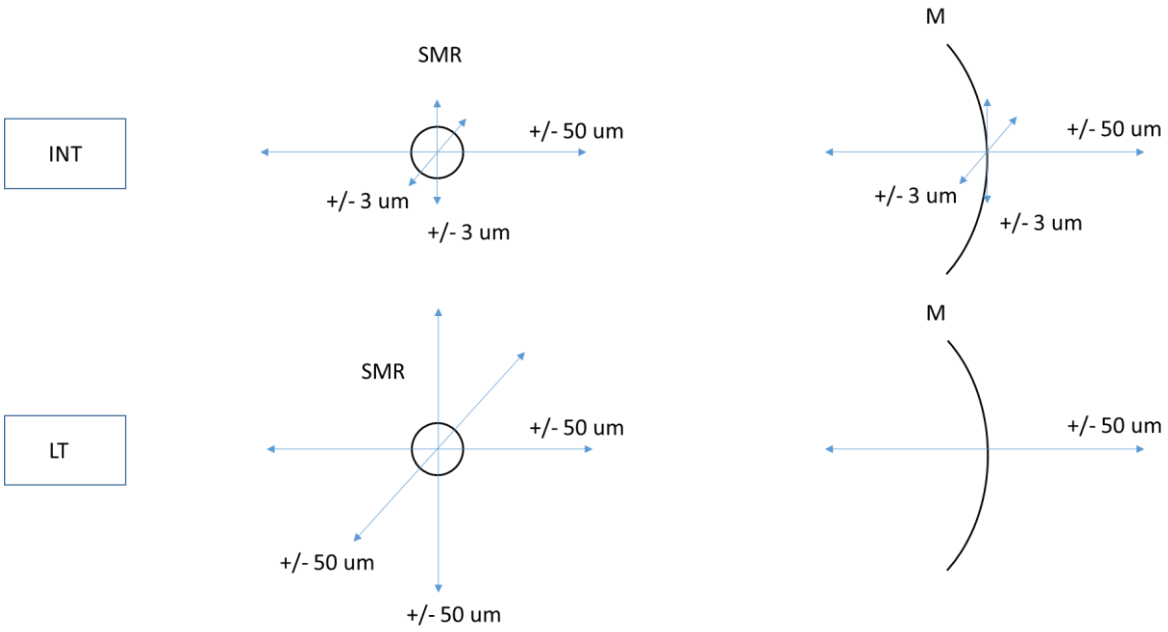

Figure 91. Ball method in set-up 2 for the determination of the SM center of curvature. Assumed errors on the determination of SM position due to interferometer alignment (top) and Laser Tracker accuracy (bottom).

The test mirror M8M is placed with Laser Tracker accuracy in x, y, z, and the tilt is adjusted to null the tilt fringes. These are the tolerances, where we considered as radius of curvature error the value specified for manufacturing (0.03%):

M8M	
dx	+/- 100 um
dy	+/- 100 um
dz	+/- 100 um
tz	+/- 10"*
dRoC	+/- 10 mm

*decreases with the number of SMRs used.

We have performed both a sensitivity analysis and a Monte Carlo simulation.

In the sensitivity analysis, for each misplacement, we optimized the tx, ty position of M8M, and we recorded the WFE in double pass. In Figure 92, the plot shows the RMS WFE of each Zernike term. The surface error is calculated dividing by 2 the WFE.

We performed a MC simulation with 1000 occurrences and a uniform statistics. The resulting WFE for each Zernike term are shown in Figure 93.

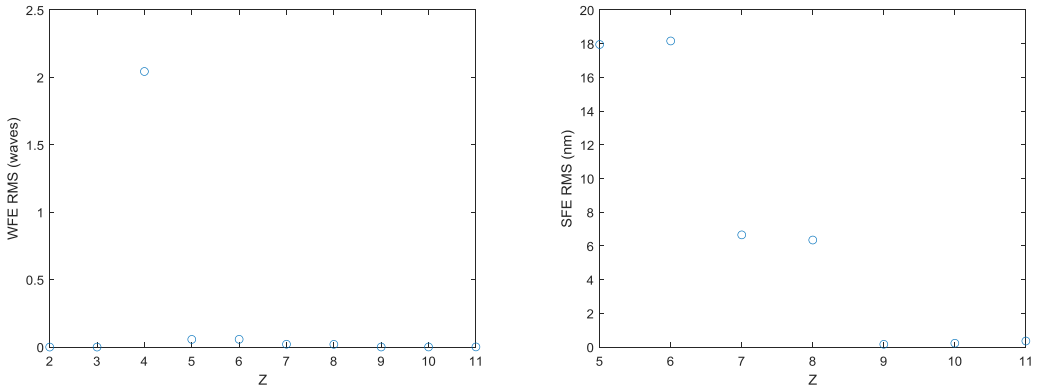

Figure 92. RMS WFE value of the Zernike terms (left) and the RMS SFE of the Zernike terms (right) in the sensitivity analysis due to the set-up errors.

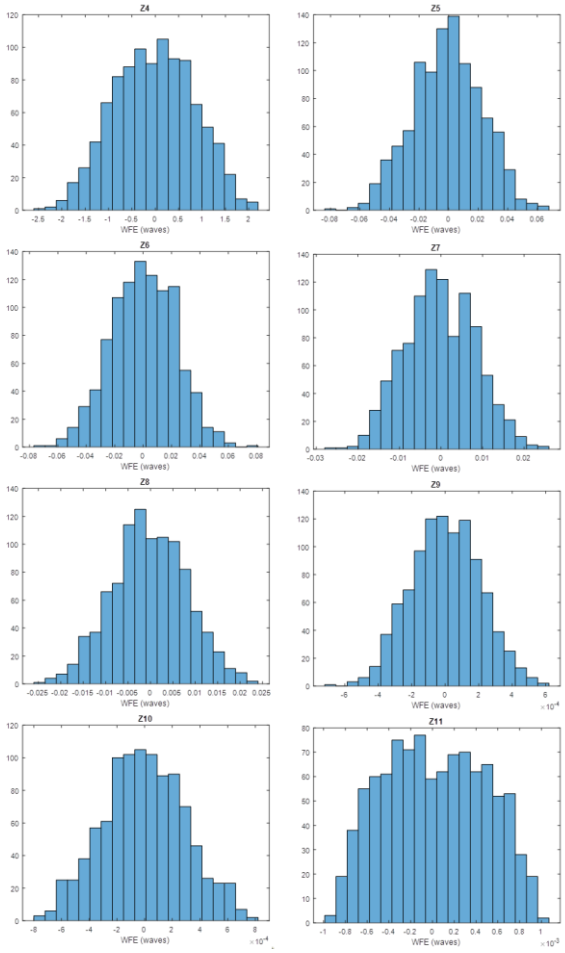

Figure 93. RMS WFE MC distributions of the Zernike terms due to the set-up errors.

For each Zernike term, we have computed the maximum and the 95 percentile WFE and SFE, as reported in Table 19. They are in good agreement with the values obtained from the sensitivity analysis above.

Similar values have been obtained for M7M.

Z	max WFE RMS (waves)	max SFE RMS (nm)	WFE RMS at 95% (waves)	SFE RMS at 95% (nm)
4	2.4170	764.8	1.6799	531.5
5	0.0783	24.7	0.0454	14.4
6	0.0803	25.4	0.0457	14.5
7	0.0273	8.6	0.0167	5.3
8	0.0244	7.7	0.0163	5.2
9	0.0007	0.2	0.0004	0.1
10	0.0008	0.3	0.0006	0.2
11	0.0011	0.3	0.0010	0.3
RMS Z5-Z11	0.1179	37.3	0.0685	21.6

Table 19. Maximum and 98-percentile WFE and SFE Zernike terms values of the Monte Carlo simulation.

The values in the table are well within the budget assumed in the manufacturing and alignment tolerance simulation. However, we have added margins because of other potential source of errors not considered here. In particular, given the long baseline of the set-up, thermal gradient stratification of the air along path may lead to an offset on the measurement of the astigmatisms. For such reason, the required accuracy is two times larger than the one obtained in the test set-up analysis.

4.1.6.3 Referencing the optical elements to the mechanical SMRs

We have estimated the accuracy that can be reached in the referencing the optical surfaces to the retroreflectors positioned onto each optic.

- **flat mirrors**: the mirror surface can be referenced to the SMRs using the Coordinate Measurement Machine (CMM), with micrometric accuracy in all directions. We estimated an accuracy +/- 5 um for x, y, and z, and +/- 1” in tip/tilt, considering CMM errors of +/- 5 um over 1 m mirror.
  Alternatively, tip/tilt can be measured directly with the laser tracker to arcsec precision with the ball/virtual ball technique. During the same test, the SMRs positions are measured with laser tracker accuracy and referenced to the mirror axis. The mirror orientation can be measured with accuracies of the order of 1 arcsec (verified on a similar structure during the alignment of the M4 Optical test Tower) and referenced to the SMRs. The accuracy limitation in this case is the measurement of the SMRs, that can be estimated in +/- 50 um x, y, z, and +/- 10 arcsec in tip/tilt (over a mirror of 1 m, conservative).
- **concave spherical mirrors** (M10M DM2 only): the technique consists in the identification with a spherical retroreflector (which can be both aligned in auto-reflection to the interferometer and measured with the laser) of the mirror center of curvature. The mirror is aligned to the interferometer and its references measured

with the laser tracker. Considering the long radius of curvature of the DM, the accuracy in the determination of the center of curvature is limited by the laser tracker accuracy in x-y, and by the interferometer accuracy in z, given by the fraction of focus fringes visible. Considering 15 m of radius of curvature and 1.2 m of diameter for spherical mirror, we estimated an accuracy of +/- 100 um in the knowledge of the center of curvature position with respect to the reference points on the mirror mount in all three directions. This accuracy in the references position would lead to an accuracy in the tip-tilt positioning of DM2 of approximately less than +/- 30 arcsec.

- **convex spherical mirrors** (M9M DM1 only): given the convex shape of the surface, the referencing as for the previous method is more complex. Nevertheless, a procedure to optically reference the mirror vertex during the DM optical calibration will be developed, depending on the DM test setup (elliptical mirror is foreseen as auxiliary mirror to close the cavity). Similarly to DM2, the expected accuracy in the references position would lead to an accuracy in the tip-tilt positioning of DM2 of approximately less than +/- 30 arcsec.
  As an alternative, CMM can be used to measure the mirror reference body along with the mechanical references and, with some hypothesis, define the shell position as respect to the mechanical references. Further investigations and interaction with the DM manufacturer are necessary to consolidate these numbers.

- **aspherical mirrors and CPM** (CPM, M7M and M8M): concerning the two aspherical surfaces, we foresee two possible scenarios where the references can be placed and/or measured: 1) during the optical test, by means of the Laser Tracker; 2) with CMM, with a measurement at the end of the manufacturing process.
  1) assuming a correctly aligned test set-up similar as in 4.1.6.2, the knowledge of the position of the optical surface given by the interferometer is few tenths of micron in x-y and at sub-arcsec level in tip/tilt. The referencing of the mirror is performed tracking with the LT the positions of all the optical elements of the test setup, the accuracy being limited by the Laser Tracker itself. Auxiliary patterns on the CGH projecting focal points at the proximity of the test mirror can also be designed, measured with the LT, and used as crosscheck of the mirror referencing.
  2) This approach consists in the measurement of the mirror surface with a CMM, followed by its fitting with a theoretical surface of unknown parameters. In the case of large optics, such as the CPM, M7M and M8M, the expected error associated to the CMM single sag point measurement is estimated to be about 2-5 um. As reference value for the following computation, we have assumed an error of 3 um. In order to estimate the impact of this error on the knowledge of the surfaces, we performed a sensitivity analysis to the limit of the CMM error. In particular, we introduced a misalignment on each degree of freedom (dx, dy, clock z) up to reach a difference between the nominal surface and the misaligned surface (sag difference) of approximately +/- 3 um. For the mirrors, the obtainable knowledge in de-centering is about 200 µm while for the CPM it is about 2.6 mm. The knowledge in clock z is about 2 and 0.5 degrees for M7M and M8M respectively, and 0.4 degrees for the CPM. For clock characterization, we would have probably relay on mechanical references, needed during the manufacturing of the mirrors. Concerning the tilt x and y for all elements, we can assume as conservative estimation that the maximum CMM error is encountered at the mirror

edges, with an entity of about 6 um/1200 mm = 1 arcsec for mirrors and about 6 um/800 mm = 1.5 arcsec for the CPM

4.2 LGSO

LGSO tolerances analysis has been carried out in two steps. The two steps mimic an initial alignment of the objective outside the MMS and then the integration of the aligned LGSO into the already aligned MPO. In particular, the two steps have been implemented as follow:

1. Considering the LGSO as a stand-alone system:
    a. The MPO is supposed to be perfect
    b. Only defects of LGSO elements (and their mutual alignment errors) are taken into account
2. Considering LGSO mated with already 'tolerated' MPO systems:
    a. The MPO system used is an already 'tolerated' one, which takes into account manufacturing errors and alignment errors for elements of MPO. Only step 1 and step 2 MPO MC distributions have been considered, given the limited impacts that step 3 of MPO tolerance seems to have on properties as F# , WFE, etc.
    b. Alignment and manufacturing errors of LGSO are the same of point 1.

In this section, the 'step' concept is slightly different in meaning with respect the procedure presented for the MPO. There the steps are used to separate different contributors to the total 'error' of the system; here they are used to 'mimic' the AIT of the LGSO: step 1 gives the performances of the LGSO when aligned in stand-alone, step 2 shows what happens when the LGSO subsystem is mounted after the MPO.

Obviously, the latter is the configuration in which one really wants to verify the requirements, but the first step is useful to give performance figures that can be a reference during LGSO alone and to understand the contribution of the MPO on the final performances of the LGSO.

4.2.1 Accuracy values

Table 20 summarizes the accuracy values assumed on the simulations. The values in the table have to be intended as +/-.

Radius of Curvature (spherical elements)	0.1% 0.05% for L1 faces
Index of refraction	5 10^{-4} (uniform over the element volume)
Abbe number	0.7 (about 1%)
Thickness	1 mm
Wedges of lenses faces	6 10^{-3} degrees both in X and Y direction About 100 micron runout for 1 meter diameter element
Positioning errors	100 micrometres for xyz displacement 6 10^{-3} degrees both in X and Y direction

Figure error	50 nm for each surface, distributed in Zernike modes 5-11 (18.9 nm per mode) This error is intended to include the low order frequency errors due to the inhomogeneity of index of refraction for lenses
Flat elements non planarity (Z4)	100nm

Table 20. Tolerances values used for elements manufacturing and alignment

These values are the result of a first allocation of values, based:

- on some considerations of what may be 'easily achievable' (e.g. uniform index of refraction, Abbe number , positioning of elements)
- on a first sensitivity analysis, mainly showing that one of the biggest offender for the WFE of the LGS alone is the error on the radius of curvature of L1 S1, that has been reduced from the standard 0.1% of the nominal value to a more strict 0.05% (but still feasible) .

4.2.2 Procedure

The procedure used in both steps is similar, and is here described stressing the differences when occurring.

Starting from the nominal design, 1000 Montecarlo files are produced:

- For step 1, introducing errors compatible with the values of Table 20, with a uniform statistic. In this way, files of 'tolerated' LGSO are produced, mounted on a 'ideal MPO'.
- For step 2 , files of step 1 have been merged with files obtained from the MPO tolerance analysis procedure:
    - 1000 files of MPO-Step1 have been randomly selected;
    - for each one errors corresponding to MPO step2 has been generated, obtaining as-built MPO nominally mounted;
    - to each one of this files has been applied one of the LGSO-Step1 subsystem, obtaining 1000 files with as-built MPO and as-built LGSO.

Note that MPO step 3 has been disregarded, given his small effect on WFE and first order parameters (e.g. F#) of MPO.

Each file of the step 2 has been re-optimized via a MATLAB- ZOS-API procedure, aiming to:

- Align the LGSO with the chief-ray of the MPO: this is done by tilting FM1 and by decentring the whole LGSO (starting from L1) as a rigid body.
- Optimize the F#: mainly due to the tolerances of MPO, the final F# of the LGSO varies. If necessary, this is done by moving L4 along its optical axis. It allows to recover the F# (and consequently an exit pupil) within the required range (see later), without introducing a sensible degradation in WFE.
- Tilt FM3 so that the chief ray results parallel to the gravity vector and the LGS WFS entrance focal plane is gravity invariant.

The obtained system is then refocused (with a Zemax quick-focus wavefront error driven routine), obtaining the best focal plane position and permitting the evaluation of all main performances parameters (WFE, Pupil Image Size, Telecentric Error and FoV Size).

The degrees of freedom used as compensators (for different merit functions) are:

- Decenter X and Y of LGSO as a whole and Tilt X and Y of FM1. to optimize WFE;
- Displacement Z of LGSO-L4: to optimize F/# and pupil size;
- Tilt X and Y of LGSO-FM3: gravity invariant exit focal plane.
- Image plane position (along optical axis): re-focusing.

4.2.3 Tolerance analysis results and requirements verification

We present here results of the procedure for Step 1 and Step 2.

We have verified the requirements for the sodium layer at 100 Km, corresponding to an azimuth angle of 30 degrees. The requirements we have verified are:

MAO-SF0-1.3.3.5.20: *The LGS asterism centroids shall be imaged by the PFRO within the annulus 45 +/- 0.5 arcsec at the LGS WFS entrance focal plane, assuming paraxial F/# equal to 5, for each sodium layer altitude in the working range [RD2].*

Assuming paraxial F/# equal to 5, the paraxial effective focal length is equal to 192710 mm, giving a requirement linear range of 42.043 +/- 0.467 mm.

MAO-SF0-1.3.3.5.23: *The image of the pupil in the LGS WFS channels shall have a diameter variation, due to as-built PFRO, within +/- 1/2 of the pupil sub-apertures size for the LGS 45 arcsec asterism and for each sodium layer altitude in the working range [RD2].*

MAO-SF0-1.3.3.5.22: *The telecentricity error induced by PFRO shall be within +/-1/20 pupil sub-apertures size, averaging opposite pupil edges positions, for the LGS 45 arcsec asterism and for each sodium layer altitude in the working range [RD2].*

MAO-SF0-1.2.4.2: The WFE (tilt and defocus corrected) delivered by the as-built PFRO shall be below 300 nm RMS for the LGS 45 arcsec asterism *[RD2].*

4.2.3.1 Step 1: LGSO in 'Stand-Alone Configuration'

4.2.3.1.1 FOV Size

The requirement MAO-SF0-1.3.3.5.20 of a 45 +/- 0.5 arcsec would translate (assuming a paraxial F#=5) in a requirement of linear FOV size of 42.043 +/- 0.467 mm. Figure 94 shows the FoV linear size of the 1000 MC files as function of the azimuthal angle. It demonstrates that for each MC realization, the FOV size satisfies the requirement: green lines mark the allowed range. Values are centred on the nominal value of about 40.25 mm and the variation range is about +/-0.15 mm.

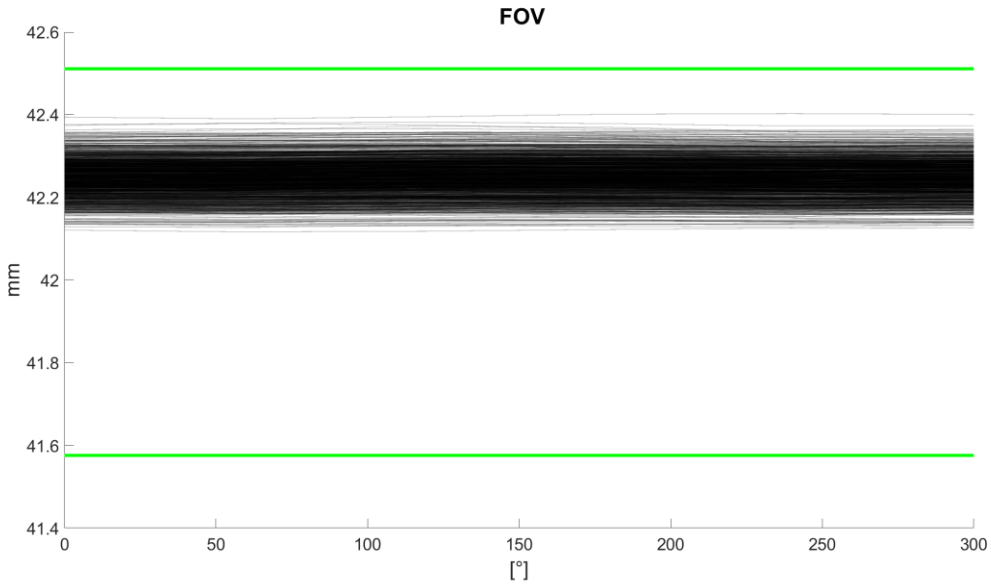

Figure 94. FoV size of the 1000 MC files as function of the azimuthal angle.

4.2.3.1.2 Pupil Image Size

Requirement on the size of the image pupil size delivered by as-built LGSO (MAO-SF0-1.3.3.5.23) foresees an acceptable variation of the diameter of +/- 0.5 sub-aperture, corresponding to 0.74% of the pupil size (given the number of sub-apertures, 68 as prescribed by MAO-SF0-1.3.3.5.). Figure 95 shows that for the 1000MC realization of the LGSO as stand-alone, the pupil size is always in the allowed range, marked by the green lines.

Note that the result is obtained without displacement of L4, that as would allow in case to recover an acceptable F# and, as consequence, a pupil image size in the allowed ranges.

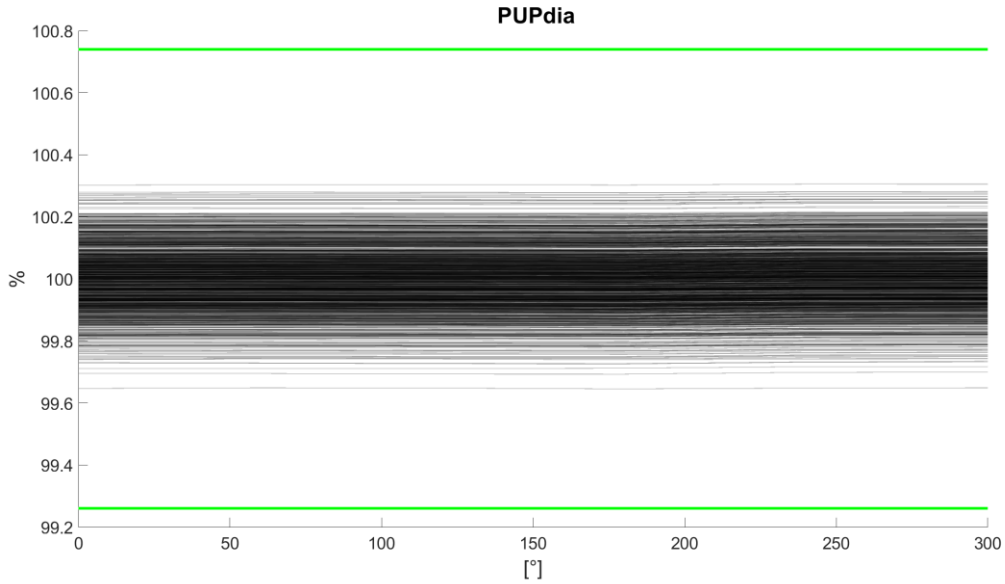

Figure 95. Pupil size of the 1000 MC files as function of the azimuthal angle.

4.2.3.1.3 Telecentricity Error

Telecentricity error has been defined in 3.2.6 and requirement MAO-SF0-1.3.3.5.22 regulates the allowed range, limiting it to 1/20 of the sub-aperture. Assuming apertures (MAO-SF0-1.3.3.5), it corresponds to 0.074% of the pupil size. In Figure 96, the telecentric error as function of the azimuthal angle for the 1000MC is plotted, showing values always in the allowed range.

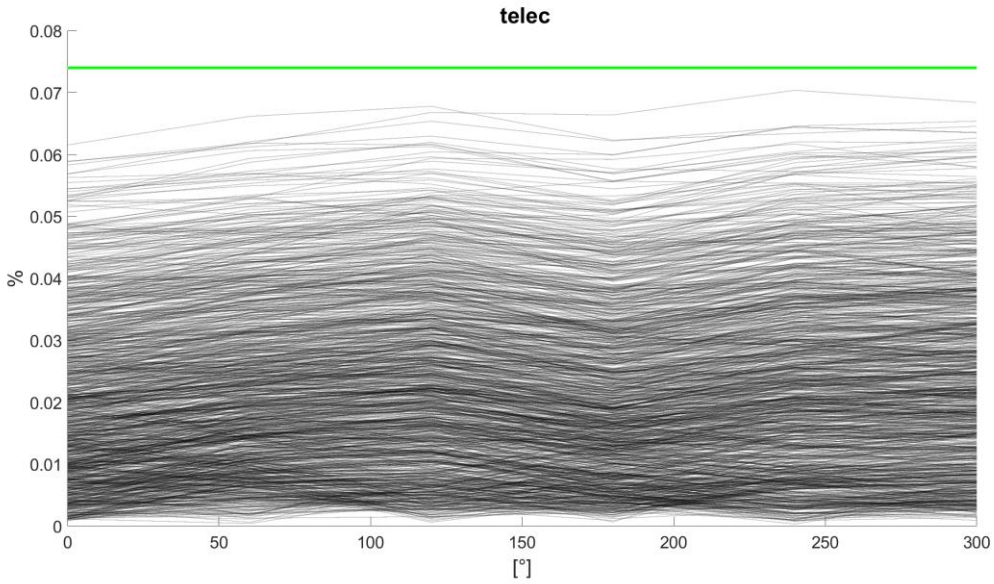

Figure 96. Telecentricity error of the 1000 MC files as function of the azimuthal angle.

We have also computed the chief ray angle at the exit focal plane as function of the of the azimuth angle. Results are shown in Figure 97.

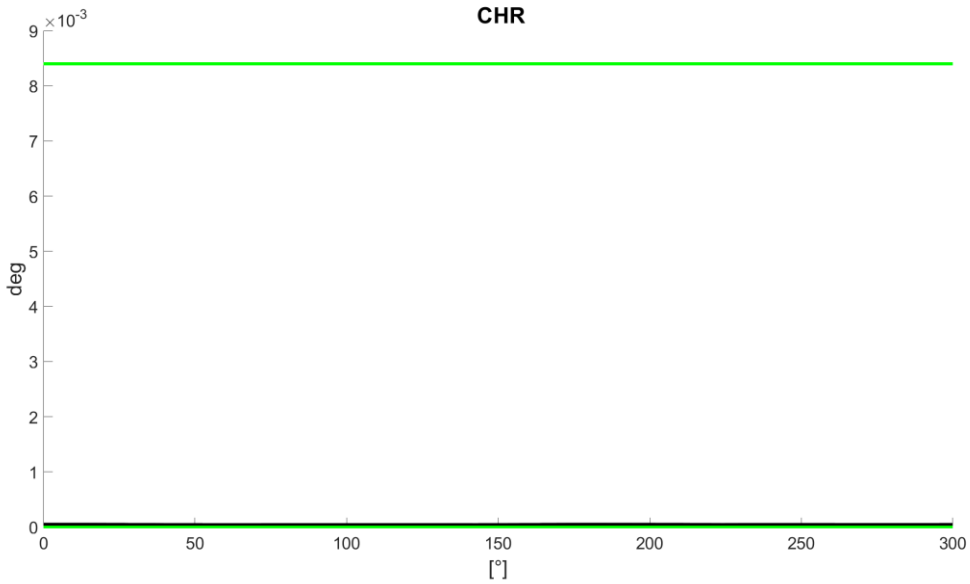

Figure 97. Chief ray angle at the exit focal plane of the 1000 MC files as function of the azimuthal angle.

4.2.3.1.4 Wavefront Error

The WFE of the as-built LGSO (MAO-SF0-1.2.4.2) has to be below 300 nm (tilt and defocus removed).

Figure 98 shows the values of WFE (Tilt and Focus Removed) for the 1000 MC. Values are always smaller than 300 nm (about 0.5 waves for the LGS wavelength) and only marginally larger than 200 nm (0.35 waves).

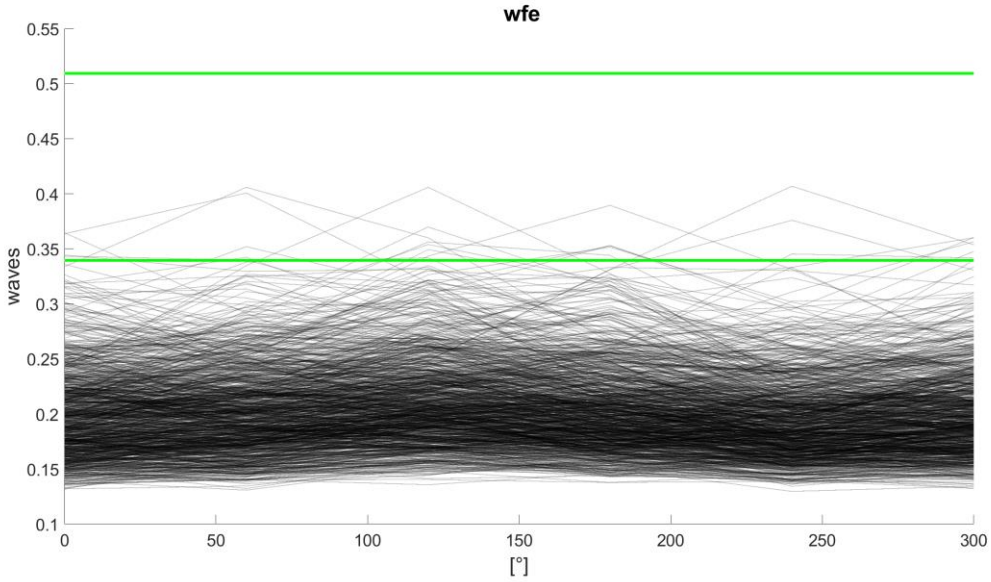

Figure 98. WFE of the 1000 MC files as function of the azimuthal angle.

4.2.3.2 Step 2: LGSO mated with MPO

The 1000 MC occurrences of Step2 capture the configuration of as-built LGSO aligned with as-built MPO. Consequently, the performances here presented are those that have to be ultimately compared with the requirements.

4.2.3.2.1 FOV Size

For the FOV size, consideration done in 3.2.5 and 4.2.3.1.1 are still valid. In Figure 99 the FOV sizes of the 1000 MC realization is plotted, showing a small non-conformity to MAO-SF0-1.3.3.5.20 for a few occurrences.

As already stated in 3.2.5, this discrepancy can be compensated during the integration of the LGS WFS channels. Alternatively, the same optimization of the F/# (pupil size), exploiting L4 displacement, can be used to recover the non-conformity.

In Figure 100 average and standard deviation of the FOV size is presented: it shows that the only few occurrences have a mean value out of allowed range (<42.51 mm), and that the field is anyway always circular (values along the filed azimuthal angle present a maximum standard deviation of 10 micrometers).

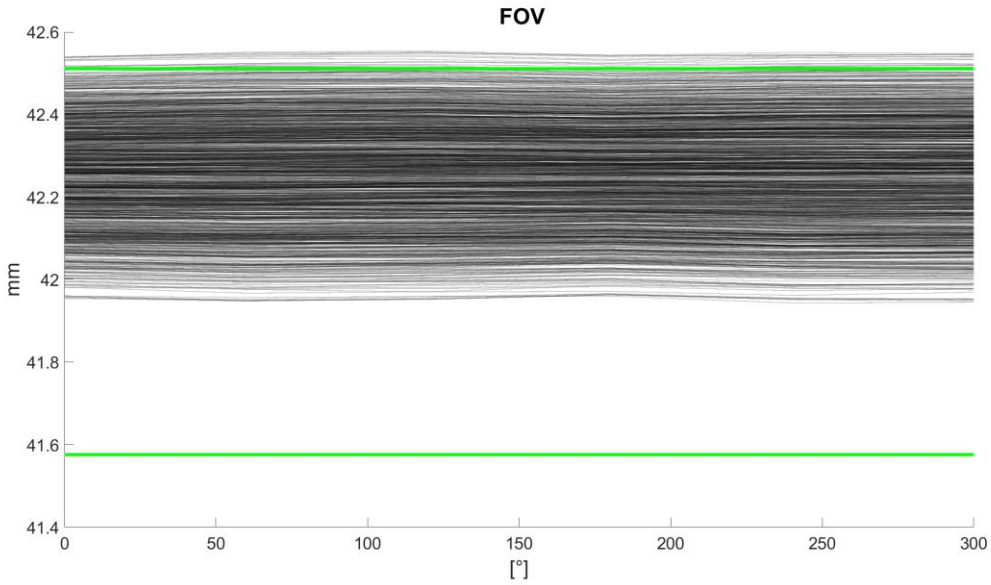

Figure 99. FoV size of the 1000 MC files as function of the azimuthal angle for as-built MPO+LGSO.

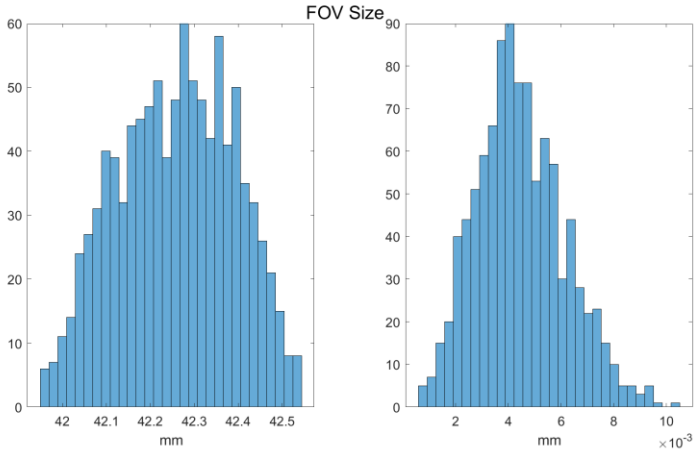

Figure 100. Average and standard deviation of the FoV size of the 1000 MC files for as-built MPO+LGSO.

4.2.3.2.2 Pupil Image Size

Pupil Image Size variation is presented in Figure 101. Thanks to the re-optimization acting on LGSO-L4 displacement along the optical axis, the pupil size remains inside the allowed range (0.7%, corresponding to 0.5 a sub-aperture).

Note that only in few cases it has been necessary to act on LGSO-L4 movement, and, anyway, it is limited to few mm and well inside the adjustment capabilities. Figure 102 shows the position of LGSO-L4 as function of MC realization number, showing that less that 10 (<0.1%) realizations required moving the lens, and never more than 3mm.

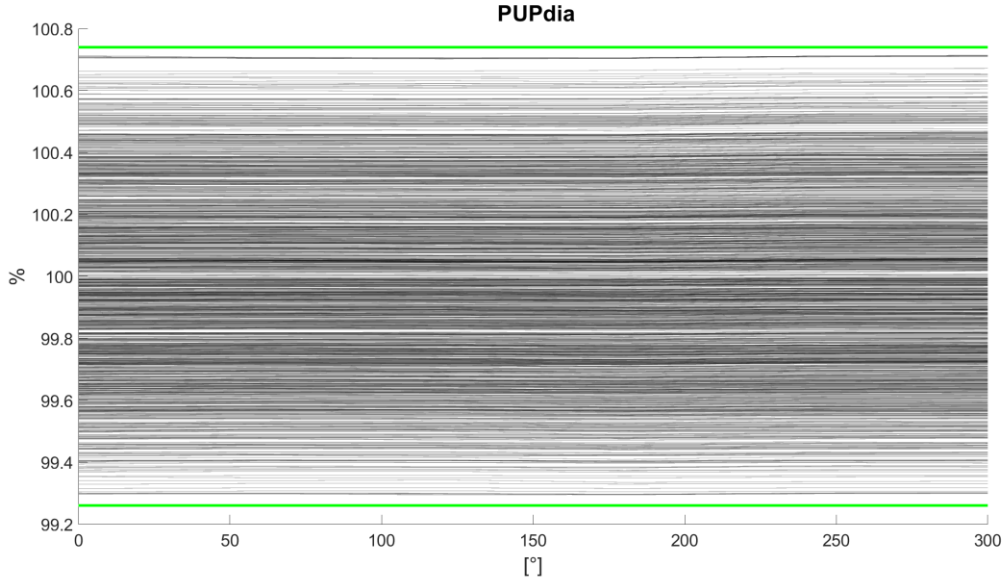

Figure 101. Pupil size of the 1000 MC files as function of the azimuthal angle for as-built MPO+LGSO.

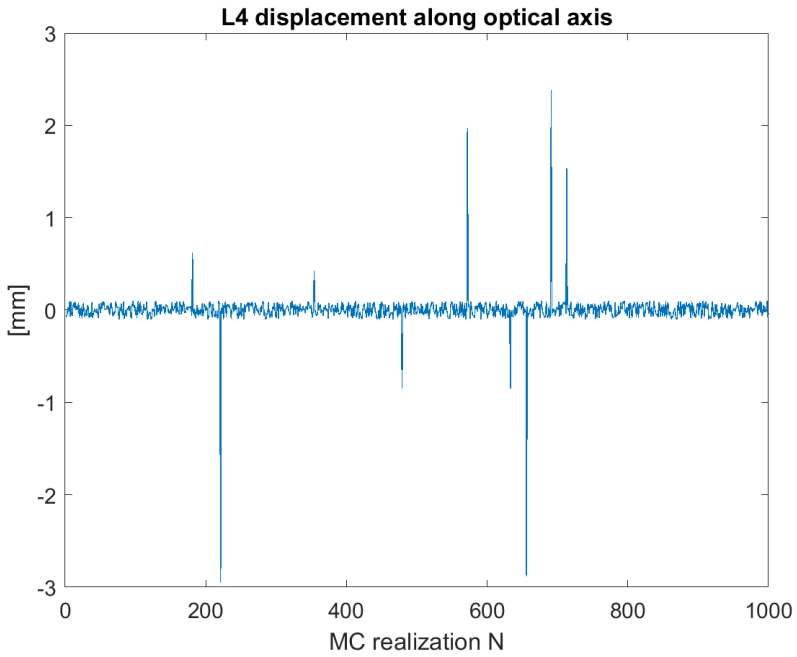

Figure 102. LGSO-L4 displacement along optical axis for pupil size compensation of the 1000 MC files for as-built MPO+LGSO.

As for the FOV size, the pupil average dimension varies (due to the variation of the F/# of the system), while the shape remains circular, given the small value of the standard deviation (see Figure 103).

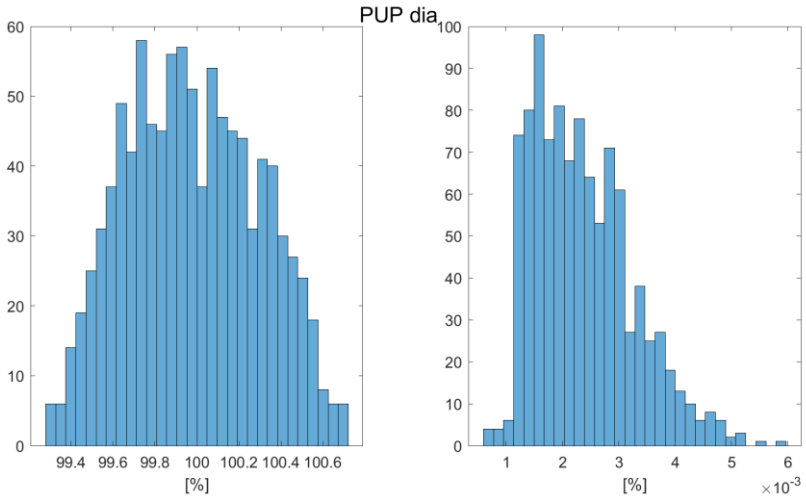

Figure 103. Average and standard deviation of the pupil size percentage variation of the 1000 MC files for as-built MPO+LGSO.

4.2.3.2.3 Telecentricity Error

The telecentricity error of the 1000 MC occurrences of step 2 is shown in Figure 104. The results are larger with respect to the range specified by the requirement (+/-1/20 sub-aperture) by about a factor 3.5 in the worst case.

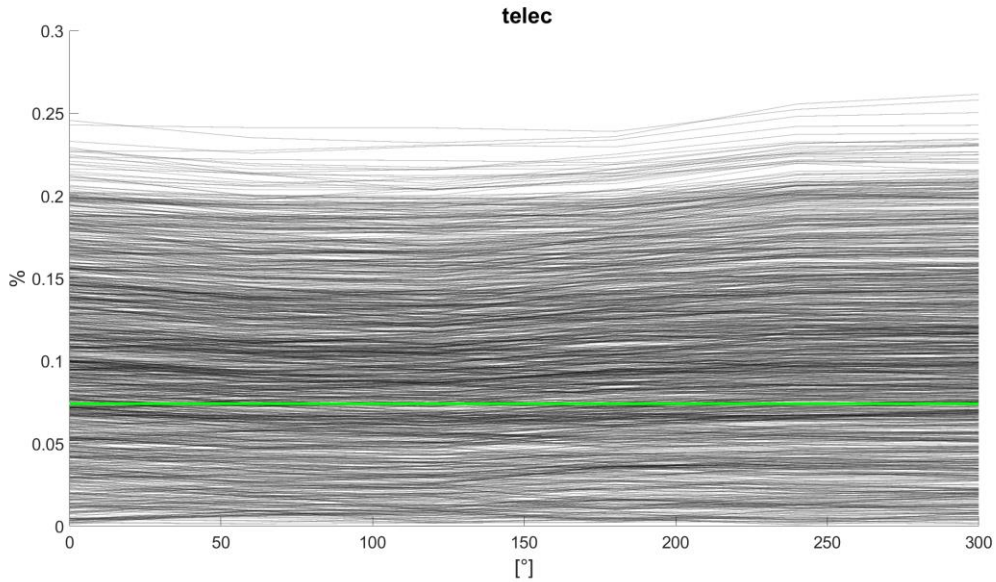

Figure 104. Telecentricity error of the 1000 MC files as function of the azimuthal angle for as-built MPO+LGSO.

The average and the standard deviation of the telecentricity error over the azimuthal angle are shown in Figure 105.

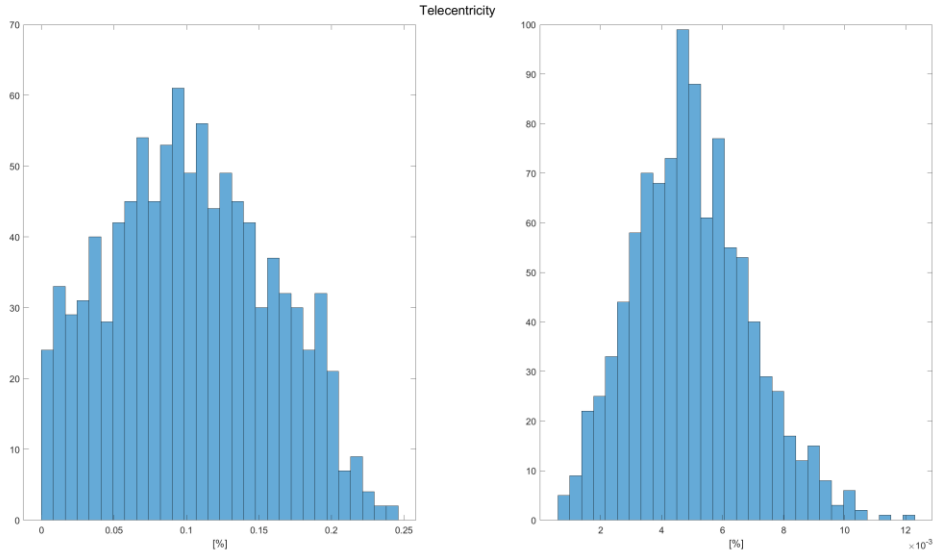

Figure 105. Average and standard deviation of the telecentricity error of the 1000 MC files for as-built MPO+LGSO.

We have also computed the chief ray angle at the exit focal plane as function of the of the azimuth angle. Results are shown in Figure 106.

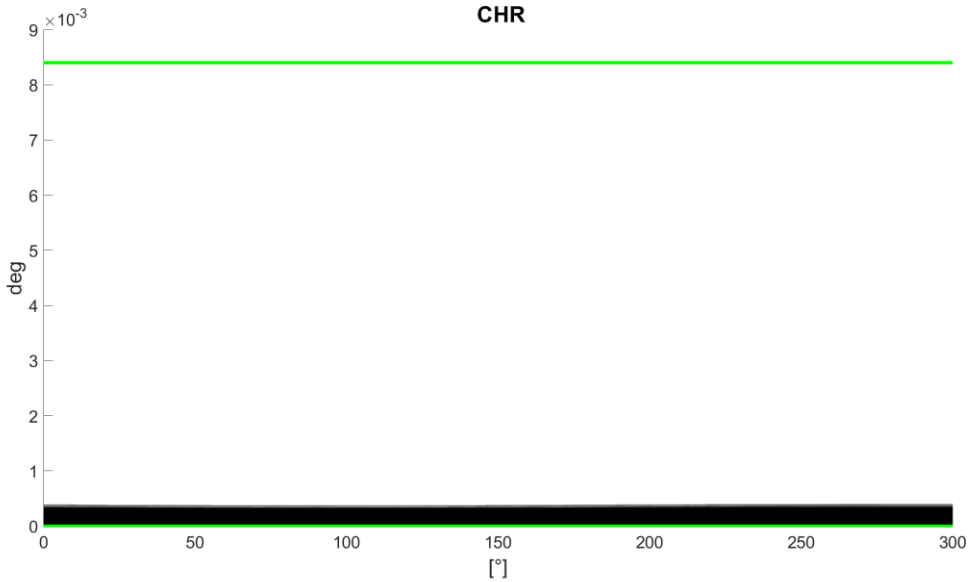

Figure 106. Chief ray angle at the exit focal plane of the 1000 MC files as function of the azimuthal angle for as-built MPO+LGSO.

Looking to the chief rays angles distribution, the exit pupil is basically at infinite distance. However, considering the computation based on the marginal rays angles (i.e. accounting the asymmetry on the pupil shape) we experienced a discrepancy by about a factor 3.5 in the worst case. Such discrepancy has been considered acceptable by the consortium at this working level. It will be addressed together with the requirement in the next phase.

4.2.3.2.4 Wavefront Error

The WFE of the 1000 MC occurrences of step 2 is shown in Figure 107. The 99% of the MC population have a WFE below 300 nm (tilt and defocus removed), corresponding to about 0.5 waves for the LGS wavelength. The average and the standard deviation of the WFE over the azimuthal angle are shown in Figure 108.

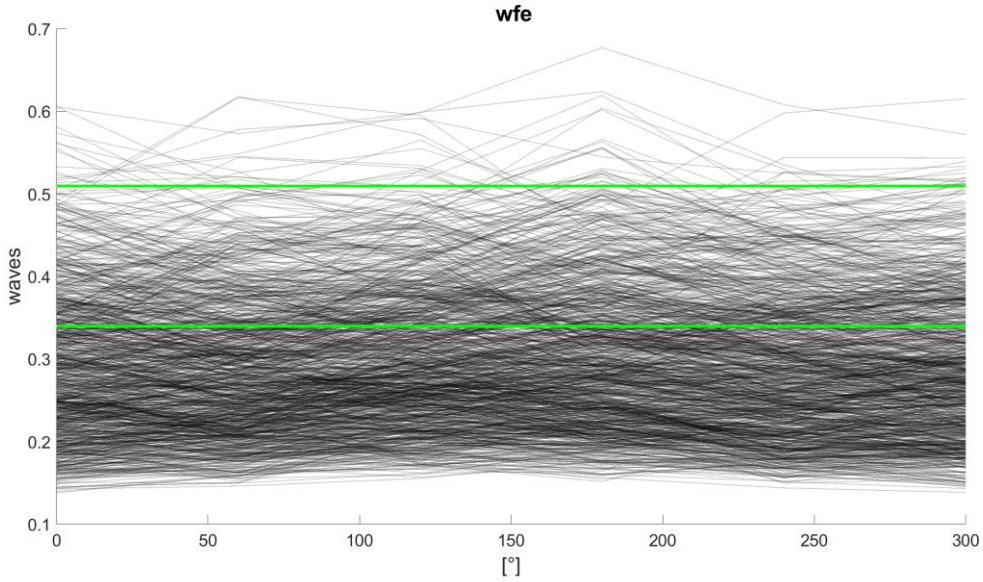

Figure 107. WFE of the 1000 MC files as function of the azimuthal angle for as-built MPO+LGSO.

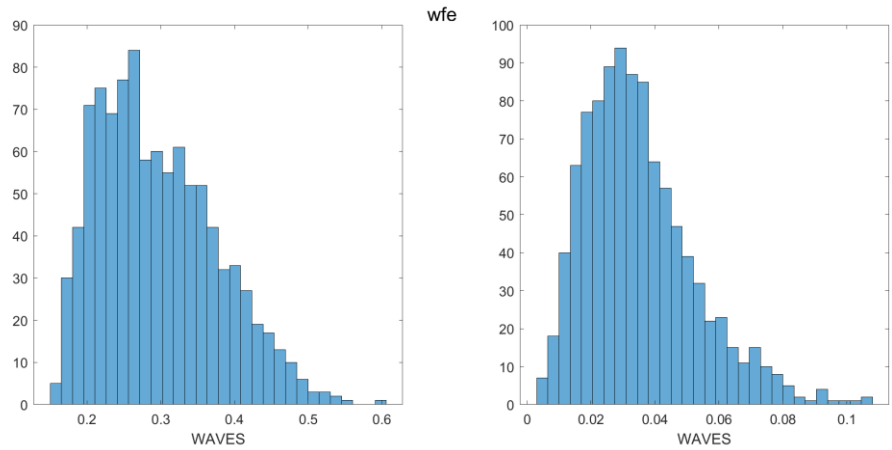

Figure 108. Average and standard deviation of the WFE of the 1000 MC files for as-built MPO+LGSO.

4.2.3.3 Elements positions

We have estimated the positional parameters of the as-built LGSO after the integration on the as-built MPO in order to check:

- LGSO fits in the allocated space envelope
- The element mounts foreseen a sufficient range of movement
- The adjusting range of the I/F with the LGS WFS Module are sufficient.

The results are reported from Figure 109 to Figure 113.

For the alignment degrees of freedom, we have that:

- Whole LGSO displacement along local X and Y axis (LGSO-L1), used to align the LGSO with the chief ray exiting from the MPO; the full range is +/-1.5 mm.
- LGSO-FM1 tilt used to align LGSO with the chief ray exiting from the MPO. It requires a range of movement of about +/-0.06 degrees around local X axis and +/-0.02 degrees around local Y axis.
- LGSO-FM3 tilt used to adjust the pupil position above the LGS WFS module. It needs a range of regulation of about +/- 0.008 degrees around local X axis and of about +/- 0.012 degrees around local Y axis.
- LGSO-L4 displacement along local Z used to adjust the pupil size. It needs a regulation of +/- 3 mm.

We have verified that the degrees of freedom ranges are well within the available capabilities of the foreseen adjustments.

For the available space envelope, we have that:

- LGSO-FM2 position: this mirror position is varying because of the displacement of whole LGSO and because of their own positioning error in the stand-alone LGSO. It represents the most critical optics position for the space envelope. Their center moves in a volume having the size:
    - LGSO-FM2: X: +/-2.5 mm, Y: +/-0.5 mm, Z: +/-2.0 mm

We have verified that the LGSO is within the assigned space envelope.

For the I/F with the LGS WFS Module, we have that:

- Focal plane position: It translates in the X and Y global coordinate because of LGSO movements; it varies in Z (focus direction) due to the manufacturing alignment errors of all elements of MPO and LGSO. The ranges are:
    - X: +/-2 mm, Y: +/-2mm, Z: +/-10 mm.

We have verified that the required range is within the adjustment range of the LGS WFS module.

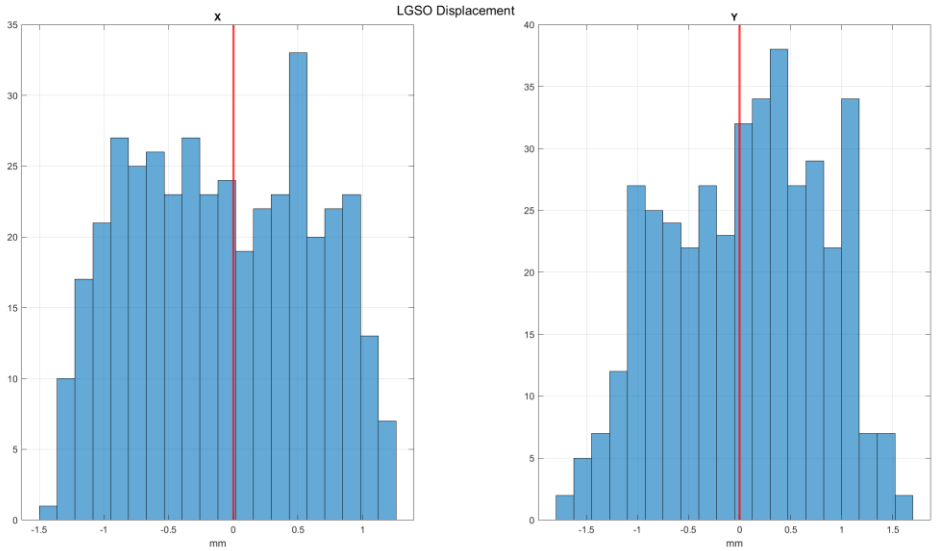

Figure 109. Whole LGSO displacement in X and Y direction.

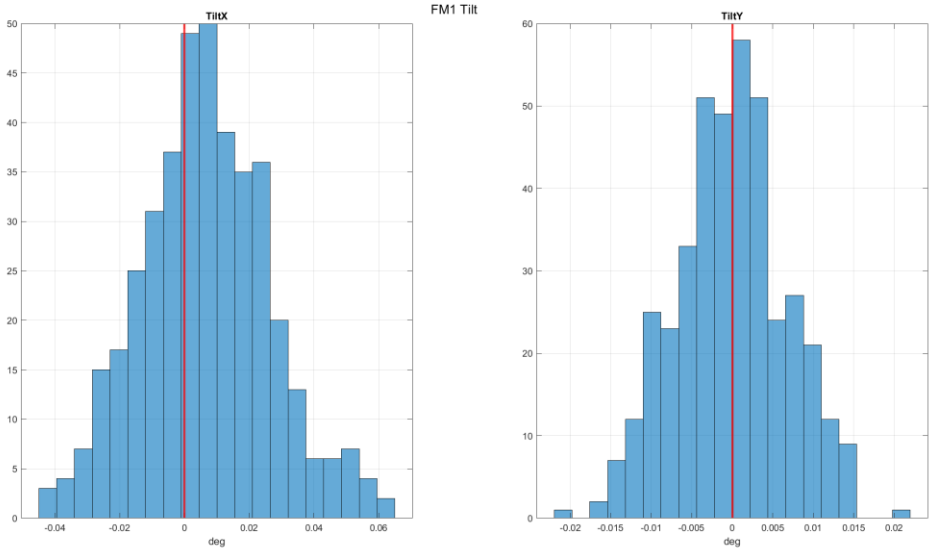

Figure 110. LGSO-FM1 tilt in X and Y direction.

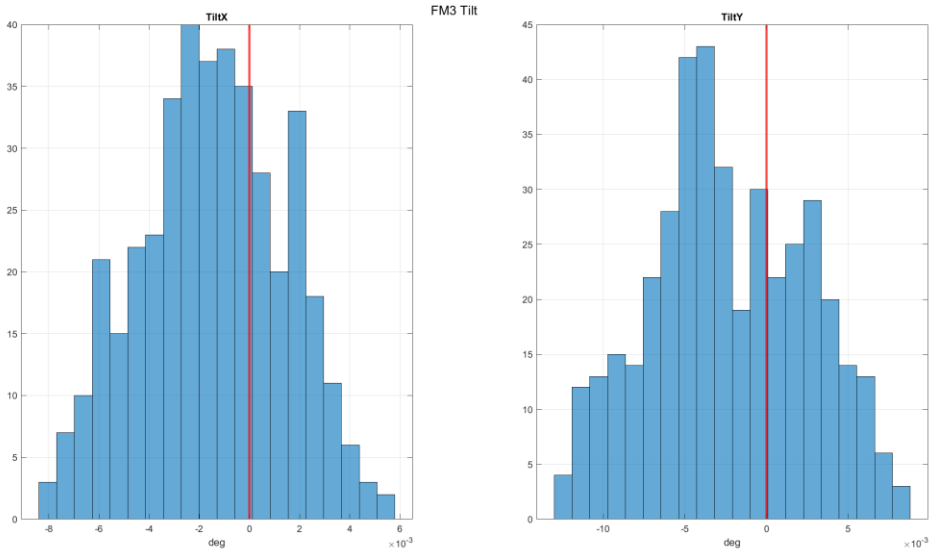

Figure 111. LGSO-FM3 tilt in X and Y direction.

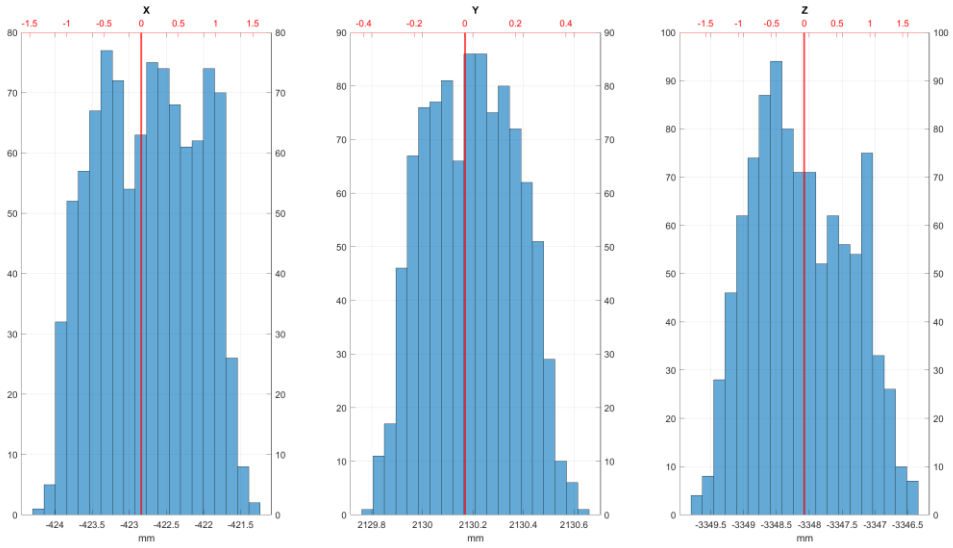

Figure 112. LGSO-FM2 absolute position (MAORY reference system) in X, Y and Z.

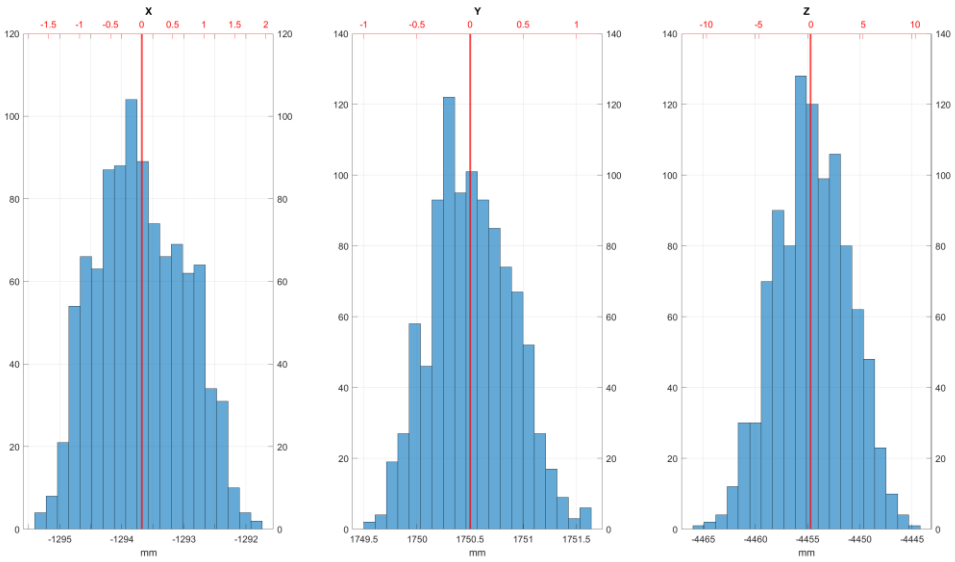

Figure 113. Exit focal plane absolute position (MAORY reference system) in X, Y and Z.

5. Stability analysis

The stability of MAORY is intended here as the ensemble of all the dynamical contributors. At this working level, we have considered:

- The rigid body motion between MAORY and ELT
- MAORY and Nasmyth-induced thermos-elastic deformation
- Optics surface thermo-elastic deformation induced by mounts thermal loads

For each case, we have evaluated the impacts on the MAORY performance on output focal plane and the capability to recover the variation through MAORY collimation (i.e. acting on M10M, M11M and M12M).

MAORY collimation implies to act on M10M (piston dz, tilt x, tilt y in local coordinates system), M11M (tilt x, tilt y in local coordinates system) and M12M (tilt x, tilt y in local coordinates system). It uses as feedback five reference sources at the edge of the MICADO fields and the exit pupil position. MAORY is re-optimizes for WFE in terms of defocus (Z4) and astigmatisms (Z5, Z6), for focal plane position and exit pupil position.

The analysis has been limited to the main path. The impacts on LGSO will be analysed in the next phase.

5.1 Rigid body motion between MAORY and ELT

The rigid body motion between MAORY (Nasmyth, straight through focal plane) and ELT (PFS exit focal plane) is described in I-INS/ELT-257 [RD1]. It represents the combined rigid body motion between the instrument attachment points and the ELT exit focal plane. The maximum motions under operational conditions (thermal expansion subtracted) in the MAORY reference system are given in Table 21:

	displacement	**unit**
dx	1.5	mm
dy	1.5	mm
dz	1.5	mm
tx	0.05	Mrad
ty	0.05	Mrad
tz	0.05	Mrad

Table 21. Maximum motions between MAORY and ELT under operational conditions (thermal expansion subtracted) in the Azimuth reference system.

We have agreed with ESO that the pivot center coordinates for the rotations has to be intended as the barycentre of the instrument attachment points. For MAORY, it corresponds to -2050, -1500, -6000 mm in the MAORY reference system (corresponding to -29250, -1500, -6000 mm in the Azimuth reference system).

The simulation has been done on the nominal optical configuration. We displaced the whole instrument mounted on the bench, i.e., from the entrance CPM to M11M.

M12M, being mounted on MICADO, is subjected to its movements and has been considered fixed in this simulation, i.e. fixed with respect to the entrance focal plane. This assumption is a sort of worst case. No information on MICADO displacement is available at the time being.

For each displacement, we have computed the motions of the central field centroid (pointing) on the MAORY exit focal plane in the MAORY absolute reference system. Results are reported in Table 22.

CASE	MAORY displacements	Centroid displacement (mm)			
		dx	Dy	dz	module
1	1.5 mm dx	1.436	-0.209	-1.879	2.374
2	-1.5 mm dx	-1.436	0.209	1.879	2.374
3	1.5 mm dy	-1.451	1.656	-1.243	2.528
4	-1.5 mm dy	1.451	-1.656	1.243	2.528
5	1.5 mm dz	-1.221	-2.485	-0.750	2.868
6	-1.5 mm dz	1.221	2.485	0.749	2.868
7	0.05 mrad tx	0.141	-0.869	0.105	0.887
8	-0.05 mrad tx	-0.141	0.869	-0.105	0.887
9	0.05 mrad ty	0.460	0.014	-0.414	0.619
10	-0.05 mrad ty	-0.460	-0.014	0.414	0.619
11	0.05 mrad tz	-0.555	0.119	0.211	0.606
12	-0.05 mrad tz	0.555	-0.119	-0.211	0.606

Table 22. Central field centroid coordinates on the exit focal plane due to rigid body motion.

The movement of the central field centroid position variation (i.e. pointing) in the local reference system and the pupil position variation are shown in Figure 114.

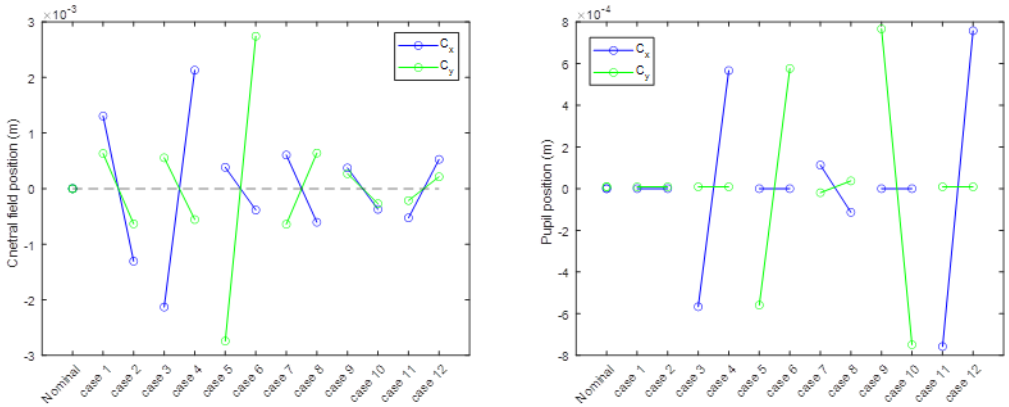

Figure 114. Position of the central field on the exit focal plane, in the local coordinate system (left) and pupil position (right) in the different cases.

A maximum pupil shift of 0.8 mm is observed, corresponding to about 0.1% of the pupil size. The footprint size on the optics does not change sensibly. The footprint has a maximum shift of 1.5 mm on M11M and 3 mm on M12M.

We have evaluated the displacements impacts on the WFE. Results are shown in Figure 115. The WFE largely increases but it is basically due just to defocus. The WFE decomposition in Zernike polynomials for the central field is shown in Figure 116.

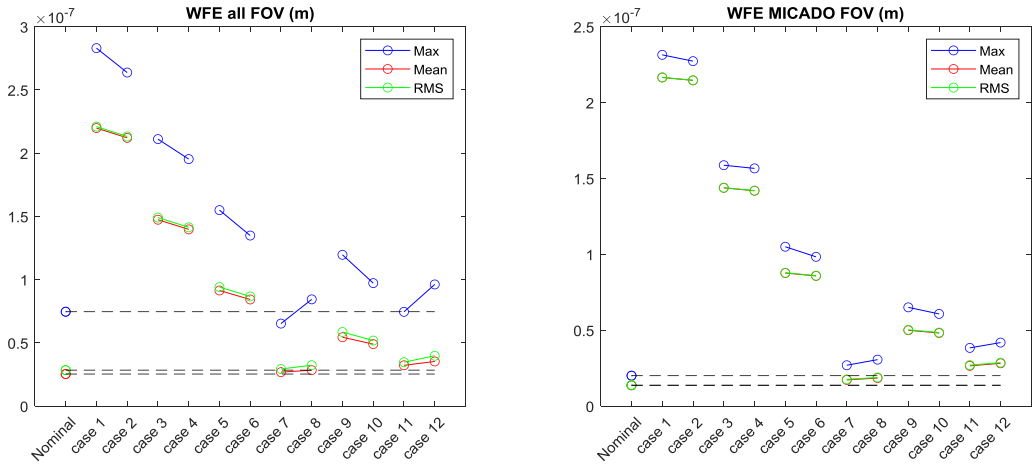

Figure 115. WFE on the full FOV (left) and MICADO FOV (right) in the different cases.

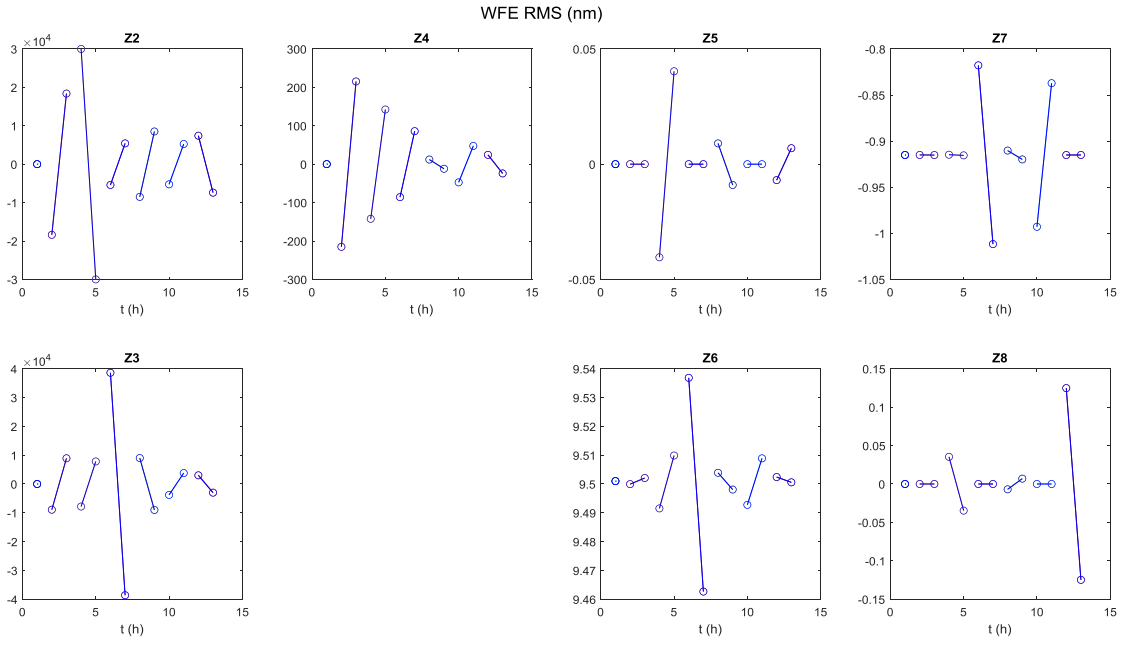

Figure 116. WFE decomposition in Zernike polynomials for the central field in the different cases.

The only term affecting the WFE is the defocus (in the range of +/- 230 nm). All higher order Zernike polynomials are negligible with respect to the nominal value.

We have verified that inter-epoch distortion variation shows negligible residuals after the subtraction up to the third order polynomial fitting with respect to the nominal distortion map as shown in Figure 117.

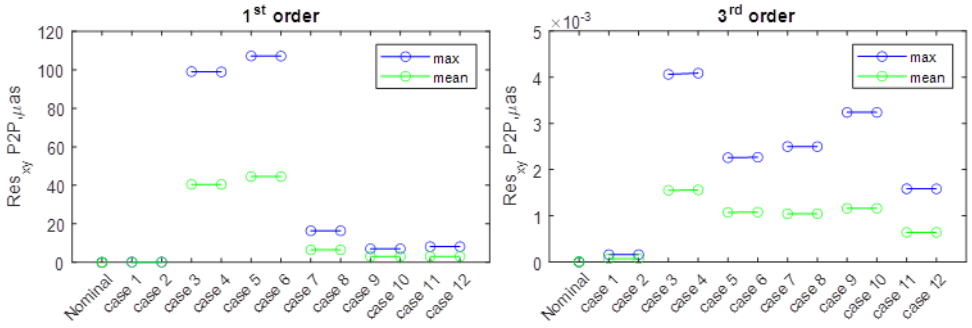

Figure 117. Inter-epoch distortion variation on MICADO FOV after first and third order polynomial fitting after MAORY collimation.

Assuming as worst case the RSS of the parameters value at the motion range edge for all the cases, we obtained the worst ranges reported in Table 23.

pointing	exit pupil displacement		Z4	Z5	Z6
[arcsec]	[mm]	[%]	[nm]	[nm]	[nm]
1,20	1,4	0,18%	277	Negligible	Negligible

Table 23. Worst case estimate of the pointing, exit pupil defocus and astigmatism variation due to rigid body motion.

For such variations, the collimation of MAORY requires to act on M10M (only in dz, tilt x and tilt y are not required since there is no need for astigmatism compensation), on M11M (tilt x, tilt y), M12M (tilt x, tilt y) and on MICADO de-rotator in order to compensate for pointing, WFE and exit pupil position over MICADO. All the performances are completely recovered after the MAORY collimation as shown in Figure 118. The required movements to compensate the rigid body motion in the local coordinate system have been computed as the RSS of the movements for all the cases. The results are given in Table 24.

	dz [mm]	tilt x [degrees]	tilt y [degrees]
M10M	0.820	N/A	N/A
M11M	N/A	0.048	0.020
M12M	N/A	0.013	0.013

Table 24. Movement ranges of the degrees of freedom for rigid body compensation.

After aligning the exit pupil, the footprint on M12M is almost nominal.

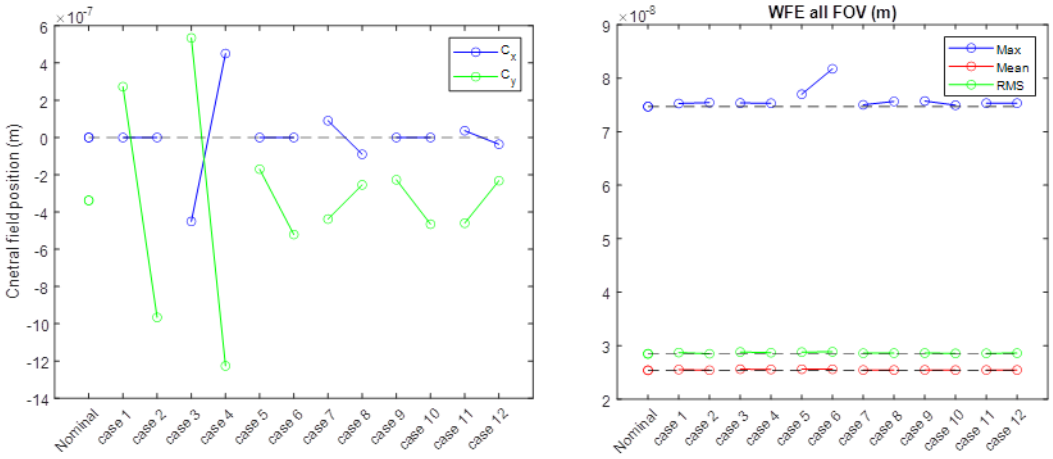

Figure 118. Position of the central field on the exit focal plane (left) and WFE on the full FOV (right) after MAORY collimation in the different cases. Dash lines refer to nominal value.

Finally, after the collimation of MAORY, we have verified that inter-epoch distortion variation shows negligible residuals after the subtraction up to the third order polynomial fitting with respect to the nominal distortion map as shown in Figure 119.

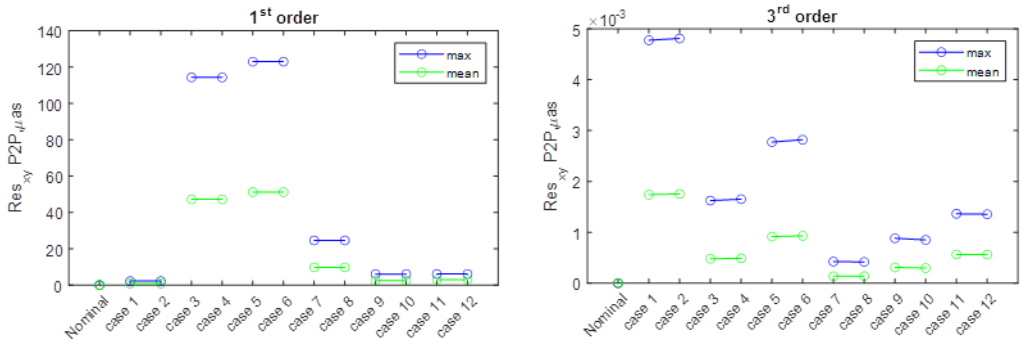

Figure 119. Inter-epoch distortion variation on MICADO FOV after first and third order polynomial fitting after MAORY collimation.

5.2 MAORY and Nasmyth-induced thermo-elastic deformation

Since the combined motion information between the Nasmyth attachment points and the entrance focal plane due to thermo-elastic deformation are not available at the time being, we have evaluated the sensitivity of the instrument under different thermal loads, applied to both MAORY and the Nasmyth platform.

We developed a combined Ansys-Matlab-Zemax model. The load cases were applied in Ansys to the MAORY structure (reported in Figure 120), and displacements and rotations of the single optical elements were calculated in the local reference system using the deformations of the connection points to the optics mounts.

The obtained values were processed with a Matlab script and automatically inserted into the Zemax model to perform the optical analysis, including optimizations. We report hereafter the main conclusions of the sensitivity analysis, focusing on the optical

performances. The detailed description of the thermo-elastic model and analysis is included in [RD12].

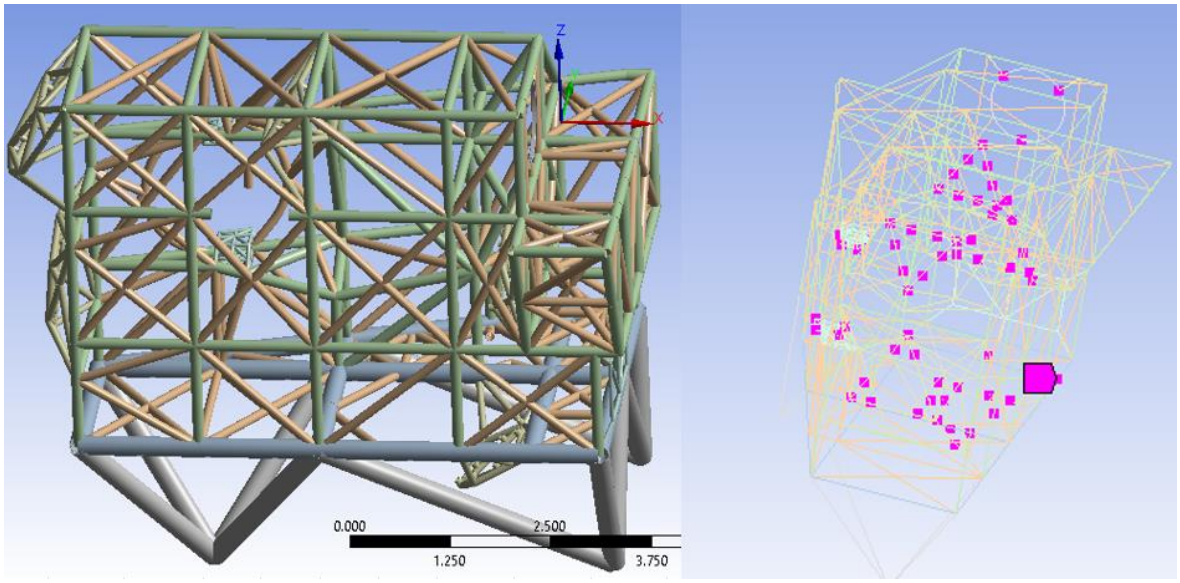

Figure 120. Beam model used for the sensitivity analysis (left). Nodes used to evalaute dispacements and rotations of the optical elements (right).

We have considered different scenarios:

- homogeneous temperature variation of both MAORY and the Nasmyth (+1/+2/+3 K); MAORY is hinged to the Nasmyth;
- homogeneous temperature variation of MAORY (+1/+2/+3 K) with the Nasmyth at the original temperature; MAORY is hinged to the Nasmyth;
- homogeneous temperature variation of the Nasmyth (+1/+2/+3 K) with MAORY at the original temperature; MAORY is hinged to the Nasmyth;
- gradients in the X, Y and Z directions (0.25K/m) on the MAORY structure with the Nasmyth platform kinematically connected to the structure feet (in order to decouple the Nasmyth effect and to highlight the effect on MAORY).

The studied cases are summarized in Table 25. Two examples of the deformations induced on MAORY are shown in Figure 121.

Also in this simulation, we have assumed a M12M fixed over MICADO.

	DT [K] Nasmyth	**DT [K] MAORY**
Case 1	1	1
Case 2	2	2
Case 3	3	3
Case 4	0	1
Case 5	0	2
Case 6	0	3
Case 7	1	0
Case 8	2	0
Case 9	3	0
Case 10	-	0.25 deg/m X

Case 11	-	0.25 deg/m Y
Case 12	-	0.25 deg/m Z

Table 25. Thermal scenarios for the sensitivity analysis.

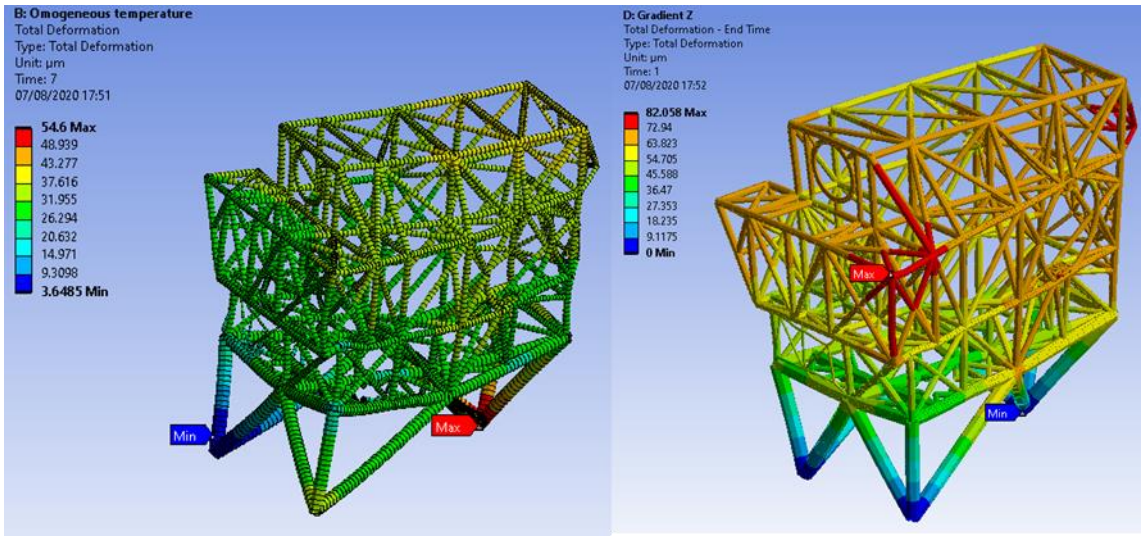

Figure 121. Deformation examples of the thermoelastic analyses: case 7 (left) and case 12 (right).

For each case, we have evaluated the effects on the WFE (and Zernike polynomials), on the pointing (expressed as position of the central field centroid on the exit focal plane), on the exit pupil displacement and inter-epoch distortion variation. Results are shown in Figure 122, Figure 123, Figure 124 and Figure 125.

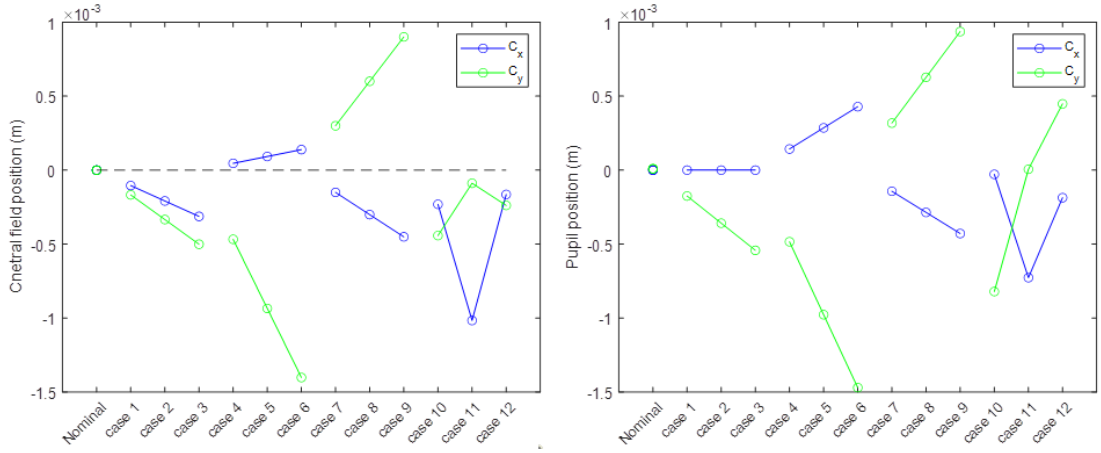

Figure 122. Central field position on the MAORY exit focal plane (left) and exit pupil position for the different study cases.

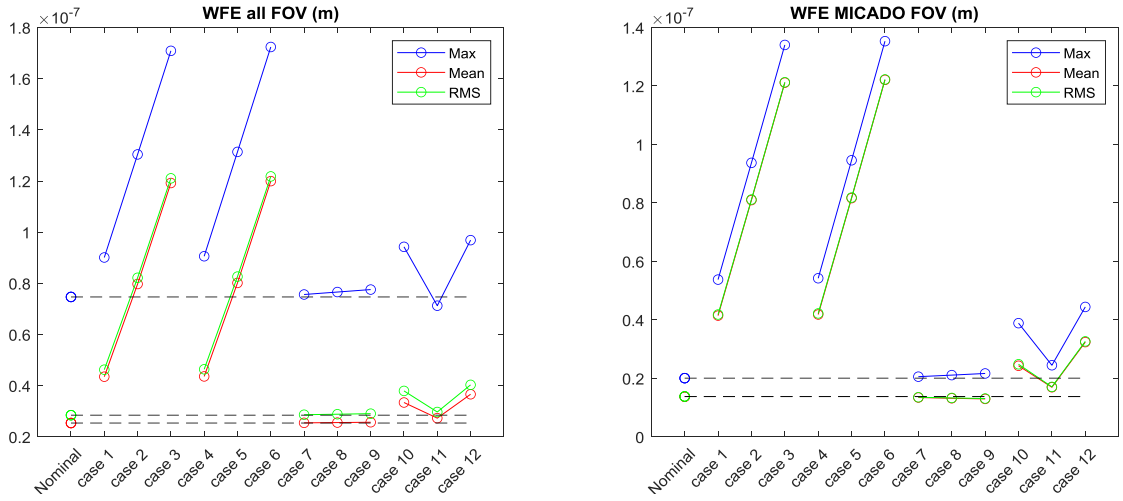

Figure 123. WFE on the full FOV (left) and MICADO FOV (right) in the different cases.

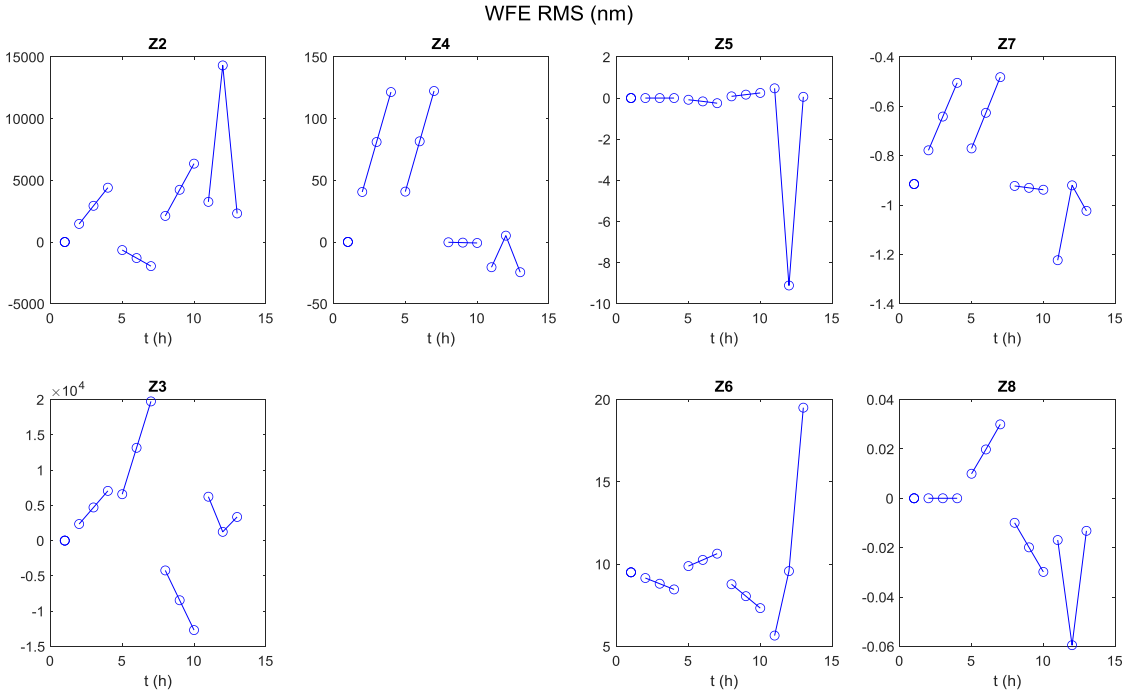

Figure 124. WFE decomposition in Zernike polynomials for the central field in the different cases.

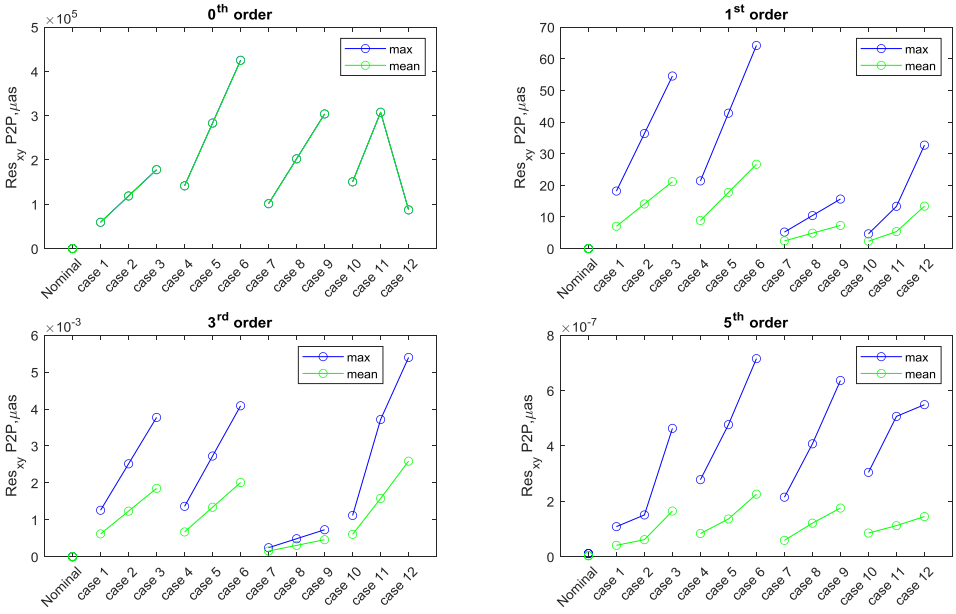

Figure 125. Modulus of the distortion residuals on the MICADO FOV after applying no correction, a 1st order polynomial fit correction, a 3rd order polynomial fit correction, and a 5th order polynomials fit correction between the different thermal load cases and the nominal condition (reference distortion map).

For uniform temperature variation (cases 1-9), the pointing and the pupil displacement have a linear dependency with the temperature variation amplitude, as well as the WFE. When only the Nasmyth temperature varies (cases 7-9), the impact on WFE is almost negligible. This is because the three legs compensate the deformation and the net effect is a rigid body motion. The cases when both temperatures vary (1-3) and only MAORY temperature varies (4-5) have almost the same behaviour in terms of WFE, with large defocus and negligible astigmatism.

For temperature gradients (cases 10-12), pointing, pupil displacement and WFE varies. For gradient along the Y (case 11), i.e. perpendicular to the plane along which almost all opto-mechanics are positioned, the WFE is almost all astigmatism. For the temperature gradients along X (case 10) and along Z (case12), the WFE presents both defocus and astigmatism.

The inter-epoch distortion variation with respect to the nominal condition show negligible residuals after the subtraction of the third order polynomial in all the cases.

The summary of the results is reported in Table 26.

Uniform temperature variation							
		pointing	exit pupil displacement		Z4	Z5	Z6
		[arcsec/K]	[mm/K]	[%D/K]	[nm/K]	[nm/K]	[nm/K]
MAORY-Nasmyth	case 1	0,06	0,17	0,02%	40,6	0,0	-0,3
MAORY	case 4	0,14	0,50	0,06%	40,9	-0,1	0,4
Nasmyth	case 7	0,10	0,35	0,04%	-0,2	0,1	-0,7

Gradient temperature 0.25K/m							
		pointing	exit pupil displacement		Z4	Z5	Z6
		[arcsec]	[mm]	[%D]	[nm]	[nm]	[nm]
gradient X	case 10	0,15	0,82	0,10%	-20,4	0,5	-3,8
gradient Y	case 11	0,31	0,73	0,09%	5,2	-9,1	0,1
gradient Z	case 12	0,09	0,49	0,06%	-24,5	0,1	10,0

Table 26. Summary of the results of the sensitivity analysis due to uniform temperature variation on MAORY and Nasmyth platform and temperature gradients on MAORY.

We have applied the collimation of MAORY acting on M10M (piston dz, tilt x and tilt y), on M11M (tilt x, tilt y), M12M (tilt x, tilt y) and on MICADO de-rotator in order to compensate for pointing, WFE and exit pupil position over MICADO. Results are shown in Figure 126 and Figure 127. All the performances are completely recovered after the MAORY collimation.

The required movements to compensate the cases in the local coordinate system are given in Table 27.

		M10			M11		M12	
		dz	tilt x	tilt y	tilt x	tilt y	tilt x	tilt y
		[mm/K]	[arcsec/K]	[arcsec/k]	[arcsec/K]	[arcsec/K]	[arcsec/K]	[arcsec/k]
MAORY-Nasmyth	case 1	0,122	-0,70	0,00	-1,81	1,22	-2,59	1,49
MAORY	case 4	0,123	-0,88	0,02	-8,67	-5,43	-7,95	-1,26
Nasmyth	case 7	0,001	-0,58	-0,02	9,24	7,93	6,71	2,65
		[mm]	[arcsec]	[arcsec]	[arcsec]	[arcsec]	[arcsec]	[arcsec]
gradient X	case 10	-0,059	0,18	-0,12	-13,56	-1,91	-12,63	2,42
gradient Y	case 11	0,017	-0,78	2,25	0,96	14,84	0,36	13,29
gradient Z	case 12	-0,071	-3,20	-0,01	2,80	7,94	9,48	2,15

Table 27. Movement of the degrees of freedom for compensation.

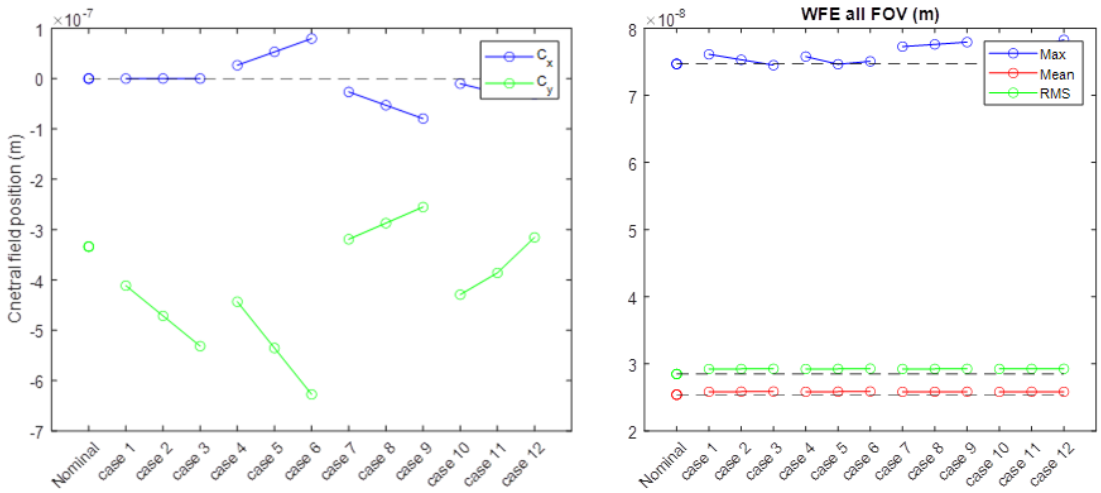

Figure 126. Position of the central field on the exit focal plane (left) and WFE on the full FOV (right) after MAORY collimation in the different cases. Dash lines refer to nominal value.

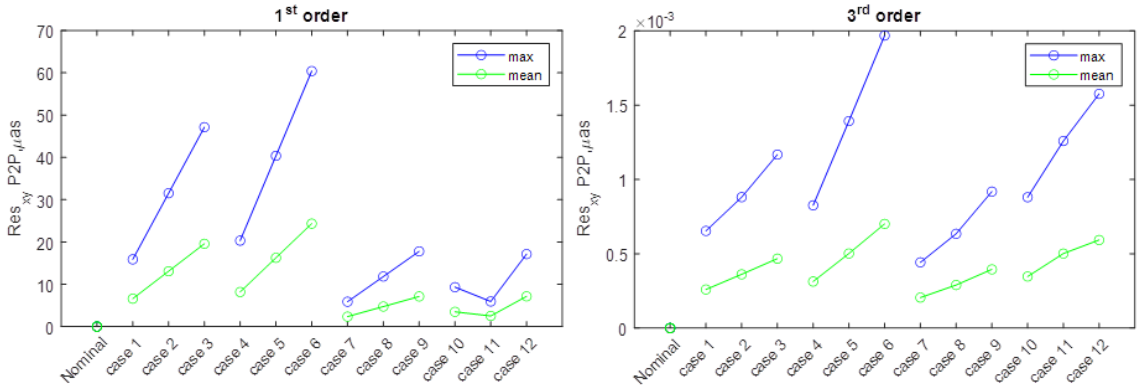

Figure 127. Inter-epoch distortion variation on MICADO FOV after first and third order polynomial fitting after MAORY collimation.

In summary, the sensitivity analysis indicates that:

- thermos-elastic movements of the Nasmyth induce pointing errors and pupil misalignment only in MAORY
- thermos-elastic movements of MAORY induce mainly pointing errors, pupil misalignment and defocus
- pointing, exit pupil position and WFE are recovered with MAORY collimation
- there is no evidence of inter-epoch distortion residuals that cannot be corrected

5.2.1 Thermal stability analysis under operational conditions

The thermal stability analysis has been performed based on a worst thermal case (three days long), applied to the baseline thermo-mechanical design of MAORY. The MAORY structure has been kinematically connected to the Nasmyth platform through three legs, so that the Nasmyth effects have been not accounted.

All the details is contained in [RD12], hereafter we present a brief description of the model and the assumptions, with the related optical results.

The temperature profile during the night-time has been obtained starting from the data in [RD14], stretching the median profile expected in Armazones to obtain a maximum negative gradient of 0.5 K/hour (Req. 542). The temperature between the first and the second night has been increased by 4 K (it includes 95% of the night-to-night variations expected at the Armazones observatory (Req. 543). The same 4 K variation has been applied also between the second night and the third night. This occurrence is extremely unlikely to happen (conservative case). The full thermal load is reasonably representing a seasonal period.

The analysis is still under development, and up to now includes a time dependent thermos-elastic analysis with the MAORY main structure, the passive panels and, as a

future development, the opto-mechanical elements. Up to now, it has been considered conduction and radiation as thermal exchange processes.

This analysis is sufficient to evaluate the thermo-elastic effects on the optical beam. For all the other effects related to the air inside MAORY and air close to optical surfaces, we postpone the discussion to next phase.

A conservative convection coefficient of 10 W/m^2K has been applied over the entire outer layer. The structure has been kinematically connected to the Nasmyth platform through its three legs. A thermal point mass of 225000 J/K has been finally connected to the aluminium plates above MICADO to simulate the supporting aluminium structure holding the panels.

The radiative contribution has been considered both towards the telescope (low emissivity paint with a coefficient of 0.1725) and between the aluminium panels (IR black paint with a coefficient of 0.9).

The temperature profile applied and the temperature distribution on the MAORY-MICADO regions are reported in Figure 128. Without a heating system, the temperature difference between the external environment and MAORY increases but, overall, the average temperatures of the components inside MAORY remain close to each other. The first twelve hours represent the night-time, while the second twelve hours represent the day-time, and so on. The temperature jump at the beginning of the night represents the telescope dome opening. MAORY is maintained at colder temperature with respect to the external air temperature in order to better match the air temperature during the night.

The deformations on the steel structure have been calculated applying the temperature distributions in a static structural analysis, and the obtained deformation imported in the Zemax model as displacement and tilt of the I/F points with the opto-mechanical assemblies. Also for this simulation, M12M has been considered fixed over MICADO.

We have computed the effects of the thermo-elastic deformation as function of the time on WFE, central field centroid position (pointing), exit pupil displacement, inter-epoch and distortion variation. The results are shown from Figure 129 to Figure 132.

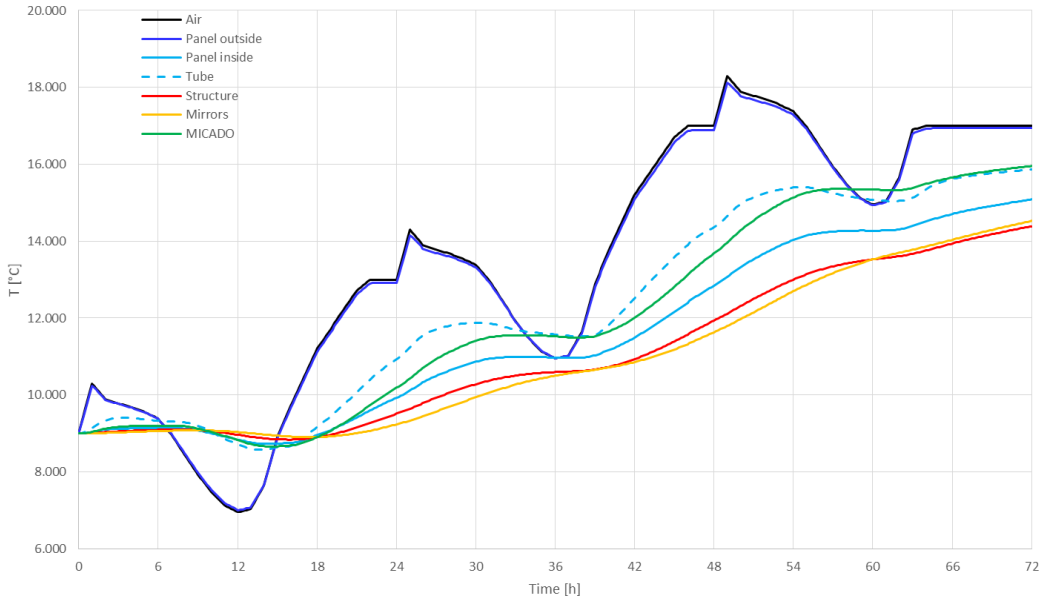

Figure 128. Temperature profile along three days: air, thermal cover (panel inside and outside), tube (connection MAORY-MICADO), MAORY structure, MAORY mirrors, and MICADO (entrance focal plane).

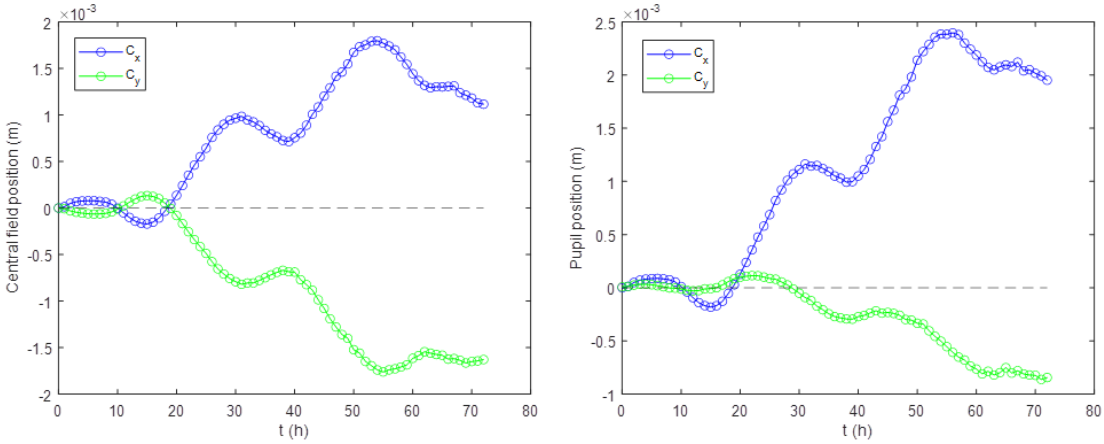

Figure 129. Central field position on the MAORY exit focal plane (left) and exit pupil position as function of time.

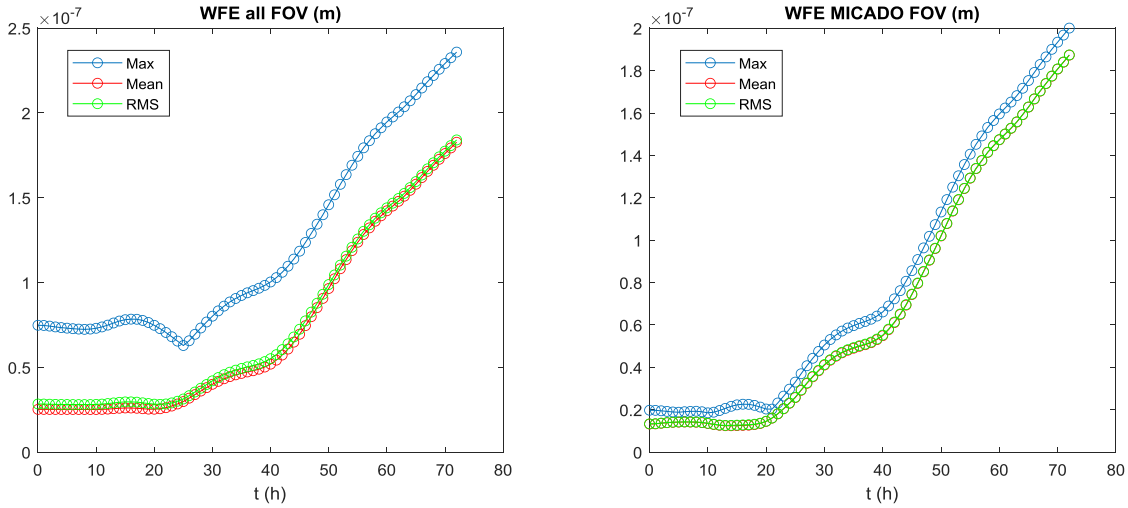

Figure 130. WFE on the full FOV (left) and MICADO FOV (right) as function of time.

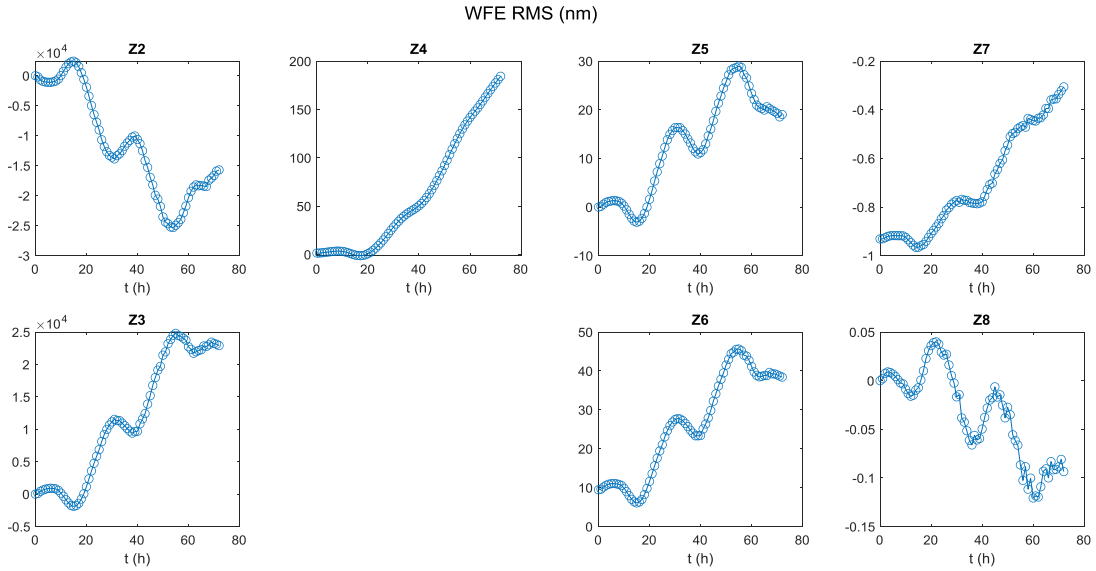

Figure 131. Decomposition of the central field WFE in Zernike Standard terms as function of time.

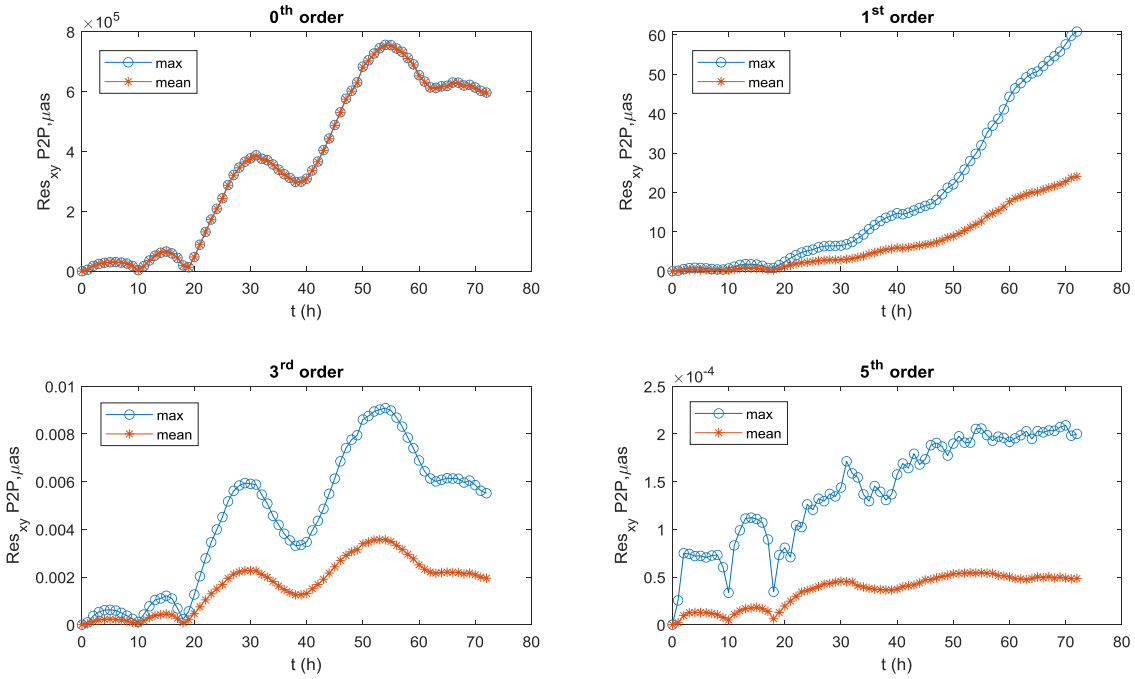

Figure 132: Inter-epoch distortion variation after polynomial fitting as function of time.

The main effects after the three days are mainly on pointing (few mm on the exit focal plane), exit pupil displacement (few mm) and on the WFE (degradation up to a maximum of 250 nm RMS on the technical FoV), due mainly to defocus and astigmatism.

In particular, the maximum variations during the second and the third night are reported in Table 28.

	pointing	exit pupil displacement		Z4	Z5	Z6
	[arcsec]	[mm]	[%D]	[nm]	[nm]	[nm]
2nd night	0,39	1,167	0,14%	43,4	16,3	18,3
3rd night	0,76	2,472	0,31%	141,8	29,0	36,2

Table 28. Pointing, pupil displacement and central field defocus and astigmatism maximum variations during the second and the third night.

The inter-epoch distortion variation performance is completely recovered after the 3rd order polynomial fitting.

In order to verify the capability of the system to recover the full performance, we have applied the MAORY collimation procedure during the third day (also during day time) every four hours. In this case the degrees of freedom are M10M (with piston, tip/tilt), M12M (with tip/tilt), and the MICADO de-rotator (clock). We optimized the fields only (Z4-Z6) on five reference stars at the edge of the MICADO FoV. We do not re-aligned the exit pupil (i.e. we do not act on M11M). However, this is always possible.

Results are given in Figure 133.

The maximum range of the degrees of freedom used for MAORY collimation is given in Table 29.

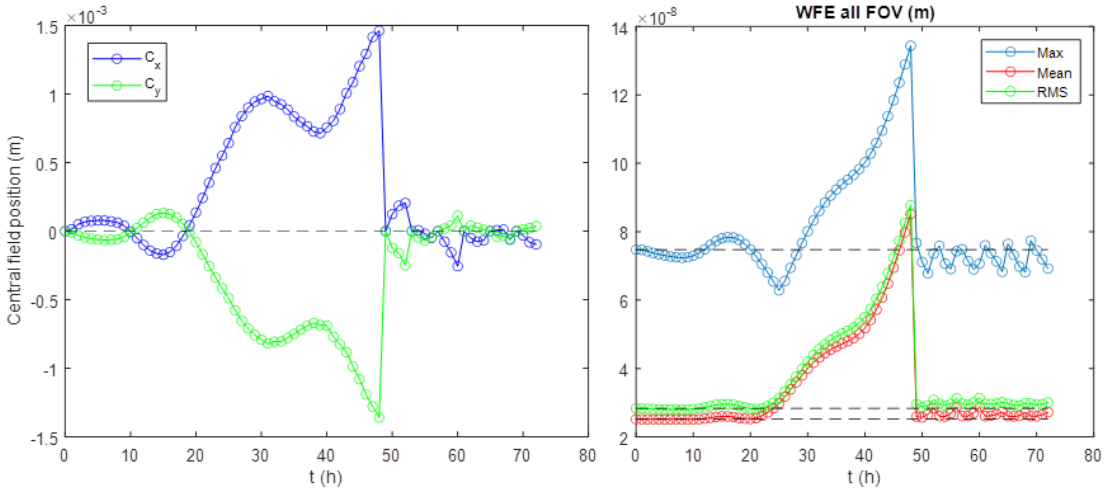

Figure 133. Position of the central field on the exit focal plane (left) and WFE on the full FOV (right) after MAORY collimation every 4 hours during third day. Dash lines refer to nominal value.

	M10M			M12M	
	dz [mm]	tilt x [arcsec]	tilt y [arcsec]	tilt x [arcsec]	tilt y [arcsec]
Maximum range	0.514	-9.6	-7.2	7.0	20.4

Table 29. Maximum range of the degrees of freedom for compensation.

Inter-epoch distortion variation has been calculated using different references, at the beginning of each night or every four hours, to estimate the residuals in the different cases and to sense the frequency required for the distortion calibration inserting the calibration unit. Results are given in Figure 134.

Residuals are negligible after the subtraction of the third order polynomial with both strategies, even if the calibration is performed only at the beginning of each night.

Summarizing, as result of the thermos-elastic simulation, MAORY could withstand an operative night and a night-to-night variation of 4 K with a collimation procedure and astrometric calibration at the beginning of the night.

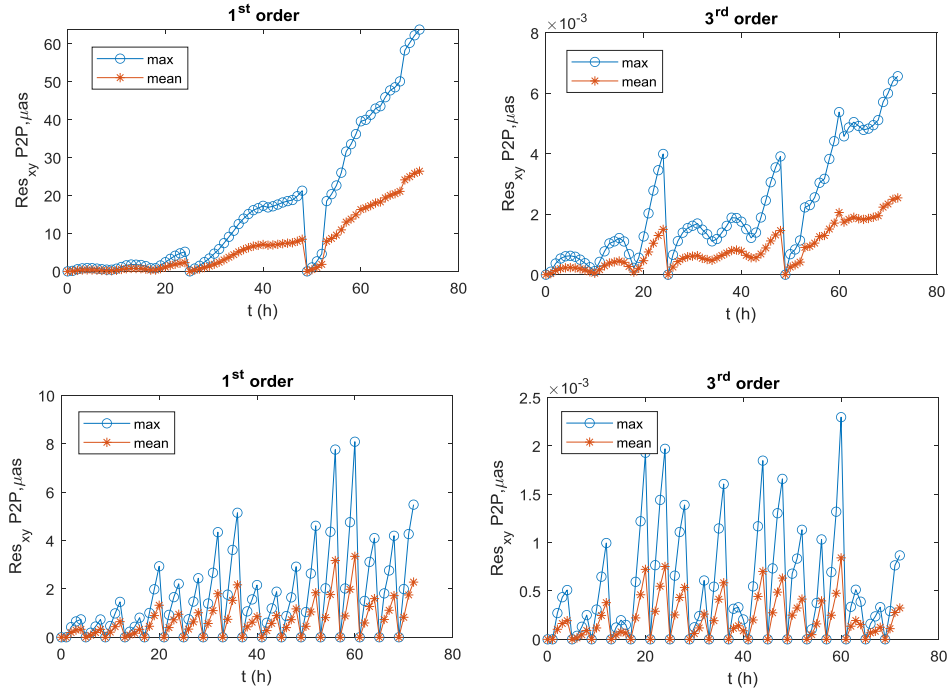

Figure 134: Inter-epoch distortion variation as function of time after first and third order polynomial subtraction, in the case of calibration performed at the beginning of each night (top) or every four hours (bottom).

5.3 Optics surface thermo-elastic deformation induced by mounts thermal loads

The temperature variation of the environment affects also the temperature of the opto-mechanical assemblies. The thermal loads generate stresses that perturb the optical surfaces figure.

The current strategy is to optimize the opto-mechanical assemblies to deliver the best performance at about 10 C. This will affect, of course, the design and manufacturing of the mountings and the gluing process.

The simulation of the thermos-elastic effect on the opto-mechanical assemblies is fully described in [RD13]. The simulation account for a temperature variation of 10 C +/- 10 C, i.e. around the temperature for which the opto-mechanical assemblies are optimized. The expected surface deformation in terms of standard Zernike polynomials are reported in Table 30.

The simulation does not consider the DMs. The strategy for the DMs is to calibrate the flat surface as function of the temperature. The description of the strategy and of the assumptions are reported in [RD11]. The expected residuals on the DMs surface variation is due to the knowledge of the DM temperature (assumed 1 K) and on the presence of spatial temperature gradient variations (0.55 K/hour in X, Y and Z direction). In the simulations, tip/tilt and defocus are not considered in the calibration process. The expected surface residuals in terms of standard Zernike polynomials are reported in Table 31.

Z RMS [nm]	CPM S1	CPM S2	M6M	M7M	M8M	DICHROIC S1	M11M	M12M
1	-15545.94	15969.39	6405.88	9959.38	9975.58	1992.51	9817.05	6364.34
2	0.40	0.40	8.23	0.18	0.19	-0.01	351.07	6.29
3	-2.59	2.60	247.70	0.38	0.40	-0.04	219.05	189.28
4	-0.13	-0.13	77.09	168.24	173.69	-0.23	85.88	64.82
5	0.08	0.08	1.04	0.00	0.00	0.01	-51.13	0.63
6	0.00	0.01	9.05	0.48	0.49	0.02	-22.54	2.94
7	0.00	0.00	3.73	0.08	0.08	0.00	0.26	1.58
8	0.00	0.00	0.01	-0.03	-0.03	0.00	-0.09	0.02
9	0.05	-0.04	0.71	2.81	3.05	0.03	0.08	-0.10
10	0.07	0.07	-0.21	0.01	0.01	0.03	-0.02	-0.10
11	0.01	0.00	-16.77	-29.01	-30.65	-0.12	4.10	-17.33
12	0.00	0.00	4.98	-0.11	-0.11	0.00	-7.45	0.82
13	-0.01	0.00	-0.01	-0.01	-0.01	0.00	-15.78	0.01
14	0.00	-0.01	0.95	-0.07	-0.08	0.00	-5.55	0.10
15	-0.01	-0.01	-0.08	-0.01	-0.01	0.00	7.50	-0.03
16	0.00	0.00	-0.03	0.01	0.01	0.00	-0.07	0.00
17	0.00	0.00	-1.32	-0.05	-0.05	0.00	0.10	-0.86
18	0.00	0.00	0.03	0.01	0.00	0.00	0.09	-0.02
19	0.00	0.00	0.58	-0.07	-0.11	0.00	0.00	-0.05
20	0.00	0.00	0.03	0.02	0.01	0.00	0.14	0.02
21	-0.01	0.00	0.11	-0.01	0.00	0.00	-0.07	-0.01
22	0.13	0.13	13.98	9.02	9.32	0.02	17.57	6.90
23	0.00	0.00	-0.02	0.01	0.01	0.00	-8.28	0.01
24	0.00	0.00	3.49	0.01	0.02	0.00	-4.01	0.63
25	0.00	0.00	-0.01	0.02	0.02	0.00	1.44	-0.04
26	0.00	0.00	0.43	0.02	0.02	0.00	-1.19	0.05
27	-0.08	0.09	-0.01	-0.01	-0.02	-0.01	0.11	-0.01
28	-0.18	-0.19	0.16	0.05	0.04	-0.37	0.72	0.35
29	0.00	0.00	1.50	0.02	0.02	0.00	0.07	0.23
30	0.00	0.00	-0.01	0.01	0.00	0.00	-0.01	-0.02
31	0.00	0.00	0.32	0.00	-0.02	0.00	0.00	-0.04
32	0.00	0.00	0.05	-0.02	-0.02	0.00	0.02	0.04
33	0.00	0.00	-0.02	0.00	0.01	0.00	0.00	-0.07
34	0.00	0.00	0.00	-0.02	-0.02	0.00	0.00	0.02
35	0.00	0.00	0.03	0.01	0.01	0.00	-0.04	0.04
36	0.00	0.00	-0.02	0.01	0.01	0.00	-0.06	0.00

Table 30. Optical surface deformation (in Zernike standard polynomials) induced by the thermos-elastic deformation of the opto-mechanical assemblies for a temperature variation of 10 degrees.

Z RMS [nm]	Z1	Z2-3	Z4	Z5-6	Z7-8	Z9-10	Z11
M9M DM1	6931.6	5169.0	44.9	15.7	0.7	3.1	2.7
M10M DM2	11363.6	23317.1	77.7	0.5	0.9	0.2	3.9

Table 31. Optical surface deformation (in Zernike standard polynomials) due to residuals of the DMs temperature calibration.

The surface deformations have been converted in the local coordinate system and inserted in the nominal Zemax model in order to estimate the impact on the WFE. The WFE has been computed before and after the collimation of MAORY. The resulting RMS WFE maps in the full FoV and in the MICADO FoV are shown in Figure 135.

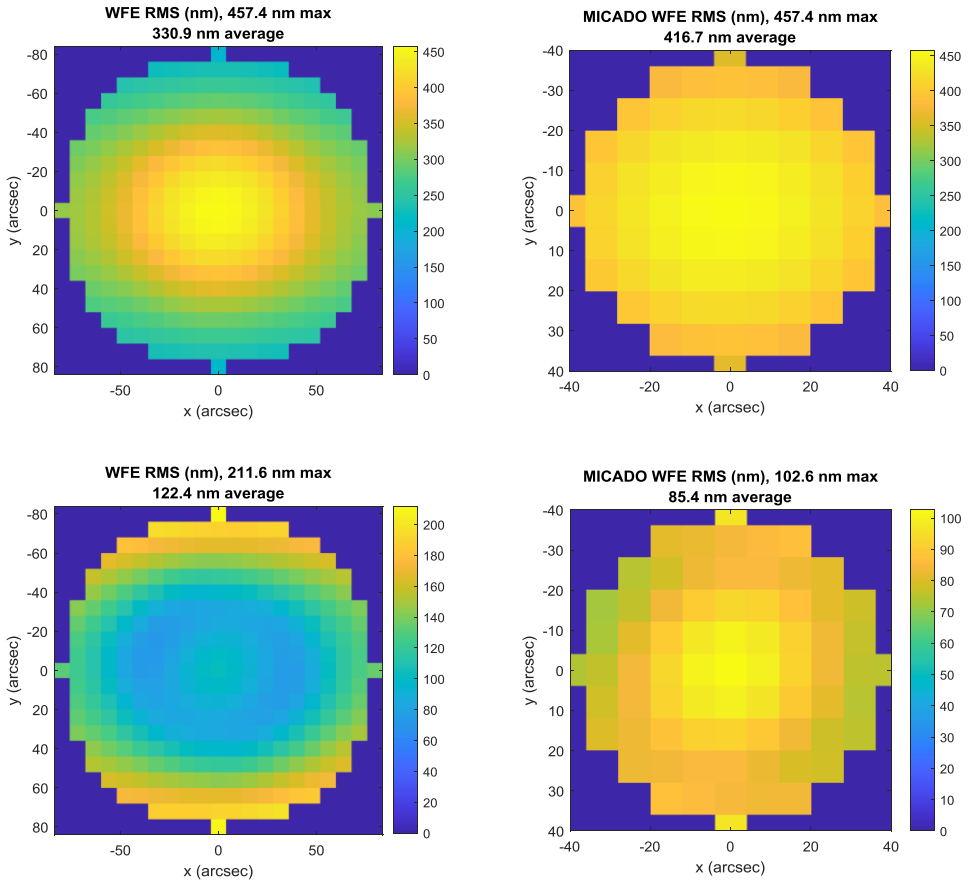

Figure 135: RMS WFE maps in the full FoV (left) and MICADO (right) before (top) and after MAORY collimation (bottom) due to 10 K temperature variation.

For a temperature variation of 10 K, the average RMS WFE in the full FoV is equal to 122.4 nm. The average RMS WFE in the MICADO FoV is equal to 85.4 nm. The average RMS WFE in the NGSWFS patrol FoV is equal to 133.1 nm.

The range of degrees of freedom of the MAORY collimation for 10 K temperature variation is reported in Table 32.

M10M			M11M		M12M	
dz	tx	ty	tx	ty	tx	ty
[mm]	[arcsec]	[arcsec]	[arcsec]	[arcsec]	[arcsec]	[arcsec]
1.082	-2.2	1.3	5.3	-1.6	0.8	-2.6

Table 32. Ranges of the degrees of freedom in the MAORY collimation for 10 K temperature variation.

We have evaluated the impact of such deformations on the inter-epoch distortion variations. The results are shown in Figure 136.

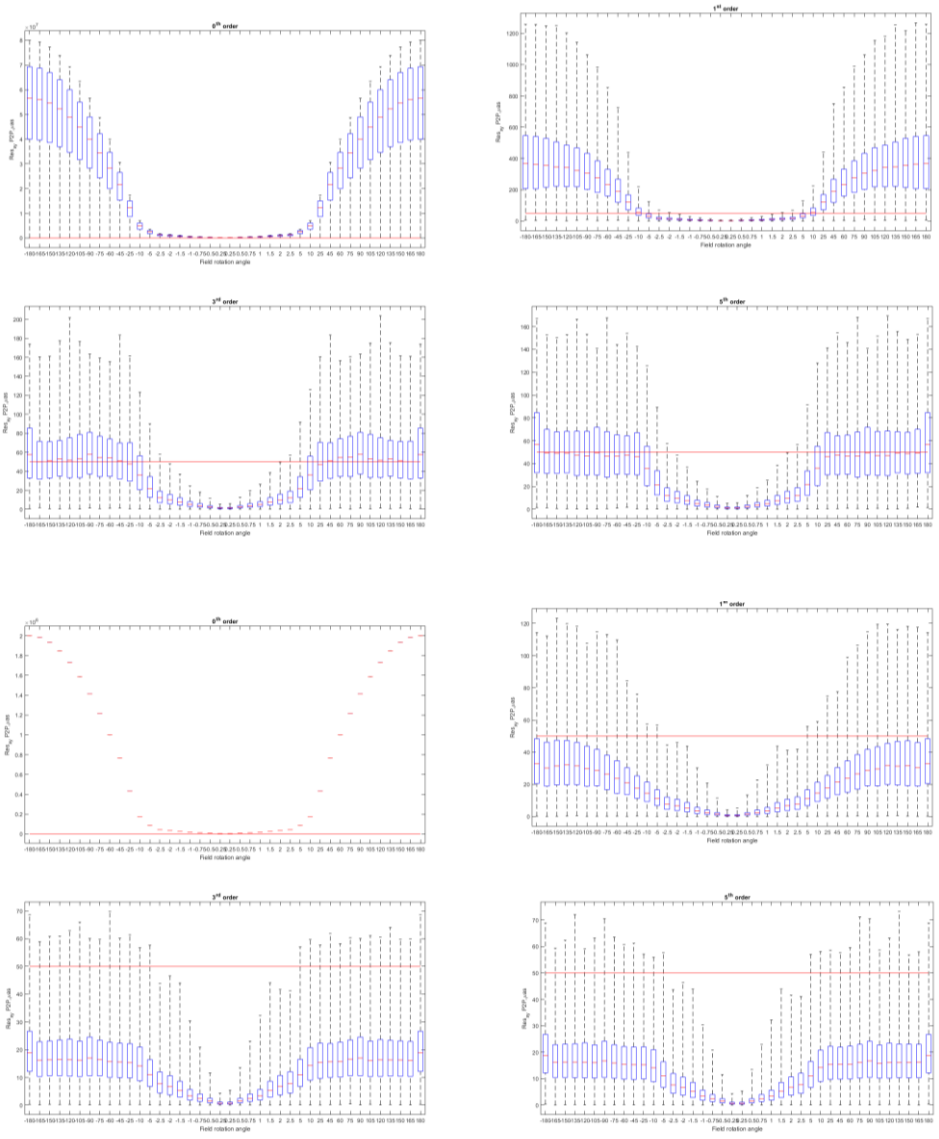

Figure 136: Variations of the residual as function of the rotation azimuthal angle over the MICADO FoV (top) and for two sources 1 arcsec apart (bottom). The central red mark indicates the median, and the bottom and top edges of the box indicate the 25th and 75th percentiles, respectively. The whiskers extend to the extreme data points.

The large part of the MICADO FoV is still within the specification of 50 µarcsec for two stars one arcsec apart. However, the impact of the mid-spatial frequencies on the optical surfaces (captured by the surfaces map sampling, 2.5 mm) is clearly the worst offender for the astrometric performance. The footprints effect of the surface residuals (especially the ones generated by surfaces close to focal planes such M12M) are still clearly visible after the 5th order polynomial fit subtractions. An example for azimuth angle 60 degrees over the MICADO FoV is shown in Figure 137.

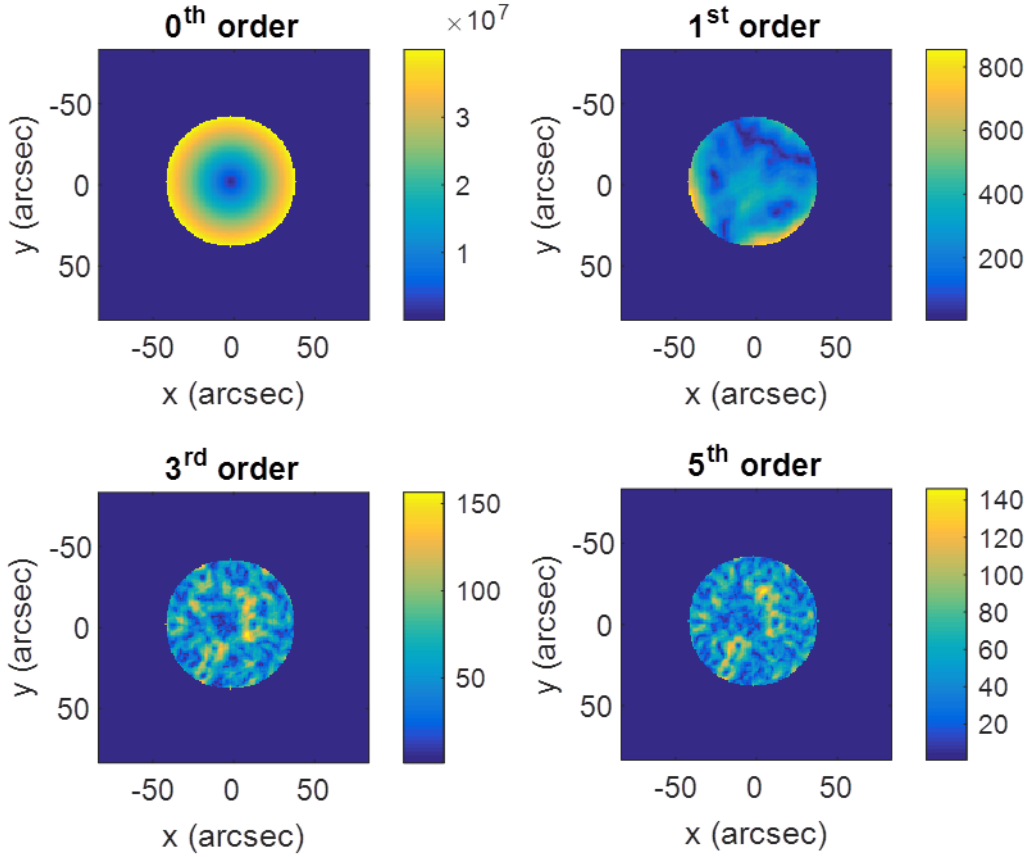

Figure 137: Residual maps for rotation azimuthal angle 60 degrees over the MICADO FoV.

5.4 Summary on WFE budget

For the as-built 'static' opto-mechanical model, the estimated RMS WFE in average on the MICADO FoV is 85 nm and in average on the NGS patrol FoV 112 nm.

The stability simulation shows that, after the collimation of MAORY, the only contributor to the WFE is the thermo-elastic deformation of the opto-mechanical assemblies. For a temperature variation of 10 K, the average RMS WFE in the full FoV is equal to 122.4 nm. The average RMS WFE in the MICADO FoV is equal to 85.4 nm. The average RMS WFE in the NGSWFS patrol FoV is equal to 133.1 nm.

MAO-SF0-1.2.4.4*: The as-built PFRO shall not introduce more than 150 nm RMS (goal 100 nm RMS) Wavefront error in average on the scientific field of view at the reference wavelength of 1 µm [RD2].*

MAO-SF0-1.2.4.3*: The as-built PFRO shall not introduce more than 200 nm RMS Wavefront error in average on the technical field of view at the reference wavelength of 1 µm [RD2].*

By applying the RSS between the 'static' average RMS WFE and the 'stability' average RMS WFE, we obtain that the estimated RMS WFE in average on the MICADO FoV is 121 nm and in average on the NGS patrol FoV 174 nm.

Even if a more consolidated analysis is required, we have estimated the impact of a MAORY collimation strategy that foresees one collimation at the beginning of the night on the WFE and pointing error.

As case study, we assumed a maximum temperature variation equal to 3 K during the night. The results are shown in Table 33.

Given that during a night the telescope pointing can range over full declination angle, we have assumed the full error for the rigid body motion. We assumed a MAORY temperature variation of 3 K with respect to the Nasmyth platform (worst case). The gradient has been considered included in the 2nd night scenario. The thermos-elastic effect of to opto-mechanical assemblies have been included by linearly scaling the variations to 3 K.

	pointing [arcsec]	Z4 [nm]	Z > Z4 [nm]
RIGID BODY MOTION	1,2	277	0
MAORY uniform T Variation	0,4	123	0
MAORY 2nd night scenario	0,4	43	25
Thermo-elastic O-M assemblies	0,0	138	17
RSS	**1,3**	**335**	**30**

Table 33. Estimated pointing error, defocus and higher order aberration for an observation night with a maximum temperature variation of 3 K.

The expected pointing variation is about 1.3 arcsec. The expected defocus variation is about 335 nm. Higher order aberration variation is about 30 nm. Such variation has to be intended on top of the WFE delivered after the collimation of MAORY.

6. ELT as-built and in-operation variation

The optical interface between the ELT telescope and the Nasmyth instruments is described in RD1. We have evaluated the impact of the ELT as-built variation range and operational variation as follow. Given that no mathematical models (e.g. Zemax files) describing the telescope variation with respect to the nominal configuration are available, we have arbitrarily varied the nominal telescope in order to reproduce the range of the parameters specified in RD1. Such a modified telescope models have been then connected to the nominal MMS model, in order to evaluate the impact on MAORY itself. Given that the representatives of such models in terms of WFE are poor, we have not evaluated wavefront-dependent parameters.

The considered parameters in the analysis are reported in Table 34.

The as-built parameters are not independents. We have modified the telescope configuration by constraining the model to have an effective focal length and an exit pupil position equal to the values at the edges of the variation ranges. The maximum (minimum) value of the effective focal length has been coupled with the maximum (minimum) value of the exit pupil position, in order to reproduce also the other parameters variation ranges (image F/#, exit pupil diameter, etc.). In the two Zemax models, mimicking these two extreme cases, we have arbitrarily varied the curvature radius of M1, M2, M3 and the relative distance of M2, M3 and focal extraction. The telescope focal plane has been maintained fixed in the nominal position. The variation of the parameters on MMS is shown in Table 35.

As built parameters						
Code	Parameter	Units	nominal	delta (+/-)	max	min
I-INS/ELT-137	Field curvature	[mm]	-9884	70	-9814	-9954
I-INS/ELT-137	Effective focal length	[mm]	684022	2933	686955	681089
I-INS/ELT-137	Image space F/#	[mm]	17,747	0,080	17,827	17,667
I-INS/ELT-137	Pupil compression	[mm]	18,06	0,04	18,10	18,02
I-INS/ELT-137	Plate scale	[mm/arcsec]	3,316	0,014	3,33	3,30
I-INS/ELT-170	Exit pupil diameter	[mm]	2134	5	2139	2129
I-INS/ELT-171	Exit pupil position	[mm]	37868	78	37946	37790

In operation parameters						
Code	Parameter	Units	nominal	delta (+/-)	max	min
I-INS/ELT-512	Pupil lateral motion	[%]	0	0,8	0,8	-0,8

Table 34. As-Built and In-Operation ELT parameters and variation ranges.

As built parameters: impact on MAORY		
Parameter	Units	delta (+/-)
Field curvature	[mm]	-
Effective focal length	[mm]	2930
Image space F/#	[mm]	0,077
Plate scale	[mm/arcsec]	0,014
Exit pupil diameter	[mm]	2,84
Exit pupil position	[mm]	11,3
LGSO working F/#		0,020

Table 35. As-Built ELT parameters impacts on MMS.

The as-built parameters does not change the footprints center but varies their size. The maximum footprint envelope semi-axis variation on the main path is reported in Table 36.

The in-operation parameter has been simulated by changing the tip/tilt of M4 and M5 in order to reproduce the exit pupil decenter as specified. The telescope focal plane has been maintained fixed and, in particular, the on-axis field lies on the center of the focal plane.

The MMS exit pupil varies, as expected, by the same percentage 0.8% (6.5 mm) in all the direction consistently. The pupil shift does not change the size of the footprints but it moves their centres. We have computed the maximum relative decenter variation of the footprints envelope with respect to the aperture center for each surface. For the main path, the results are reported in Table 37.

	maximum footprint semi-axis variation	
	X [mm]	Y [mm]
CPM S1	1.7	1.7
CPM S2	1.7	1.7
M6M	0.8	1.0
M7M	0.4	0.4
M8M	0.5	0.5
M9M	1.0	1.1
M10M	2.2	2.2
Dichroic S1	1.2	1.2
Dichroic S2	1.2	1.1
M11M	0.7	0.5
MICADO Mec	0.2	0.2
M12M	0.6	0.7

Table 36. Maximum footprint envelope semi axis variation due to as-built ELT on main path.

	maximum footprint relative decenter wrt aperture center	
	X [mm]	Y [mm]
CPM S1	0.2	0.2
CPM S2	0.2	0.2
M6M	1.5	1.7
M7M	3.6	3.8
M8M	5.3	5.4
M9M	5.1	5.2
M10M	8.1	8.2
Dichroic S1	5.8	5.8
Dichroic S2	5.8	5.8
M11M	5.2	3.5
MICADO Mec	2.4	2.4
M12M	1.3	1.5

Table 37. Maximum footprint envelope decenter with respect to the aperture center due to in-operation ELT on main path.

7. Appendix A – Coordinates reference systems

The MAORY **standard global coordinate system** is aligned with telescope standard absolute coordinate systems (see [RD16]), with its origin at (-27200, 0, 0) mm.

For each optical surface, we defined two local coordinate systems:

- The **optical local coordinate system**, corresponding to the local coordinate system of the Zemax model. The optical local coordinate system for any surface is shown in Figure 138 - Figure 140.
- The **standard local coordinate system**, as parent frame of the optical local coordinate system. It is centred to the optical local coordinate system and built with the following conventions for any physical surface: the z axis is coincident with the z axis of the optical local coordinate system, but always exiting the physical surface; the y axis is in the plane formed by the z axis and the gravity vector, oriented against gravity. The standard local coordinate system for any surface is shown in Figure 141 - Figure 143.

The rotation matrices between the standard global reference system and the two local reference systems are reported in Table 38.

For the moving mirror M11M, we consider as nominal configuration the one directed to the first port, where MICADO is installed.

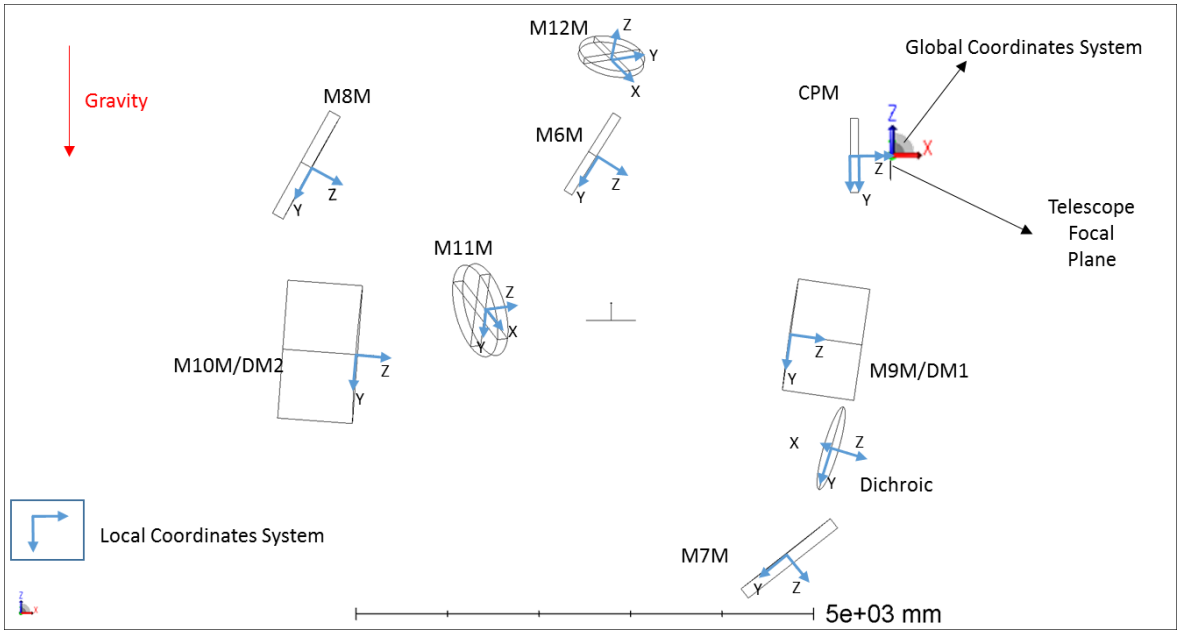

Figure 138: Optical local coordinate system for each optical surface in MAORY MPO.

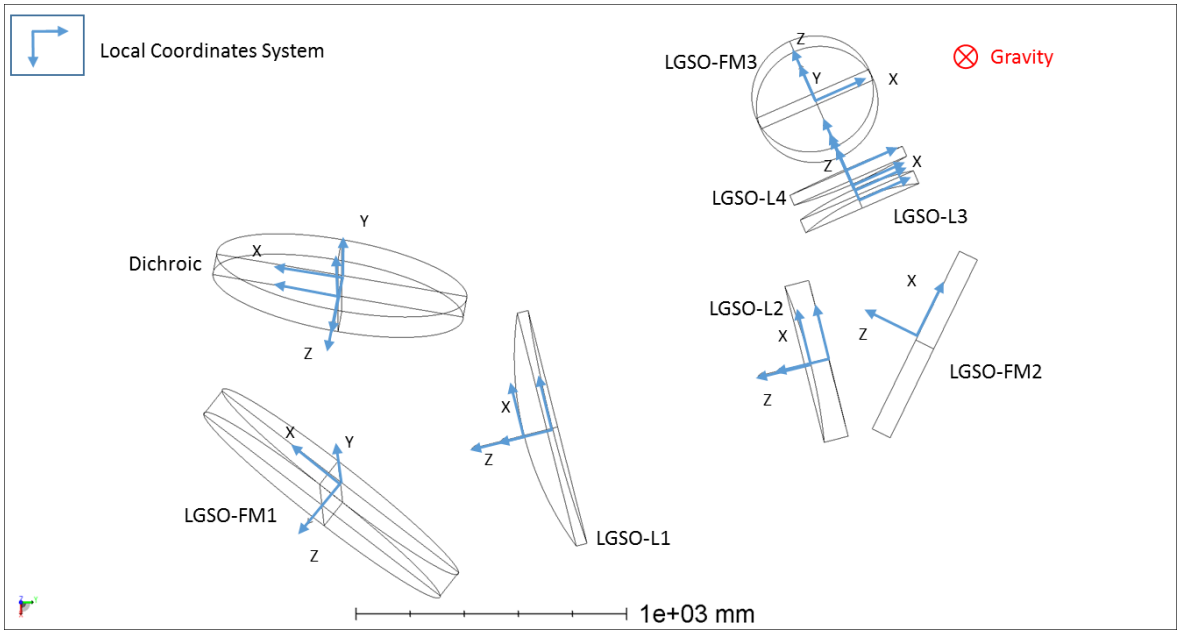

Figure 139: Optical local coordinate system for each optical surface in MAORY LGSO.

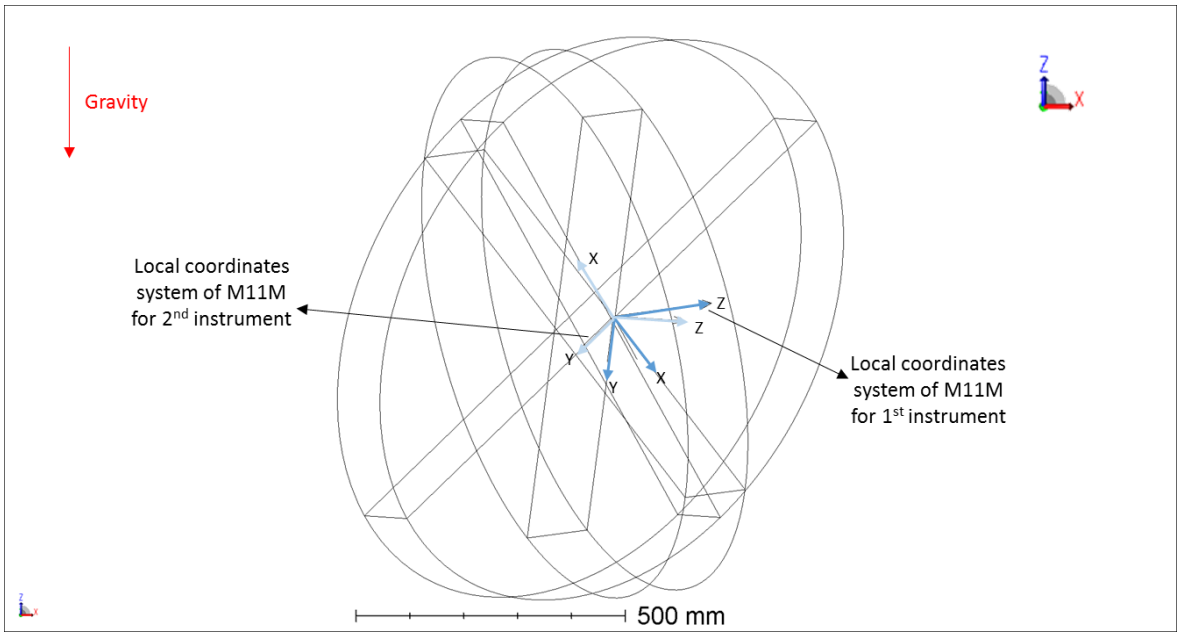

Figure 140: Optical local coordinate system of M11M.

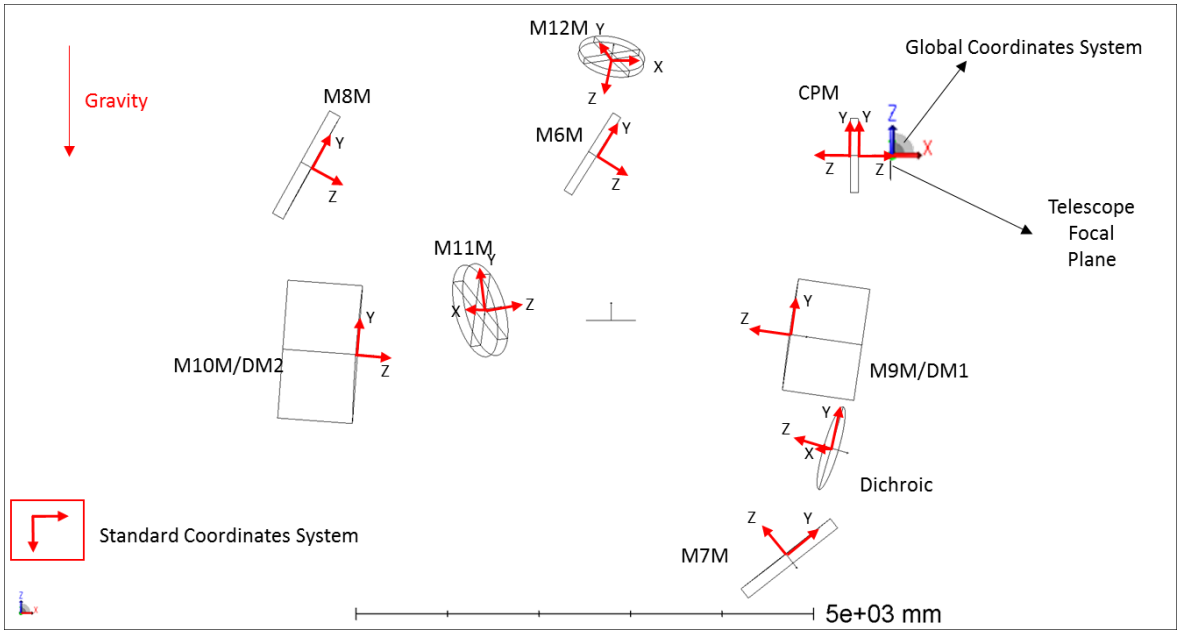

Figure 141: Standard local coordinate system for each optical surface in MAORY MPO.

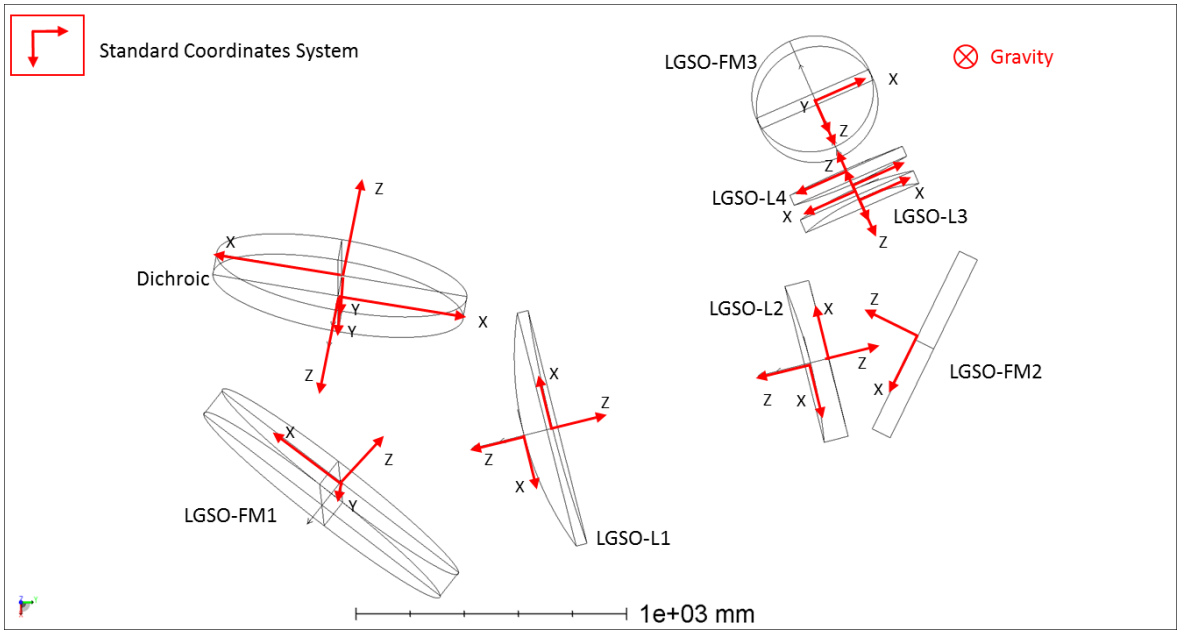

Figure 142: Standard local coordinate system for each optical surface in MAORY LGSO.

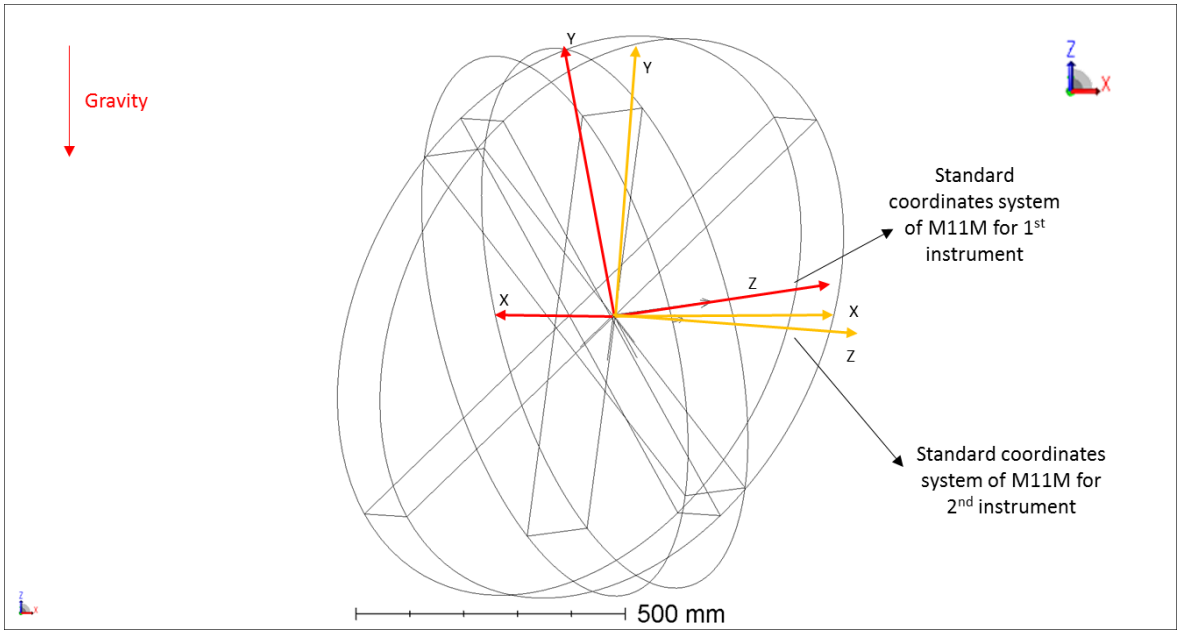

Figure 143: Standard local coordinate system of M11M.

Table 38: Roto-translation matrices of the local coordinate systems.

ELEMENT	SURFACE	OPTICAL LOCAL COORDINATE SYSTEM				STANDARD LOCAL COORDINATE SYSTEM			
		R			O	R			O
CPM	**S1**	0.000	0.000	1.000	-350.000	0.000	0.000	1.000	-350.000
		-1.000	0.000	0.000	0.000	1.000	0.000	0.000	0.000
		0.000	-1.000	0.000	0.000	0.000	1.000	0.000	0.000
CPM	**S2**	0.000	0.000	1.000	-435.000	0.000	0.000	-1.000	-435.000
		-1.000	0.000	0.000	0.000	-1.000	0.000	0.000	0.000
		0.000	-1.000	0.000	0.000	0.000	1.000	0.000	0.000
M6M		0.000	-0.534	0.845	-3206.217	0.000	0.534	0.845	-3206.217
		-1.000	0.000	0.000	0.000	1.000	0.000	0.000	0.000
		0.000	-0.845	-0.534	0.000	0.000	0.845	-0.534	0.000
M7M		0.000	-0.787	0.617	-1139.020	0.000	0.787	-0.617	-1139.020
		-1.000	0.000	0.000	0.000	-1.000	0.000	0.000	0.000
		0.000	-0.617	-0.787	-4353.506	0.000	0.617	0.787	-4353.506
M8M		0.000	-0.487	0.873	-6327.054	0.000	0.487	0.873	-6327.054
		-1.000	0.000	0.000	0.000	1.000	0.000	0.000	0.000
		0.000	-0.873	-0.487	-131.581	0.000	0.873	-0.487	-131.581
M9M		0.000	-0.144	0.990	-1101.521	0.000	0.144	-0.990	-1101.521
		-1.000	0.000	0.000	0.000	-1.000	0.000	0.000	0.000
		0.000	-0.990	-0.144	-1952.463	0.000	0.990	0.144	-1952.463
M10M		0.000	-0.074	0.997	-5840.655	0.000	0.074	0.997	-5840.655
		-1.000	0.000	0.000	0.000	1.000	0.000	0.000	0.000
		0.000	-0.997	-0.074	-2173.139	0.000	0.997	-0.074	-2173.139
Dichroic	**S1**	-0.167	-0.281	0.945	-645.752	-0.182	0.273	-0.945	-645.752
		-0.985	0.000	-0.174	0.000	-0.983	-0.050	0.174	0.000
		0.049	-0.960	-0.277	-3195.387	0.000	0.961	0.277	-3195.387
M11M 1st instrument		0.397	-0.112	0.911	-4426.382	-0.397	-0.111	0.911	-4426.382
		-0.759	0.518	0.394	1483.861	0.918	-0.048	0.394	1483.861
		-0.516	-0.848	0.121	-1676.202	0.000	0.993	0.121	-1676.202
M12M		0.859	0.492	0.146	-3050.000	0.957	-0.252	-0.146	-3050.000
		-0.496	0.725	0.478	6000.000	-0.292	-0.828	-0.478	6000.000

		0.130	-0.483	0.866	1047.272	0.000	0.500	-0.866	1047.272
		-0.624	0.438	0.647	-4426.382	0.762	0.028	0.647	-4426.382
M11M 2nd instrument		-0.497	0.417	-0.761	1483.861	0.648	-0.033	-0.761	1483.861
		-0.604	-0.796	-0.043	-1676.202	0.000	0.999	-0.043	-1676.202
		-0.167	-0.281	0.945	-570.164	0.182	0.273	0.945	-570.164
Dichroic	**S2**	-0.985	0.000	-0.174	-13.959	0.983	-0.050	-0.174	-13.959
		0.049	-0.960	-0.277	-3217.561	0.000	0.961	-0.277	-3217.561
		-0.604	-0.170	0.779	117.578	-0.620	0.096	-0.779	117.578
LGSO-FM1		-0.788	-0.019	-0.615	-4.487	-0.785	-0.076	0.615	-4.487
		0.119	-0.985	-0.123	-3348.076	0.000	0.992	0.123	-3348.076
		-0.969	0.000	0.245	-54.218	0.969	0.000	0.245	-54.218
LGSO-L1	**S1**	-0.245	0.000	-0.969	674.104	0.245	0.000	-0.969	674.104
		0.000	-1.000	0.000	-3348.076	0.000	1.000	0.000	-3348.076
		-0.969	0.000	0.245	-80.723	-0.969	0.000	-0.245	-80.723
LGSO-L1	**S2**	-0.245	0.000	-0.969	778.801	-0.245	0.000	0.969	778.801
		0.000	-1.000	0.000	-3348.076	0.000	1.000	0.000	-3348.076
		-0.969	0.000	0.245	-322.218	0.969	0.000	0.245	-322.218
LGSO-L2	**S1**	-0.245	0.000	-0.969	1732.707	0.245	0.000	-0.969	1732.707
		0.000	-1.000	0.000	-3348.076	0.000	1.000	0.000	-3348.076
		-0.969	0.000	0.245	-339.398	-0.969	0.000	-0.245	-339.398
LGSO-L2	**S2**	-0.245	0.000	-0.969	1800.566	-0.245	0.000	0.969	1800.566
		0.000	-1.000	0.000	-3348.076	0.000	1.000	0.000	-3348.076
		-0.898	0.000	-0.440	-422.841	0.898	0.000	-0.440	-422.841
LGSO-FM2		0.440	0.000	-0.898	2130.168	-0.440	0.000	-0.898	2130.168
		0.000	-1.000	0.000	-3348.076	0.000	1.000	0.000	-3348.076
		-0.400	0.000	-0.917	-927.011	-0.400	0.000	0.917	-927.011
LGSO-L3	**S1**	0.917	0.000	-0.400	1910.366	0.917	0.000	0.400	1910.366
		0.000	-1.000	0.000	-3348.076	0.000	1.000	0.000	-3348.076
		-0.400	0.000	-0.917	-963.678	0.400	0.000	-0.917	-963.678
LGSO-L3	**S2**	0.917	0.000	-0.400	1894.380	-0.917	0.000	-0.400	1894.380
		0.000	-1.000	0.000	-3348.076	0.000	1.000	0.000	-3348.076
		-0.400	0.000	-0.917	-982.011	-0.400	0.000	0.917	-982.011
LGSO-L4	**S1**	0.917	0.000	-0.400	1886.387	0.917	0.000	0.400	1886.387
		0.000	-1.000	0.000	-3348.076	0.000	1.000	0.000	-3348.076
		-0.400	0.000	-0.917	-1037.011	0.400	0.000	-0.917	-1037.011
LGSO-L4	**S2**	0.917	0.000	-0.400	1862.409	-0.917	0.000	-0.400	1862.409
		0.000	-1.000	0.000	-3348.076	0.000	1.000	0.000	-3348.076
		-0.400	-0.648	-0.648	-1293.679	-0.400	0.648	0.648	-1293.679
LGSO-FM3		0.917	-0.283	-0.283	1750.509	0.917	0.283	0.283	1750.509
		0.000	-0.707	0.707	-3348.076	0.000	0.707	-0.707	-3348.076

***** End of document *****